Coupling of the Finite Element Method and the Boundary Element Method for the multi-physic modeling of magnetoelectric effects in composite structures

Alberto Urdaneta Calzadilla

THÈSE

Pour obtenir le grade de

DOCTEUR DE L'UNIVERSITÉ GRENOBLE ALPES

École doctorale : EEATS - Electronique, Electrotechnique, Automatique, Traitement du Signal (EEATS)
Spécialité : Génie électrique
Unité de recherche : Laboratoire de Génie Electrique

Modélisation multiphysique des effets magnétoélectriques dans les structures composites par couplage de la méthode des éléments finis et de la méthode des éléments de frontière.

Coupling of the Finite Element Method and the Boundary Element Method for the multi-physics modeling of magnetoelectric effects in composite structures.

Présentée par :

Alberto URDANETA CALZADILLA

Direction de thèse :

Olivier CHADEBEC DIRECTEUR DE RECHERCHE, CNRS	Directeur de thèse
Nicolas GALOPIN MAITRE DE CONFERENCES, Université Grenoble Alpes	Co-directeur de thèse
Innocent NIYONZIMA MAITRE DE CONFERENCES,Université Grenoble-Alpes	Co-encadrant de thèse

Rapporteurs :

Ruth VAZQUEZ SABARIEGO
PROFESSEUR ASSOCIE, Katholieke Universiteit Leuven
Xavier MININGER
PROFESSEUR DES UNIVERSITES, Université Paris-Saclay

Thèse soutenue publiquement le **12 juin 2023**, devant le jury composé de :

Olivier CHADEBEC DIRECTEUR DE RECHERCHE, CNRS	Directeur de thèse
Ruth VAZQUEZ SABARIEGO PROFESSEUR ASSOCIE, Katholieke Universiteit Leuven	Rapporteure
Xavier MININGER PROFESSEUR DES UNIVERSITES, Université Paris-Saclay	Rapporteur
Laurent KRAHENBUHL DIRECTEUR DE RECHERCHE EMERITE, CNRS	Examinateur
Jérôme DELAMARE PROFESSEUR DES UNIVERSITES, GRENOBLE INP	Président

Invités :

Nicolas GALOPIN
MAITRE DE CONFERENCES, Université Grenoble Alpes
Innocent NIYONZIMA
MAITRE DE CONFERENCES, Université Grenoble Alpes

Abstract

Energy conversion in electrical transducers or actuators is based on electromagnetic interactions, which link the electromotive force to temporal variations of the magnetic flux density. However, these phenomena are sometimes difficult to exploit, especially for small devices submitted to very low frequency fields. The use of active composite structures, in particular, magnetoelectric composite structures can help address this issue. The magnetoelectric coupling consists in the existence of an electric polarization induced by a magnetization or, conversely, of a magnetization induced by an electric polarization. In this thesis, such coupling is obtained by the mechanical association of piezoelectric and magnetostrictive materials. This work concerns the numerical modeling of problems involving magnetoelectric structures. Although the reference method for modeling this type of problems is the finite element method (FEM), it has several drawbacks related to the need to consider a big enough air region, whose size and mesh are related to the accuracy of the solution. The coupling of FEM with the boundary element method (BEM) allows overcoming these problems. In this thesis, a FEM-BEM coupling to the modeling of magnetoelectric composite structures is developed. Three formulations of the problem are proposed with relevant constitutive laws for electro-mechanical and magneto-mechanical coupling. From a numerical point of view, this coupling between the FEM and the BEM induces challenges in the resolution of the discrete system of equations, overcome by the use of a dedicated algorithm. The proposed modeling approaches are applied to the modeling of two devices. The first, an energy harvester in the form of a three-layer structure, the second, a rotating coilless magnetoelectric device, which can be both used as an alternating voltage generator and an actuator.

Keywords: magnetoelectric, FEM, BEM, FEM-BEM coupling, multi-physics, magnetostriction, piezoelectricity, block Gauss-Seidel method, rotating coilless ME device.

Résumé

La conversion d'énergie dans les transducteurs ou les actionneurs électriques est basée sur les interactions électromagnétiques, qui lient la force électromotrice aux variations temporelles du flux magnétique. Cependant, ces phénomènes sont parfois difficiles à exploiter, en particulier pour les dispositifs de faibles dimensions, soumis à des champs de très basse fréquence. L'utilisation de structures composites actives, en particulier de structures composites magnétoélectriques, peut permettre de résoudre ce problème. Le couplage magnétoélectrique consiste en l'existence d'une polarisation électrique induite par une aimantation ou, inversement, d'une aimantation induite par une polarisation électrique. Dans cette thèse, ce couplage est obtenu par l'association mécanique de matériaux piézoélectriques et magnétostrictifs. Ce travail concerne la modélisation numérique de problèmes impliquant des structures magnétoélectriques. Bien que la méthode de référence pour modéliser ce type de problèmes soit la méthode des éléments finis (FEM), elle présente plusieurs inconvénients liés à la nécessité de considérer une région d'air suffisamment grande, dont la taille et le maillage influent fortement sur la précision de la solution. Le couplage de la méthode des éléments finis avec la méthode des éléments de frontière (BEM) permet de surmonter ces problèmes. Dans cette thèse, un couplage FEM-BEM pour la modélisation des structures composites magnétoélectriques est développé. Trois formulations du problème sont proposées avec des lois constitutives pertinentes pour le couplage électro-mécanique et magnéto-mécanique. D'un point de vue numérique, ce couplage entre FEM et BEM induit des difficultés dans la résolution des équations discrètes, surmontés par l'utilisation d'un algorithme approprié. Les approches de modélisation proposées sont appliquées à la modélisation de deux dispositifs. Le premier, un récupérateur d'énergie sous la forme d'une structure tri-couche, le second d'un dispositif magnétoélectrique rotatif sans bobines, qui peut être utilisé à la fois comme générateur de tension alternative et comme actionneur.

Mots-cléfs: magnétoélectrique, FEM, BEM, couplage FEM-BEM, multiphysique, magnétostriction, piézoélectricité, méthode de Gauss-Seidel par bloc, dispositif ME rotatif sans bobines.

Contents

List of Figures

List of Tables

Notations and Definitions

Fields

Table 0.1 presents the used physical fields encountered in this manuscript.

Table 0.1: Magnetic, electric and mechanical fields and their SI-Units

Symbol	Description	SI-unit
G	Gibbs free energy	J
ψ	Helmholtz free energy	J
$\boldsymbol{f}$	Body forces density	$\mathrm{N\,m^{-3}}$
$\boldsymbol{S}$	Linear strain tensor	-
$\boldsymbol{T}$	Cauchy stress tensor	Pa
$\boldsymbol{u}$	Mechanical displacement	m
ϱ	Mass density	$\mathrm{kg\,m^{-3}}$
ρ	Electric volume charge density	$\mathrm{C\,m^{-3}}$
Q_S	Electric surface charge density	$\mathrm{C\,m^{-2}}$
$\boldsymbol{E}$	Electric field	$\mathrm{V\,m^{-1}}$
$\boldsymbol{D}$	Electric displacement	$\mathrm{C\,m^{-2}}$
φ	Electric scalar potential	V
$\boldsymbol{J}$	Electric current density	$\mathrm{A\,m^{-2}}$
I	Electric current	A - At
$\boldsymbol{P}$	Electric polarization density	$\mathrm{C\,m^{-2}}$
$\boldsymbol{H}$	Magnetic field	$\mathrm{A\,m^{-1}}$
$\boldsymbol{B}$	Magnetic flux density	T
$\boldsymbol{M}$	Magnetization density	$\mathrm{A\,m^{-1}}$
ϕ_{red}	Magnetic reduced scalar potential	A
$\boldsymbol{a}$	Magnetic vector potential	$\mathrm{T\,m^{-3}}$
θ	temperature	K

η	entropy	$\mathrm{J\,K^{-1}}$

Coupling tensors

Table 0.2 recapitulates the coupling tensors present in this manuscript.

Table 0.2: Constitutive laws for passive materials

Coupling Tensor	description	SI-Units
μ	magnetic permeability tensor	$\mathrm{H\,m^{-1}}$
ν	magnetic reluctivity tensor	$\mathrm{m\,H^{-1}}$
ε	electric permittivity tensor	$\mathrm{F\,m^{-1}}$
$\boldsymbol{c}$	fourth order elasticity tensor	Pa
$\boldsymbol{s}$	fourth order rigidity tensor	$\mathrm{Pa^{-1}}$
$\boldsymbol{e}$	third order piezoelectric tensor	$\mathrm{N\,V^{-1}\,m^{-1}}$
$\boldsymbol{h}$	third order piezomagnetic tensor	$\mathrm{N\,T^{-1}\,m^{-2}}$
$\boldsymbol{q}$	third order piezoelectric tensor	$\mathrm{N\,A^{-1}\,m^{-1}}$

Operators

The operators used in the presented mathematical developments are defined in Table 0.3, using a Cartesian coordinate system.

Table 0.3: Operators

Symbol	Description
∇	partial differential operator
$\nabla\cdot$	divergence operator
$\nabla\times$	curl operator
Δ	Laplacian operator
$\cdot$	dot product
:	double dot product
$\times$	vector product
tr	trace of a tensor
${}^{t}\bullet$	transpose of tensor

For vectors $\boldsymbol{u}$ and $\boldsymbol{v}$, second order tensors $\boldsymbol{T}$ and $\boldsymbol{S}$, fourth order tensor $\boldsymbol{c}$, a third order tensor $\boldsymbol{h}$, $\boldsymbol{e}_i,\ i \in \{1,2,3\}$ an orthonormal base of $\mathbb{R}^3$ and using Einstein's notation (sum on repeating indices), the previous operators are defined as follows.

Scalar product

$$\boldsymbol{u} \cdot \boldsymbol{v} = u_i v_i, \tag{0.1}$$
$$(\boldsymbol{T} \cdot \boldsymbol{v})_i = T_{ij} v_j, \tag{0.2}$$
$$(\boldsymbol{S} \cdot \boldsymbol{T})_{ij} = T_{ik} S_{kj}, \tag{0.3}$$
$$(\boldsymbol{h} \cdot \boldsymbol{u})_{ij} = h_{ijk} u_k, \tag{0.4}$$

Double dot product

$$\boldsymbol{S} : \boldsymbol{T} = T_{ij} S_{ij}, \tag{0.5}$$
$$(\boldsymbol{c} : \boldsymbol{S})_{ij} = c_{ijkl} S_{kl}, \tag{0.6}$$
$$(\boldsymbol{h} : \boldsymbol{S})_i = h_{ijk} S_{jk}, \tag{0.7}$$

Vector product

$$\boldsymbol{u} \times \boldsymbol{v} = \begin{pmatrix} u_2 v_3 - u_3 v_2 \\ u_3 v_1 - u_1 v_3 \\ u_1 v_2 - u_2 v_1 \end{pmatrix} \tag{0.8}$$

Transpose operator

$${}^{\mathrm{t}}(T_{ij}) = T_{ji} \tag{0.9}$$
$${}^{\mathrm{t}}(h_{ijk}) = h_{kij} \tag{0.10}$$
$$\tag{0.11}$$

Voigt notation

The fourth order elasticity tensor, the third order piezoelectric tensor and the second order Cauchy stress tensor and strain tensor have the following symmetries,

$$\boldsymbol{c}_{ijkl} = \boldsymbol{c}_{ijlk} = \boldsymbol{c}_{jikl} = \boldsymbol{c}_{klij}, \tag{0.12}$$
$$\boldsymbol{e}_{ijk} = \boldsymbol{e}_{ikj}, \tag{0.13}$$
$$\boldsymbol{T}_{ij} = \boldsymbol{T}_{ji}, \tag{0.14}$$
$$\boldsymbol{S}_{ij} = \boldsymbol{S}_{ji}, \tag{0.15}$$

they can then be written in matrix form with the following notation rules [17]:

Table 0.4: Index change from tensor to Voigt notation

ij or kl	p or q
11	1
22	2
33	3
23 or 32	4
13 or 31	5
12 or 21	6

The second order tensors, $\boldsymbol{T}$ and $\boldsymbol{S}$ can be written in vector form as,

$$\boldsymbol{T} \equiv {}^{\mathrm{t}}(T_{11}, T_{22}, T_{33}, T_{23}, T_{13}, T_{13}), \tag{0.16}$$
$$\boldsymbol{S} \equiv {}^{\mathrm{t}}(S_{11}, S_{22}, S_{33}, 2S_{23}, 2S_{13}, 2S_{13}). \tag{0.17}$$

The fourth order tensor $\boldsymbol{c}$, becomes the matrix,

$$
\begin{aligned}
\boldsymbol{c} &\equiv \begin{bmatrix}
c_{1111} & c_{1122} & c_{1133} & c_{1123} & c_{1113} & c_{1112} \\
 & c_{2222} & c_{2233} & c_{2223} & c_{2213} & c_{2212} \\
 & & c_{3333} & c_{3323} & c_{3313} & c_{3312} \\
 & \text{sym} & & c_{2323} & c_{2313} & c_{2312} \\
 & & & & c_{13} & c_{1312} \\
 & & & & & c_{1212}
\end{bmatrix} \\
&\equiv \begin{bmatrix}
c_{11} & c_{12} & c_{13} & c_{14} & c_{15} & c_{16} \\
 & c_{22} & c_{23} & c_{24} & c_{25} & c_{26} \\
 & & c_{33} & c_{34} & c_{35} & c_{36} \\
 & \text{sym} & & c_{44} & c_{45} & c_{46} \\
 & & & & c_{55} & c_{56} \\
 & & & & & c_{66}
\end{bmatrix}.
\end{aligned}
\tag{0.18}
$$

The third order tensor $\boldsymbol{e}$ becomes,

$$
\begin{aligned}
\boldsymbol{e} &\equiv \begin{bmatrix}
e_{111} & e_{122} & e_{133} & e_{123} & e_{113} & e_{112} \\
e_{211} & e_{222} & e_{233} & e_{223} & e_{213} & e_{212} \\
e_{311} & e_{322} & e_{333} & e_{323} & e_{313} & e_{312}
\end{bmatrix} \\
&\equiv \begin{bmatrix}
e_{11} & e_{12} & e_{13} & e_{14} & e_{15} & e_{16} \\
e_{21} & e_{22} & e_{23} & e_{24} & e_{25} & e_{26} \\
e_{31} & e_{32} & e_{33} & e_{34} & e_{35} & e_{36}
\end{bmatrix}
\end{aligned}
\tag{0.19}
$$

and so on for the third order tensors $\boldsymbol{h}$ and $\boldsymbol{q}$

Differentiation of vector or tensor quantities

The differentiation of scalar or vector quantities in respect to vectors or tensors is defined as follows: for ease of reading, by

$$
\boldsymbol{H} = \frac{\partial \psi}{\partial \boldsymbol{B}}, \tag{0.20}
$$

it is meant,

$$
\forall i \in \{1,2,3\}, \quad \forall \boldsymbol{x} \in \Omega,\ H_i(\boldsymbol{x}) = \frac{\partial \psi}{\partial B_i}(\boldsymbol{x}). \tag{0.21}
$$

with $\Omega \subset \mathbb{R}^3$ a volume domain. Equivalently, by,

$$\boldsymbol{T} = \frac{\partial \psi}{\partial \boldsymbol{S}}, \tag{0.22}$$

it is meant :

$$\forall (i,j) \in \{1,2,3\}^2, \quad \forall \boldsymbol{x} \in \Omega,\ T_{ij}(\boldsymbol{x}) = \frac{\partial \psi}{\partial S_{ij}}(\boldsymbol{x}). \tag{0.23}$$

Henceforth, the heavy $\forall \boldsymbol{x} \in \Omega$ and $\forall \boldsymbol{x} \in \mathbb{R}^3$ will be implicit in most presented differential field equations.

Function spaces

The use of the Finite Element Method and the Boundary Element Method requires the introduction of some function spaces for the considered fields. For this purpose, let us consider a domain $\Omega \subset \mathbb{R}^3$. Let us denote $L^2(\Omega)$ and $\boldsymbol{L^2}(\Omega)$ the functional spaces of Lebesgue integrable fields, defined for a scalar field v or a vector field $\boldsymbol{v}$ as,

$$L^2(\Omega) = \{v : \Omega \to \mathbb{R} \ \Big| \int_\Omega |v|^2 \ d\Omega < \infty\}, \tag{0.24}$$

$$\boldsymbol{L^2}(\Omega) = \{\boldsymbol{v} : \Omega \to \mathbb{R}^3 \ \Big| \int_\Omega |\boldsymbol{v}|^2 \ d\Omega < \infty\}, \tag{0.25}$$

equipped with the scalar products and induced norms:

$$(u,v)_\Omega \coloneqq \int_\Omega u\ v\ d\Omega, \tag{0.26}$$

$$(\boldsymbol{u},\boldsymbol{v})_\Omega \coloneqq \int_\Omega \boldsymbol{u} \cdot \boldsymbol{v}\ d\Omega, \tag{0.27}$$

$$\|u\|_{L^2(\Omega)} \coloneqq \sqrt{(u,u)_\Omega}, \tag{0.28}$$

$$\|\boldsymbol{u}\|_{\boldsymbol{L}^2_{(\Omega)}} \coloneqq \sqrt{(\boldsymbol{u},\boldsymbol{u})_\Omega} \tag{0.29}$$

From these function spaces, the following sub-spaces, related to the gradients, curl and divergence of integrable fields, are defined [18] [19]:

$$H_{\text{grad}}(\Omega) \coloneqq \{u \in L^2(\Omega) \;\big|\; \nabla u \in \boldsymbol{L}^2(\Omega)\}, \tag{0.30}$$

$$H_{\text{curl}}(\Omega) \coloneqq \{u \in \boldsymbol{L}^2(\Omega) \;\big|\; \nabla \times u \in \boldsymbol{L}^2(\Omega)\}, \tag{0.31}$$

$$H_{\text{div}}(\Omega) \coloneqq \{u \in \boldsymbol{L}^2(\Omega) \;\big|\; \nabla \cdot f \in L^2(\Omega)\}, \tag{0.32}$$

equipped with the inner products,

$$(u, v)_{H_{\text{grad}}(\Omega)} \coloneqq (u, v)_\Omega + (\nabla \boldsymbol{u}, \nabla \boldsymbol{v})_\Omega, \tag{0.33}$$

$$(\boldsymbol{u}, \boldsymbol{v})_{H_{\text{curl}}(\Omega)} \coloneqq (\boldsymbol{u}, \boldsymbol{v})_\Omega + (\nabla \times \boldsymbol{u}, \nabla \times \boldsymbol{v})_\Omega, \tag{0.34}$$

$$(\boldsymbol{u}, \boldsymbol{v})_{H_{\text{div}}(\Omega)} \coloneqq (\boldsymbol{u}, \boldsymbol{v})_\Omega + (\nabla \cdot \boldsymbol{u}, \nabla \cdot \boldsymbol{v})_\Omega, \tag{0.35}$$

and the corresponding induced norms. As the integration domains are explicit, for ease of notation, the abusive notations H_{grad}, H_{curl} and H_{div} will be used instead of the more rigorous notations, $H_{\text{grad}}(\Omega)$, $H_{\text{curl}}(\Omega)$ and $H_{\text{div}}(\Omega)$. When establishing weak forms in the boundary of the considered domain, functions first defined in a volume Ω will be integrated over its closed surface boundary $\partial\Omega$. This restriction, called the trace operator of a function, will be denoted, for a field $\boldsymbol{u}$ as,

$$^{tr}\boldsymbol{u}, \tag{0.36}$$

It is represented by the operator,

$$\gamma : u \longmapsto {}^{tr}u, \tag{0.37}$$

It can be shown [18] that the space of the image of the operator γ, defined in $H_{\text{grad}}(\Omega)$, $H^{\frac{1}{2}}(\partial\Omega)$ is a Hilbert space which satisfies,

$$H^{\frac{1}{2}}(\partial\Omega) \subset L^2(\partial\Omega). \tag{0.38}$$

Other relevant function spaces can be constructed in order to formally introduce the function spaces of the weak form of the BEM, for example, the topological dual of $H^{\frac{1}{2}}(\partial\Omega)$, $H^{-\frac{1}{2}}(\partial\Omega)$. The formal mathematical framework of such developments can be found in [20] and [21] and is outside the scope of this manuscript.

Introduction

The discovery of active materials, which display an intrinsic coupling between their electric and magnetic properties have been the subject of much interest, for the novel applications they allow, and for applications where the wanted electromagnetic coupling is otherwise small. Indeed, energy conversion in electrical transducers or actuators is based on electromagnetic interactions, which link the electromotive force to temporal variations of the magnetic flux density. These phenomena are sometimes difficult to exploit, especially for small devices submitted to fields of very low frequency.

The magnetoelectric effect occurs in the form of an electric polarization induced by a magnetization or, conversely, of a magnetization induced by an electric polarization. The aforementioned materials, which are ferroelectric and ferromagnetic, display ME effects. While single-phase ME materials show promising properties, for the moment, this effect appears mainly at cryogenic temperatures. The use of active composite structures made of the mechanical association of ferroelectric and ferromagnetic materials results in an ME effect at room temperature, and several orders of magnitude greater than the ME effect in single-phase materials. These composite structures are made of piezoelectric materials, which display strong electro-mechanical coupling, and magnetostrictive materials, which display strong magneto-mechanical properties. The resulting heterogeneous structures display ME effects. They allow for novel applications and rival their conventional counterparts. The present work will concern the modeling of such structures.

The modeling of ME devices can be done by analytical approaches to get an estimate of their response. They are however limited to trivial geometries. Numerical methods, such as the Finite Element Method, do not suffer from such limitations. However, the modeling of magnetic phenomena requires the modeling of magnetic phenomena not only in the ME device but also in

the air surrounding the device, as magnetic phenomena take place in all free space surrounding the device and surrounding the source of the magnetic field. A large air region representing the truncation of the infinite free space surrounding the device and the field source has then to be considered, and the accuracy of the solution will depend on the size of the considered truncated air domain: the bigger the air region, the more accurate the solution. Nevertheless, the consideration of this large air region translates into numerous, or even most unknowns of the problem (otherwise called degrees of freedom, or DoFs, of the problem) being located outside the device to be modeled. For our application, in a pure FEM context, to keep a reasonable number of unknowns to the problem is incompatible with an acceptable accuracy of the solution.

In this work, a novel approach to the modeling of ME effects consisting on the coupling of the FEM with the Boundary Element Method (BEM) is proposed. This approach reduces the problem outside the domain to a problem on the boundary of the device, thus considerably decreasing the number of DoFs. Furthermore, by avoiding the truncation of the free space surrounding the device, it better predicts the behavior of the magnetic field inside the active domain. Despite its more complex implementation and the numerical challenges it involves, in particular related to the resolution of the discrete problem, in this work we see how this coupling of the FEM and the BEM is a very powerful approach for the modeling of ME effects in composite structures.

This manuscript is organized into four chapters. In the first chapter, the ME effect is presented in more detail, in single-phase materials as well as in composite structures. We present the constitutive phenomena behind the ME effect, local electro-mechanical and magneto-mechanical couplings, and their modeling. Afterward, we introduce the modeling approaches of ME effects: first by analytical approaches and then by numerical methods. The last section concerns the introduction of the proposed strategy for the numerical modeling of ME effects in composite structures.

The second chapter is dedicated to the formulation of the numerical tools for single-physics problems, without multi-physics coupling. We introduce the equations to be solved: Maxwell's equations and the equations of continuum media, in their strong and weak forms. These equations are discretized, resulting in a matrix system to be solved. The accuracy of the two magnetic FEM-BEM formulations, less classical than their electric and mechanical counterparts, are studied for linear and nonlinear constitutive laws.

The third chapter concerns the multi-physics modeling of active materials,

the FEM modeling of electro-mechanical effects and the FEM-BEM approach to the modeling of magnetic phenomena. The chosen constitutive laws are be derived and the involved multi-physics problems formulated in terms of their weak and discrete forms. The challenges related to the resolution of the discrete systems are be treated and adapted resolution algorithms are proposed and studied.

In the fourth chapter, we apply the proposed modeling approaches to ME effects to the modeling of two ME composite structures. The first is a three-layer ME composite which functions as an energy harvester. All developed formulations are applied to the modeling of this device, in particular, the two linear formulations are compared and validated against a FEM approach. The other chosen application is a rotating coilless ME composite made of ME composite under the effect of a permanent magnet. By its magnetic interaction with the magnet, this device can function as a generator or as an actuator. It is studied in both situations. In particular, the computation of mechanical forces and torques are studied and two methods for their computing presented. The last section concerns the conclusions and perspectives

Chapter 1

The magnetoelectric effect, applications and modeling

1.1 Introduction

In this chapter, we explore the intrinsic and extrinsic magnetoelectric effect. We introduce the magnetoelectric effect in single-phase materials and its limitations. Afterward, we present the extrinsic magnetoelectric effect as a way of overcoming the previously mentioned limitations and obtaining a greater electromagnetic coupling. We therefore introduce piezoelectricity, magnetostriction and the Villari effect as the constitutive phenomena at the source of the extrinsic magnetoelectric effect. Some applications are presented in order to illustrate this effect. The modeling of piezoelectric and magneto-mechanical structures are presented, as well as the approaches to the modeling of magnetoelectric structures, mainly analytical and the Finite Element Method (FEM). At last, we discuss the interest of the proposed numerical approach to the modeling of composite structures, a coupling between the FEM and the Boundary Element Method (BEM).

1.2 Description and motivations

1.2.1 Electromagnetic coupling

Electromagnetic coupling and energy exchange can usually rely on the coupled nature of Maxwell's equations (1.1)-(1.4) which describe the behavior of electromagnetic fields, here presented in their classic form and in Cartesian coordinates:

$$\boldsymbol{\nabla} \cdot \boldsymbol{B} = 0, \tag{1.1}$$

$$\boldsymbol{\nabla} \times \boldsymbol{H} = \boldsymbol{J} + \frac{\partial \boldsymbol{D}}{\partial t}, \tag{1.2}$$

$$\boldsymbol{\nabla} \cdot \boldsymbol{D} = \rho, \tag{1.3}$$

$$\boldsymbol{\nabla} \times \boldsymbol{E} = -\frac{\partial \boldsymbol{B}}{\partial t}, \tag{1.4}$$

with $\boldsymbol{B}$ the magnetic flux density, $\boldsymbol{H}$ the magnetic field, $\boldsymbol{E}$ the electric field, $\boldsymbol{D}$ the electric displacement field, ρ the electric charge density, and $\boldsymbol{J}$ the current density. It is clear in equations (1.2) and (1.4) that for situations in which fields have high enough temporal variation, a natural coupling between electric and magnetic quantities exists. This condition is not sufficient, and the reason can be seen in the integral expression of Maxwell's equations (1.5)-(1.8), which can be obtained by applying vector calculus identities to (1.1)-(1.4) [22] on a volume domain $\boldsymbol{\Omega}$, with its closed boundary $\partial\boldsymbol{\Omega}$, a surface domain $\boldsymbol{\Gamma}$ with its closed line boundary $\partial\boldsymbol{\Gamma}$:

$$\int_{\partial\Omega} \boldsymbol{B} \cdot \boldsymbol{d}\, \boldsymbol{\partial\Omega} = 0, \tag{1.5}$$

$$\int_{\partial\Gamma} \boldsymbol{H} \cdot \boldsymbol{d\Gamma} = \int_{\Gamma} \boldsymbol{J} \cdot \boldsymbol{d\Gamma} + \frac{\partial}{\partial t} \int_{\Gamma} \boldsymbol{D} \cdot \boldsymbol{d\Gamma}, \tag{1.6}$$

$$\int_{\partial\Omega} \boldsymbol{D} \cdot \boldsymbol{d}\, \boldsymbol{\partial\Omega} = \int_{\Omega} \rho \; d\Omega, \tag{1.7}$$

$$\int_{\partial\Gamma} \boldsymbol{E} \cdot \boldsymbol{d}\, \boldsymbol{\partial\Gamma} = -\frac{\partial}{\partial t} \int_{\Gamma} \boldsymbol{B} \cdot \boldsymbol{d\Gamma}. \tag{1.8}$$

In equations, (1.6) and (1.8), the circulation of electromagnetic fields is tied to the temporal derivatives of surface fluxes. In the case of (1.8), the

electromotive force is linked to the variation of the flux of the magnetic flux density. We see that for devices of small dimensions, where circulations and fluxes are small, the electromagnetic coupling deriving from Maxwell's equations is weak. Therefore, for low frequency situations and/or devices of small dimensions, the natural coupled properties of Maxwell's equations are hard to exploit, and such an interaction cannot be achieved through Maxwell's equations alone.

The discovery of novel materials displaying a coupling between their electric and magnetic properties has expanded the possibilities of electromagnetic coupling and gave rise to novel devices that rival their conventional counterparts. Before introducing this coupling between electric and magnetic properties, called the magnetoelectric effect. The concept of electric and magnetic forces has to be introduced in order to clarify the meaning of *electro-mechanical* and *magneto-mechanical* coupling.

1.2.2 Global couplings: electric and magnetic forces

Electro-mechanical and magneto-mechanical couplings exist in passive materials in the form of electric and magnetic forces, many methods for expressing these forces exist in the literature, such as the virtual work method [23] or the magnetic charge method [24]. One method is to express electric forces as the consequence of the interaction between charges and an electric field, and magnetic forces as the consequence of the interaction between currents and a magnetic field. These forces will act on every material, active or passive, and their effect on the mechanics of a material is referred to as *global coupling*. The multi-physics coupling of active materials does not rely on the previously described forces, but on a local, intrinsic coupling which comes from the change on the microstructure of active materials when subjected to the different fields.

1.3 The Magnetoelectric effect

1.3.1 The magnetoelectric effect in single-phase materials

The ME effect is the coupling of the electric and magnetic properties of a material, not relying on Maxwell's equations, more precisely, a material which displays an electric polarization $\boldsymbol{P}$ as a consequence of an applied magnetic

field and conversely, the magnetization of a material as a consequence of an applied electric field [1, 25]. This effect, in its intrinsic form, can be found in single phase materials, specially in multiferroic materials, which are both ferroelectric and ferromagnetic [26]. Figure 1.1 shows the intrinsic coupling between electric and magnetic properties of $Ni_3B_7O_{13}I$.

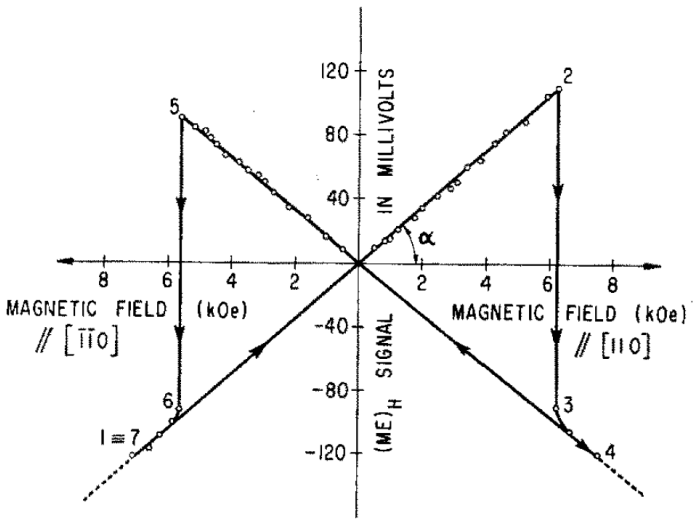

Figure 1.1: Hysteresis loop of $Ni_3B_7O_{13}I$ between $\boldsymbol{P}$ in mV and $\boldsymbol{H}$ in $\mathrm{A\,m^{-1}}$ at 46 K [1] showing the intrinsic coupling between electric and magnetic quantities

The magnetoelectric effect, given by the linear coupling between the electric and magnetic properties of a material $\boldsymbol{\alpha}$, is bounded by their electric and magnetic susceptibilities χ [27].

$$\alpha_{ij} < 4\pi\sqrt{\chi^e_{ii}\chi^m_{jj}} \tag{1.9}$$

As this effect is mainly found in materials with low ferroic properties, it is usually weak in most materials. It is particularly large for materials such as $BiFeO_4$ or $TbPO_4$, but their ME properties are hardly exploitable for everyday applications as, in most cases, a strong ME effect doesn't happen at room temperature. $BiFeO_4$ is an exception and for this reason, studies on its synthesis and characterization have been performed [28, 29].

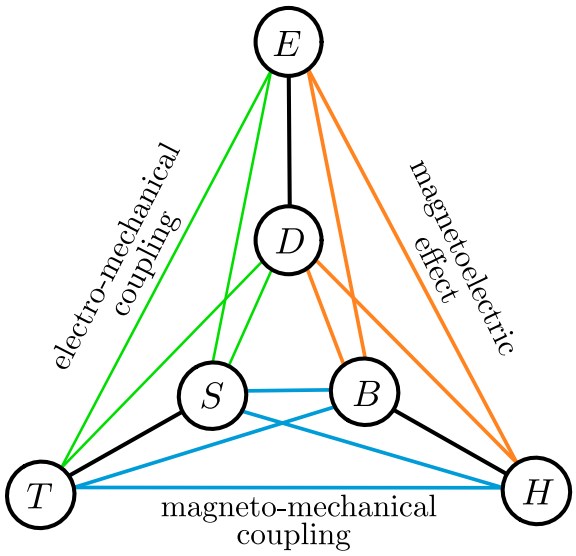

Figure 1.2: Couplings between electric, magnetic and mechanical quantities. Single-physics couplings are denoted by black lines, green lines signify electro-mechanical coupling, blue lines the magneto-mechanical coupling and orange lines the magnetoelectric coupling

1.3.2 Magnetoelectric effect in composite structures

Composite structures displaying the ME effect can be constructed without the disadvantages of single phase materials. These composite structures are obtained through the mechanical association of materials which exhibit strong electro-mechanical coupling, and materials which exhibit strong magneto-mechanical properties. The multi-physics couplings involved in the strain-induced magnetoelectric effect are presented in Figure 1.2. In composite structures, no intrinsic coupling between electric and magnetic quantities is present in each constituent phase, but their global behavior displays the ME effect. In these situations, the ME effect is said to be extrinsic or strain-induced.

1.3.2.1 Local electro-mechanical coupling

Local electro-mechanical coupling, often referred to as piezoelectric effect, consists in the coupling of mechanical and electrical properties of some materials. More precisely, in its direct form, it consists in the electric polarization, otherwise referred to as poling, of a material following the application of mechanical stress [30]. The inverse effect consists in the deformation of a material when subjected to an electric field [31]. This effect

was first discovered in monocrystals, such as quartz and tourmaline, and for this type of materials, its origin in the apparition of electric dipoles under a certain temperature, called Curie temperature, when the microstructure of non-centrosymmetric crystals is changed by the application of mechanical stress [32].

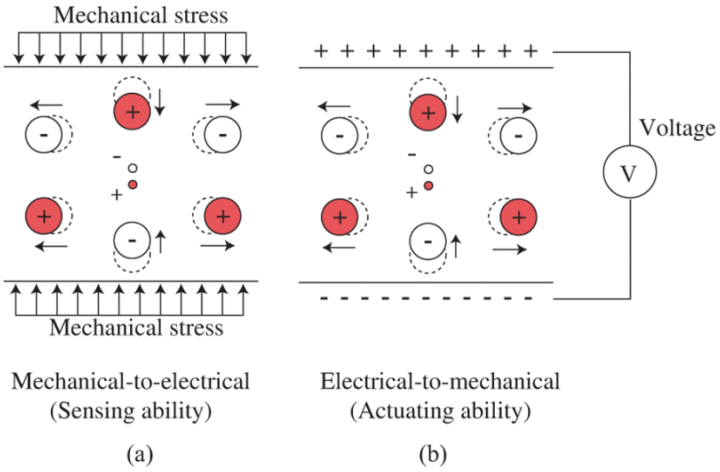

Figure 1.3: Piezoelectric effect in quartz single crystals [2]

Figure 1.4: Microstructure of $BaTiO_3$, a piezoelectric ceramic, after etching and polishing, showing its complex polycrystal structure. Picture obtained by a petrographic microscope using transmitted light [3]

In Figure 1.3 is presented the microstructure of quartz (SiO_2). In an unconstrained state or above a certain temperature called Curie temperature, the barycenter of negative and positive charges are superposed. Therefore,

the material does not show any macroscopic poling. When constrained and below a certain temperature, the shift of the barycenter of positive and negative charges creates a local electric dipole. The field created by the said dipole will constitute the poling of the material. Piezoelectric materials are also ferroelectric, meaning that besides the poling resulting from the applied mechanical stress, these materials also polarize when subjected to an electric field alone. Conversely, when an electric voltage is applied, electric forces onto the charges particles composing the single-crystal induce a macroscopic displacement.

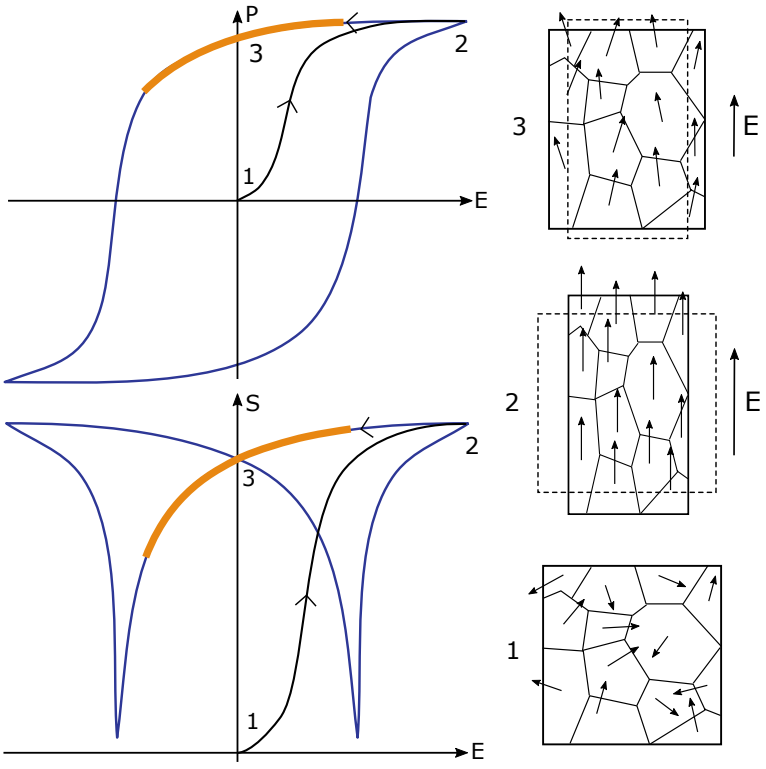

Figure 1.5: Poling process of piezoelectric materials

Piezoelectric ceramics are composed of an assembly of ferroelectric subdomains (see Figure 1.4), called Weiss domains. In an unpoled state, these domains have a remanent poling which is along a random orientation (state 1. of Figure 1.5). When subjected to a high enough electric field (called coercive field), the domains will align with the direction of this field (state 2. of Figure 1.5). If the exciting field is then removed, the hysteretic behavior of some materials will leave them with a remanent poling (state 3. of Figure 1.5. In this poled state and below a certain threshold field, called coercive

field, their behavior shows little nonlinearity around this operating point.

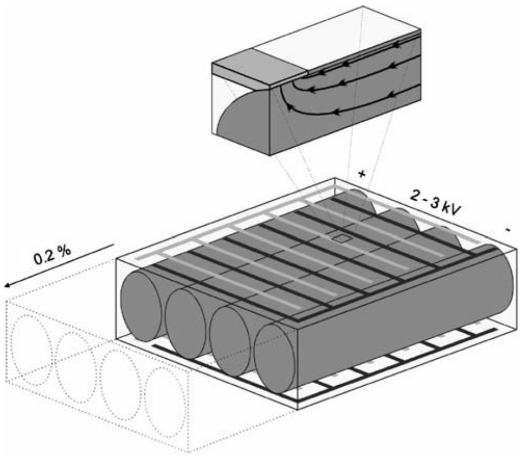

Figure 1.6: Interdigitated electrode placement, allowing for maximum deformation. The black stripes constitute one electrode and the white stripes the other one. In this case, in contact with a polymer matrix with cylindrical piezoelectric inclusions [4]

The general response of a piezoelectric material is highly dependent on the disposition of the poling electrodes and the exciting electrodes. A poled piezoelectric material elongates if the direction of the electric field applied is in the same direction as the poling direction. If excited in an opposite direction to its poling direction, it shortens. A field applied in another direction creates shear strains. In order to maximize the strain response of a piezoelectric material, it is ideal to excite the device with the same electrodes it was poled by. This way, the exciting field is locally the closest to the poling field. This is the principle of interdigitated electrode (IDE) placement, an example of IDE is presented in Figure 1.6. These electrodes may be placed linearly [4, 33] or even radially for disk shaped piezoelectric materials [34, 35]. IDE's also allows increasing the value of the local electric field because of the spatial periodicity of electrodes close to each other.

1.3.2.2 Piezoelectric materials and orders of magnitude

Although discovered in 1880, growing interest in piezoelectricity for energy harvesting applications followed the discovery in the 1950s of lead zirconate titanate, also known as PZT, and barium titanate ($BaTiO_3$). These materials can display very large strains, of around 10^{-3} but come in the form of ceramics and are therefore brittle and can't form complex shapes. These materials are therefore often embedded in polymer matrices in order to

obtain composite materials with greater flexibility [5].

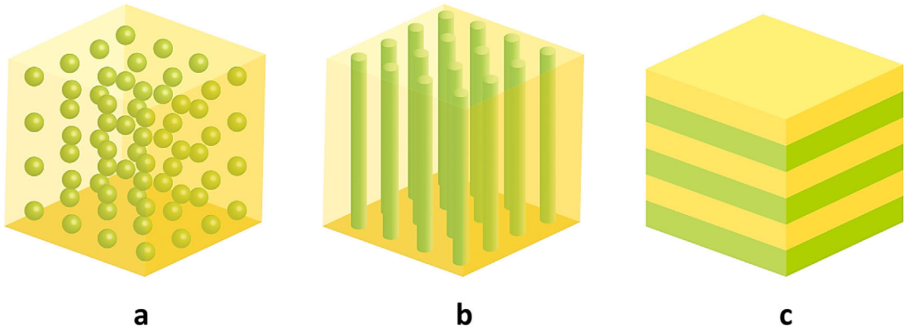

Figure 1.7: Schematic of the connectivity of composite structures: a) 0–3 composite, b) 1–3 composite, and c) 2–2 composite [5]

There are many possibilities regarding the geometrical assembly of composite structures, whether in the form of grain inclusions (0-3 composites), nanotubes (1-3 composites), or laminate structures (2-2 composites). The previously mentioned topologies are presented in Figure 1.7, the numbers referring to the dimensions to the spatial dimensions of the inclusions and the matrix in which they are included. The highest piezoelectric coefficients are obtained from 1-3 and 2-2 topologies, described in Figure 1.7, i.e., piezoelectric fibers embedded in a polymer matrix or piezoelectric/polymer laminates.

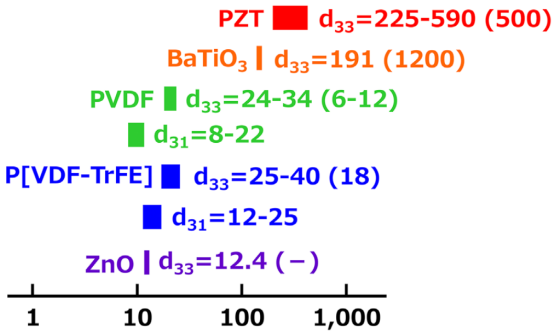

Figure 1.8: Piezoelectric coefficients ($\mathrm{pC\,N^{-1}}$) of some materials [5]. Between parenthesis are the relative permittivities of some piezoelectric materials

Polymer piezoelectric materials offer other possibilities. Materials such as poly-vinilidene fluoride (PVDF) or a copolymer P(VDF-TrFE), are flexible, more compliant and can be easily formed into complex shapes, for example, deposited onto a curved surface and in general cheaper. Other advantages

of polymer piezoelectric materials is their non-toxicity, as they are lead-free. Nevertheless, as seen in Figure 1.8, their major disadvantage is that they display a weaker piezoelectric coupling and much lower electric permittivity compared to piezoelectric ceramics, which can limit their ability to canalize electric fields.

1.3.2.3 Local magneto-mechanical coupling

Local magneto-mechanical coupling consists of two effects, magnetostriction, which consists in the deformation of a material when subjected to a magnetic field [36] and the Villari effect, sometimes abusively referred to as inverse magnetostriction, which consists in the change of magnetic properties of a material when subjected to mechanical stress. Magnetostriction was first discovered in iron and is, like for piezoelectricity, a direct consequence of the material microstructure and thus a local coupling as defined in Section 1.2.2.

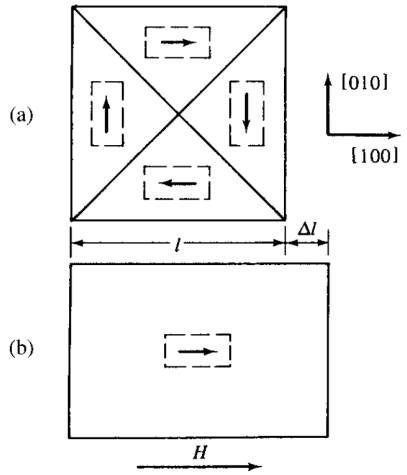

Figure 1.9: Magnetostriction Δl of an iron crystal as a consequence of an applied field in the [100] direction [6]

In monocrystals, magnetostriction is a consequence of the spatial deformation of the electronic cloud of its constituting elements under an applied magnetic field [37, 38]. Magnetostrictive materials have a ferroelectric behavior, meaning that they magnetize following the application of a magnetic field. They present a microstructure made of magnetic subdomains called Weiss domains. As the applied magnetic field increases, many phenomena will take place simultaneously related to the volume fraction and orientation and

of the Weiss domains. The volume fraction of subdomains magnetized in a direction parallel to the exciting field increases, whereas the volume fraction of domains with a magnetization direction perpendicular to the exciting field decreases, this situation is illustrated by Figure 1.9. As the amplitude of the magnetic field increases, these ferromagnetic subdomains rotate in order to align their magnetization direction with the exciting field [37]. In magnetostrictive materials, the magnetization process is accompanied by the mechanical deformation of the material, this deformation is referred to as magnetostrictive strain, denoted as $\boldsymbol{S^{\mu}}$.

The change in volume and the rotation of the subdomains are both nonlinear phenomena, temperature dependent, hysteretic and involve energy losses. For example, in iron, at a fixed temperature, an applied magnetic field first induces an elongation in the direction of the applied field, as the field gets stronger, magnetostriction saturates and then turns into compression, as shown in Figure 1.10 [6, 7]. Nickel displays negative magnetostriction resulting in contraction in the direction of the applied field when a magnetic field is applied, while materials such as Galfenol or Terfenol show positive magnetostriction. Alloys, such as FeCo or FeNi may show positive magnetostriction or magnetostriction changing sign depending on the applied field.

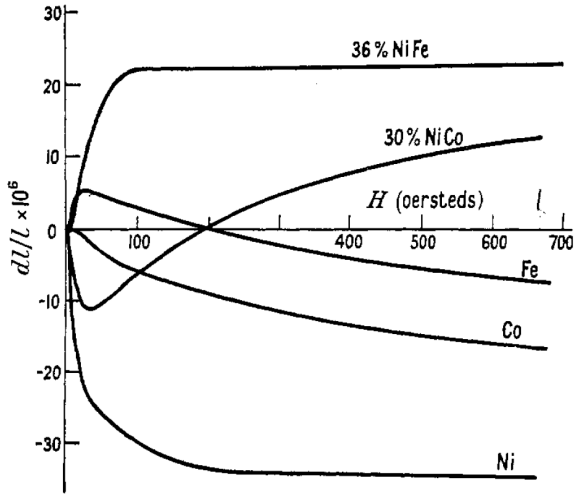

Figure 1.10: Magnetostriction $\Delta l/l$ vs applied magnetic field H [7]

Under mechanical stress, the magnetic subdomains change in volume and magnetization direction. When subjected to a magnetic field, they behave differently in respect to their unconstrained response. In particular, the

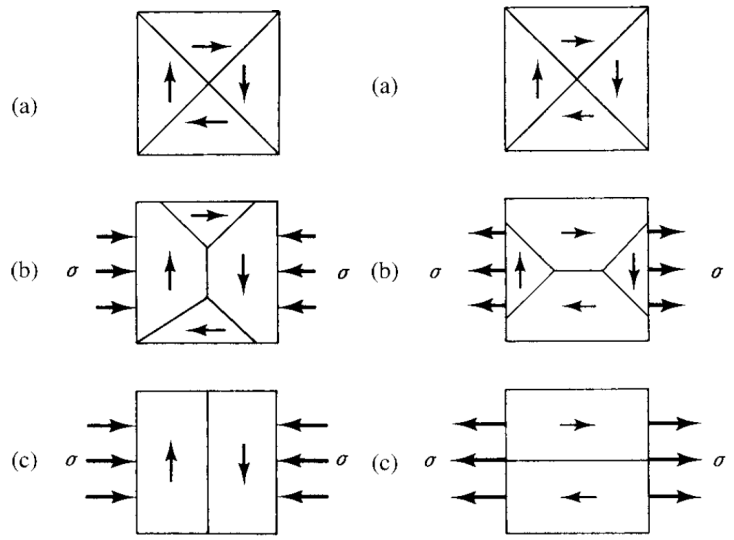

(a) Effect of compressive stress **(b)** Effect of tensile stress

Figure 1.11: Effect of stress in magnetic materials [6]

applied stress induces an anisotropic magnetic response of the material, as a result, some directions become favored magnetization directions. In some materials with positive magnetostriction, as shown in Figures 1.11a and 1.11b, tension induces a preferred magnetization direction in the axis of applied stress, whereas compression along an axis has the opposite effect: the direction of magnetization in the direction of the applied stress will be disfavored in favor of the other directions.

These magneto-mechanical coupled properties can be visualized by the change of the $\boldsymbol{B}(\boldsymbol{H})$ curves following a change in the mechanical state of the material. In Figure 1.12 are presented the $\boldsymbol{B}(\boldsymbol{H})$ curves of Terfenol-D for different mechanical loadings. We observe the important effect of the mechanical stress on the magnitude of the resulting magnetic flux density for a given magnetic field. Conversely, in Figure 1.13 are presented the strains in Terfenol-D vs the magnetic field. We observe the very important strains developed in Terfenol-D under an applied magnetic field, and also, the important effect of applied stress on the magnetostrictive strain.

1.3.2.4 Magnetostrictive materials and orders of magnitude

Magnetostriction occurs in most ferromagnetic materials such as iron, cobalt, nickel, and their alloys with magnetostrictive strains of the order of 10^{-5}.

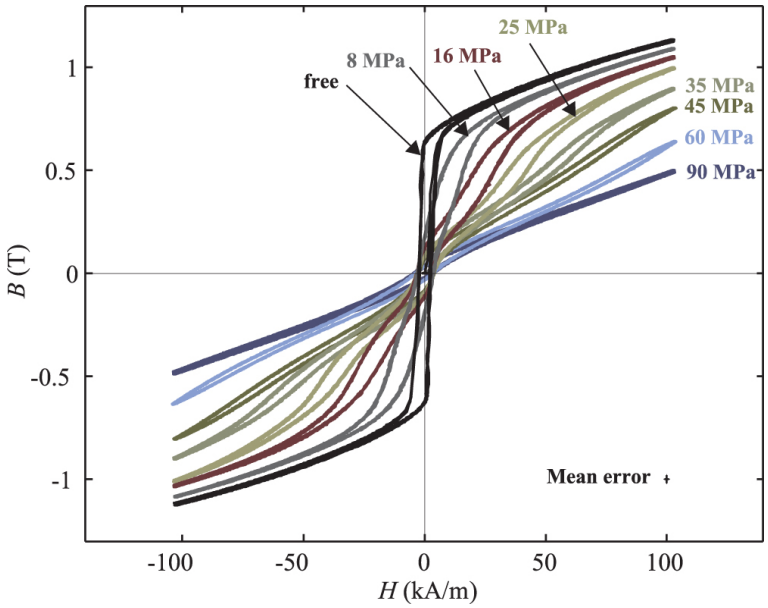

Figure 1.12: Stress-dependent $\boldsymbol{B}(\boldsymbol{H})$ curves of Terfenol-D [8]

These strains, however low in comparison to other materials, have nevertheless been the subject of research as magnetostriction in steel and iron alloys is at the source, along with magnetic forces, of mechanical vibration and noise in electrical engineering applications such as electrical machines [39, 40] or electrical transformers [41, 42].

Among giant magnetostriction materials, Terfenol-D, an alloy of Terbium, Dysprosium and Iron, has the largest deformation at room temperature with strains up to 10^{-3}, as seen in Figures 1.14 and 1.15. Terfenol-D has been the subject of mush interest for its magnetostrictive properties, notably for ME applications. It has however some disadvantages. It displays relatively strong hysteresis, is sensitive to tensile stress and is brittle. This brittleness can somewhat be overcome by including Terfenol-D particles or rods in an epoxy matrix [43].

Another alloy displaying large magnetostriction coefficient is Galfenol, made of iron and gallium, it has a lower magnetostriction coefficient of around 10^{-4} but also lower losses. Galfenol is also less brittle than Terfenol-D and can be made into complex shapes. As seen in Figure 1.14, Galfenol has higher magnetic permeability and a higher magnetic saturation than Terfenol-D. It has therefore better magnetic properties: it canalizes better the flux lines. It has however relatively low permeability compared to other magnetic materials.

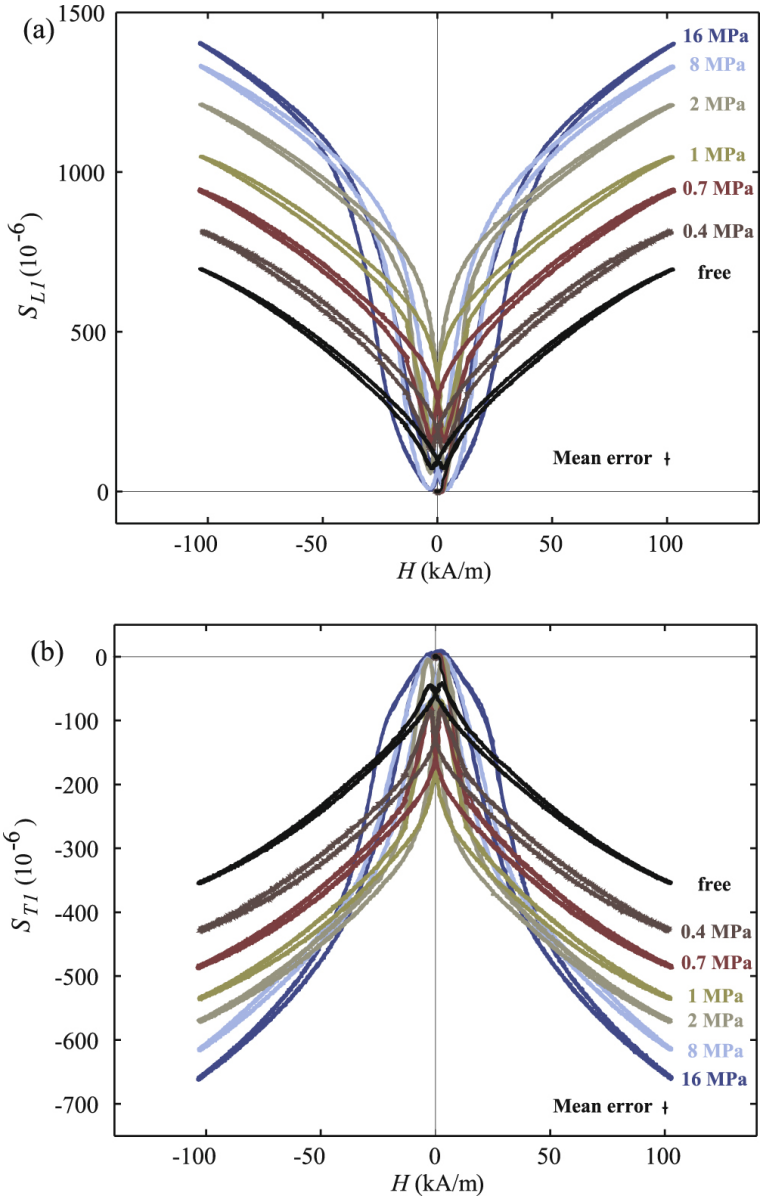

Figure 1.13: Stress-dependent $\boldsymbol{S^{\mu}(H)}$ curves of Terfenol-D [8]

1.3.3 Applications of the ME effect

1.3.3.1 Example of a modulable magnetic pump

In this section, an example of a composite structure containing active materials is presented in order to illustrate an application of the extrinsic ME effect, as such, this structure is made of the assembly of a piezoelectric ma-

		Fe–Co alloys	Terfenol-D	Galfenol
Magnetostrictive	Magnetostriction (ppm)	Max >140 80–140	Max 3000 800–1200	Max 300 120–240
Magnetic	Coercivity (A/m)	< 200	300	3000
	Saturation flux density (T)	2.0 <	1.0	1.5
	Relative permeability	100	< 10	< 100
Mechanical	Tensile strength (MPa)	600 <	30	400
	Elongation (%)	< 30	< 1	1 <
	Young's modulus (GPa)	200	< 100	< 100
Thermal	Coefficient of thermal expansion ($10^{-6}\,K^{-1}$)	11.9	12	–
	Curie temperature (°C)	900	380	680
Electrical	Volume resistivity ($\mu\Omega \cdot cm$)	10	58	–
Density ($g\,cm^{-3}$)		8.4	9.25	–

Figure 1.14: Material properties of some magnetostrictive materials [5], These coefficients are dependent on the thermal and mechanical history of the sample

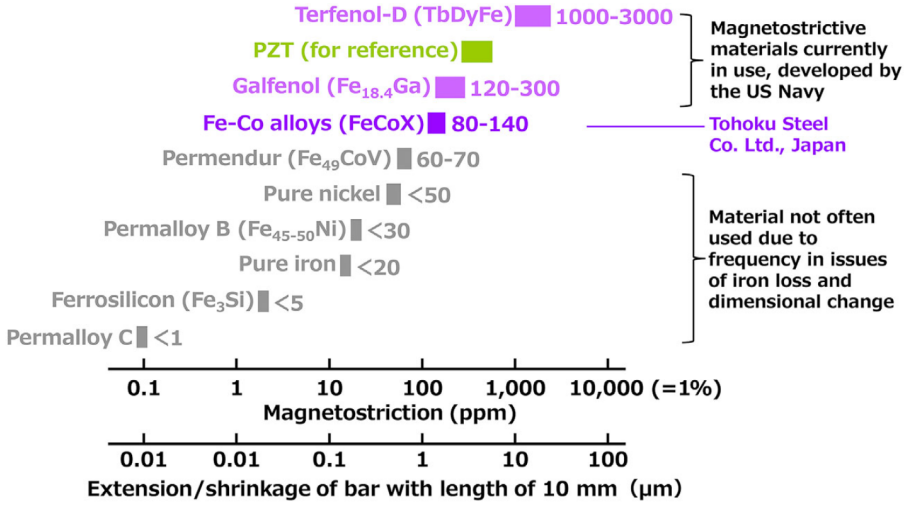

Figure 1.15: Magnetostrictive and piezoelectric properties of some materials. These coefficients are dependent on the thermal and mechanical history of the sample [5]

terial, PZT-5A, and a magnetostrictive material, Terfenol-D. The following structure is a magnetic pump whose purpose is to produce a force onto a movable yoke [9]. The device is presented in Figures 1.16 and 1.17. It

functions as follows: the magnetic field created by the permanent magnets (yellow in Figure 1.17b) present is canalized by the iron core.

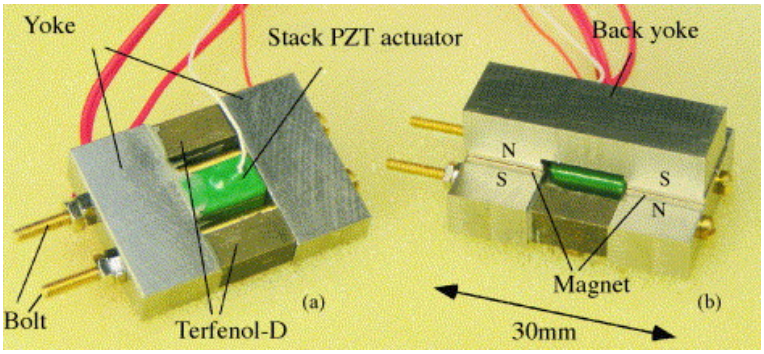

Figure 1.16: Photograph of the considered device [9]

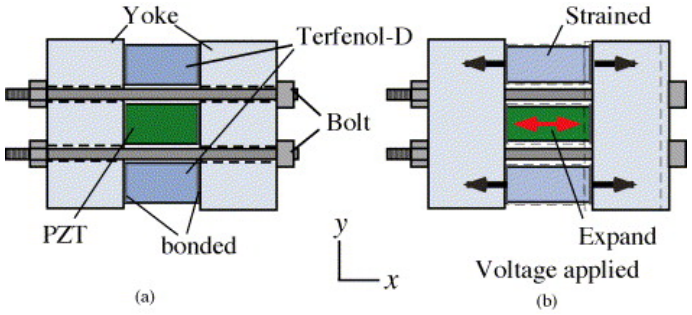

(a) Mechanical effects

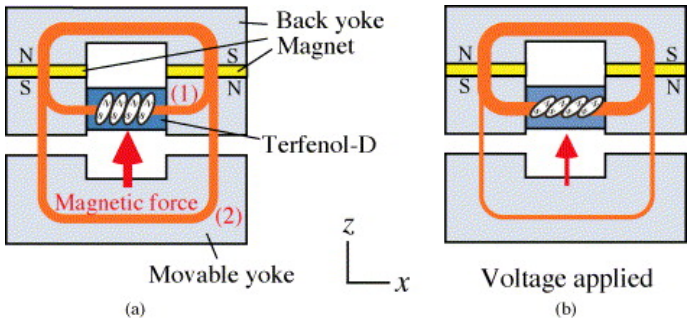

(b) Magnetic effects

Figure 1.17: Physical phenomena at play in the magnetoelectric structure [9]

By applying an electric voltage to the piezoelectric material, a polarization state is induced and through its electro-mechanical properties it changes in shape. The structure being elastic, the deformation of the piezoelectric phase generates a deformation of the magnetostrictive phase, the mechanical

response of the device is presented in Figure 1.17a. As seen in Figure 1.17b, the deformation of the magnetostrictive phase changes its magnetic properties, which changes the amount of the total magnetic flux flowing through the movable yoke. It is then possible to modulate the force applied to the yoke by changing the electric voltage applied to the piezoelectric phase.

One interesting property of the previously described device is that once the piezoelectric material is poled, all the properties of the device remain in their present state. This also applies to the magnetic force applied to the yoke. No power has to be supplied to the device for the magnetic force to remain the same [9]. Contrary to a device working on remanent magnetization, which would need the application of an electric current to be demagnetized, the presented ME composite structure returns into its previous state by the discharge of the electrodes, requiring no power to be supplied. Other advantages are its low power consumption, due to the capacitive effects of the PZT-5A phase and the use of a permanent magnet to generate the magnetic flux.

1.3.3.2 Some other applications of the ME effect

ME composite devices have many applications at different spatial and temporal scales. For low frequency applications, many topologies of energy harvesters based on the ME effect have been explored [5], allowing for small power production of the order of the mW [44]. Some applications for high frequency and low scale applications are ME antennas or even ME random access memory (MeRAM). For data storage applications, MeRAM could be written electrically and read magnetically by the use of the ME effect [45]. A particularly interesting feature of MeRAM is its very low energy consumption, compared to traditional magnetic RAM (MRAM) it is three orders of magnitude smaller. For low frequencies and higher scales, ME composites have applications in field sensing, distance sensing, energy harvesting, etc.

Some other applications of the same coupled properties and materials are tunable inductances [10, 46], one example of such a device is shown in Figure 1.18a. For this type of application, the deformation of a magnetostrictive core, driven by piezoelectric actuators, allow for tuning the inductance of the core by the change in its magnetic properties, as shown in Figures 1.18b and 1.18c. For some energy harvesting applications, the deformation of a magnetostrictive phase under an applied magnetic field drives the deformation of a

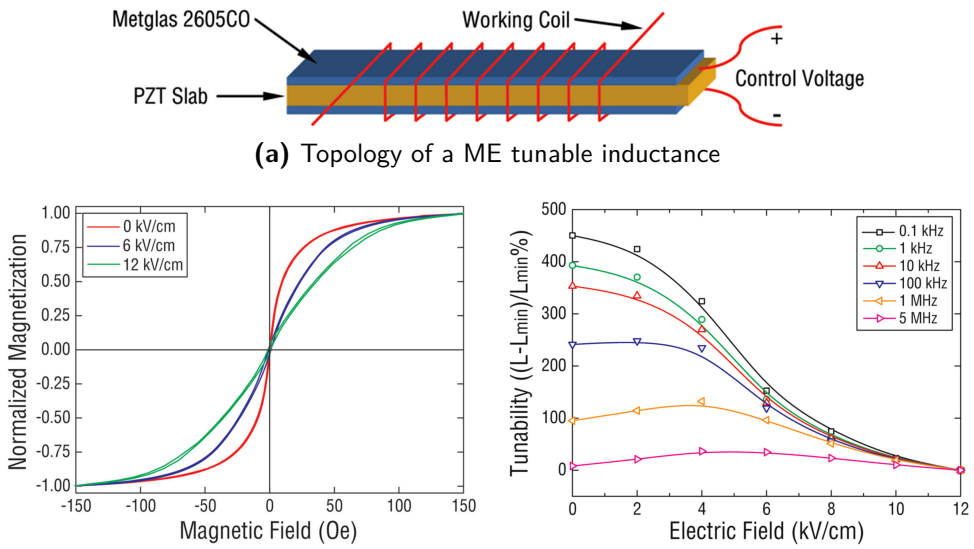

(a) Topology of a ME tunable inductance

(b) Measured Magnetic hysteresis loops of the multiferroic composite core under different electric fields

(c) Inductance vs applied electric field

Figure 1.18: Example of a tunable inductance obtained though the use of the strain-induced ME effect [10]

piezoelectric phase, thus creating an electric voltage which are exploited for low-power applications [47]. Similar topologies and working principles are used for magnetic field sensing [47]. Composite devices showing the extrinsic magnetoelectric effect have also been used as step-up transformers [47]: an AC voltage is used to generate a magnetic field, this field causes the deformation of a bonded piezoelectric phase thus creating an AC electric voltage which can be as high as 30 times than the input voltage if the frequency of the input voltage correspond to the mechanical resonant frequency of the device [48].

1.4 Modeling of the strain-induced magnetoelectric effect

In this section, we present the modeling of the constitutive phenomena behind the strain-induced ME effect: electro-mechanical and magneto-mechanical coupling. Afterwards, we introduce the modeling approaches of the ME effect and ME structures.

1.4.1 Constitutive laws of electro-mechanical coupling

Local electro-mechanical coupling is in general a nonlinear, hysteretic phenomenon [49, 50]. The change in polarization is nonlinear, and the effect of the electric poling on the strains, not symmetric [51]. Phenomenological constitutive laws have also been established to describe the coupled dynamical electro-mechanical response of ferroelectric materials from hypotheses about the switching of local dipoles in an idealized material for the 1D [52] and 3D cases [53].

Macroscopic approaches have been used to obtain constitutive laws, which for some situations give accurate predictions about the hysteretic electromechanical response of ferroelectric materials [54, 55]. Models for hysteretic behavior were obtained by the separation of the remanent part and the total electric polarization and strains. The subtraction between the two terms is considered to behave linearly, and different expressions of the remanent part are obtained by the analytical differentiation of the Helmholtz free energy. Other approaches [56, 57] express the total polarization and strain into a reversible and an irreversible part, and also express their difference by the analytical differentiation of the Helmholtz free energy. The description of the electro-mechanical Helmholtz free energy in terms of its invariants has also been pursued, leading to lengthy developments involving scalar invariants, the electric field, mechanical strain and the polarization vector [58].

Phenomenological models for ferroelectric coupling based on linear interpolations of the hysteresis loops have also been established [59, 55] and applied to the modeling of structures and thin shells [60]. Another phenomenological widely used approach to the modeling of local electro-mechanical coupling has been the linearized approach. Indeed, once poled or for small signal analysis, the behavior of active electro-mechanical materials can be approximated by a set of linear relations linking the electric to the mechanical local properties through coupling tensors [49]. These relations depend on the considered set of state variables [61]. This approach has been widely used for analytical approaches to the modeling of structures [62] and applied to the modeling of structures [63], thin shells [64], acoustic application [65], or even studies on vibration control [66]. This approach has the advantage of being simpler to implement than the nonlinear models, and its linear nature makes it adapted to applications linked to the control of active systems and is easy to implement within numerical tools such as the FEM.

1.4.2 Constitutive laws of magneto-mechanical coupling

Magnetostriction and the Villari effect are both strongly nonlinear, hysteretic processes, and their accurate description is an active research subject. In some situations, if preconstrained and under a bias field, local magneto-mechanical coupling can be linearized in the frame of piezomagnetism, and expressed as sets of two tensorial equations, which are different depending on the choice of state variables [67]. These expressions can accurately describe the response of magnetostrictive materials around an operating point, classically a pre-stress and bias field, but have a limited range of validity. In an analogy with piezoelectric material, this operating point is often called poling of the material. These linearized expressions are particularly useful for small signal analysis [68] and have been applied to the analytical modeling of a wide range of devices such as sensors [69], actuators [69], or energy harvesters [70]. Their simplicity make them adapted to the analytical treatment of the response of materials displaying magneto-elastic effects.

Energy approaches have been widely used in order to derive constitutive laws for magneto-mechanical coupling. In [71], a model for the 3D response of magneto-mechanical response of Tb0.3Dy0.7Fe2 to uni-axial stress is proposed. This model is based on an expression of the free energy in terms of three contributions, that of the magnetic field, the magnetocrystalline energy and magnetoelastic energy. Each of these expressions is developed as functions of material parameters and the orientation of magnetic moments in the crystals composing the material in question. The same approach has been applied to the modeling of Tb(0.27-0.30)Dy(0.73-0.70)Fe(1.9-2.0) [72] and to composites of Terfenol-D particles in an epoxy matrix [73]. This method was later applied to the modeling of Galfenol, in order to deduce the parameters of the model based on experimental data [74]. The response of a Galfenol poly-crystal was also studied from the response of single-crystals using a rule of mixtures method [75]. These energy models predict accurately the magnetostrictive response of magnetostrictive materials, however, they take into account the effect of the stress on the magnetization but neglect the effect of the predicted magnetostrictive strain on the stress.

Other expressions of the magnetic field and mechanical strains can be obtained by a Taylor development of an expression of the Gibbs free energy [76]. The expression of the magnetic displacement, mechanical strain and entropy are given by analytical differentiation of this thermodynamic potential. With the hypothesis of an adiabatic process, which comes down to neglecting the effect of temperature, the obtained expression of the mechanical strains are

then fitted to experimental data for a 1D case as a second order polynomial of the magnetic field. The previous model was perfected for the 1D case in [77] by the introduction of hyperbolic tangents into the expressions in order to impose a saturation. The introduction of Langevin functions into the constitutive laws, first derived from a Taylor development of the expression in [76] allowed for a better fit to experimental data for the 1D and 2D cases [78]. Other modifications have been made to this model to better take into account the saturation of the magnetic field and magnetostrictive strains by the introduction of more complex statistical functions such as the Brillouin function [79, 80, 81].

Multiscale methods have been used in order to numerically predict the response of materials displaying local magneto-mechanical coupling. The mesoscale problem explicitly considers the microstructure of the studied material and its subdomain structure. The multiscale approach often involves iterating between the macroscopic and mesoscale problems until convergence. In this case, the macroscopic excitation is localized in order to solve the mesoscale problem, and the mesoscale solution homogenized to obtain the macroscopic response. The choice of the communicated information between scales is a central part of the method. This approach has been very successful at predicting the response of magnetostrictive materials [82, 83, 84] compared to other phenomenological approaches [85]. However, it is a very time-consuming procedure and some recent work on the multiscale approach to magnetostriction concerns the simplification of the full model [86] or its linearization [87]. A simplified model similar to the one presented in [86] has successfully been introduced into 2D finite element simulations of a switched reluctance machine [88].

A model for 3D local magneto-mechanical coupling can be found in [89], where magnetostriction is taken as an even tensorial function of the magnetic flux density. This expression was introduced into a FEM simulation of ME devices with good agreement with experimental data. The previous model was linearized in [90] and also applied to the modeling of ME devices. Another fruitful approach is the invariant approach to magnetostriction and magneto-mechanical coupling. The invariant approach to magnetostriction was first developed in [91] and it consisted in applying invariant theory to the Helmholtz free energy as a function of the magnetic flux density and the second order strain tensor. These developments were first applied to magnetostriction in iron [92, 85] for the use in FEM simulation of electrical machines and were later applied to the modeling of giant magnetostriction materials such as Galfenol [93, 14, 94]. Such developments can be easily incorporated into FEM simulations. They have however been mostly applied

to 2D simulations or 3D axisymmetric geometries.

1.4.3 Analytical models for the ME effect

Some effort has been put to develop analytical models which for some particular geometries can predict the response of ME composite structures. One approach is to express the magnetoelectric coefficient as a function of the volume fractions of the piezoelectric and piezomagnetic phases, supposing a trivial orientation of the poling directions [95]. Other approaches used in the analytical description of ME composites are the equivalent circuit approaches, in which parameters such as impedances and quality factors are computed from material coefficients and geometrical properties of the modeled devices and its response put in the form of an electric circuit [96, 97]. They use an extension of Mason's model which allows establishing an equivalent electrical circuit of the ME composites, whose equivalent electrical parameters are established via a coupled equation of motion and the integration of the piezoelectric and magnetostrictive behavior laws. More specifically, these methods can be used to investigate the ME coefficient for different modes of static and dynamic conditions and the electrical resistance load effect on the resonant ME coupling.

Others employ the Green's function of elastic, electric and magnetic phenomena [98, 99]. These approaches give in general rough approximations of the response of ME devices [100] and are in general obtained for trivial geometries such as laminate structures. Elastodynamic methods combining the equation of motion of continuous media with mechanical and electrical boundary conditions have also been proposed [101, 102, 103, 104]. In the previous approach, the response of ME materials was studied, assuming linear behaviors for the ferroelectric and ferromagnetic phases. These models have shown how the volume fractions of each phase, the connectivity [105] seen in Figure 1.7, as well as the piezoelectric, piezomagnetic and elastic properties participate in the ME coupling. The nonlinear response and stress dependence of the ME composite are addressed, for example, in [106, 107] who considered the nonlinear anhysteretic behavior and the effect of stress in the constitutive relationships of the ferromagnetic phase. It results that pre-stress and a bias magnetic field improve the ME coefficients and the frequency-multiplying behavior of laminated composites. The interfaces between ferroelectric and ferromagnetic phases, which are not perfect and usually correspond to a layer of epoxy glue, are accounted for by means of an interface coupling factor [108, 106]. Taking these interface effects into

consideration allows for better prediction of the coupling behavior of ME composites.

To describe and predict the behavior and effective properties of ME composites considering the microstructure and anisotropy of the materials, various micromechanical analyses were developed. Such analytical or semi-analytical solutions are for example based on the homogenization and self-consistent models [109, 110, 111, 112, 113], Mori-Tanaka mean field theory [114, 115], variational asymptotic approach [116, 117] or Eshelby's equivalent inclusion approach [118, 119].

All the previously described methods make it possible to study ME composites with trivial geometries, such as composites with perfect ellipsoidal inclusions, perfect laminated structures or composites involving simple boundary value problems. Despite being computationally expensive, numerical tools are not restricted to specific topologies.

1.4.4 FEM modeling of extrinsic ME effects

Another approach to the modeling of ME composite structures is the modeling by the FEM. Indeed, the ME effect can translate into a boundary value problem. After discretization of the considered geometry into a finite set of geometrical elements, called a mesh. The FEM computes the relevant fields, assuming a behavior given by the considered set of *shape functions* and which approximate the exact solution. The FEM solution has an error with respect to the exact solution. In general, the smaller the elements, the more accurate the solution [120, 121, 122]. More details on the FEM will be given in the following chapter.

The modeling of extrinsic ME effect using the FEM is usually performed through the combination of electro-mechanical and magneto-mechanical constitutive laws. The modeling by the FEM has several advantages. It allows the modeling of devices with arbitrary geometries, nonlinear materials, in time or frequency domain. In the case of the modeling of ME effects, for example, contrary to analytical approaches, no assumptions on the stress direction have to be made. The modeling by the FEM of the ME effect has concerned both linear [123] and nonlinear magneto-elastic effects [56, 89, 124, 125]. Despite being computationally expensive, numerical tools are not restricted to specific topologies. The modeling by the FEM has also been used to study the homogenized response of multiphase materials [57, 126, 127].

Nevertheless, the modeling of ME effects by the FEM has several disadvantages related to the considered domains. For the modeling of mechanical and electrical phenomena, for reasons developed later, a treatment by the FEM requires a mesh containing only the active material. For the treatment of magnetic fields, appropriate boundary conditions can be obtained by explicitly considering and meshing an air region surrounding the device to be studied, thus increasing the numerical complexity of the discretized problem. Another disadvantage is caused by the applications of ME devices, they involve in most cases noncanalized field sources, which in a FEM simulation have to be included in the air region, thus increasing its size. In some situations, 75 % of the magnetic degrees of freedoms may be located in the air region, translating into higher computational cost [128]. Other numerical methods presented in the following section do not have this limitation.

1.5 Proposed strategy

Methods such as the Volume Integral method (VIM) use a volume integration of fundamental solutions, such as Green's functions or its gradient, to account for the electromagnetic interaction between elements of a meshed domain only containing the volume of the active material [129, 130]. It has been applied to nonlinear magnetostatic problems [131, 132]. However, the volume integration of these fundamental solutions is costly. Indeed, these integrations have to be performed to compute the interaction between every two volume elements, leading to matrix systems to be solved involving large full matrices.

For linear constitutive laws, the Boundary Element Method (BEM) has also successfully been applied to model electromagnetic phenomena with a mesh restricted to the boundary of the active domain, notably, to solve eddy current problems [133, 21, 134, 135]. It involves the coupling and resolution of two BEM equations established, one inside the active domain and one in the air region, and therefore, requires only surface integrations of Green's function and its normal derivative on the meshed boundary of the active domain. However, the limitation of the BEM to linear materials makes it not adapted to the modeling of nonlinear ME effects.

A coupling of the FEM with the BEM has already been used to avoid explicitly considering and meshing an air region for the modeling of magnetic phenomena, while allowing for considering nonlinear constitutive laws [136, 137]. It results from the treatment by the FEM of the interior problem, and a

treatment by the BEM of the exterior problem. Contrary to a VIM approach, a FEM-BEM coupling requires only the integration of low order polynomial functions inside the volume and the integration of the fundamental solution only in the boundary of the domain.

In the present work, a coupling of the FEM and the BEM will be applied to the modeling of ME effects in composite structures. This allows us only to consider a mesh containing the active material, and thus to reduce the number of unknowns of the discrete problem. Also, relevant material models will be employed, both linearized models for piezoelectricity and magnetostriction, and nonlinear magneto-mechanical constitutive laws of magneto-mechanical phenomena based on the invariant description of the magneto-elastic Helmholtz free energy, such as those described in 1.4.2, which to the author's knowledge, have not yet been applied to the modeling of magnetoelectric effects in composite structures.

1.6 Conclusion

In this chapter, we introduce the ME effect in single phase materials, also, piezoelectricity and magnetostriction as the constitutive phenomena of the strain-induced ME effects in composite structure. Several examples of magnetoelectric structures are presented in order to illustrate our explanations. These explanations are however qualitative. We also present the modeling of piezoelectric and magneto-mechanical structures before introducing the modeling of the ME effect, both the analytical approaches and numerical methods. In the next chapter, the numerical methods allowing for the modeling of the considered structures are introduced. First, we treat the case of materials with no local coupling, otherwise called passive materials, as a first step into the numerical modeling of ME effects in composite structures.

Chapter 2

Single-physics formulations

2.1 Introduction

In this chapter, we introduce the single-physics formulations of the constitutive phenomena of the extrinsic ME effect for quasi-static fields: electrostatics, mechanics and magnetostatics. They are presented in terms of strong, weak and discrete forms. First, are introduced the partial differential equations to be solved, the single-physics constitutive laws in passive materials, the relevant boundary conditions of the single-physics problems and the particular challenges related to the modeling of magnetic phenomena. Then, are presented the electric and mechanical weak forms leading to a treatment with the FEM, and two magnetostatic formulations based on a coupling of the FEM and the BEM. Finally, both magnetostatic formulations are compared and validated with respect to an analytical solution.

2.2 Strong forms

2.2.1 Maxwell's equations

At the macroscopic scale, the behavior of electromagnetic fields can be described by Maxwell's equations in their classical form, they state,

$$\nabla \cdot \boldsymbol{B} = 0, \tag{2.1}$$

$$\nabla \times \boldsymbol{H} = \boldsymbol{J} + \frac{\partial \boldsymbol{D}}{\partial t}, \tag{2.2}$$

$$\nabla \cdot \boldsymbol{D} = \rho, \tag{2.3}$$

$$\nabla \times \boldsymbol{E} = -\frac{\partial \boldsymbol{B}}{\partial t}. \tag{2.4}$$

At an interface Γ between two regions of different material properties, these fields display some interface conditions which can be deduced from Maxwell's equations,

$$[\ \boldsymbol{B} \cdot \boldsymbol{n}\ ]_\Gamma = 0, \tag{2.5}$$

$$[\ \boldsymbol{H} \times \boldsymbol{n}\ ]_\Gamma = \boldsymbol{J}_\Gamma, \tag{2.6}$$

$$[\ \boldsymbol{D} \cdot \boldsymbol{n}\ ]_\Gamma = Q_S, \tag{2.7}$$

$$[\ \boldsymbol{E} \times \boldsymbol{n}\ ]_\Gamma = 0, \tag{2.8}$$

where $[\bullet]_{\partial\Omega}$ denotes the jump across the surface Γ, $\boldsymbol{J}_\Gamma$ the current density at the surface region Γ and Q_S the surface charge density. For quasi static fields, the time derivatives can be set to zero, the previous set of equations becomes,

$$\nabla \cdot \boldsymbol{B} = 0, \tag{2.9}$$

$$\nabla \times \boldsymbol{H} = \boldsymbol{J}, \tag{2.10}$$

$$\nabla \cdot \boldsymbol{D} = \rho, \tag{2.11}$$

$$\nabla \times \boldsymbol{E} = 0. \tag{2.12}$$

The electric and magnetic fields are now uncoupled. Equations (2.9) and (2.10) are the equations of magnetostatics and (2.11) and (2.12) are the equations of electrostatics.

2.2.2 Mechanical equilibrium equation

In the frame of mechanics of continuous media, the mechanical response of materials is given by the conservation of linear momentum equation:

$$\varrho \frac{\partial^2 \boldsymbol{u}}{\partial t^2} = \nabla \cdot \boldsymbol{T} + \boldsymbol{f}, \tag{2.13}$$

with $\boldsymbol{T}$ is the Cauchy stress tensor, $\boldsymbol{u}$ the mechanical displacement and $\boldsymbol{f}$ the volume force density. For quasi static fields, the mechanical conservation of linear momentum becomes:

$$\nabla \cdot \boldsymbol{T} + \boldsymbol{f} = 0. \tag{2.14}$$

2.2.3 Potentials and gauges

These partial differential equations can be enforced by expressing the fields in question as deriving from potentials.

2.2.3.1 Electric scalar potential

Equation (2.12) can be enforced by describing $\boldsymbol{E}$ as the gradient of an electric scalar potential φ.

$$\boldsymbol{E} = -\nabla \varphi. \tag{2.15}$$

2.2.3.2 Mechanical displacement

For small strains, second order terms in the strain tensor can be neglected, which corresponds to the small strains hypothesis. Within this approximation,

$$\boldsymbol{S} = \frac{1}{2}(\nabla \boldsymbol{u} + {}^{\mathrm{t}}\nabla \boldsymbol{u}). \tag{2.16}$$

with $\boldsymbol{u}$ the mechanical displacements.

2.2.3.3 Magnetic vector potential

Relation (2.9) can be enforced by describing the magnetic flux density $\boldsymbol{B}$ as the curl of a magnetic vector potential $\boldsymbol{a}$,

$$\boldsymbol{B} = \nabla \times \boldsymbol{a}. \tag{2.17}$$

2.2.3.4 Magnetic scalar potential

The magnetic field $\boldsymbol{H}$ being of finite energy, according to a Helmholtz decomposition [22], it can be written as the sum of two terms:

- the source field $\boldsymbol{H_0}$, the source created by currents
- the field $\boldsymbol{H_{red}}$ created by the magnetization of matter.

The source field $\boldsymbol{H_0}$ can be expressed in terms of the current density $\boldsymbol{J^s}$,

$$\nabla \times \boldsymbol{H_0} = \boldsymbol{J^s}. \tag{2.18}$$

Taking into account (2.10), it results that $\boldsymbol{H_{red}}$ is curl free, it can then be expressed as the gradient of a magnetic reduced scalar potential ϕ_{red}, giving,

$$\boldsymbol{H} = \boldsymbol{H_0} - \nabla\phi_{red}. \tag{2.19}$$

2.2.3.5 Gauges

The previously defined potentials as presented are not uniquely defined. For them to be uniquely defined, gauges have to be considered, for scalar potentials such as φ or $\boldsymbol{u}$, fixing the value of a sub-region of the domain to a given potential solves this problem. For $\boldsymbol{a}$ to be uniquely defined, a Coulomb gauge can be used, it comes down to imposing,

$$\nabla \cdot \boldsymbol{a} = 0. \tag{2.20}$$

Other gauges for the magnetic vector potential will be presented later, such as the tree-cotree gauge [138].

2.2.4 Constitutive laws for passive materials

In order to solve for these equations and obtain a unique solution for the boundary value problem given by the equations described above, another set of relations has to be taken into account: the constitutive relations between fields, representative of the material response. For passive materials, materials with no local coupling as defined in the previous chapter, these constitutive relations are usually written in the form of tensor equations involving coupling tensors, in all generality, nonlinear and hysteretic.

2.2.4.1 Dielectric behavior

In dielectric materials and in the frame of electrostatics, the relation linking the electric field $\boldsymbol{E}$ to the electric displacement $\boldsymbol{D}$ field involves a 2nd-order tensor ε, it reads:

$$\boldsymbol{D} = \boldsymbol{\varepsilon} \cdot \boldsymbol{E}. \tag{2.21}$$

The 2nd-order tensor ε is referred to as the electric permittivity. Its coefficients are given in $\mathrm{F\,m^{-1}}$.

2.2.4.2 Mechanical behavior

Mechanical constitutive laws involve a relation between the strain and stress tensors $\boldsymbol{S}$ and $\boldsymbol{T}$. They are usually expressed as:

$$\boldsymbol{T} = \boldsymbol{c} : \boldsymbol{S}, \tag{2.22}$$

and,

$$\boldsymbol{S} = \boldsymbol{s} : \boldsymbol{T}. \tag{2.23}$$

Coupling tensors $\boldsymbol{c}$ and $\boldsymbol{s}$ are 4th-order tensors, are referred to as elasticity and stiffness tensors and are expressed in Pa and $\mathrm{Pa^{-1}}$ respectively. In passive materials, they are related to one another by: $\boldsymbol{c} = \boldsymbol{s}^{-1}$.

2.2.4.3 Magnetic behavior

The behavior of magnetic materials in the frame of magnetostatics is usually expressed by coupling tensors $\boldsymbol{\mu}$ or $\boldsymbol{\nu}$, given by:

$$\boldsymbol{B} = \boldsymbol{\mu} \cdot \boldsymbol{H}, \tag{2.24}$$

and,

$$\boldsymbol{H} = \boldsymbol{\nu} \cdot \boldsymbol{B}. \tag{2.25}$$

The magnetic permeability $\boldsymbol{\mu}$ is given in $\mathrm{H\,m^{-1}}$ whereas the magnetic reluctivity $\boldsymbol{\nu}$ is given in $\mathrm{m\,H^{-1}}$. In passive materials, they are related to one another by the relation: $\boldsymbol{\nu} = \boldsymbol{\mu}^{-1}$.

2.3 Weak forms of the single physic phenomena

Finding analytical solutions to the systems of equations described in the previous section is only possible for trivial geometries. For example, solutions for the magnetic fields exist for spheroids or degenerated spheroids. For electric fields, analytical solutions exist for electrodes in contact with the material and trivial geometries. In mechanics, analytical formulae exist for beams and simple geometries. Numerical methods, such as the FEM or the BEM, can be used to find approximate solutions to the previous set of equations.

2.3.1 Weak form of the electrostatic problem

The weak form of the electrostatic phenomena can be obtained from solving (2.11) in a domain Ω_m with the value of φ known in $\partial\Omega_m^\varphi \neq \varnothing$ and the normal derivative of the solution $\frac{\partial\varphi}{\partial \boldsymbol{n}}$, equivalent to $\boldsymbol{D}\cdot\boldsymbol{n}$, known in $\partial\Omega_m^d$ with $\partial\Omega_m^\varphi \cup \partial\Omega_m^d = \partial\Omega_m$ and $\partial\Omega_m^\varphi \cap \partial\Omega_m^d = \varnothing$.

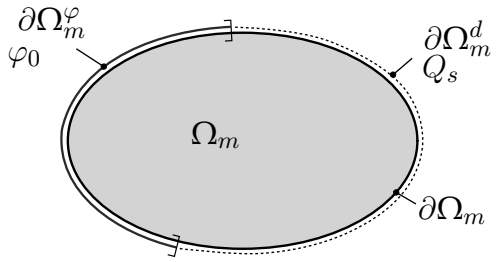

Figure 2.1: Domains of the electrostatic problem. Potentials are imposed on region $\partial\Omega_m^\varphi$ and charges (equal to $\boldsymbol{D}\cdot\boldsymbol{n}$) are imposed on $\partial\Omega_m^d$

With $\rho = 0$. Finding a solution to (2.12), in a domain Ω_m, along with (2.15) and (2.21) comes down to finding φ such that,

$$\nabla\cdot(\boldsymbol{\varepsilon}\cdot\nabla\varphi) = 0, \tag{2.26}$$

Equation (2.26) can be projected onto a virtual field $\delta\varphi \in H_{\text{grad}}$.

$$\int_{\Omega_m} \delta\varphi\nabla\cdot(\boldsymbol{\varepsilon}\cdot\nabla\varphi)\, d\Omega_m = 0 \;\forall\delta\varphi, \tag{2.27}$$

After an integration by parts, to find a weak solution for (2.26) in Ω_m, can otherwise be formulated as, find φ such that,

$$\int_{\Omega_m} \nabla\delta\varphi \cdot \boldsymbol{\varepsilon} \cdot \nabla\varphi \; d\Omega_m \; = \int_{\partial\Omega_m^d} \delta\varphi \; D_n \; d\partial\Omega_m^d \; \forall\delta\varphi, \tag{2.28}$$

with $D_n = \boldsymbol{D} \cdot \boldsymbol{n}$, along with the appropriate boundary conditions: $\varphi = \varphi_0$ in $\partial\Omega_m^\varphi$. Relation (2.28) is said to be the weak form of the electrostatic problem as the differentiablility conditions of the solution has been reduced after the integration by parts.

In all generality, a treatment of the electric field in the air region should be used in order to account for the leaks of the electric displacement field. The study of electric fields with a domain restrained to the active material is possible for reasons related to our particular applications: the electric field is canalyzed inside the active material because of the high permittivity of the considered materials and because the electrodes are in direct contact with the materials, making its leaks negligible, i.e, $D_n = 0$. With these hypothesis, the weak form reads: find φ such that,

$$\int_{\Omega_m} \nabla\delta\varphi \cdot \boldsymbol{\varepsilon} \cdot \nabla\varphi \; d\Omega_m \; = 0 \; \forall\delta\varphi, \tag{2.29}$$

Or, in general, find φ such that,

$$\int_{\Omega_m} \nabla\delta\varphi \cdot \boldsymbol{\varepsilon} \cdot \boldsymbol{D} \; d\Omega_m \; = 0 \; \forall\delta\varphi, \tag{2.30}$$

along with the appropriate boundary conditions.

2.3.2 Weak form of the mechanical problem

The weak form of the mechanical problem in a domain Ω_m is established from (2.14), appropriate constitutive law and known displacements and constraints on complementary surfaces, $\partial\Omega_m^u$ and $\partial\Omega_m^T$ with $\partial\Omega_m^u \cup \partial\Omega_m^T = \partial\Omega_m$ and $\partial\Omega_m^\varphi \cap \partial\Omega_m^d = \varnothing$. In these conditions, a treatment by the FEM is possible.

The development of the mechanical weak form follows the application of the virtual work principle, i.e., the projection of (2.14) onto a field of admissible virtual displacements $\boldsymbol{\delta u} \in H_{\text{grad}}$ inside the mechanical domain Ω_m. This projection gives:

$$\int_{\Omega_m} \boldsymbol{\delta u} \cdot \nabla \cdot \boldsymbol{T}(\boldsymbol{u}) \; d\Omega_m + \int_{\Omega_m} \boldsymbol{\delta u} \cdot \boldsymbol{f} \; d\Omega_m = 0 \quad \forall \boldsymbol{\delta u} \tag{2.31}$$

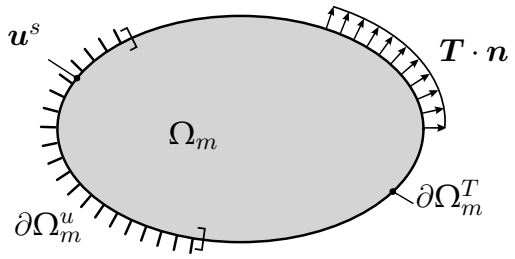

Figure 2.2: Domains of the mechanical problem

Integrating by parts gives,

$$\int_{\Omega_m} \nabla\boldsymbol{\delta u} : \boldsymbol{T}\ d\Omega_m - \int_{\Omega_m} \boldsymbol{\delta u}\cdot\boldsymbol{f}\ d\Omega_m - \int_{\partial\Omega_m^T} \boldsymbol{\delta u}\cdot(\boldsymbol{T}\cdot\boldsymbol{n}) d\partial\Omega_m = 0 \quad \forall\boldsymbol{\delta u}. \tag{2.32}$$

Because $\boldsymbol{T}$ is symmetric,

$$\boldsymbol{T} : \nabla\boldsymbol{\delta u} = \boldsymbol{T} : \nabla^S\boldsymbol{\delta u} = \boldsymbol{T} : \boldsymbol{\delta S}. \tag{2.33}$$

Considering (2.33), (2.32) becomes:

$$\int_{\Omega_m} \nabla^S\boldsymbol{\delta u} : \boldsymbol{T}(\boldsymbol{u})\ d\Omega_m = \int_{\Omega_m} \boldsymbol{\delta u}\cdot\boldsymbol{f}\ d\Omega_m + \int_{\partial\Omega_m^T} \boldsymbol{\delta u}\cdot(\boldsymbol{T}\cdot\boldsymbol{n}) d\partial\Omega_m \quad \forall\boldsymbol{\delta u}. \tag{2.34}$$

With the relation between $\boldsymbol{S}$ and $\boldsymbol{T}$ given by (2.22) and the proper boundary conditions: $\boldsymbol{u} = \boldsymbol{u^s}$ in $\partial\Omega_m^u$ and $\boldsymbol{T}\cdot\boldsymbol{n}$ imposed on $\partial\Omega_m^T$. The mechanical weak form can then be written as: find $\boldsymbol{u}$ such that,

$$\int_{\Omega_m} \nabla^S\delta\boldsymbol{u} : \boldsymbol{c} : \nabla^S\boldsymbol{u}\ d\Omega_m = \int_{\Omega_m} \boldsymbol{\delta u}\cdot\boldsymbol{f}\ d\Omega_m + \int_{\partial\Omega_m^T} \boldsymbol{\delta u}\cdot(\boldsymbol{T}\cdot\boldsymbol{n}) d\partial\Omega_m \quad \forall\boldsymbol{\delta u}, \tag{2.35}$$

along with the appropriate boundary conditions. For our particular applications, the volume force density $\boldsymbol{f}$ will be considered negligible in comparison to the local couplings introduced in Chapter 1. In this case,

$$\int_{\Omega_m} \nabla^S\delta\boldsymbol{u} : \boldsymbol{c} : \nabla^S\boldsymbol{u}\ d\Omega_m = \int_{\partial\Omega_m^T} \boldsymbol{\delta u}\cdot(\boldsymbol{T}\cdot\boldsymbol{n}) d\partial\Omega_m \quad \forall\boldsymbol{\delta u}. \tag{2.36}$$

2.3.3 Weak form of the magnetostatic problem

Contrary to the electric problem, the magnetic field is not canalyzed by the active material. This is a consequence of the magnetic excitation J^s being located far from the active material. Therefore, in order to account for the behavior of the magnetic field outside the active material, Maxwell's equations have to be solved in the air region. A way of modeling magnetic phenomena with the FEM is to consider and mesh a large enough closed air region and to impose the magnetic reaction of the material equal to zero at its boundary, therefore a large air region has to be considered, adding a significant number of DoFs to the problem to be solved. The accuracy of the solution will depend on the size of the truncated air domain. For our application, in a pure FEM context, to keep a reasonable number of DoFs is incompatible with an acceptable accuracy of the solution. We will see in the next section how a coupling of the FEM with the BEM will make it possible to compute accurate solutions with a domain limited to the active material.

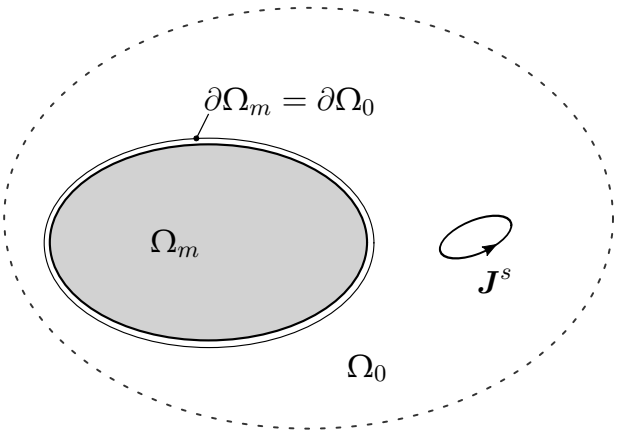

Figure 2.3: Domains of the magnetostatic problem

Two FEM-BEM formulations of the magnetostatic problem are established in the following sections. The first is based on the magnetic reduced scalar potential ϕ_{red} in the domain Ω_m and its boundary $\partial\Omega_m$. The second is a mixed formulation derived from a magnetic vector potential $\boldsymbol{a}$ inside the active domain Ω_m and a magnetic reduced scalar potential ϕ_{red} in its boundary $\partial\Omega_m$.

2.3.3.1 FEM-BEM ϕ_{red}-ϕ_{red} formulation

Weak form of the FEM magnetic problem inside the magnetic material

This formulation is said to be H-oriented or H-conforming, as the relation between the solving variable ϕ_{red} and $\boldsymbol{H}$ is strongly enforced by Relation (2.19). Relation (2.9) projected onto the virtual scalar field $\delta\phi \in H_{grad}$ in the domain Ω_m gives,

$$\int_{\Omega_m} \delta\phi \nabla \cdot \boldsymbol{B} \; d\Omega_m = 0. \tag{2.37}$$

Integrating by parts gives,

$$\int_{\Omega_m} \nabla\delta\phi \cdot \boldsymbol{B} \; d\Omega_m - \int_{\partial\Omega_m} \delta\phi \; B_n \; d\partial\Omega_m = 0. \tag{2.38}$$

With $B_n = \boldsymbol{B} \cdot \boldsymbol{n}$. Introducing (2.24) into (2.38) gives the following weak form: find (ϕ_{red}, B_n) such that,

$$\int_{\Omega_m} \nabla\delta\phi \cdot \boldsymbol{\mu} \cdot \nabla\phi_{red} \; d\Omega_m + \int_{\partial\Omega_m} \delta\phi \; B_n \; d\partial\Omega_m = \int_{\Omega_m} \nabla\delta\phi \cdot \boldsymbol{\mu} \cdot \boldsymbol{H_0} \; d\Omega_m \forall\delta\phi, \tag{2.39}$$

BEM scalar formulation outside the magnetic material

In the air region Ω_0 and particularly at its boundary $\partial\Omega_0 = \partial\Omega_m$, because of the linear permeability of the air region μ_0, the magnetic reduced scalar potential ϕ_{red} fulfills the Laplace equation [139]. Indeed, in Ω_0,

$$\nabla \cdot (\mu_0 \nabla\phi_{red}) = 0 \tag{2.40}$$

which leads to

$$\Delta\phi_{red} = 0. \tag{2.41}$$

A solution to such an equation, integrable in $\mathbb{R}^3$, can be expressed as integral expressions of the kernel of the Laplacian operator [140],

$$G = \frac{1}{r}, \tag{2.42}$$

in 3D. Indeed for any pair of scalar functions (u, v) twice differentiable over a closed domain $\mathbf{\Omega}$ [22],

$$\int_{\Omega} u\Delta v - v\Delta u d\Omega = \int_{\partial\Omega} u\frac{\partial v}{\partial \boldsymbol{n}} - v\frac{\partial u}{\partial \boldsymbol{n}} d\partial\Omega. \tag{2.43}$$

with,

$$\int_{\Omega} \varphi\Delta G \; d\Omega = \frac{\Theta}{4\pi}\varphi = c\varphi, \tag{2.44}$$

where Θ is equal to the solid angle of the point where this equation is formulated onto the surface $\partial\Omega$. Green's third identity applied to ϕ_{red} and G on the closed surface $\partial\Omega_m$, and considering (2.41), we obtain,

$$c \; \phi_{red} = \int_{\partial\Omega_m} \phi_{red} \; \frac{\partial G}{\partial \boldsymbol{n}} d\partial\Omega_m - \int_{\partial\Omega_m} G \; \frac{\partial \phi_{red}}{\partial \boldsymbol{n}} d\partial\Omega_m, \tag{2.45}$$

with c as defined earlier. Taking into account (2.24) in the air domain, the normal component of the magnetic field density can be expressed as:

$$B_n = \mu_0 \left((\boldsymbol{H_0} \cdot \boldsymbol{n}) - \frac{\partial \phi_{red}}{\partial \boldsymbol{n}} \right), \tag{2.46}$$

which, introduced into (2.45) gives,

$$\frac{\partial \phi_{red}}{\partial \boldsymbol{n}} = H_{0n} - \frac{B_n}{\mu_0}, \tag{2.47}$$

with $H_{0n} = \boldsymbol{H_0} \cdot \boldsymbol{n}$. Introducing (2.47) into the strong formulation (2.45) gives,

$$c \; \phi_{red} = \int_{\partial\Omega_m} \frac{\partial G}{\partial \boldsymbol{n}} \phi_{red} \; d\partial\Omega_m - \int_{\partial\Omega_m} G \left(H_{0n} - \frac{B_n}{\mu_0} \right) d\partial\Omega_m. \tag{2.48}$$

Rearranging the terms, the strong formulation of the magnetic problem in the air domain $\partial\Omega_0$, and in particular at its boundary with Ω_m, $\partial\Omega_m$, becomes:

$$-c \; \phi_{red} + \int_{\partial\Omega_m} G\frac{B_n}{\mu_0} d\partial\Omega_m + \int_{\partial\Omega_m} \phi_{red}\frac{\partial G}{\partial \boldsymbol{n}} d\partial\Omega_m = \int_{\partial\Omega_m} G \; H_{0n} d\partial\Omega. \tag{2.49}$$

The weak form of the magnetic formulation in the air domain can be obtained by projecting (2.49) onto an appropriate virtual scalar field $\delta\phi$ in the closed surface $\partial\Omega_m$ corresponding to the boundary of the active material. The weak formulation of magnetic phenomena in the air domain reads: find (ϕ_{red}, B_n) such that,

$$\begin{aligned}&\int_{\partial\Omega_m}\delta\phi\int_{\partial\Omega_m}\phi_{red}\frac{\partial G}{\partial \boldsymbol{n}}\;d\partial\Omega_m d\partial\Omega_m+\int_{\partial\Omega_m}\delta\phi\int_{\partial\Omega_m}G\frac{B_n}{\mu_0}\;d\partial\Omega_m d\partial\Omega_m\\&-\int_{\partial\Omega_m}\delta\phi\;c\;\phi_{red}\;d\partial\Omega_m=\int_{\partial\Omega_m}\delta\phi\int_{\partial\Omega_m}G\;H_{0n}\;d\partial\Omega_m d\partial\Omega_m\quad\forall\delta\phi.\end{aligned}\tag{2.50}$$

Interface conditions

The magnetic interface conditions across $\partial\Omega_m$ in the absence of surface current density are,

$$[\;\boldsymbol{H}\times\boldsymbol{n}\;]_{\partial\Omega_m}=0,\tag{2.51}$$

$$[\;\boldsymbol{B}\cdot\boldsymbol{n}\;]_{\partial\Omega_m}=0,\tag{2.52}$$

where $[\bullet]_{\partial\Omega}$ denotes the jump across the surface $\partial\Omega_m$. These two conditions are satisfied by considering B_n and ϕ_{red} continuous across $\partial\Omega$. Coupling (2.38) and (2.50) therefore respects the physical constraints of fields across $\partial\Omega$. This coupling of equations finalizes the coupling of the weak problems inside and outside the active material.

2.3.3.2 FEM-BEM a-ϕ_{red} formulation

Another approach to the magnetic phenomena allows using a B-conforming formulation inside Ω_m while using the same weak form (2.50) at the boundary of the active material. Projecting (2.10) onto a virtual vector field $\boldsymbol{\delta a}\in H_{\text{curl}}$ gives,

$$\int_{\Omega_m}\boldsymbol{\delta a}\cdot\nabla\times\boldsymbol{H}\;d\Omega_m=0.\tag{2.53}$$

Integrating by parts we get:

$$-\int_{\Omega_m}\nabla\cdot(\boldsymbol{\delta a}\times\boldsymbol{H})d\Omega_m+\int_{\Omega_m}\nabla\times\boldsymbol{\delta a}\cdot\boldsymbol{H}\;d\Omega_m=0.\tag{2.54}$$

As, $\boldsymbol{H} = \boldsymbol{\nu} \cdot \nabla \times \boldsymbol{a}$, the second term of (2.54) becomes:

$$\int_{\Omega_m} \nabla \times \boldsymbol{\delta a} \cdot \boldsymbol{H} \; d\Omega_m = \int_{\Omega_m} \nabla \times \boldsymbol{\delta a} \cdot \boldsymbol{\nu} \cdot \nabla \times \boldsymbol{a} \; d\Omega_m. \tag{2.55}$$

Introducing (2.19) into the first term of (2.54) gives,

$$\int_{\Omega_m} \nabla \cdot (\boldsymbol{\delta a} \times \boldsymbol{H}) \; d\Omega_m = \int_{\Omega_m} \nabla \cdot (\boldsymbol{\delta a} \times \boldsymbol{H_0} - \boldsymbol{\delta a} \times \nabla \phi_{red}) \; d\Omega_m. \tag{2.56}$$

Applying the Green-Ostrogradski theorem and rearranging the left-hand side terms of (2.56) gives,

$$\begin{aligned} \int_{\Omega_m} \nabla \cdot (\boldsymbol{\delta a} \times \boldsymbol{H_0}) \; d\Omega_m &= \int_{\partial\Omega_m} (\boldsymbol{\delta a} \times \boldsymbol{H_0}) \cdot \boldsymbol{n} \; d\partial\Omega_m, \\ &= \int_{\partial\Omega_m} (\boldsymbol{\delta a} \times \boldsymbol{n}) \cdot \boldsymbol{H_0} \; d\partial\Omega_m. \end{aligned} \tag{2.57}$$

Relation (2.57) will constitute the second hand term of the magnetic equation. Also,

$$\int_{\Omega_m} \nabla \cdot (-\boldsymbol{\delta a} \times \nabla \phi_{red}) \; d\Omega_m = \int_{\Omega_m} \nabla \cdot (\nabla \phi_{red} \times \boldsymbol{\delta a}) \; d\Omega_m, \tag{2.58}$$

Considering the vector identity :

$$\nabla \phi_{red} \times \boldsymbol{\delta a} = \nabla \times (\phi_{red} \; \boldsymbol{\delta a}) - \phi_{red} \; \nabla \times \boldsymbol{\delta a}, \tag{2.59}$$

then (2.58) can be written as :

$$\begin{aligned} \int_{\Omega_m} \nabla \cdot (\nabla \phi_{red} \times \boldsymbol{\delta a}) \; d\Omega_m &= \int_{\Omega_m} \nabla \cdot (\nabla \times (\phi_{red} \boldsymbol{\delta a})) \; d\Omega_m \\ &- \int_{\Omega_m} \nabla \cdot (\phi_{red} \; \nabla \times \boldsymbol{\delta a}) \; d\Omega_m. \end{aligned} \tag{2.60}$$

Using,

$$\nabla \cdot \nabla \times (\nabla \phi_{red} \cdot \boldsymbol{\delta a}) = 0, \tag{2.61}$$

and applying the Green-Ostrogradski theorem, we obtain:

$$\begin{aligned}\int_{\Omega_m} \nabla \cdot (\nabla \phi_{red} \times \boldsymbol{\delta a})\ d\Omega_m &= -\int_{\partial\Omega_m} (\phi_{red}\ \nabla \times \boldsymbol{\delta a}) \cdot \boldsymbol{n}\ d\partial\Omega_m, \\ &= -\int_{\partial\Omega_m} \phi_{red}\ \nabla \times \boldsymbol{\delta a} \cdot \boldsymbol{n}\ d\partial\Omega_m.\end{aligned} \tag{2.62}$$

Finally, the mixed weak form of the magnetic problem reads: find $(\boldsymbol{a}, \phi_{red})$ such that,

$$\begin{aligned}\int_{\Omega_m} \nabla \times \boldsymbol{\delta a} \cdot \boldsymbol{\nu} \cdot\ \nabla \times \boldsymbol{a}\ d\Omega_m\ +\ \int_{\partial\Omega_m} (\nabla \times \boldsymbol{\delta a} \cdot \boldsymbol{n}) \phi_{red}\ d\partial\Omega_m \\ = \int_{\partial\Omega_m} (\boldsymbol{\delta a} \times \boldsymbol{n}) \cdot \boldsymbol{H_0}\ d\partial\Omega_m, \quad \forall \boldsymbol{\delta a}.\end{aligned} \tag{2.63}$$

In this equation, the magnetic flux density inside the magnetic material, Ω_m, is calculated with a B-conforming formulation [1], while, at its boundary $\partial\Omega_m$, with the same weak BEM formulation as for the magnetic reduced scalar potential formulation, (2.50). The coupling between both weak forms involve taking $\boldsymbol{a}$ and ϕ_{red} continuous across $\partial\Omega$. It will be rendered explicit after discretization of the weak forms.

2.4 Discretization of the weak forms

2.4.1 General framework

The previously described weak forms establish the mathematical framework to obtain what are called continuous solutions, as opposed to discrete solutions, which come from the discretization of the geometry. In [141] and [120] the existence and uniqueness of these continuous solutions for single-physics problems are treated. Later work was applied to coupled problems, some notable work is presented in [142, 143], in which the conditions for the existence and uniqueness of a solution for linear problems is stated, notably the inf sup condition. In [144, 145], some conditions on the existence and uniqueness of FEM formulations of piezomagnetic formulations have been established, nevertheless, our FEM-BEM approach is outside their scope.

[1] as the relation between the solving variable $\boldsymbol{a}$ and $\boldsymbol{B}$ is strongly enforced

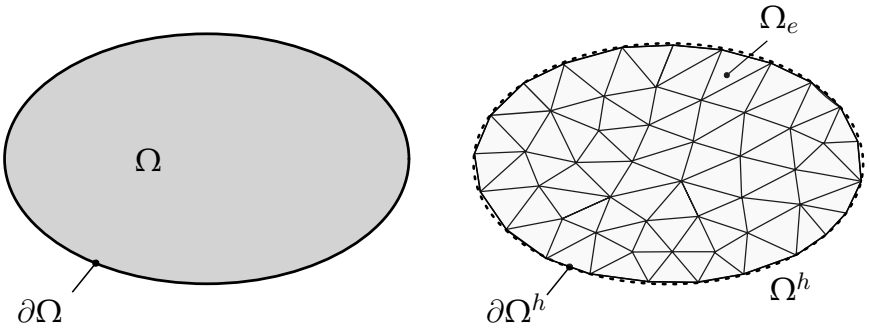

(a) Geometry to be discretized **(b)** Discretized domain

Figure 2.4: Geometrical domain Ω approximated by the discretized domain Ω^h made of a finite set of elements

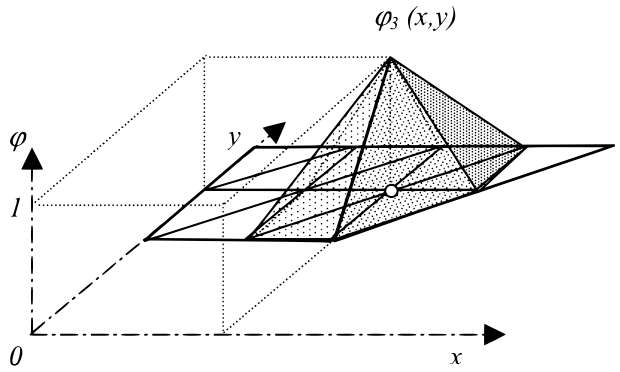

Figure 2.5: 1st-order nodal shape functions linked to node "3" [11]. They are equal to one at node and 0 at all others, in the neighboring elements, they vary linearly

An explicit analytical solution to the continuous problem, expressed as the solution to the weak form of the considered problem, is impossible for most applications. The domain of study can however be discretized into a set of finite elements, hexagonal or tetragonal in general, resulting in a polygonal discrete approximation of the considered domain in which the weak form was formulated. As shown in Figures 2.4a and 2.4b, the domain Ω was discretized into a finite set of elements, whose union Ω^h approximates Ω, i.e., $\Omega^h = \cup_e^{n_{elem}} \Omega_e \approx \Omega$. The discretization of the geometry into a finite set of elements leads to the choice of a finite set of interpolating shape functions that will describe the behavior of the given field in the discretized domain. The weak forms of the continuous problems are then replaced by their discrete counterparts, associated to the discrete representation of the physical problem.

In general, the shape functions are polynomials of the parameters of the ele-

ment to which they belong, and the integration in the weak forms performed by Gauss quadrature. The solving of the discrete formulation, which is in the form of a finite system of equations, then gives a global solution. This solution is an approximation of the continuous solution and the discrete solution converges towards the continuous solution as the mesh is refined, and more elements are added [120, 121, 122]. This type of refinement is called *h-refinement*, and this convergence *h-convergence*.

2.4.2 Whitney elements

The chosen type of elements that will carry the DoFs depends on the nature of the computed field. The Tonti diagram [18] [146] illustrates the links between the structure of the different fields present in Maxwell's equations and how they relate to a type of element.

2.4.2.1 Nodal elements

Scalar quantities in general translate into gradients present in the weak forms, it is for example the case for (2.28) and (2.36). Therefore, in general shape functions of scalar quantities will be chosen as belonging to the set of integrable functions whose gradient is integrable over the domain, i.e, H_{grad} [146]. Nodal elements are in general used to collocate scalar quantities and nodal shape funtions used to interpolate them, indeed, the use of nodal colocation ensures the belonging of the solution to the discrete problem to H_{grad}. A 1st-order nodal shape function for a 2D mesh is presented in Figure 2.5, *1st-order* because 1st degree polynomials are used as interpolating functions, they are taken equal to 1 at their corresponding node, and 0 at the others.

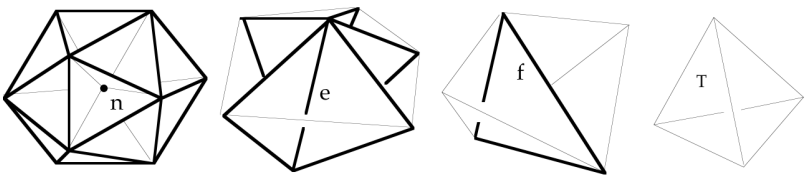

Figure 2.6: Nodal, edge, facet and cell elements on an example mesh [12]

2.4.2.2 Edge elements

Edge elements [18] [147] are the natural way of representing fields that appear as integrated over 1D domains (called 1-forms), such as the magnetic and electric fields $\boldsymbol{H}$ and $\boldsymbol{E}$. The test functions are taken within the set of integrable functions whose curl is integrable over the domain, i.e, H_{curl}. They enforce the continuity of the tangent component of the interpolated field ($\boldsymbol{E} \times \boldsymbol{n}$ or $\boldsymbol{a} \times \boldsymbol{n}$) between facets of the mesh.

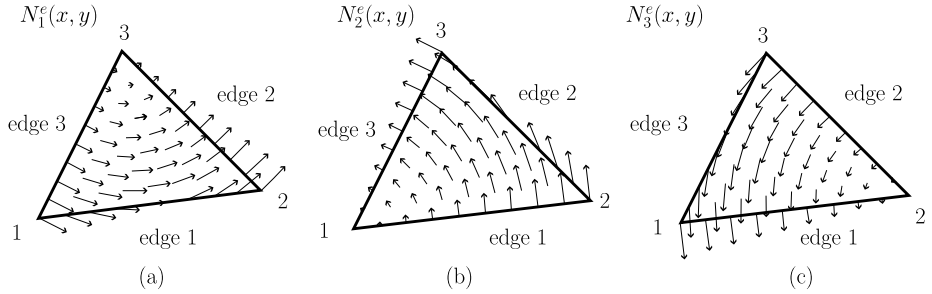

Figure 2.7: Interpolation of Nédélec edge shape functions within a 2D triangular element [13]

The interpolation of the considered edge shape functions inside a triangular element is presented in Figure 2.7. The stored discrete quantity, for example for the field $\boldsymbol{a}$, is given by the circulation of $\boldsymbol{a}$ accross the given edge, i.e.,

$$a_k = \int_{\text{edge}_k} \boldsymbol{a} \cdot \boldsymbol{d}\ \text{edge}_{\boldsymbol{k}}. \tag{2.64}$$

The use of edge elements as collocation element enforce the belonging of the solution to the discrete problem to H_{curl}.

2.4.2.3 Facet elements

Facet elements [147, 148] are chosen for quantities which appear integrated over a surface (2-forms) and the associated shape functions belong to the set of integrable functions whose divergence is integrable over the domain, i.e. H_{div}. The use of facet elements helps enforce the continuity of the normal fields, B_n or D_n for example, across elements of the mesh. This is the case of the magnetic flux density $\boldsymbol{B}$ and electric displacement field $\boldsymbol{D}$. The stored discrete quantity, for example for a field $\boldsymbol{B}$, is given by:

$$B_k = \int_{\text{facet}_k} (\boldsymbol{B} \cdot \boldsymbol{n}) \; d \; \text{facet}_k \tag{2.65}$$

The use of facet elements as collocation element enforce the belonging of the solution to the discrete problem to H_{div}. Also, expressing $\boldsymbol{a}$ in edge elements results in a natural expression of $\boldsymbol{B}$ in facet elements.

2.4.2.4 Higher order FEM

Higher order FEM are obtained by using higher order polynomials as shape functions and adding degrees of freedom to the polynomials by introducing intermediary collocation points, which may be edges or facets and which will carry additional degrees of freedom, this type of refinement is called (p-refinement). The best convergence is obtained by both refining the mesh and increasing the degree of the FEM approach (*hp*- FEM) [122]. We will however use 1-st order FEM in this manuscript for their ease of implementation.

2.4.2.5 Discretization of BEM equations

For the discretization of BEM equations, 0th-order surface elements can be used for the discretization of BEM elements, this means that a single value (DoFs) is attributed to each cell, the value of the quantity is taken uniform per surface element. Higher order elements can also be used with several DoFs per surface element, resulting in higher order polynomial variations of the shape functions at one exterior facet and better convergence towards the continuous solution [140].

2.4.3 Discretization of the electrostatic problem

The previously described scalar field φ and as its virtual counterpart $\delta\varphi$ can be expressed as:

$$\{\varphi, \delta\varphi\} = \sum_{I=1}^{n_{node}} N_\varphi^I \left\{\varphi^I, \delta\varphi^I\right\} \tag{2.66}$$

where φ^I denote the discrete nodal electric potential at node I, $\underline{\boldsymbol{\varphi}}$ the associated element vectors of unknowns and n_{node} the number of nodes of the discretized geometry. In the same way, $\delta\varphi^I$ and $\underline{\boldsymbol{\delta\varphi}}$ denote the respective

discrete virtual counterparts of φ^I and $\underline{\boldsymbol{\varphi}}$. N_φ^I are shape functions associated with node I. The solution to the electric weak (2.30) form can then be approximated by solving for $\boldsymbol{\varphi}$ in the following discrete equation:

$$\sum_{I,J}^{n_{node}} \delta\varphi^I \int_{\Omega_m} \mathbb{B}_\varphi^I \cdot \boldsymbol{\varepsilon} \cdot \mathbb{B}_\varphi^J \, \varphi^J d\Omega_m = 0 \quad \forall \delta\varphi^I, \tag{2.67}$$

where $\mathbb{B}_\varphi^I$ are the gradient matrices of the N_φ^I. Because the scalar potential carried by the DoFs is unconstrained, the discretized virtual field $\underline{\boldsymbol{\delta\varphi}}$ has all independent coefficients (all the $\delta\varphi^I$), then we must have [149]:

$$\sum_{I,J}^{n_{node}} \int_{\Omega_m} \mathbb{B}_\varphi^I \cdot \boldsymbol{\varepsilon} \cdot \mathbb{B}_\varphi^J \, \varphi^J d\Omega_m = 0, \tag{2.68}$$

which in matrix form gives:

$$[\underline{\boldsymbol{K}}_{\varphi\varphi}] \cdot \underline{\boldsymbol{\varphi}} = 0 \tag{2.69}$$

And only the imposing of $\varphi^I = \varphi_0$ for nodes belonging to $\partial\Omega_m^\varphi$ will drive the system and serve to gauge the electric scalar potential.

2.4.4 Discretization of the mechanical problem

The mechanical weak form (2.36) can be discretized using nodal elements for each of the components of $\boldsymbol{u}$, u_x, u_y and u_z, and as its virtual counterpart $\delta\boldsymbol{u}$ as:

$$\{\boldsymbol{u}, \boldsymbol{\delta u}\} = \sum_{I=1}^{n_{node}} N_u^I \left\{u^I, \delta u^I\right\} \tag{2.70}$$

where u^I denote the discrete nodal displacement at node I, $\underline{\boldsymbol{u}}$ the associated element vectors of unknowns. In the same way, δu^I and $\underline{\boldsymbol{\delta u}}$ denote the respective discrete virtual displacements. N_u^I are shape functions associated with node I. It follows the discrete form:

$$\sum_{I,J}^{n_{node}} \delta\boldsymbol{u}^I \int_{\Omega_m} \mathbb{B}_u^I : \boldsymbol{c} : \mathbb{B}_u^J \cdot \boldsymbol{u}^J d\Omega_m = \sum_{I}^{n_{node}} \delta\boldsymbol{u}^I \int_{\partial\Omega_m^T} {}^{tr}N_u^I \cdot (\boldsymbol{T} \cdot \boldsymbol{n}) \, d\partial\Omega_m \quad \forall \delta u^I \tag{2.71}$$

and $\mathbb{B}_u^I$ the symmetric gradient matrices of the nodal mechanical shape functions N_u. Because, the $\underline{\boldsymbol{u}}$ correspond to unconstrained body motion for the DoFs [149], the discretized virtual field $\underline{\boldsymbol{\delta u}}$ has all independent coefficients, then we must have:

$$[\underline{\boldsymbol{K}}_{uu}] \cdot \underline{\boldsymbol{u}} = \underline{\boldsymbol{Sh}}_{mecha} \tag{2.72}$$

with

$$\underline{\boldsymbol{K}}_{uu}^{IJ} = \int_{\Omega_m} \mathbb{B}_u^I \cdot \ \boldsymbol{c} \cdot \mathbb{B}_u^J \ d\Omega_m, \tag{2.73}$$

$$\underline{\boldsymbol{Sh}}_{mecha}^I = \int_{\partial\Omega_m^T} {}^{tr}N_u^I \cdot (\boldsymbol{T} \cdot \boldsymbol{n}) \ d\partial\Omega_m \tag{2.74}$$

For some situations, in order to model an unconstrained material, no imposed displacements can be considered, in this case, $\boldsymbol{u}$ is not uniquely defined. For these situations, an iterative solver can be used in order to obtain a solution which gives accurate strains though Relation (2.16).

2.4.5 Discretization of the ϕ_{red}-ϕ_{red} formulation

In (2.38), ϕ_{red} will be discretized into 1st order nodal shape functions N_ϕ, $\delta\phi$ and B_n into surface shape functions constant by surface elements N_0. As equation (2.45) is applied at the Gauss points of the surface elements of the polygonal approximation of the considered geometry, a flat surface, $c = \frac{1}{2}$.

$$\phi_{red} = \sum_{I=1}^{n_{node}} N_\phi^I \ \phi_{red}^I, \tag{2.75}$$

$$B_n = \sum_{I=1}^{n_{fExt}} N_0^I \ B_n^I, \tag{2.76}$$

$$\delta\phi = \sum_{I=1}^{n_{fExt}} N_0^I \ \delta\phi^I, \tag{2.77}$$

with n_{fExt} the number of surface elements at the boundary of the domain. The discrete set of test functions N_0^I associated with $\delta\phi_0$ will be taken as 0th-order surface elements. Given these discretizations, the approximate

solution of weak formulations (2.38) and (2.50) can be expressed as the solution to the following algebraic system:

$$\begin{bmatrix} \underline{\boldsymbol{K}}_{\phi\phi} & \underline{\mathbf{0}} \\ & \underline{\boldsymbol{K}}_{\phi b_n} \\ \underline{\mathbf{0}} \quad \underline{\mu_0 \boldsymbol{H}} & \underline{\boldsymbol{T}} \end{bmatrix} \begin{pmatrix} \underline{\boldsymbol{\phi}}_{red}^{int} \\ \underline{\boldsymbol{\phi}}_{red}^{surf} \\ \underline{\boldsymbol{B_n}} \end{pmatrix} = \begin{pmatrix} \underline{\boldsymbol{Sh}}_{mag}^{\Omega_m} \\ \underline{\boldsymbol{Sh}}_{mag}^{\partial\Omega_m} \end{pmatrix} \tag{2.78}$$

where:

$$\underline{\boldsymbol{K}}_{\phi\phi}^{IJ} = \int_{\Omega_m} \mathbb{B}_{\varphi}^{I} \cdot \boldsymbol{\mu} \cdot \mathbb{B}_{\varphi}^{J} \, d\Omega_m \tag{2.79}$$

$$\underline{\boldsymbol{K}}_{\phi b_n}^{IJ} = \int_{\partial\Omega_m} \mathbb{B}_{\varphi}^{I} \cdot N_0^J d\partial\Omega_m \tag{2.80}$$

$$\underline{\boldsymbol{H}}^{IJ} = \int_{\partial\Omega_m} N_0^I \int_{\partial\Omega_m} \frac{\partial G}{\partial \boldsymbol{n}} \, {}^{tr}N_{\phi}^{J} \, d\partial\Omega_m d\partial\Omega_m - \frac{1}{2} \int_{\partial\Omega_m} N_0^I \, {}^{tr}N_{\phi}^{J} d\partial\Omega_m \tag{2.81}$$

$$\underline{\boldsymbol{T}}^{IJ} = \int_{\partial\Omega_m} N_0^I \int_{\partial\Omega_m} \frac{G}{\mu_0} \, N_0^J \, d\partial\Omega_m \, d\partial\Omega_m \tag{2.82}$$

$$\underline{\boldsymbol{Sh}}_{mag}^{\Omega_m \, I} = \int_{\Omega_m} \mathbb{B}_{\phi}^{I} \, \boldsymbol{\mu} \, \boldsymbol{H_0} \, d\Omega_m \tag{2.83}$$

$$\underline{\boldsymbol{Sh}}_{mag}^{\partial\Omega_m \, I} = \int_{\partial\Omega_m} N_0^I \int_{\partial\Omega_m} G \, H_{0n} \, d\partial\Omega_m d\partial\Omega_m \tag{2.84}$$

In (2.78), sparse matrices are presented in light blue whereas full matrices are presented in dark blue. Indeed, the double integration of shape functions translate the non-null influence of every surface elements on every surface element.

Without a gauge, this matrix system is singular, and therefore the solution not uniquely defined. The use of an iterative solver will allow us to nevertheless obtain an admissible solution. Another disadvantage of this formulation is that it can produce error cancellation problems for problems with high permeability ($\boldsymbol{H_{red}} \approx \boldsymbol{H_0}$). This problem can be overcome by projecting $\boldsymbol{H_0}$ onto edge elements [150]. Indeed, ϕ_{red} being a nodal quantity the natural space for its gradient are the edges of the mesh. Other formulations such as the total scalar potential - reduced scalar potential [151] can be used for these situations. For our particular application, considering the properties of the materials in question: relatively low permeabilities, this will not be a problem.

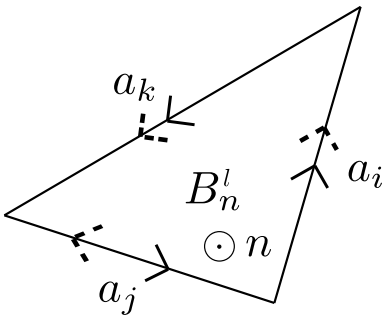

Figure 2.8: Local Stockes theorem on a surface element. The dotted arrows denote the orientation of the element, the full arrows, the positive orientation of the circulation over the 1-form boundary of the surface element with respect its outwards oriented normal vector $\boldsymbol{n}$. Here $B_n^l = a_i + a_k - a_j$

2.4.6 Discretization of the a-ϕ_{red} formulation

Regarding the magnetic problem inside the active material, $\boldsymbol{a}$ will be discretized using edge shape functions N_e, matrix $\mathbb{B}_a$ will denote their curl. The magnetic reduced scalar potential ϕ_{red} will be discretized using 0th-order surface shape functions N_0, and $\delta\phi$ along (2.77), i.e.,

$$\{\boldsymbol{a}, \delta\boldsymbol{a}\} = \sum_{I=1}^{n_{edge}} N_e^I \left\{a^I, \delta a^I\right\} \tag{2.85}$$

$$\phi_{red} = \sum_{I=1}^{n_{fExt}} N_0^I \ \phi_{red}^I \tag{2.86}$$

The BEM equation in the air region (2.50) still holds. The normal component of the magnetic flux density can be obtained by the application of a local Stokes theorem at each surface element of Ω_m^h. An example of such development is presented in Figure 2.8. From a discrete point of view, The value of the normal component of the magnetic flux density can indeed be written as:

$$\begin{aligned} B_n^l &= \iint_{\mathrm{fExt}_k} (\boldsymbol{B}\cdot\boldsymbol{n})\ d\mathrm{fExt}_k \\ &= \oint \boldsymbol{a}\cdot\boldsymbol{dl} \\ &= \sum_{i=\mathrm{edges}} C_{ki}\ a_i \end{aligned} \tag{2.87}$$

The discretized B_n in column form can then be linked to the discretized $\boldsymbol{a}$ by a matrix C which is in fact the trace of a discrete curl operator onto the

exterior surface $\partial\Omega$. Matrix C can be expressed as an incidence matrix C containing only 0s, 1s and -1s,

- $C_{ki} = 0$ if the edge "i" is not an edge of the exterior facet "k",
- $C_{ki} = 1$ if the edge "i" is an edge of exterior facet "k" and the orientation of the edge element is the same as the orientation of the positive circulation along the edge of the exterior facet,
- $C_{ki} = -1$ if the edge "i" is an edge of exterior facet "k" and the orientation of the edge element is opposite to the orientation of the positive circulation along the edge of the exterior facet.

ϕ_{red} will also be discretized using 0th-order surface shape functions N_0 in the weak form of Green's third identity. Taking both ϕ_{red} and B_n continuous, B_n later transformed into $\boldsymbol{a}$ by matrix C, enforces the two interface conditions (2.51) and (2.52) so the two discretized equations can be coupled, thus finalizing the mixed formulation of the magnetic problem.

$$\begin{bmatrix} \underline{\boldsymbol{K}}_{aa} & \underline{0} & \\ & \underline{\boldsymbol{K}}_{a\phi_{red}} & \\ \underline{\mathbf{0}} & \underline{\boldsymbol{TC}} & \underline{\boldsymbol{H}} \end{bmatrix} \begin{pmatrix} \underline{\boldsymbol{a}}^{int} \\ \underline{\boldsymbol{a}}^{surf} \\ \underline{\boldsymbol{\phi_{red}}} \end{pmatrix} = \begin{pmatrix} \underline{\boldsymbol{Sh}}_{mag}^{\Omega_m} \\ \underline{\boldsymbol{Sh}}_{mag}^{\partial\Omega_m} \end{pmatrix} \tag{2.88}$$

where

$$\underline{\boldsymbol{K}}_{aa}^{IJ} = \int_{\Omega_m} \mathbb{B}_a^I \cdot \boldsymbol{\nu} \cdot \mathbb{B}_a^J \; d\Omega_m \tag{2.89}$$

$$\underline{\boldsymbol{K}}_{a\phi} = \int_{\partial\Omega_m} \mathbb{B}_a^I \cdot N_0^J \; d\partial\Omega_m \tag{2.90}$$

$$\underline{\boldsymbol{H}}^{IJ} = \int_{\partial\Omega_m} N_0^I \int_{\partial\Omega_m} \frac{\partial G}{\partial \boldsymbol{n}} N_0^J \; d\partial\Omega_m d\partial\Omega_m - \frac{1}{2} \int_{\partial\Omega_m} N_0^I N_0^J d\partial\Omega_m \tag{2.91}$$

$$\underline{\boldsymbol{T}}^{IJ} = \int_{\partial\Omega_m} N_0^I \int_{\partial\Omega_m} \frac{G}{\mu_0} \; N_0^J \; d\partial\Omega_m \; d\partial\Omega_m \tag{2.92}$$

$$\underline{\boldsymbol{Sh}}_{mag}^{\Omega_m} = \int_{\partial\Omega_m} ({}^{tr}N_a^I \times \boldsymbol{n}) \; \boldsymbol{H}_0 \; d\partial\Omega_m \tag{2.93}$$

$$\underline{\boldsymbol{Sh}}_{mag}^{\partial\Omega_m\,I} = \int_{\partial\Omega_m} N_0^I \int_{\partial\Omega_m} G \; H_{0n} \; d\partial\Omega_m \tag{2.94}$$

For the discretization of the $\boldsymbol{a} - \phi_{red}$ matrix system, a gauge, such as a Coulomb gauge [152] [153] or a tree-cotree gauge [138] can be used in order

to impose the uniqueness of the solution. A tree-cotree gauge also allows to reduce the number of DoFs of the total matrix system by setting to 0 the value of $\boldsymbol{a}$ in the edges of the tree of the mesh, contrary to a Coulomb gauge which adds DoFs to the system. Its implementation is however not trivial and we prefer, as we did for the scalar formulation, to solve the system using an iterative solver, this approach gives a solution not uniquely defined but whose curl is uniquely defined [154].

2.4.7 Numerical treatment of the discrete systems

2.4.7.1 Resolution of the FEM systems

As the interaction between two nodes or edges will be limited to their shared elements, FEM matrices are sparse. For gauged formulations, these matrix systems can be solved by direct solvers adapted to sparse matrices such as Multifrontal Massively Parallel sparse direct Solver (MUMPS) direct solver [155] or by using iterative solvers implementing gradient descent, such as Incomplete Cholesky Conjugate Gradient solver (ICCG). Iterative solvers can also be used to find solutions to ungauged problems, also, MUMPS direct solver uses automatic regularisation and allows to solve for ungauged problems.

2.4.7.2 Storage and resolution of the FEM-BEM systems

As stated before, BEM matrices are full, this translates into a complexity of the discrete problem of the order of $O(\text{nbDoFs}^2)$. Matrix compression techniques such as Fast Multipole Method (FMM) [156] or Hybrid Cross Approximation (HCA) [157] can be applied to BEM matrices in order to reduce storage space, this storage is particularly useful for very large matrices where high compression ratios can be obtained (up to 80% for the meshes used in the current manuscript).

Solving the sparse matrix system derived form the FEM can be fairly straightforward, this is not the case for the FEM-BEM matrix systems. As mentioned before, the assembled FEM-BEM matrix systems contain indeed both sparse and full matrices. GMRES [158] iterative solver is used to solve the assembled matrix systems. Preconditionners are used to ease the resolution. A block preconditionner is used in both formulations, an incomplete LU (ILU) is used on the FEM block with a shift of the diagonal

in order to avoid the singularity of the matrix as no reference potential is imposed in both formulations.

For the BEM bloc, if no compression technique is considered, a Jacobi preconditioner is used. HCA compression can also be used to obtain an approximation of either $\underline{\boldsymbol{H}}$ or $\underline{\boldsymbol{T}}$, depending on which matrix is diagonal in the assembled matrix system of the given formulation. In the case HCA is used in the diagonal block, HCA-LU decomposition of the diagonal matrix can be used as a preconditioner for the BEM block. This leads to faster convergence of the resolution algorithm, with a GMRES iterative solver for linear problems or a Newton-Raphson solver for nonlinear constitutive laws. The Newton-Raphson requires the computation and integration of $\frac{\partial \boldsymbol{B}}{\partial \boldsymbol{H}}$ or $\frac{\partial \boldsymbol{H}}{\partial \boldsymbol{B}}$ and used a GMRES solver for the linear resolutions.

2.5 Computation of the source field

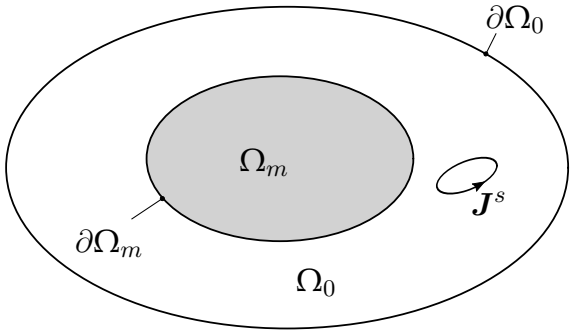

Figure 2.9: Subdomains considered for the computation of the source field based on a FEM formulation. Now $\Omega = \Omega_m \cup \Omega_0$ is closed

To this point, the source field $\boldsymbol{H_0}$ has been merely treated as an input of the problem. Many methods exist for computing the source field. Three of them will be presented.

2.5.1 Computation of the source field by projection onto edge elements

One way of computing the source field by the FEM derives from projecting (2.10) onto a virtual field $\delta\boldsymbol{H_0} \in H_{\text{curl}}$. Giving the following weak form find

$\boldsymbol{H_0}$ such that,

$$\int_\Omega \nabla \times \boldsymbol{\delta H_0} \cdot \nabla \times \boldsymbol{H_0}\ d\Omega = \int_\Omega \nabla \times \boldsymbol{\delta H_0} \cdot \boldsymbol{J^s}\ d\Omega \quad \forall \boldsymbol{\delta H_0}, \tag{2.95}$$

with

$$\nabla \cdot \boldsymbol{J^s} = 0. \tag{2.96}$$

In order for this source field to verify Maxwell's equations, in particular (2.1), one equation has to be added to the system of equations. As $\boldsymbol{B} = \boldsymbol{B_0} = \mu_0 \boldsymbol{H_0}$ in the absence of matter, imposing (2.1) is then equivalent as imposing,

$$\nabla \cdot \boldsymbol{H_0} = 0. \tag{2.97}$$

This equation can be verified weakly by projecting it onto a set of scalar test functions $\delta\phi' \in H_{\text{grad}}$. Integrated by parts and neglecting the boundary term, (2.97) becomes,

$$\int_\Omega \nabla \delta\phi' \cdot \boldsymbol{H_0}\ d\Omega = 0. \tag{2.98}$$

In order to make the system not singular after discretization, the transpose of the equation above can be added to (2.95) [153], giving the following weak forms: find $(\boldsymbol{H_0}, \phi')$:

$$\begin{aligned} \int_\Omega \nabla \times \boldsymbol{\delta H_0} \cdot \nabla \times \boldsymbol{H_0}\ d\Omega + \int_\Omega \boldsymbol{\delta H_0} \cdot \nabla\phi'\ d\Omega \\ = \int_\Omega \nabla \times \boldsymbol{\delta H_0} \cdot \boldsymbol{J^s}\ d\Omega \quad \forall \boldsymbol{\delta H_0}, \end{aligned} \tag{2.99}$$

$$\int_\Omega \nabla \delta\phi' \cdot \boldsymbol{H_0}\ d\Omega = 0 \quad \forall \delta\phi', \tag{2.100}$$

which gives an admissible solution if $\phi' = 0$ is imposed at the boundary of the meshed domain. This system can be discretized into edge elements for $\boldsymbol{H_0}$ and its virtual counterpart $\delta\boldsymbol{H_0}$ and nodal elements for ϕ' and $\delta\phi'$. As this method is derived from the FEM, a air region large enough to emulate the natural evanescence of magnetic fields has to be explicitly considered and meshed.

2.5.2 Magnetic vector potential formulation

Another approach can be to compute the vector potential $\boldsymbol{a_0}$ such that,

$$\boldsymbol{H_0} = \mu_0^{-1} \nabla \times \boldsymbol{a_0}. \tag{2.101}$$

Its development starts by the projection of (2.10) onto a virtual vector field $\delta\boldsymbol{a} \in H_{\text{curl}}$,

$$\int_\Omega \boldsymbol{\delta a} \cdot \nabla \times \boldsymbol{H}\ d\Omega = \int_\Omega \boldsymbol{\delta a} \cdot \boldsymbol{J^s} d\Omega, \tag{2.102}$$

with

$$\nabla \cdot \boldsymbol{J^s} = 0. \tag{2.103}$$

Integrating by parts and neglecting the boundary term gives the following weak form: find $\boldsymbol{a_0}$ such that,

$$\int_\Omega \nu_0 \nabla \times \boldsymbol{\delta a} \cdot \nabla \times \boldsymbol{a_0}\ d\Omega = \int_\Omega \boldsymbol{\delta a} \cdot \boldsymbol{J^s} d\Omega \quad \forall \delta\boldsymbol{a} \tag{2.104}$$

This equation leads to a singular matrix system when discretized. In consequence, either an iterative solver has to be used, in which case, $\boldsymbol{a_0}$ is not uniquely defined, or a proper gauge has to be employed. Whether it be a Coulomb gauge, used in the previous method of computing the source field, or either, the previously presented tree-cotree gauge [159]. Once $\boldsymbol{a_0}$ is known, $\boldsymbol{H_0}$ can then be obtained by (2.101).

2.5.3 Biot-Savart law

The Biot-Savart law can also be applied to compute the source field. It states,

$$\boldsymbol{H_0} = \int_\Omega \boldsymbol{\nabla} G \times \boldsymbol{J^s}\ d\Omega. \tag{2.105}$$

The integration in (2.105) can be computed numerically, by Gauss quadrature, or analytically [160]. This method of obtaining the source field can have a clear advantage in respect to both explored FEM approaches, its computational cost is independent of the distance between the coil and the device. In addition, both presented FEM-BEM approaches only need the computation of the source field inside and on the boundary of the active materials. Therefore, the approach of computing the source field by the

Biot-Savart law will lead to a reduction of the amount of memory necessary to store the computed source field with respect to the approaches presented in Sections 2.5.1 and 2.5.2. As $\nabla\phi_{red}$ is the gradient of a nodal quantity, its natural function space is in the edges of the mesh. After computing $\boldsymbol{H_0}$ by (2.105), it can then be projected onto edge elements by a FEM resolution in order to avoid problems of cancellation errors when considering materials with high permeability.

2.6 Validation of the magnetostatic formulations

Contrary the FEM formulations of mechanics, derived from linear elasticity, and electrostatics, which are fairly classical, we will now validate both FEM-BEM formulations and their convergence.

2.6.1 h-Convergence of the FEM-BEM formulations

These formulations can be validated vs an analytical solution giving the exact magnetic field inside a sphere under an uniform source magnetic field and a homogeneous magnetic permeability [24]:

$$\boldsymbol{H}_{exact} = \frac{3\ \boldsymbol{H_0}}{\mu_r + 2}. \tag{2.106}$$

For a sphere of homogeneous magnetic permeability $\mu_r = 10$ and a uniform source field $H_0 = 50\ \mathrm{kA\,m^{-1}}$, the magnetic field inside the sphere is uniform, of magnitude equal to $12.5\ \mathrm{kA\,m^{-1}}$ and oriented in the same direction of the source field. The L^2 error of the FEM-BEM solution, $\varepsilon_{L^2}(H)$, can then be calculated as follows,

$$\varepsilon_{L^2}(X) = \frac{\sqrt{\int_\Omega \left|\boldsymbol{X} - \boldsymbol{X_{exact}}\right|^2 d\Omega}}{\sqrt{\int_\Omega \left|\boldsymbol{X_{exact}}\right|^2 d\Omega}}, \tag{2.107}$$

in order to evaluate the local error of the formulation. The magnetostatic formulations were solved on a sequence of increasingly refined spheres meshed with the software Gmsh 4.11.0 [161]. The results of both FEM-BEM formulations were compared to the analytical solutions, in particular their

local error as a function of the number of DoFs of the discrete problem. We obtained the convergence curves shown in figure 2.10. We observe the h-convergence towards 0 of the L_2 error of both FEM-BEM formulations.

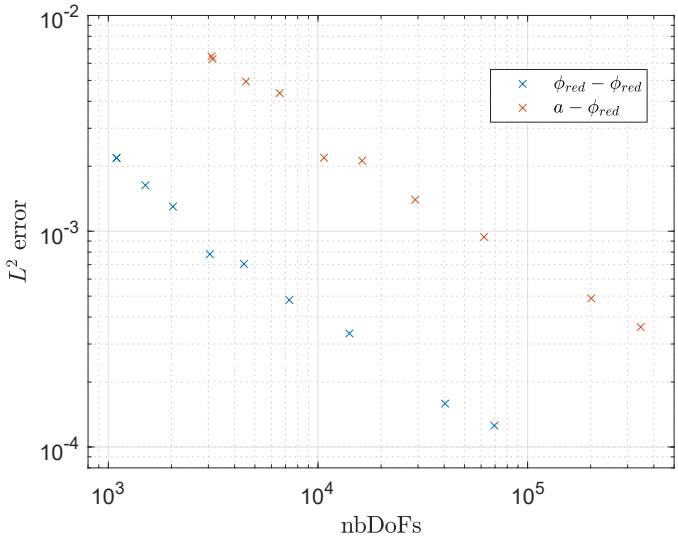

Figure 2.10: $\varepsilon_{L^2}(H)$ for the solution of both FEM-BEM formulation vs the analytical solution

We also observe that for the problem of a sphere under a uniform source field, the a-ϕ_{red} formulation needs more degrees of freedom for the same degree of accuracy than the scalar potential formulation. This is both due to the greater number of edges than nodes for a given mesh [162] and also, to the lesser order of the shape functions of the a-ϕ_{red}.

For the BEM equations, in the a-ϕ_{red} formulation, both ϕ_{red} and B_n, later transformed into surface edge elements via an incidence matrix, are discretized by 0th-order surface shape functions while in the scalar formulation, ϕ_{red} is discretized into 1st-order nodal elements and B_n into 0th-order surface shape functions. Discretizing ϕ_{red} into nodal elements translates into a linear variation of ϕ_{red} within an exterior facet element, so it is expected that it will better capture the behavior of ϕ_{red} than an interpolation constant by surface facet element.

Besides the lower order of shape functions related to the BEM formulation, the accuracy of the solution between nodal and edge elements also depends on the problem to be modeled: the use of edge elments for description of the magnetic vector potential $\boldsymbol{a}$ enforce the continuity of B_n between elements, it is expected to have better accuracy for problems where this continuity

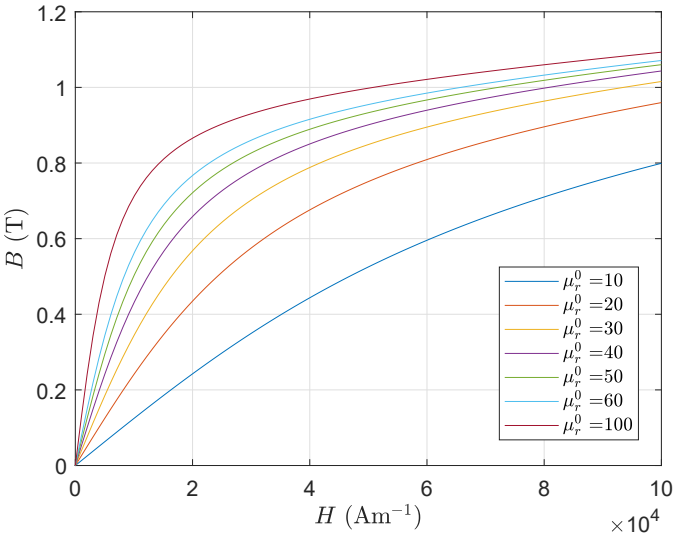

Figure 2.11: B(H) laws resulting from (2.108) and used for the testing of the Newton-Raphson solver of the magnetic formulations

plays a more important role than the continuity of $\boldsymbol{H} \times \boldsymbol{n}$, enforced by the use of nodal elements for the magnetic reduced scalar potential ϕ_{red}.

2.6.2 Case of nonlinear constitutive laws

The use of a magnetic vector potential formulation has several advantages, for example related to the convergence of the Newton-Raphson solvers when considering nonlinear constitutive laws [163]. To illustrate this phenomenon, the convergence of the resolution algorithm of both FEM-BEM formulations is studied for the modeling of a magnetostatic problem made of a sphere (discretized into 1138 nodes) in an uniform source field with a nonlinear isotropic constitutive law, described by (2.108).

$$B_i = \mu_0 H_i + B_{\text{sat}} \frac{2}{\pi} \arctan\left(\frac{\pi(\mu_r^0 - 1)}{2B_{\text{sat}}} H_i\right), i \in \{1, 2, 3\}. \tag{2.108}$$

This constitutive law ensures a saturation at B_{sat} for every component of $\boldsymbol{B}$ and a slope at the origin of μ_r^0. The $B(H)$ curves of the considered constitutive laws are presented in Figure 2.11. For these convergence tests, B_{sat} was set at 1 T and a parametric study was performed for μ_r^0 and the amplitude of the source field $\boldsymbol{H_0}$.

Table 2.1: Number of Newton-Raphson iterations for the solving of a magnetostatic problem with the ϕ_{red}- ϕ_{red} formulation, "-" denote the non convergence of the resolution algorithm

$\boldsymbol{H_0}, z$ $(\mathrm{kA\,m^{-1}})$ | μ_r^0	10	20	30	40	50	60	100
1	1	1	1	1	2	2	2
2.5	1	1	2	2	2	2	2
5	1	2	2	2	2	2	3
7.5	2	2	2	2	3	3	6
10	2	2	2	3	3	4	-
20	2	2	4	5	-	-	-
30	2	3	5	-	-	-	-
40	3	4	-	-	-	-	-
50	3	5	-	-	-	-	-
70	3	11	-	-	-	-	-
100	3	-	-	-	-	-	-

Table 2.2: Number of Newton-Raphson iterations for the solving of a magnetostatic problem with the a-ϕ_{red} formulation

$\boldsymbol{H_0}, z$ $(\mathrm{kA\,m^{-1}})$ | μ_r^0	10	20	30	40	50	60	100
1	1	1	1	1	1	1	1
2.5	1	1	1	1	1	1	1
5	2	1	1	1	1	1	1
7.5	2	2	2	2	2	1	1
10	2	2	2	2	2	2	1
20	2	2	2	2	2	2	2
30	2	2	2	2	2	2	2
40	2	2	2	2	2	2	2
50	2	2	2	2	2	2	2
70	2	2	2	2	2	2	2
100	2	2	2	2	2	2	2

Table 2.3: Number of Newton-Raphson iterations for the solving of a magnetostatic problem with the ϕ_{red}- ϕ_{red} formulation and an adaptive relaxation procedure [16]

$\boldsymbol{H_0}, z$ (kA m^{-1}) | μ_r^0	10	20	30	40	50	60	100
1	1	1	1	1	2	2	2
2.5	1	1	2	2	2	2	2
5	1	2	2	2	2	2	3
7.5	2	2	2	2	3	3	2
10	2	2	2	3	3	4	3
20	2	2	4	3	3	4	3
30	2	3	3	3	4	6	3
40	3	4	3	4	5	4	3
50	3	3	3	5	7	5	4
70	3	3	3	5	7	4	6
100	3	3	3	4	4	5	5

Tables 2.1 and 2.2 show the number of iterations of the Newton-Raphson solver with a tolerance of 10^{-5}, without relaxation. In these Tables we see that for the nonlinear case, the scalar formulation did not converge for the higher source fields and higher μ_r^0, while the mixed formulation easily converged for all test cases. Using relaxation can help the convergence of the Newton-Raphson solver. In particular using a line search to find an appropriate relaxation coefficient for each iteration of the Newton-Raphson solver [16] proved to be very useful for the resolution of the magnetostatic problem using the scalar formulation. Tables 2.1 can be compared with Table 2.3, where the same solver was used but with a line search relaxation procedure, which allows for under relaxation and a dichotomy to find an optimal relaxation coefficient [16].

In Table 2.3 we observe that although relaxation helps the convergence of the ϕ_{red}-ϕ_{red} formulation the number of iterations of the Newton-Raphson solver remains higher than for the a-ϕ_{red} formulation.

2.7 Conclusion

In this chapter we presented the single-physics approaches for passive materials necessary to the description of the strain-induced magnetoelectric effect: a FEM approach to electrostatics, a FEM treatment of linear elasticity and two formulations of the magnetostatics problem based on a coupling between

the FEM and the BEM. The first of the magnetic formulations, a magnetic reduced scalar potential, referred as ϕ_{red}- ϕ_{red}, and the second, a mixed formulation using magnetic vector potential inside the volume and a reduced scalar potential at the boundary of the active material, referred as a- ϕ_{red}. We validated both presented magnetostatic formulations by comparison to an analytical solution. Both formulations were compared in terms of accuracy for a linear constitutive law, and ease of convergence for the nonlinear case. We observed the h-convergence of both formulations, better for the ϕ_{red}- ϕ_{red} formulation. For the nonlinear case, the a- ϕ_{red} formulation proved to converge better and, contrary to the ϕ_{red}- ϕ_{red} formulation, it did not require relaxation of the nonlinear solver. In the next chapter, we will introduce the coupled problem formulations and the challenges that arise by the introduction of coupled properties, in particular to the resolution of the discrete systems.

Chapter 3

Multi-physics formulations

3.1 Introduction

In this chapter, we develop the coupled formulations describing the multi-physics coupling of active materials. For that we first develop the chosen constitutive laws of magneto-mechanical coupling: two linear sets of relations and a nonlinear relation derived from invariant theory applied to the Helmholtz free energy. We then present the strong, weak and discrete forms of the developed coupled magneto-mechanical formulations. These formulations are compared to an analytical solution and their h-convergence evaluated. Afterward, we introduce the chosen constitutive laws of electro-mechanical coupling, and the derived weak and discrete forms. The discrete form is validated by comparison to an analytical solution for the case of a piezoelectric beam. Three formulations of the three-physics, fully coupled problem, the strain-induced magnetoelectric effect, are presented. They result from the three previously described formulations of magneto-mechanical coupling. The challenges related to the resolution of the discrete forms, in particular the magneto-mechanical formulations which involve both sparse and full matrices, are presented, as well as the implemented resolution algorithms allowing to overcome this issue, block Gauss-Seidel type iterative solvers.

3.2 Magneto-mechanical FEM-BEM formulations and validation

In a first place, we develop the implemented FEM-BEM formulations of the magneto-mechanical problem. Two of them take into account a linear magneto-mechanical coupling, while the third, more general, considers a nonlinear magneto-mechanical behavior. They are based on the two previously developed FEM-BEM magnetostatic formulations and the mechanical weak formulation.

3.2.1 Magneto-mechanical linearized constitutive laws

In the frame of piezomagnetism, as stated in Section 1.4.2, the Gibbs free energy in an active magneto-mechanical material, under the hypothesis of an adiabatic process, can be expressed as:

$$G = \frac{1}{2}\boldsymbol{S} : \boldsymbol{c}^{\boldsymbol{H}} : \boldsymbol{S} - \boldsymbol{H} \cdot \boldsymbol{q} : \boldsymbol{S} - \frac{1}{2}\boldsymbol{H} \cdot \boldsymbol{\mu}^{\boldsymbol{S}} \cdot \boldsymbol{H}, \tag{3.1}$$

with $\boldsymbol{c}^{\boldsymbol{H}}$ the 4th-order elasticity tensor at a fixed magnetic field, $\boldsymbol{q}$ the piezomagnetic 3rd-order tensor and $\boldsymbol{\mu}^{\boldsymbol{S}}$ the magnetic permeability at a fixed strain. The expressions of the magnetic induction and mechanical stress can then be obtained by the analytical derivation of the Gibbs free energy,

$$\boldsymbol{T}(\boldsymbol{S}, \boldsymbol{H}) = \frac{\partial G}{\partial \boldsymbol{S}}, \tag{3.2}$$

$$\boldsymbol{B}(\boldsymbol{S}, \boldsymbol{H}) = -\frac{\partial G}{\partial \boldsymbol{H}}, \tag{3.3}$$

which, for constant coefficients of $\boldsymbol{c}^{\boldsymbol{H}}$, $\boldsymbol{q}$ and $\boldsymbol{\mu}^{\boldsymbol{S}}$, gives the two linear constitutive laws which describe the linearized response of magnetostrictive materials:

$$\boldsymbol{T}(\boldsymbol{S}, \boldsymbol{H}) = \boldsymbol{c}^{\boldsymbol{H}} : \boldsymbol{S} - {}^{\mathrm{t}}\boldsymbol{q} \cdot \boldsymbol{H}, \tag{3.4}$$

$$\boldsymbol{B}(\boldsymbol{S}, \boldsymbol{H}) = \boldsymbol{q} : \boldsymbol{S} + \boldsymbol{\mu}^{\boldsymbol{S}} \cdot \boldsymbol{H}. \tag{3.5}$$

Other expressions can be obtained if another set of state variables are considered [67], such as:

$$\boldsymbol{T}(\boldsymbol{S},\boldsymbol{B}) = \boldsymbol{c^B} : \boldsymbol{S} - {}^{\mathrm{t}}\boldsymbol{h} \cdot \boldsymbol{B}, \tag{3.6}$$

$$\boldsymbol{H}(\boldsymbol{S},\boldsymbol{B}) = -\ \boldsymbol{h} : \boldsymbol{S} + \boldsymbol{\nu^S} \cdot \boldsymbol{B}, \tag{3.7}$$

with $\boldsymbol{c^B}$ the elasticity tensor measured at a fixed magnetic flux density level, $\boldsymbol{h}$ the piezomagnetic coupling tensor and $\boldsymbol{\nu^S}$ the magnetic reluctivity at a fixed strain. Tensors $\boldsymbol{c^H}$, $\boldsymbol{q}$ and $\boldsymbol{\mu^S}$ can be linked to tensors $\boldsymbol{c^B}$, $\boldsymbol{h}$ and $\boldsymbol{\nu^S}$ by the following relations:

$$\boldsymbol{c^B} = \boldsymbol{c^H} + {}^{\mathrm{t}}\boldsymbol{q}\ \boldsymbol{\mu^S}^{-1}\ \boldsymbol{q}, \tag{3.8}$$

$$\boldsymbol{h} = \boldsymbol{\mu}^{-1}\ {}^{\mathrm{t}}\boldsymbol{q}, \tag{3.9}$$

$$\boldsymbol{\nu^S} = (\boldsymbol{\mu^S})^{-1}. \tag{3.10}$$

3.2.2 ϕ_{red}-ϕ_{red}-u Formulation

The FEM-BEM treatment of piezomagnetic phenomena can be obtained by the solving of the generic mechanical weak form (2.36) and the generic magnetic weak form combined with the piezomagnetic constitutive laws (3.2) and (3.3). The mechanical weak form obtained by introducing (3.2) into (2.34) while neglecting volume forces, which reads, find $\boldsymbol{u}$ such that,

$$\begin{aligned}&\int_{\Omega_m} \nabla^S \delta\boldsymbol{u} : \boldsymbol{c^H} : \nabla^S \boldsymbol{u}\ d\Omega_m - \int_{\Omega_m} \nabla^S \delta\boldsymbol{u} : {}^{\mathrm{t}}\boldsymbol{q} \cdot \nabla\phi_{red}\ d\Omega_m \\ &= \int_{\Omega_m} \nabla^S \delta\boldsymbol{u} : {}^{\mathrm{t}}\boldsymbol{q} \cdot \boldsymbol{H_0} d\Omega_m + \int_{\partial\Omega_m^T} \boldsymbol{\delta u} \cdot (\boldsymbol{T}\cdot\boldsymbol{n}) d\partial\Omega_m, \quad \forall \boldsymbol{\delta u}.\end{aligned} \tag{3.11}$$

with $\boldsymbol{u} = \boldsymbol{u}^s$ at $\partial\Omega_m^u$. In equation (3.11) we observe that a second hand term, equivalent to a volume force appears, and it involves the source field $\boldsymbol{H_0}$ and the piezomagnetic tensor $\boldsymbol{q}$. A magnetic weak form inside the active materials can be obtained by introducing (3.3) into (2.38). It reads, find (ϕ_{red}, B_n) such that,

$$\begin{aligned}&\int_{\Omega_m} \nabla\delta\phi \cdot \boldsymbol{\mu^S} \cdot \nabla\phi_{red}\ d\Omega_m - \int_{\Omega_m} \nabla\delta\phi \cdot \boldsymbol{q} : \nabla^S \boldsymbol{u}\ d\Omega_m + \int_{\partial\Omega_m} \delta\phi\ B_n\ d\partial\Omega_m \\ &= \int_{\Omega_m} \nabla\delta\phi \cdot \boldsymbol{\mu^S} \cdot \boldsymbol{H_0}\ d\Omega_m \quad \forall\delta\phi,\end{aligned} \tag{3.12}$$

plus the magnetic equation in the air (2.50) which remains unchanged as mechanical phenomena is limited to the active material domain. The previous weak forms (3.11), (3.12) and (2.50) were discretized by using 1-st order FEM and nodal elements for $\boldsymbol{u}$, $\boldsymbol{\delta u}$ and ϕ_{red}. Also, $\delta\phi$ and B_n were discretized using 0th-order surface shape functions, i.e. (2.70), (2.75), (2.76) and (2.77). The resulting global matrix system is presented in (3.13).

$$\begin{bmatrix} \underline{\boldsymbol{K}}_{\phi\phi} & \underline{\mathbf{0}} & \underline{\boldsymbol{K}}_{\phi u} \\ & \underline{\boldsymbol{K}}_{\phi b_n} & \\ \underline{\mathbf{0}} & \underline{\boldsymbol{H}} \quad \underline{\boldsymbol{T}} & \\ \underline{\boldsymbol{K}}_{u\phi} & \underline{\mathbf{0}} & \underline{\boldsymbol{K}}_{uu} \end{bmatrix} \begin{pmatrix} \underline{\boldsymbol{\phi}}_{red} \\ \underline{\boldsymbol{B_n}} \\ \underline{\boldsymbol{u}} \end{pmatrix} = \begin{pmatrix} \underline{\boldsymbol{Sh}}_{mag}^{\Omega_m} \\ \underline{\boldsymbol{Sh}}_{mag}^{\partial\Omega_m} \\ \underline{\boldsymbol{Sh}}_{meca} \end{pmatrix} \tag{3.13}$$

where,

$$\underline{\boldsymbol{K}}_{uu}^{IJ} = \int_{\Omega_m} \mathbb{B}_u^I \cdot \ \boldsymbol{c^H} \cdot \mathbb{B}_u^J \ d\Omega_m, \tag{3.14}$$

$$\underline{\boldsymbol{K}}_{u\phi}^{IJ} = \int_{\Omega_m} \mathbb{B}_u^I \cdot {}^{\mathrm{t}}\boldsymbol{q} \cdot \mathbb{B}_\phi^J \ d\Omega_m, \tag{3.15}$$

$$\underline{\boldsymbol{K}}_{\phi\phi}^{IJ} = \int_{\Omega_m} \mathbb{B}_\varphi^I \cdot \ \boldsymbol{\mu^S} \cdot \mathbb{B}_\varphi^J \ d\Omega_m, \tag{3.16}$$

$$\underline{\boldsymbol{K}}_{\phi u}^{IJ} = \int_{\Omega_m} \mathbb{B}_\phi^I \cdot \boldsymbol{q} \cdot \mathbb{B}_u^J \ d\Omega_m, \tag{3.17}$$

$$\underline{\boldsymbol{K}}_{\phi b_n}^{IJ} = \int_{\partial\Omega_m} \mathbb{B}_\varphi^I \cdot N_0^J d\partial\Omega_m, \tag{3.18}$$

$$\underline{\boldsymbol{H}}^{IJ} = \int_{\partial\Omega_m} N_0^I \int_{\partial\Omega_m} \frac{\partial G}{\partial \boldsymbol{n}} \ {}^{tr}N_\phi^J \ d\partial\Omega_m d\partial\Omega_m - \frac{1}{2}\int_{\partial\Omega_m} N_0^I \ {}^{tr}N_\phi^J d\partial\Omega_m, \tag{3.19}$$

$$\underline{\boldsymbol{T}}^{IJ} = \int_{\partial\Omega_m} N_0^I \int_{\partial\Omega_m} \frac{G}{\mu_0} \ N_0^J \ d\partial\Omega_m \ d\partial\Omega_m, \tag{3.20}$$

$$\underline{\boldsymbol{Sh}}_{mag}^{\partial\Omega_m\ I} = \int_{\partial\Omega_m} N_0^I \int_{\partial\Omega_m} G \ H_{0n} \ d\partial\Omega_m d\partial\Omega_m, \tag{3.21}$$

$$\underline{\boldsymbol{Sh}}_{mag}^{\Omega_m\ I} = \int_{\Omega_m} \mathbb{B}_\phi^I \cdot \boldsymbol{\mu^S} \cdot \boldsymbol{H_0} \ d\Omega_m, \tag{3.22}$$

$$\underline{\boldsymbol{Sh}}_{meca}^I = \int_{\Omega_m} \mathbb{B}_u^I \cdot {}^{\mathrm{t}}\boldsymbol{q} \cdot \boldsymbol{H_0} \ d\Omega_m + \int_{\partial\Omega_m^T} {}^{tr}N_u^I \cdot (\boldsymbol{T} \cdot \boldsymbol{n}) \ d\partial\Omega_m. \tag{3.23}$$

3.2.3 a-ϕ_{red}-u Formulation

Another linear magneto-mechanical formulation can be obtained by considering another magnetic weak form and consitutive laws: considering the magneto-mechanical constitutive law (3.7) and (2.34), we obtain the following weak form: find $\boldsymbol{u}$ such that,

$$\begin{aligned}\int_{\Omega_m} \nabla^S \delta\boldsymbol{u} : \boldsymbol{c^B} : \nabla^S \boldsymbol{u} d\Omega_m - \int_{\Omega_m} \nabla^S \delta\boldsymbol{u} : {}^{\mathrm{t}}\boldsymbol{h} \cdot \nabla\times\boldsymbol{a} d\Omega_m \\ = \int_{\partial\Omega_m^t} \boldsymbol{\delta u} \cdot (\boldsymbol{T}\cdot\boldsymbol{n})\ d\partial\Omega_m \quad \forall \boldsymbol{\delta u},\end{aligned} \tag{3.24}$$

with $\boldsymbol{u} = \boldsymbol{u}^s$ at $\partial\Omega_m^u$. Considering (3.7) and the a-ϕ_{red} formulation inside the active material (2.63), we obtain the following weak form: find $\boldsymbol{a}$ such that,

$$\begin{aligned}\int_{\Omega_m} \nabla\times\boldsymbol{\delta a}\cdot\boldsymbol{\nu}^S\cdot\nabla\times\boldsymbol{a}\ d\Omega_m + \int_{\partial\Omega_m} (\nabla\times\boldsymbol{\delta a})\cdot\boldsymbol{n}\ \phi_{red}\ d\partial\Omega_m \\ - \int_{\Omega_m} \nabla\times\boldsymbol{\delta a}\cdot\boldsymbol{h} : \nabla^S\boldsymbol{u}\ d\Omega_m = \int_{\partial\Omega_m} (\boldsymbol{\delta a}\times\boldsymbol{n})\cdot\boldsymbol{H_0}\ d\partial\Omega_m\ \forall\ \boldsymbol{\delta a}.\end{aligned} \tag{3.25}$$

As mechanical phenomena are limited to the active material domain, the magnetic equation in the air remains unchanged in its weak form (2.50). The previous equations can then be discretized using 1-st order nodal elements for $\boldsymbol{u}$ and $\boldsymbol{\delta u}$, edge elements for $\boldsymbol{a}$ and 0th-order shape functions for ϕ_{red} and $\delta\phi$, i.e., (2.70), (2.77) (2.85) and (2.86). We obtain the following matrix system:

$$\begin{bmatrix} \underline{\boldsymbol{K}}_{aa} & \underline{\boldsymbol{0}} & \underline{\boldsymbol{K}}_{au} \\ & \underline{\boldsymbol{K}}_{a\phi} & \\ \underline{\boldsymbol{0}} \quad \underline{\boldsymbol{TC}} & \underline{\boldsymbol{H}} & \\ \underline{\boldsymbol{K}}_{ua} & \underline{\boldsymbol{0}} & \underline{\boldsymbol{K}}_{uu} \end{bmatrix} \begin{pmatrix} \underline{\boldsymbol{a}} \\ \underline{\boldsymbol{\phi}}_{red} \\ \underline{\boldsymbol{u}} \end{pmatrix} = \begin{pmatrix} \underline{\boldsymbol{Sh}}_{mag}^{\Omega_m} \\ \underline{\boldsymbol{Sh}}_{mag}^{\partial\Omega_m} \\ \underline{\boldsymbol{Sh}}_{meca} \end{pmatrix} \tag{3.26}$$

where,

$$\underline{\boldsymbol{K}}_{uu}^{IJ} = \int_{\Omega_m} \mathbb{B}_u^I \cdot \ \boldsymbol{c}^{\boldsymbol{B}} \cdot \mathbb{B}_u^J \ d\Omega_m, \tag{3.27}$$

$$\underline{\boldsymbol{K}}_{ua}^{IJ} = \int_{\Omega_m} \mathbb{B}_u^I \cdot {}^{\mathrm{t}}\boldsymbol{h} \cdot \mathbb{B}_a^J \ d\Omega_m, \tag{3.28}$$

$$\underline{\boldsymbol{K}}_{aa}^{IJ} = \int_{\Omega_m} \mathbb{B}_a^I \cdot \ \boldsymbol{\nu}^S \cdot \mathbb{B}_a^J \ d\Omega_m \tag{3.29}$$

$$\underline{\boldsymbol{K}}_{au}^{IJ} = \int_{\Omega_m} \mathbb{B}_a^I \cdot \boldsymbol{h} \cdot \mathbb{B}_u^J \ d\Omega_m, \tag{3.30}$$

$$\underline{\boldsymbol{H}}^{IJ} = \int_{\partial\Omega_m} N_0^I \int_{\partial\Omega_m} \frac{\partial G}{\partial \boldsymbol{n}} N_0^J \ d\partial\Omega_m d\partial\Omega_m - \frac{1}{2} \int_{\partial\Omega_m} N_0^I N_0^J d\partial\Omega_m, \tag{3.31}$$

$$\underline{\boldsymbol{T}}^{IJ} = \int_{\partial\Omega_m} N_0^I \int_{\partial\Omega_m} \frac{G}{\mu_0} \ N_0^J \ d\partial\Omega_m \ d\partial\Omega_m, \tag{3.32}$$

$$\underline{\boldsymbol{Sh}}_{mag}^{\Omega_m} = \int_{\partial\Omega_m} ({}^{tr}N_a^I \times \boldsymbol{n}) \ \boldsymbol{H}_0 \ d\partial\Omega_m, \tag{3.33}$$

$$\underline{\boldsymbol{Sh}}_{mag}^{\partial\Omega_m{}^I} = \int_{\partial\Omega_m} N_0^I \int_{\partial\Omega_m} G \ H_{0n} \ d\partial\Omega_m, \tag{3.34}$$

$$\underline{\boldsymbol{Sh}}_{mecha}^{I} = \int_{\partial\Omega_m^T} {}^{tr}N_u^I \cdot (\boldsymbol{T} \cdot \boldsymbol{n}) \ d\partial\Omega_m, \tag{3.35}$$

and $\underline{\boldsymbol{C}}$ as defined in section 2.4.6.

3.2.4 Resolution the coupled problem

3.2.4.1 The block Gauss-Seidel method

The resolution of multi-physics problems is not a trivial problem and is encountered for example in the study of fluid-structure interactions, where multiple resolutions in the fluid and solid subdomains are performed in order to obtain a coupled solution. This approach is called *partitioned approach*, to be opposed to the *monolithic approach* which tries to solve all discretized equations at once. For fluid-structure interaction or sound transmission problems, the partitioned approach is particularly useful [164, 165]. It also allows for parallelization of the resolution algorithm [166].

The overall matrix systems of the presented discrete forms (3.13) and (3.26) are not easy to solve using a monolithic approach. Indeed, the full systems are not symmetric and are made of both sparse (FEM) and full (BEM)

matrices. Solvers are in general adapted to one type of matrix and not both. A GMRES solver was used to solve for the magnetostatics problems which contained both sparse and full matrices. Nevertheless, the coupled formulations have much larger sparse sub-matrices due to the addition of FEM mechanical DoFs in comparison to the magnetostatic formulations, making a GMRES solver not adapted to solve these global matrix systems. Therefore, another approach has to be considered to solve for the coupled discrete forms.

An approach to the resolution of the discrete form of these multiphysics problems is to solve the single-physics problems iteratively with partial solutions until all solutions converge. Indeed, as expressed in chapter 2, different solvers are adapted to each physics. This resolution algorithm takes advantage of this fact, leading to fast single-physics resolutions. For linear problems, this approach comes down to a block Gauss-Seidel if the solutions are updated or a block Jacobi, which allows for the parallelized resolution of single-physics problems. As no parallelization of the resolution of multi-physics is used, the block Gauss-Seidel is used. It is expressed by the iterative solving of the following matrix system [158]:

$$[\underline{\boldsymbol{K}}_{ii}] \cdot \underline{\boldsymbol{x}}_i^{n+1} = \underline{\boldsymbol{Sh}}_i - \sum_{j=1}^{i-1} [\underline{\boldsymbol{K}}_{ij}] \cdot \underline{\boldsymbol{x}}_j^{n+1} - \sum_{j=i+1}^{nb_{prob}} [\underline{\boldsymbol{K}}_{ij}] \cdot \underline{\boldsymbol{x}}_j^{n}, \tag{3.36}$$

where nb_{prob} denotes the number of single-physics problems to be solved, $\underline{\boldsymbol{K}}_{ii}$ the single-physics matrix of problem "i", $\underline{\boldsymbol{K}}_{ij}$ represents coupling matrices between problems "i" and "j" and $\underline{\boldsymbol{x}}_j^n$, the solution of the problem "j" at iteration "n". Single-physics matrices are therefore in the diagonal of the assembled matrix systems of multi-physics problems.

Additionally, because of the different nature of coefficients of the assembled matrices (elasticities, permeabilities, reluctivities, etc) there is a large scaling difference between coupling coefficients of the global matrices. This difference in coupling coefficients translates into a big difference of eigenvalues of the global matrices, and therefore in a poor conditioning number of the global matrices. The use of a block Gauss-Seidel solver, avoids these scaling problems and implies solving homogeneous, smaller and in general better conditioned sub-systems with coupling terms introduced as second hand terms.

3.2.4.2 Convergence conditions

Block diagonal dominance

The block Gauss-Seidel resolution algorithm has been used to solve multi-physics problems and its convergence conditions investigated. For a classical Gauss-Seidel resolution algorithm, the diagonal dominance of the global matrix is a sufficient condition for the convergence of the algorithm. For a matrix $\underline{\boldsymbol{A}}$, the diagonal dominance defined by

$$\forall i, |A_{ii}| > \sum_{j,j\neq i} A_{ij}. \tag{3.37}$$

A similar development can be performed using matrix norms to obtain a sufficient condition for the convergence of the block Gauss-Seidel [158]. Lets subtract (3.36) at iteration n from (3.36) at iteration $n+1$, we obtain,

$$[\underline{\boldsymbol{K}}_{ii}] \cdot \underline{\boldsymbol{\epsilon}}_i^{n+1} = -\sum_{j=1}^{i-1} [\underline{\boldsymbol{K}}_{ij}] \cdot \underline{\boldsymbol{\epsilon}}_j^{n+1} - \sum_{j=i+1}^{nb_{prob}} [\underline{\boldsymbol{K}}_{ij}] \cdot \underline{\boldsymbol{\epsilon}}_j^{n}, \tag{3.38}$$

where $\underline{\boldsymbol{\epsilon}}_i^{n+1} = \underline{\boldsymbol{x}}_i^{n+1} - \underline{\boldsymbol{x}}_i^{n}$. If now we take the norm of (3.38), we obtain,

$$\left\| [\underline{\boldsymbol{K}}_{ii}] \cdot \underline{\boldsymbol{\epsilon}}_i^{n+1} \right\| = \left\| -\sum_{j=1}^{i-1} [\underline{\boldsymbol{K}}_{ij}] \cdot \underline{\boldsymbol{\epsilon}}_j^{n+1} - \sum_{j=i+1}^{nb_{prob}} [\underline{\boldsymbol{K}}_{ij}] \cdot \underline{\boldsymbol{\epsilon}}_j^{n} \right\|, \tag{3.39}$$

for $\|\underline{\boldsymbol{\epsilon}}_i^{n+1}\| \neq 0$, the left-hand term of (3.39) can be written as,

$$\left\| [\underline{\boldsymbol{K}}_{ii}] \cdot \underline{\boldsymbol{\epsilon}}_i^{n+1} \right\| = \left\| [\underline{\boldsymbol{K}}_{ii}] \cdot \underline{\boldsymbol{\epsilon}}_i^{n+1} \right\| \frac{\left\| \underline{\boldsymbol{\epsilon}}_i^{n+1} \right\|}{\left\| \underline{\boldsymbol{\epsilon}}_i^{n+1} \right\|}, \tag{3.40}$$

and therefore,

$$\inf_{\underline{\boldsymbol{x}}\neq\underline{\boldsymbol{0}}} \left(\frac{\left\| \underline{\boldsymbol{K}}_{ii} \cdot \underline{\boldsymbol{x}} \right\|}{\left\| \underline{\boldsymbol{x}} \right\|} \right) \left\| \underline{\boldsymbol{\epsilon}}_i^{n+1} \right\| \leq \left\| [\underline{\boldsymbol{K}}_{ii}] \cdot \underline{\boldsymbol{\epsilon}}_i^{n+1} \right\|. \tag{3.41}$$

Applying the Minkowski inequality [167] to the right-hand side of (3.39), we obtain,

$$\inf_{\underline{\boldsymbol{x}}\neq\underline{\mathbf{0}}}\left(\frac{\|\underline{\boldsymbol{K}}_{ii}\cdot\underline{\boldsymbol{x}}\|}{\|\underline{\boldsymbol{x}}\|}\right)\left\|\underline{\boldsymbol{\epsilon}}_i^{n+1}\right\|\leq\sum_{j=1}^{i-1}\left\|[\underline{\boldsymbol{K}}_{ij}]\ \cdot\underline{\boldsymbol{\epsilon}}_j^{n+1}\right\|+\sum_{j=i+1}^{nb_{prob}}\left\|[\underline{\boldsymbol{K}}_{ij}]\ \cdot\underline{\boldsymbol{\epsilon}}_j^{n}\right\|. \tag{3.42}$$

Similarly to (3.41), we have $\forall\ i,j$,

$$\|[\underline{\boldsymbol{K}}_{ij}]\cdot\underline{\boldsymbol{\epsilon}}_j^n\|\leq\sup_{\underline{\boldsymbol{x}}\neq\underline{\mathbf{0}}}\left(\frac{\|\underline{\boldsymbol{K}}_{ij}\cdot\underline{\boldsymbol{x}}\|}{\|\underline{\boldsymbol{x}}\|}\right)\left\|\underline{\boldsymbol{\epsilon}}_j^n\right\|, \tag{3.43}$$

and therefore,

$$\begin{aligned}\inf_{\underline{\boldsymbol{x}}\neq\underline{\mathbf{0}}}\left(\frac{\|\underline{\boldsymbol{K}}_{ii}\cdot\underline{\boldsymbol{x}}\|}{\|\underline{\boldsymbol{x}}\|}\right)\left\|\underline{\boldsymbol{\epsilon}}_i^{n+1}\right\|\leq&\sum_{j=1}^{i-1}\sup_{\underline{\boldsymbol{x}}\neq\underline{\mathbf{0}}}\left(\frac{\|\underline{\boldsymbol{K}}_{ij}\cdot\underline{\boldsymbol{x}}\|}{\|\underline{\boldsymbol{x}}\|}\right)\left\|\underline{\boldsymbol{\epsilon}}_j^{n+1}\right\|\\&+\sum_{j=i+1}^{nb_{prob}}\sup_{\underline{\boldsymbol{x}}\neq\underline{\mathbf{0}}}\left(\frac{\|\underline{\boldsymbol{K}}_{ij}\cdot\underline{\boldsymbol{x}}\|}{\|\underline{\boldsymbol{x}}\|}\right)\left\|\underline{\boldsymbol{\epsilon}}_j^{n}\right\|.\end{aligned} \tag{3.44}$$

If we now consider $\epsilon^{n+1}=\max(\ \left\|\epsilon_j^k\right\||\ j\in\{1,...,nb_{prob}\}\setminus\{i\},k\in\{n,n+1\})$,

$$\begin{aligned}\inf_{\underline{\boldsymbol{x}}\neq\underline{\mathbf{0}}}\left(\frac{\|\underline{\boldsymbol{K}}_{ii}\cdot\underline{\boldsymbol{x}}\|}{\|\underline{\boldsymbol{x}}\|}\right)\left\|\underline{\boldsymbol{\epsilon}}_i^{n+1}\right\|\leq&\ \epsilon^{n+1}\sum_{j=1}^{i-1}\sup_{\underline{\boldsymbol{x}}\neq\underline{\mathbf{0}}}\left(\frac{\|\underline{\boldsymbol{K}}_{ij}\cdot\underline{\boldsymbol{x}}\|}{\|\underline{\boldsymbol{x}}\|}\right)\\&+\epsilon^{n+1}\sum_{j=i+1}^{nb_{prob}}\sup_{\underline{\boldsymbol{x}}\neq\underline{\mathbf{0}}}\left(\frac{\|\underline{\boldsymbol{K}}_{ij}\cdot\underline{\boldsymbol{x}}\|}{\|\underline{\boldsymbol{x}}\|}\right).\end{aligned} \tag{3.45}$$

If the matrix $\underline{\boldsymbol{K}}_{ii}$ is not singular, we have,

$$\|\underline{\boldsymbol{\epsilon}}_i^{n+1}\|\leq\frac{\displaystyle\sum_{j,j\neq i}^{nb_{prob}}\sup_{\underline{\boldsymbol{x}}\neq\underline{\mathbf{0}}}\left(\frac{\|\underline{\boldsymbol{K}}_{ij}\cdot\underline{\boldsymbol{x}}\|}{\|\underline{\boldsymbol{x}}\|}\right)}{\displaystyle\inf_{\underline{\boldsymbol{x}}\neq\underline{\mathbf{0}}}\left(\frac{\|\underline{\boldsymbol{K}}_{ii}\cdot\underline{\boldsymbol{x}}\|}{\|\underline{\boldsymbol{x}}\|}\right)}\ \epsilon^{n+1}. \tag{3.46}$$

Therefore, if $\forall i$, the condition

$$\frac{\sum_{j,j\neq i}^{nb_{prob}} \sup_{\underline{\boldsymbol{x}}\neq\underline{\mathbf{0}}} \left(\frac{\|\underline{\boldsymbol{K}}_{ij}\cdot\underline{\boldsymbol{x}}\|}{\|\underline{\boldsymbol{x}}\|} \right)}{\inf_{\underline{\boldsymbol{x}}\neq\underline{\mathbf{0}}} \left(\frac{\|\underline{\boldsymbol{K}}_{ii}\cdot\underline{\boldsymbol{x}}\|}{\|\underline{\boldsymbol{x}}\|} \right)} < 1, \tag{3.47}$$

is verified, the block Gauss-Seidel resolution algorithm converges. This condition is the *block diagonally dominant* condition for block matrices [168]. Indeed,

$$\sup_{\underline{\boldsymbol{x}}\neq\underline{\mathbf{0}}} \left(\frac{\|\underline{\boldsymbol{K}}_{ij}\cdot\underline{\boldsymbol{x}}\|}{\|\underline{\boldsymbol{x}}\|} \right), \tag{3.48}$$

is the induced norm of $\underline{\boldsymbol{K}}_{ij}$, $\|\underline{\boldsymbol{K}}_{ij}\|$. Also [168],

$$\inf_{\underline{\boldsymbol{x}}\neq\underline{\mathbf{0}}} \left(\frac{\|\underline{\boldsymbol{K}}_{ii}\cdot\underline{\boldsymbol{x}}\|}{\|\underline{\boldsymbol{x}}\|} \right) = \left(\|\underline{\boldsymbol{K}}_{ii}^{-1}\| \right)^{-1} \tag{3.49}$$

and (3.43), the Cauchy-Schwarz inequality for matrix norms [167]. In particular, if the chosen vector norm is the 2-norm, the corresponding matrix norm is,

$$\|\underline{\boldsymbol{K}}_{ij}\| = \rho \left({}^t\underline{\boldsymbol{K}}_{ij}\underline{\boldsymbol{K}}_{ij} \right)^{\frac{1}{2}}, \tag{3.50}$$

where ρ is the spectral radius of a matrix, given by the eigenvalue of highest absolute value, this makes the evaluation of block diagonal dominance possible though the comparison of the sum of the maximum singular values of extra-diagonal matrices to the inverse of the spectral radius of the inverse of diagonal matrices.

Spectral radius of iterating matrix

Another sufficient condition for two-physics problems is given in [165], it is obtained by expressing the solutions at iteration $n+1$ as functions of the solutions at iteration n in terms of an iteration matrix:

$$\underline{\boldsymbol{x}}^{n+1} = \underline{\boldsymbol{M}}\cdot\underline{\boldsymbol{x}}^{n}. \tag{3.51}$$

After expressing $\underline{\boldsymbol{M}}$ in terms of the $\underline{\boldsymbol{K_{ij}}}$, the convergence of the block Gauss-Seidel is studied by computing the spectral radius of $\underline{\boldsymbol{M}}$. For a 2×2 block matrix system of the form,

$$\begin{bmatrix} \underline{\boldsymbol{F}} & \underline{\boldsymbol{c_{FS}}} \\ \underline{\boldsymbol{c_{SF}}} & \underline{\boldsymbol{S}} \end{bmatrix} \cdot \begin{bmatrix} \underline{\boldsymbol{x_F}} \\ \underline{\boldsymbol{x_s}} \end{bmatrix} = \begin{bmatrix} \underline{\boldsymbol{Sh_F}} \\ \underline{\boldsymbol{Sh_S}} \end{bmatrix}, \tag{3.52}$$

which represents the discrete form of solid-fluid simulation, a sufficient condition for the convergence of the block Gauss-Seidel is,

$$\rho(\underline{\boldsymbol{S}}^{-1}\underline{\boldsymbol{c_{SF}}}\underline{\boldsymbol{F}}^{-1}\underline{\boldsymbol{c_{FS}}}) < 1. \tag{3.53}$$

This expression can be generalized to $n \times n$ matrix assemblies by replacing solutions at iteration $n+1$ by their expression at iteration n. It results in a weaker sufficient condition for the convergence of the block Gauss-Seidel solver. This condition has however complex expression for $n \times n$ matrix assemblies.

Remarks

For both presented methods, evaluating the convergence of the resolution algorithm is a costly procedure, involving the inverse of the diagonal matrices of the block system, and at least spectral studies on large matrices. Also, the absence of gauge in some presented simulation, gives rise to non-inversible matrices making this evaluation impossible.

Furthermore, when possible, the presented conditions proved to be too strong: the algorithm converged for all conducted simulations with the experimental coefficients of the materials considered, despite the presented conditions not being fulfilled whenever their evaluation was possible. Indeed, they evaluate the convergence of the resolution algorithm without a priori knowledge of the solution, taken as a vector of $\mathbb{R}^n$. An a priori knowledge of the space of the solutions would allow for determining more relevant conditions.

The convergence of the block Gauss-Seidel seem to be nevertheless related to the matrix norm of the diagonal matrix compare to the extra-diagonal matrices: decreasing the value of single-physics tensors, integrated in the diagonal matrices of the block matrix system, was observed to increase the number of required iterations to reach the set tolerance, or even to induce the divergence of the algorithm. The same can be said about increasing the value of coupling terms.

3.2.5 Analytical solution and validation

In order to validate the previously presented magneto-mechanical formulation, we simulated the response of an unconstrained mechanically isotropic piezomagnetic sphere, of radius of 1 mm, to a magnetic source field, $\boldsymbol{H_0}$ of amplitude 50 $\mathrm{kA\,m^{-1}}$, oriented in the (z) direction. This test case was solved for increasingly fine meshes of the modeled sphere. An analytical solution to this problem was obtained by numerically solving for both $\boldsymbol{T} = \boldsymbol{0}$ and the magnetic analytical solution (2.106) in which μ was taken equal to the ratio of B_3/H_3. Indeed, the magnetic field and flux density in a sphere under the effect of a uniform source field are both uniform and in the same direction [24].

Table 3.1: non-zero coefficients used for the modeling of the piezomagnetic sphere. The piezomagnetic tensor is given in Voigt notation

Parameter	Value
Young modulus (GPa)	100
Poisson coefficient	0.3
q_{13} ($\mathrm{N\,A^{-1}\,m^{-1}}$)	-30
q_{33} ($\mathrm{N\,A^{-1}\,m^{-1}}$)	200
q_{24} ($\mathrm{N\,A^{-1}\,m^{-1}}$)	60
q_{15} ($\mathrm{N\,A^{-1}\,m^{-1}}$)	150
μ_r	10

Table 3.2: non-zero components of magnetic field and the mechanical strain tensor of the analytical solution of the magneto-mechanical reference problem: an unconstrained sphere of radius 1 mm in a magnetic source field $\boldsymbol{H_0}$ of an amplitude of 50 $\mathrm{kA\,m^{-1}}$ oriented in the (z) direction

Parameter	H_3 ($\mathrm{A\,m^{-1}}$)	$S_{11} = S_{22}$	S_{33}
Value	12.110	$9.810 \cdot 10^{-6}$	$2.640 \cdot 10^{-5}$

The L^2 error of the ϕ_{red}-ϕ_{red}-u formulation compared to the analytical solution is given in Figure 3.1. The L^2 error of the a-ϕ_{red}-u formulation compared to the same analytical solution is presented in Figure 3.2. We observe that both formulations converge towards the analytical solution as we refine the mesh. We also observe that, similarly as for the comparison of

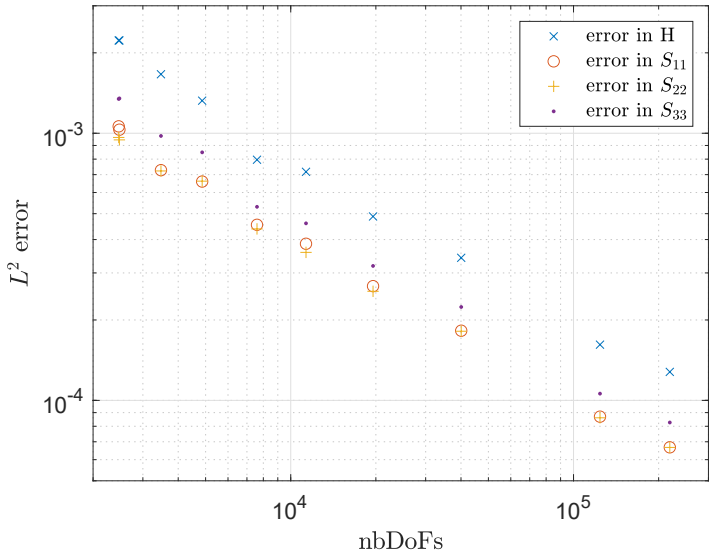

Figure 3.1: L^2 error of the ϕ_{red}-ϕ_{red}-u solutions compared to the analytical solution vs the number of DoFs of the multi-physics problem

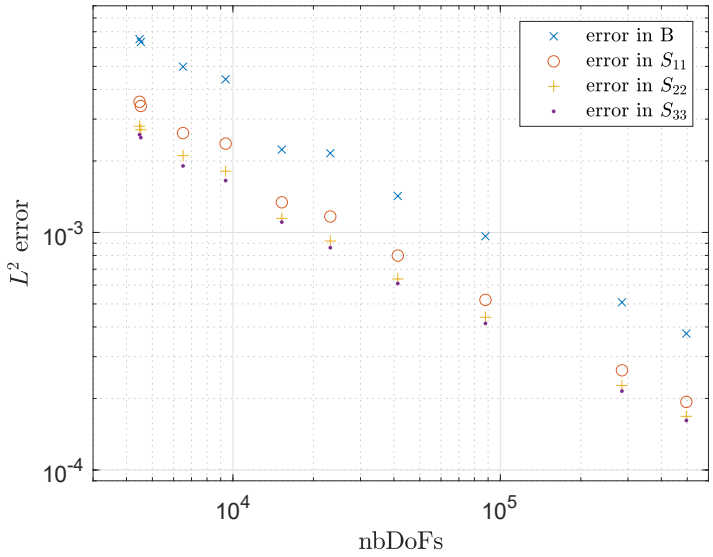

Figure 3.2: L^2 error of the a-ϕ_{red}-u solution compared to the analytical solution vs the number of DoFs of the multi-physics problem

magnetostatics formulations, the a-ϕ_{red}-u formulation needs more degrees of freedom for the same degree of accuracy than the ϕ_{red}-ϕ_{red}-u formulation. This difference may come from the different order of shape functions between the BEM equations of the magnetostatic formulations and the higher number of degrees of freedom of the magnetic problem of the a-ϕ_{red}-u formulation compared to the ϕ_{red}-ϕ_{red}-u formulation.

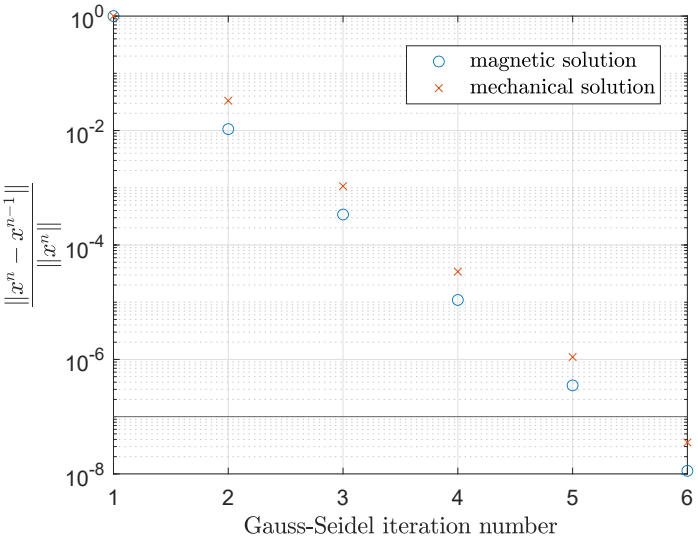

Figure 3.3: Convergence of the magneto-mechanical solutions within the block Gauss-Seidel multi-physics iterative solver for the ϕ_{red}-ϕ_{red}-u formulation

In Figures 3.3 and 3.4, we observed the rate of convergence, given by,

$$\frac{\|\underline{\mathbf{x}}^{n+1} - \underline{\mathbf{x}}^{n}\|}{\|\underline{\mathbf{x}}^{n+1}\|}, \tag{3.54}$$

vs the number of iterations of the Gauss-Seidel multi-physics solver for the finest mesh of the previous convergence test. In Figure 3.3, we observe that for the ϕ_{red}-ϕ_{red}-u formulation, the Gauss-Seidel multi-physics solver converged to a tolerance of 10^{-7} in 6 iterations, this was the case for all simulations in the convergence test. For the a-ϕ_{red}-u formulation, we observe in Figure 3.4 the same convergence of the solution given by (3.54) vs the number of Gauss-Seidel iteration. The multi-physics solver took 5 iterations instead of 6 to converge to a tolerance of 10^{-7}. Again, this was also the case for all simulations in the convergence test.

In the next section, we introduce the nonlinear constitutive laws of magneto-

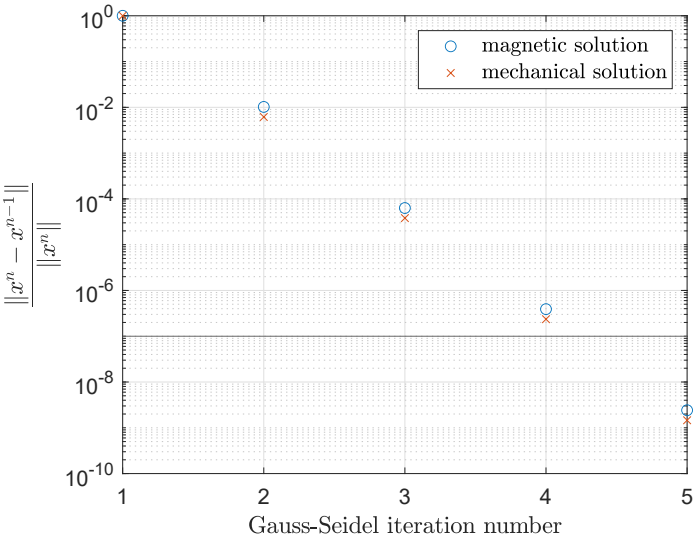

Figure 3.4: Convergence of the magneto-mechanical solutions within the block Gauss-Seidel multi-physics iterative solver for the a-ϕ_{red}-u formulation

mechanical coupling derived from invariant theory, as well as present the weak and discrete forms that derive from the introduction of these nonlinear constitutive laws into a FEM-BEM formulation.

3.3 FEM-BEM modeling of nonlinear magneto-mechanical behavior

3.3.1 Invariants description of magneto-mechanical coupling

Invariant theory is a mathematical theory dating from the 1950s. It qualifies a function of a set of vectors and tensors as invariant if it remains unchanged after an orthogonal transformation of the said vectors and tensors. A function

$$f(\boldsymbol{U}, \boldsymbol{V}, \boldsymbol{M}, \boldsymbol{N}, ...), \tag{3.55}$$

is said to be an absolute invariant of its inputs if

$$f(\boldsymbol{U}, \boldsymbol{V}, \boldsymbol{M}, \boldsymbol{N}, ...) = f(\overline{\boldsymbol{U}}, \overline{\boldsymbol{V}}, \overline{\boldsymbol{M}}, \overline{\boldsymbol{N}}, ...), \tag{3.56}$$

for every orthogonal transformation $\boldsymbol{X} \rightarrow \overline{\boldsymbol{X}}$. It can be shown that for a given set of variables, every invariant of these variables can be expressed as a finite polynomial of a finite set of invariants called an integrity base [169].

The integrity base for an isotropic scalar function of a second order tensor and a vector, here, the Helmholtz free energy as a function of the mechanical strain $\boldsymbol{S}$ and the magnetic flux density $\boldsymbol{B}$, is given by the following set of invariants [91]:

$$I_1 = tr(\boldsymbol{S}), \tag{3.57}$$
$$I_2 = tr(\boldsymbol{S}^2), \tag{3.58}$$
$$I_3 = tr(\boldsymbol{S}^3), \tag{3.59}$$
$$I_4 = \boldsymbol{B} \cdot \boldsymbol{B}, \tag{3.60}$$
$$I_5' = \boldsymbol{B} \cdot \boldsymbol{S} \cdot \boldsymbol{B}, \tag{3.61}$$
$$I_6' = \boldsymbol{B} \cdot \boldsymbol{S}^2 \cdot \boldsymbol{B}. \tag{3.62}$$

Invariants I_1, I_2 and I_3 describe the purely mechanical behavior of the material, I_4 the purely magnetic behavior, and I_5' and I_6' the coupling terms. As I_3 would imply a nonlinear purely mechanic formulation, it can be neglected. Also, because magnetostriction and the Villari effect don't depend on the hydrostatic part of the strain tensor $\boldsymbol{S}^h$, related to a uniform change in volume in every dimension, the dependence on the hydrostatic part of the strain from I_5' and I_6' can be removed, giving:

$$I_5 = \boldsymbol{B} \cdot \tilde{\boldsymbol{S}} \cdot \boldsymbol{B}, \tag{3.63}$$
$$I_6 = \boldsymbol{B} \cdot \tilde{\boldsymbol{S}}^2 \cdot \boldsymbol{B}, \tag{3.64}$$

where $\tilde{\boldsymbol{S}}$ is the deviatoric part of the strain tensor, defined as,

$$\tilde{\boldsymbol{S}} = \boldsymbol{S} - \boldsymbol{S}^h, \tag{3.65}$$
$$= \boldsymbol{S} - \frac{1}{3} tr(\boldsymbol{S}) \boldsymbol{I_3}, \tag{3.66}$$

where $\boldsymbol{I_3}$ denotes the second order identity tensor of $\mathbb{R}^3$. The Helmholtz free energy can then be written as [93, 14, 94],

$$\psi = \frac{1}{2}\lambda I_1 + \mu I_2 + \sum_{i=1}^{n_\alpha} \alpha_i I_4^i + \sum_{i=1}^{n_\beta} \beta_i I_5^i + \sum_{i=1}^{n_\gamma} \gamma_i I_6^i, \tag{3.67}$$

where, λ and μ are the Lamé coefficients of the material at low fields, and the α_i, β_i and γ_i a finite set of scalar coefficients. The expression of the magnetic field and the mechanical stress can then be obtained by the analytical differentiation of the Helmholtz free energy,

$$\boldsymbol{T}(\boldsymbol{B}, \boldsymbol{S}) = \frac{\partial \psi}{\partial \boldsymbol{S}}, \tag{3.68}$$

$$\boldsymbol{H}(\boldsymbol{B}, \boldsymbol{S}) = \frac{\partial \psi}{\partial \boldsymbol{B}}. \tag{3.69}$$

This set of constitutive laws for magneto-mechanical coupling, deriving from the invariant description of the Helmholtz free energy, are included into the volume B-conforming a-ϕ_{red} formulation for the magnetic part. Indeed, the a-ϕ_{red} has an explicit dependence on $\boldsymbol{H}$ and proved to be very stable for nonlinear constitutive laws. Relation (3.68) is used within the mechanical weak form 2.34 as it has an explicit dependence on $\boldsymbol{T}$.

The obtained relations (3.68) and (3.69), presented in Appendix A, were used within a fitting procedure in order to obtain the value of coefficients α_i, β_i and γ_i in the expression of the Helmholtz free energy. As the chosen applications are for relatively low stress, the 0 MPa curves from [14] were fitted using a method of gradient descent, resulting in an expression of the Helmholtz free energy comprising 11 n_α coefficients, 1 n_β coefficients and 2 n_γ coefficients plus the mechanical Lamé coefficients of Galfenol. The fitting procedure is described in detail in Appendix B.

3.3.2 Magnetization of Galfenol under mechanical load

Using the magneto-mechanical model based on the description of the Helmholtz free energy in terms of its invariants, we can study the effect of stress on magnetization in Galfenol. Figure 3.5 shows the reconstructed magnetization of Galfenol as a function of the applied stress for five given states of the magnetic field, using the coefficients of unconstrained Galfenol. Figure 3.5 was obtained by numerically solving for $\boldsymbol{B}$ and $\boldsymbol{S}$ in,

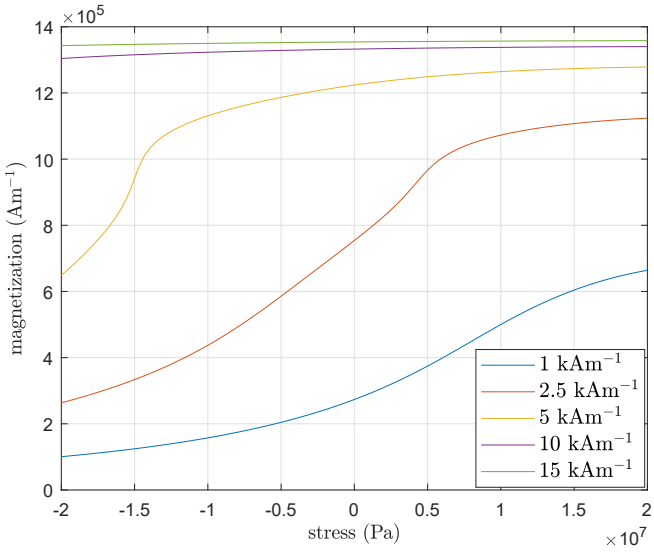

Figure 3.5: Magnetization in Galfenol as a function of the applied stress

$$\boldsymbol{T}(\boldsymbol{B},\boldsymbol{S}) = \begin{bmatrix} 0 & 0 & 0 \\ 0 & 0 & 0 \\ 0 & 0 & T_0 \end{bmatrix}, \tag{3.70}$$

$$\boldsymbol{H}(\boldsymbol{B},\boldsymbol{S}) = \begin{bmatrix} 0 \\ 0 \\ H_{ref} \end{bmatrix}, \tag{3.71}$$

for several values of T_0 and H_{ref} with the assumptions:

$$S_{11} = S_{22}, \tag{3.72}$$

$$B_1 = B_2 = 0, \tag{3.73}$$

and no extra-diagonal strains, which is equivalent to imposing uni-axial stress and a homogenous field along (z). After having computed $\boldsymbol{B}$ and $\boldsymbol{H}$ via the constitutive relation (3.69), the magnetization $\boldsymbol{M}$ was computed by applying,

$$\boldsymbol{M} = \mu_0^{-1}\boldsymbol{B} - \boldsymbol{H}, \tag{3.74}$$

and was found to be oriented in the (z) direction. We observe that for a given field, with the invariants' description of magnetostriction and, as expected, the uni-axial tensile loading in one direction leads to magnetization in this direction, while compression leads to lower magnetization. We also observe the saturation of the magnetization when tension gets higher, as well as the saturation of the magnetization when the magnetic field gets higher. This phenomenon is key to the understanding of the undergoing phenomena in the chosen applications of Chapter 4.

3.3.3 Weak form of the FEM-BEM nonlinear magneto-mechanical problem

The magnetic weak form of the nonlinear magnetic problem can be obtained by introducing the previously described nonlinear coupled $\boldsymbol{H}(\boldsymbol{B}, \boldsymbol{S})$ relations (3.69) into the magnetostatic magnetic mixed formulation 2.63. It reads: find $(\boldsymbol{a}, \phi_{red})$ such that,

$$\begin{aligned} \int_{\Omega_m} \nabla \times \delta\boldsymbol{a} \cdot \boldsymbol{H}(\boldsymbol{B}, \boldsymbol{S}) \; d\Omega_m + \int_{\partial\Omega_m} \nabla \times \delta\boldsymbol{a} \cdot \boldsymbol{n} \; \phi_{red} \; d\partial\Omega_m \\ = \int_{\partial\Omega_m} (\delta\boldsymbol{a} \times \boldsymbol{n}) \cdot \boldsymbol{H_0} \; d\partial\Omega_m \quad \forall \delta\boldsymbol{a}. \end{aligned} \tag{3.75}$$

The weak form of the exterior problem (2.50) still holds and describes the behavior of the magnetic fields at the boundary of the active material. The mechanical weak form is based on (2.34), but because of the dependence of $\boldsymbol{T}$ on powers of $\boldsymbol{S}$ in (3.68), it is now a nonlinear problem in the magnetostrictive phase. It reads, find $\boldsymbol{u}$ such that,

$$\int_{\Omega_m} \nabla^S \boldsymbol{\delta u} : \boldsymbol{T}(\boldsymbol{S}, \boldsymbol{B}) \; d\Omega_m = \int_{\partial\Omega_m} \delta\boldsymbol{u} \cdot (\boldsymbol{T} \cdot \boldsymbol{n}) \; d\partial\Omega_m \quad \forall \boldsymbol{\delta u}. \tag{3.76}$$

These equations are then discretized using (2.70) and (2.85). Both magnetic and mechanical problems are nonlinear and solved using a Newton-Raphson solver. When the magnetic problem is to be solved, the mechanical strains are interpolated at the Gauss points of the mesh and $\boldsymbol{H}$ reconstructed from its analytical expression (3.69) at the Gauss points of the mesh. The result is then projected onto the curl of the edge shape functions as expressed by (3.75).

When the mechanical problem is to be solved, from the current magnetic solution, the magnetic field is interpolated at the Gauss-Points of the mesh

and then, this field is used to construct the total stress in (3.76). This stress, computed at the Gauss points of the mesh, is then projected onto the mechanical test functions using (3.76). These two problems are then solved iteratively until both solution converge under the desired tolerance.

3.3.4 Validation

In order to replicate the fitted $\boldsymbol{B}(\boldsymbol{H})$ curves, we simulated an unconstrained sphere of a radius of 1 mm, discretized into 8,647 nodes and 45,160 tetrahedral elements, under the effect of a uniform magnetic source field parametrized between 1 kA m^{-1} and 500 kA m^{-1}. Using the material coefficients of Galfenol (see Appendix B) we calculated the resulting magnetic field inside the sphere as a post-processing of the magnetic flux density. They were both averaged on the sphere and compared to the experimental $\boldsymbol{B}(\boldsymbol{H})$ curves, these results are presented in Figure 3.6. The resulting averaged strains from the FEM-BEM simulations are presented in Figure 3.7 and compared to the analytical reconstitution of the $\boldsymbol{S}(\boldsymbol{H})$ curves. They were obtained by parametrizing $\boldsymbol{B}$ and solving for $\boldsymbol{S}$ in $\boldsymbol{T} = \boldsymbol{0}$ for every $\boldsymbol{B}$. We observe positive values of S_{33} and negative values for S_{11} and S_{22} strains, this corresponds to an elongation across the (z) axis and a contraction along the (x) and (y) axes, which is the expected result for an unconstrained sphere in a source field along the (z) direction.

To study the h-convergence of the formulation, an analytical magneto-mechanical solution can be obtained, it comes from solving the same equations as in the previously obtained analytical solutions. This time, we solved for

$$\boldsymbol{T} = \begin{bmatrix} 0 & 0 & 0 \\ 0 & 0 & 0 \\ 0 & 0 & 10 \end{bmatrix} \text{(MPa)}, \tag{3.77}$$

and $\boldsymbol{H_0} = 200$ kA m^{-1} in the (z) direction, with the assumptions:

$$S_{11} = S_{22}, \tag{3.78}$$
$$B_1 = B_2 = 0, \tag{3.79}$$

and no extra-diagonal strains, which come from the imposed uni-axial stress and the symmetry of the problem with respect to the (z) direction. The

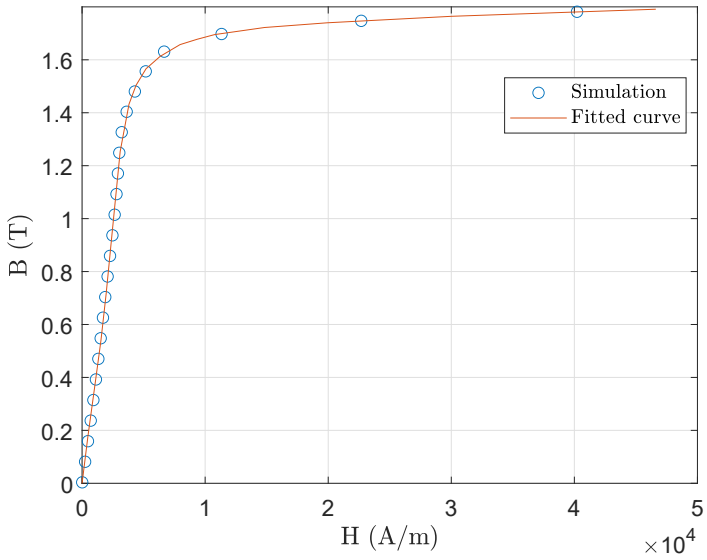

Figure 3.6: Fitted B(H) curves from [14] vs FEM-BEM simulation

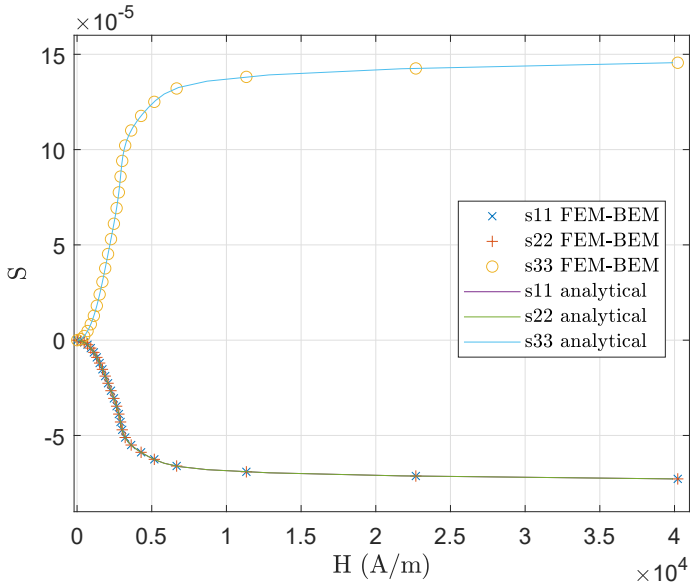

Figure 3.7: Averaged strains of the FEM-BEM solutions for the unconstrained spheres vs the strains obtained analytically

analytical solution for this case and other relevant solutions are given in Table 3.3. In it, we see the coupled magneto-mechanical behavior of Galfenol. The L^2 error of the numerical solution compared to this analytical solution for increasingly finely meshed spheres is presented in Figure 3.8. We observe the

convergence of the magnetic and mechanical solutions towards the analytical solution as we refine the mesh.

Table 3.3: Analytical solutions to the nonlinear magneto-mechanical nonlinear problem for different values of H_0 and uni-axial stress $\boldsymbol{T}$, both oriented in the (z) direction

		B_3 (T)	H_3 kA m^{-1}	S_{11} (= S_{22})	S_{33}
$H_0 = 200$ kA m^{-1}	, $T_{33} = 10$ MPa	0.75090	1.2231	$6.5943 \cdot 10^{-5}$	$1.5855 \cdot 10^{-4}$
$H_0 = 0$ kA m^{-1}	, $T_{33} = 10$ MPa	0	0	$5.3333 \cdot 10^{-5}$	$1.3333 \cdot 10^{-4}$
$H_0 = 200$ kA m^{-1}	, $T_{33} = 0$	0.74897	1.9938	$4.2039 \cdot 10^{-5}$	$2.1020 \cdot 10^{-5}$

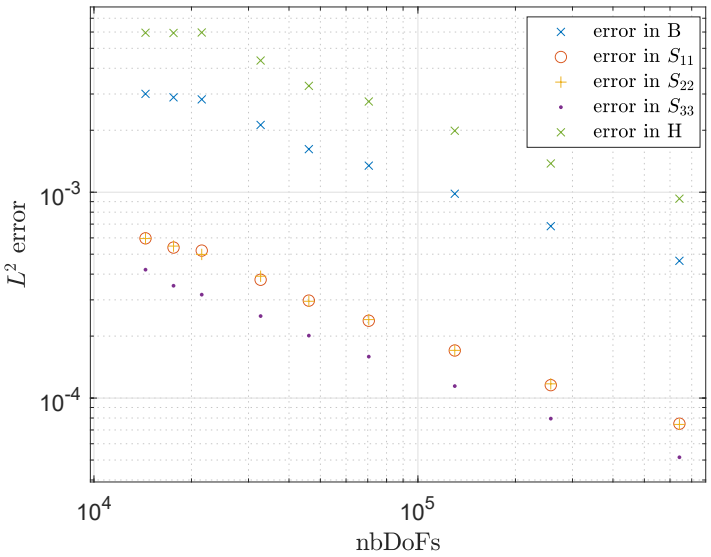

Figure 3.8: L^2 error of the magneto-mechanical solutions compared to the analytical solutions vs the number of total DoFs of the magneto-mechanical problem

For the computation of the L^2 error, each of the presented simulations of spheres under a uniform source field, the multi-physics resolution algorithm converged in three iterations to a tolerance of 10^{-5}. The magnetic as well as the mechanical problem were solved in two Newton-Raphson iterations to a relative tolerance of 10^{-6}, for these values of $\boldsymbol{H_0}$ and $\boldsymbol{T}$ given the constitutive laws, the material is far from saturation.

3.4 Electro-mechanical formulation and validation

3.4.1 Electro-mechanical constitutive laws

In the frame of adiabatic piezoelectricity, for the set of state variables $(\boldsymbol{E}, \boldsymbol{S})$, the mathematical relations describing the linear electro-mechanical coupling can be derived from the expression of the electric enthalpy H_1,

$$H_1 = \frac{1}{2}\boldsymbol{S} : \boldsymbol{c}^{\boldsymbol{E}} : \boldsymbol{S} - \frac{1}{2}\boldsymbol{E} \cdot \boldsymbol{\varepsilon}^{\boldsymbol{S}} \boldsymbol{E} - \boldsymbol{E} \cdot \boldsymbol{e} : \boldsymbol{S}, \tag{3.80}$$

where $\boldsymbol{c}^{\boldsymbol{E}}$ is the 4th-order elasticity tensor measured at a fixed field, $\boldsymbol{\varepsilon}^{\boldsymbol{S}}$ the electric permittivity, measured at a fixed strain and $\boldsymbol{e}$ the 3rd-order piezoelectric tensor. The expressions of the Cauchy stress tensor and the electric displacement field can then be obtained by the analytical differentiation of the expression of the electric enthalpy,

$$\boldsymbol{T} = \frac{\partial H_1}{\partial \boldsymbol{S}}, \tag{3.81}$$

$$\boldsymbol{D} = -\frac{\partial H_1}{\partial \boldsymbol{E}}. \tag{3.82}$$

The obtained expressions are the following,

$$\boldsymbol{T}(\boldsymbol{S}, \boldsymbol{E}) = \boldsymbol{C}^{\boldsymbol{E}} : \boldsymbol{S} - {}^{\mathrm{t}}\boldsymbol{e} \cdot \boldsymbol{E}, \tag{3.83}$$

$$\boldsymbol{D}(\boldsymbol{S}, \boldsymbol{E}) = \boldsymbol{e} : \boldsymbol{S} + \boldsymbol{\varepsilon}^{\boldsymbol{S}} \cdot \boldsymbol{E}. \tag{3.84}$$

These expressions are not unique and depending on the considered thermodynamic potential. Other similar relations can be derived by the use of other sets of state variables, for example,

$$\boldsymbol{S}(\boldsymbol{T}, \boldsymbol{E}) = \boldsymbol{s}^{\boldsymbol{E}} : \boldsymbol{T} + \boldsymbol{d}^{\boldsymbol{t}} \cdot \boldsymbol{D}, \tag{3.85}$$

$$\boldsymbol{D}(\boldsymbol{T}, \boldsymbol{E}) = \boldsymbol{d} : \boldsymbol{S} + \boldsymbol{\varepsilon}^{\boldsymbol{T}} \cdot \boldsymbol{D}. \tag{3.86}$$

These linear relations, in general, accurately describe the behavior of piezoelectric materials and the linearity hypothesis is well adapted to the considered devices. We prefer the set (3.83)-(3.84) to the others because having $\boldsymbol{S}$ as a state variable allows for an easy introduction of this set of constitutive laws into a FEM implementation of the piezoelectric problem [64] [89].

The structure of the considered coupling tensors $\boldsymbol{c^E}, \boldsymbol{e}$ and $\boldsymbol{\varepsilon^S}$ depends on the crystal structure of the considered material and on the poling direction of the material. Indeed, the response of poled piezoelectric materials highly depends on the poling direction, this translates to a structure of the coupling tensors dependent on the poling direction. These tensors are in general given for poling along the (z) axis and, to properly model a piezoelectric material poled along a given direction, these tensors have to be rotated accordingly to the direction of the poling direction.

For piezoelectric materials poled uniformly, a single tensor describes the material in every point. For nontrivial dispositions of the poling electrodes, such as the one presented in Figure 1.6, to represent the poling process, an electrostatic resolution can be performed on the material and the coupling tensors poled along the direction of the electrical solution [170].

3.4.2 Weak and discrete forms of the FEM electro-mechanical problem

In this section, we introduce the electro-mechanical weak forms related to the electro-mechanical coupling in piezoelectric materials. A first electro-mechanical weak formulation can be obtained by introducing (3.84) into the electrical weak form (2.30), it reads: find φ such that,

$$\int_{\Omega_m} \nabla\delta\varphi \cdot \boldsymbol{\varepsilon^S} \cdot \boldsymbol{E}\ d\Omega_m + \int_{\Omega_m} \nabla\delta\varphi \cdot \boldsymbol{e} : \nabla^S \boldsymbol{u}\ d\Omega_m = 0 \quad \forall\delta\varphi, \tag{3.87}$$

with $\varphi = \varphi_0$ at $\partial\Omega_m^{\varphi}$. Another electro-mechanical weak form can be obtained by introducing the mechanical piezoelectric constitutive law (3.83) into the weak form of the mechanical problem (2.34). We obtain the following weak form: find $\boldsymbol{u}$ such that,

$$\begin{aligned} \int_{\Omega_m} \nabla^S\boldsymbol{\delta u} : \boldsymbol{c^E} : \nabla^S \boldsymbol{u}\ d\Omega_m - \int_{\Omega_m} \nabla^S\boldsymbol{\delta u} : {}^{\mathrm{t}}\boldsymbol{e} \cdot \nabla\varphi\ d\Omega_m \\ = \int_{\partial\Omega_m} \boldsymbol{\delta u} \cdot (\boldsymbol{T}\cdot\boldsymbol{n})\ d\partial\Omega_m \quad \forall\boldsymbol{\delta u}, \end{aligned} \tag{3.88}$$

with $\boldsymbol{u} = \boldsymbol{u}^s$ at $\partial\Omega_m^u$. The following matrix system can be obtained from (3.87) and (3.88) considering the discretizations (2.66) (2.70):

$$\begin{bmatrix} \underline{\boldsymbol{K}}_{uu} & \underline{\boldsymbol{K}}_{u\phi} \\ \underline{\boldsymbol{K}}_{\phi u} & \underline{\boldsymbol{K}}_{\phi\phi} \end{bmatrix} \begin{pmatrix} \underline{\boldsymbol{u}} \\ \underline{\boldsymbol{\varphi}} \end{pmatrix} = \begin{pmatrix} \underline{\boldsymbol{Sh}}_{mecha} \\ \underline{0} \end{pmatrix} \tag{3.89}$$

where:

$$\underline{\boldsymbol{K}}_{uu}^{IJ} = \int_{\Omega_m} \mathbb{B}_u^I \cdot \boldsymbol{c}^{\boldsymbol{E}} \cdot \mathbb{B}_u^J \; d\Omega_m, \tag{3.90}$$

$$\underline{\boldsymbol{K}}_{\varphi\varphi}^{IJ} = \int_{\Omega_m} \mathbb{B}_\varphi^I \cdot \boldsymbol{\varepsilon}^{\boldsymbol{S}} \cdot \mathbb{B}_\varphi^J d\Omega_m, \tag{3.91}$$

$$\underline{\boldsymbol{K}}_{u\varphi}^{IJ} = \int_{\Omega_m} \mathbb{B}_u^I \cdot {}^{\mathrm{t}}\boldsymbol{e} \cdot \mathbb{B}_\varphi^J \; d\Omega_m, \tag{3.92}$$

$$\underline{\boldsymbol{K}}_{\varphi u}^{IJ} = \int_{\Omega_m} \mathbb{B}_\varphi^I \cdot \boldsymbol{e} \cdot \mathbb{B}_u^J \; d\Omega_m, \tag{3.93}$$

$$\underline{\boldsymbol{Sh}}_{mecha}^{I} = \int_{\partial\Omega_m^T} {}^{tr}N_u^I \cdot (\boldsymbol{T} \cdot \boldsymbol{n}) \; d\partial\Omega_m, \tag{3.94}$$

$$\tag{3.95}$$

while imposing $u^I = \partial\Omega_m^u$ and $\varphi^I = \varphi_0$ on $\partial\Omega_m^\varphi$.

3.4.3 Validation of the electro-mechanical formulation

In order to validate the electro-mechanical formulation, we considered the problem of a composite piezoelectric beam for which an analytical solution exists [15]. The geometry of the problem is presented in Figure 3.9. It consists of a three-layer beam made of two aluminum phases and a piezoelectric layer in between, poled along the length of the beam. Two electrodes are in direct contact with the piezoelectric material. A voltage of 10 V is applied to the bottom electrode and -10 V to the top electrode. In order to validate our electro-mechanical implementation and resolution algorithm, we replicated and meshed this geometry in 3D with a depth of 15 mm, with the same material coefficients.

The geometry was meshed into 4,625 hexagonal elements, translating into 5,616 electrical DoFs and 17,100 mechanical DoFs. The global matrix system

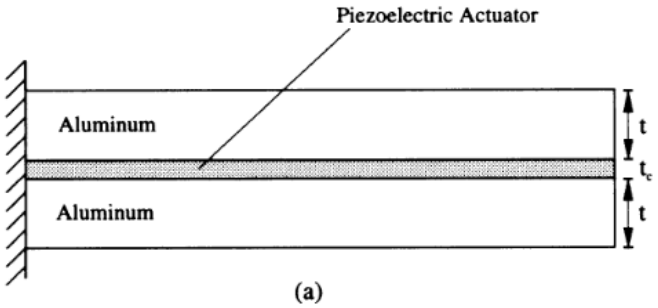

Figure 3.9: Geometry of the test case [15]. The device measures 10 cm long, $t = 8$ mm, $t_c = 2$ mm

(3.89) contains only sparse matrices. It has nevertheless big scaling differences between coefficients. Elements of the stiffness matrix are computed using coefficients of the stiffness tensor $\boldsymbol{c}$ of the order of 10-100 GPa, whereas the electric permittivity are of the order of 10^{-8} to 10^{-6} $\mathrm{F\,m^{-1}}$ and the piezoelectric coefficients of the order of 10 $\mathrm{N\,V^{-1}\,m^{-1}}$. This difference in coupling coefficients translates into a big difference of eigenvalues of the global matrix, and therefore in a poor conditioning number of this matrix. For the example presented, it has a conditioning number of the order of 10^{23}.

While this system could be solved using a single solver on the global matrix system as a block, and a scaling of sub-matrices used to overcome the scaling difference between coefficients, this system can be solved using the previously presented block Gauss-Seidel algorithm of Section 3.2.4.

We obtained the displacements presented in Figure 3.11. Figure 3.10 presents the rates of convergence of the single-physics solutions vs the iteration number of the Gauss-Seidel algorithm. We observe that the resolution algorithm reaches a rate of convergence of 10^{-7} in 44 iterations.

We observe that the FEM solution gives a vertical displacement at the tip of the beam of 0.1174 µm, which is very close to the analytical solution, which under beam theory assumptions, predicts a displacement of 0.1196 µm. The relative difference between both approaches is around 1.8 %.

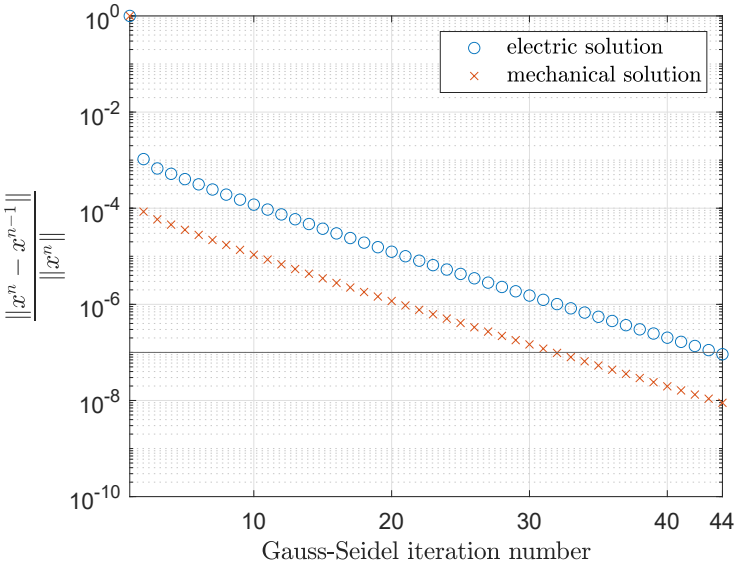

Figure 3.10: Convergence of the electro-mechanical solutions of the piezoelectric problem by iteration of the Gauss-Seidel multi-physics solver

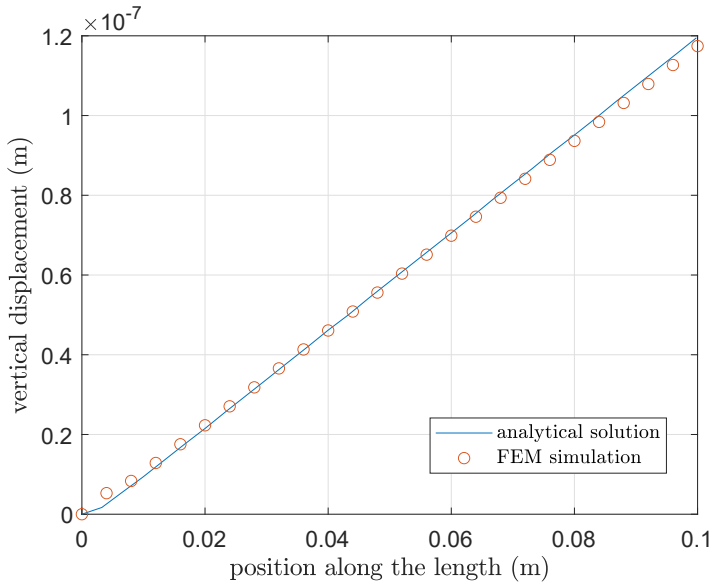

Figure 3.11: Vertical displacement in m of the FEM solution of the multi-physics problem vs the analytical solution

3.5 FEM-BEM modeling of magnetoelectric composite structures

In this section, we treat the modeling of strain induced ME effect, i.e., the modeling of composite structures made of the association of coupled electro-mechanical and magneto-mechanical phases considered to be perfectly bonded. The modeling of the ME device is then done by the superposition of electro-mechanical and magneto-mechanical constitutive laws: constitutive laws of the piezoelectric material are used when in the piezoelectric region, and magneto-mechanical constitutive laws are used in the active magneto-mechanical region.

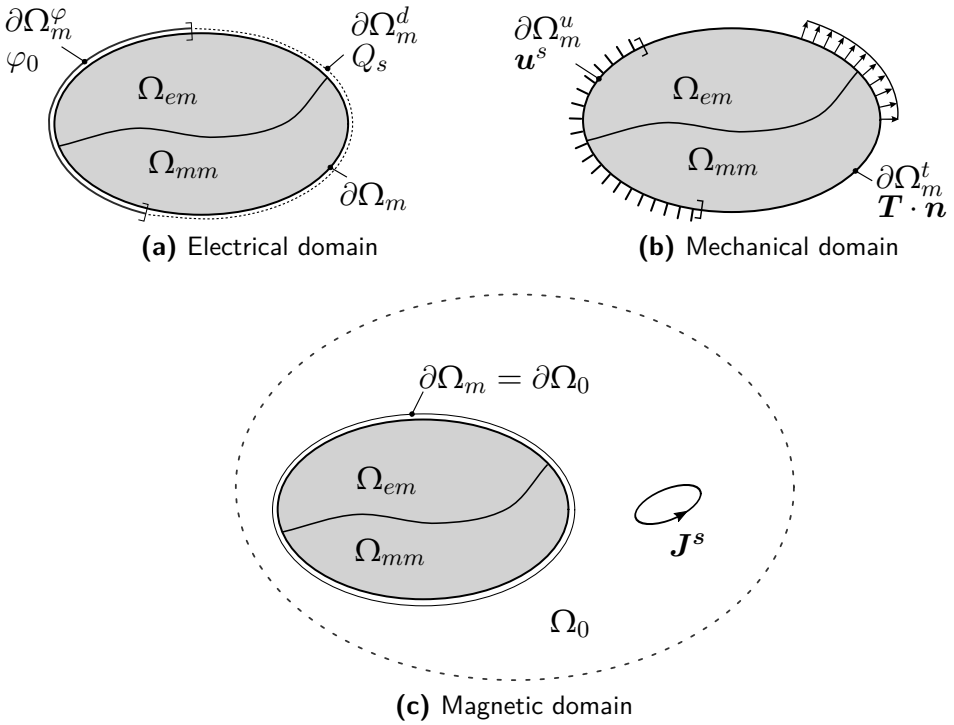

(a) Electrical domain **(b)** Mechanical domain

(c) Magnetic domain

Figure 3.12: Representation of the study domains of the FEM-BEM electro-magneto-mechanical problem. Here, Ω_{em} denotes the region with electro-mechanical properties, whereas Ω_{mm} the region with magneto-mechanical properties, therefore we have: $\Omega_m = \Omega_{em} \cup \Omega_{mm}$

The modeling of such structures involves the multi-physics resolution of three physics: electrostatics, magnetostatics and mechanics, associated to three weak and discrete forms. Figure 3.12 illustrates the domains of study

of the fully coupled problem. We establish two formulations of the linear problem, deriving from the two developed magnetostatics formulations and a nonlinear formulation based on the nonlinear description of magneto-mechanical coupling described in Section 3.3.

3.5.1 Piezoelectric-piezomagnetic formulations

3.5.1.1 ϕ_{red}-ϕ_{red}-u-φ Formulation

This formulation of the ME problem considers linear electro-mechanical and magneto-mechanical couplings. The piezoelectric and piezomagnetic phases are described by the constitutive laws (3.84)-(3.83) and (3.6)-(3.7). The ME problem can be obtained by the combination of the weak form of the respective sub-problems (3.11), (3.11), (2.50), (3.87) and (3.88). The weak form of the electric problem then reads: find φ such that,

$$\int_{\Omega_m} \nabla\delta\varphi \cdot \boldsymbol{\varepsilon} \cdot \nabla\varphi \; d\Omega_m + \int_{\Omega_{em}} \nabla\delta\varphi \cdot \boldsymbol{e} : \nabla^S \boldsymbol{u} \; d\Omega_m = 0 \quad \forall\delta\varphi, \tag{3.96}$$

with $\varphi = \varphi_0$ at $\partial\Omega_m^{\varphi}$. The weak form of the mechanical problem reads: find $\boldsymbol{u}$ such that,

$$\begin{aligned} &\int_{\Omega_m} \nabla^S \boldsymbol{\delta u} : \boldsymbol{c} : \nabla^S \boldsymbol{u} \; d\Omega_m - \int_{\Omega_{em}} \nabla^S \boldsymbol{\delta u} : {}^{\mathrm{t}}\boldsymbol{e} \cdot \nabla\varphi \; d\Omega_m \\ &- \int_{\Omega_{mm}} \nabla^S \boldsymbol{\delta u} : {}^{\mathrm{t}}\boldsymbol{q} \cdot \nabla\phi_{red} \; d\Omega_m = \int_{\Omega_{mm}} \nabla^S \boldsymbol{\delta u} : {}^{\mathrm{t}}\boldsymbol{q} \cdot \boldsymbol{H_0} \; d\Omega_m \\ &\qquad + \int_{\partial\Omega_m^T} \boldsymbol{\delta u} \cdot (\boldsymbol{T} \cdot \boldsymbol{n}) \; d\partial\Omega_m \quad \forall \boldsymbol{\delta u}, \end{aligned} \tag{3.97}$$

with $\boldsymbol{u} = \boldsymbol{u}^s$ at $\partial\Omega_m^u$. The magnetic weak form inside the active material, reading: find (ϕ_{red}, B_n) such that,

$$\begin{aligned} &\int_{\Omega_m} \nabla\delta\phi \cdot \boldsymbol{\mu} \cdot \nabla\phi_{red} \; d\Omega_m - \int_{\Omega_{mm}} \nabla\delta\phi \cdot \boldsymbol{q} : \nabla^S \boldsymbol{u} \; d\Omega_m + \int_{\partial\Omega_m} \delta\phi \; B_n \; d\partial\Omega_m \\ &\qquad = \int_{\Omega_m} \nabla\delta\phi \cdot \boldsymbol{\mu} \cdot \boldsymbol{H_0} \; d\Omega_m \quad \forall\delta\phi. \end{aligned} \tag{3.98}$$

As mechanical phenomena are limited to the active material and electric and magnetic equations uncoupled, (2.50) remains unchanged and can be added

to the system of equations to be solved. After discretizing the previous weak form along (2.66), (2.70), (2.75), (2.77) and (2.76), the global matrix system is the following:

$$\begin{bmatrix} \underline{\boldsymbol{K}}_{\phi\phi} & \underline{\boldsymbol{0}} & \underline{\boldsymbol{K}}_{\phi u} & \underline{\boldsymbol{0}} \\ & \underline{\boldsymbol{K}}_{\phi b_n} & & \\ \underline{\boldsymbol{0}} \quad \underline{\boldsymbol{H}} & \underline{\boldsymbol{T}} & \underline{\boldsymbol{0}} & \\ \underline{\boldsymbol{K}}_{u\phi} & \underline{\boldsymbol{0}} & \underline{\boldsymbol{K}}_{uu} & \underline{\boldsymbol{K}}_{u\varphi} \\ \underline{\boldsymbol{0}} & & \underline{\boldsymbol{K}}_{\varphi u} & \underline{\boldsymbol{K}}_{\varphi\varphi} \end{bmatrix} \begin{pmatrix} \underline{\boldsymbol{\phi}}_{red} \\ \underline{\boldsymbol{B_n}} \\ \underline{\boldsymbol{u}} \\ \underline{\boldsymbol{\varphi}} \end{pmatrix} = \begin{pmatrix} \underline{\boldsymbol{Sh}}_{mag}^{\Omega_m} \\ \underline{\boldsymbol{Sh}}_{mag}^{\partial\Omega_m} \\ \underline{\boldsymbol{Sh}}_{mecha} \\ \underline{0} \end{pmatrix} \tag{3.99}$$

The definition of the matrices not presented above is identical to the definitions of Sections 3.2.2 and 3.4.2. In (3.99), the colored matrices refer to single-physics problems, they are therefore in the diagonal of the assembled matrix system. Light colors relate to sparse FEM matrices, while dark colors relate to full BEM matrices. The uncoupled nature of electric and magnetic phenomena is apparent in the absence of electromagnetic coupling tensors and coupling matrices.

3.5.1.2 a-ϕ_{red}-u-φ Formulation

A second linear formulation of the ME problem can be derived from considering by describing the piezoelectric and piezomagnetic phases by the constitutive laws (3.84)-(3.83) and (3.4)-(3.5). The ME problem can be obtained by the combination of the weak form of the respective sub-problems (3.24), (3.25), (2.50), (3.87) and (3.88). The weak form of the electric problem then reads: find φ, such that,

$$\int_{\Omega_m} \nabla\delta\varphi \cdot \boldsymbol{\varepsilon} \cdot \boldsymbol{E} \; d\Omega_m + \int_{\Omega_{em}} \nabla\delta\varphi \cdot \boldsymbol{e} \cdot \nabla^S \boldsymbol{u} \; d\Omega_m = 0 \; \forall \; \delta\varphi, \tag{3.100}$$

with $\varphi = \varphi_0$ at $\partial\Omega_m^{\varphi}$. The resulting mechanical weak form reads: find $\boldsymbol{u}$ such that,

$$\begin{aligned}&\int_{\Omega_m} \nabla^S \boldsymbol{\delta u} : \boldsymbol{c} : \nabla^S \boldsymbol{u}\ d\Omega_m - \int_{\Omega_{em}} \nabla^S \boldsymbol{\delta u} : {}^{\mathrm{t}}\boldsymbol{e} \cdot \nabla \varphi\ d\Omega_m \\ -&\int_{\Omega_{mm}} \nabla^S \boldsymbol{\delta u} : {}^{\mathrm{t}}\boldsymbol{h} \cdot \boldsymbol{B}\ d\Omega_m = \int_{\partial\Omega_m} \delta \boldsymbol{u} \cdot (\boldsymbol{T} \cdot \boldsymbol{n}) d\Omega_m \quad \forall \boldsymbol{\delta u},\end{aligned} \tag{3.101}$$

with $\boldsymbol{u} = \boldsymbol{u}^s$ at $\partial\Omega_m^u$. The magnetic weak form reads: find $(\boldsymbol{a},\ \phi_{red})$ such that:

$$\begin{aligned}&\int_{\Omega_m} \nabla \times \boldsymbol{\delta a} \cdot \boldsymbol{\nu} \cdot \nabla \times \boldsymbol{a}\ d\Omega_m + \int_{\partial\Omega_m} (\nabla \times \boldsymbol{\delta a}) \cdot \boldsymbol{n}\ \phi_{red}\ d\partial\Omega_m \\ -&\int_{\Omega_{mm}} \nabla \times \boldsymbol{\delta a} \cdot \boldsymbol{h} : \boldsymbol{S}\ d\Omega_m = \int_{\partial\Omega_m} (\boldsymbol{\delta a} \times \boldsymbol{n}) \cdot \boldsymbol{H_0}\ d\partial\Omega_m\ \forall\ \boldsymbol{\delta a}.\end{aligned} \tag{3.102}$$

Together with the magnetic weak form outside the active material (2.50). After discretizing the previous weak forms along (2.66), (2.70), (2.77), (2.85) and (2.86), the global matrix system is the following:

$$\begin{bmatrix} \underline{\boldsymbol{K}}_{aa} & \underline{\boldsymbol{0}} & \underline{\boldsymbol{K}}_{au} & \underline{\boldsymbol{0}} \\ & \underline{\boldsymbol{K}}_{a\phi} & & \\ \underline{\boldsymbol{0}} & \underline{\boldsymbol{TC}} & \underline{\boldsymbol{H}} & \underline{\boldsymbol{0}} \\ \underline{\boldsymbol{K}}_{ua} & \underline{\boldsymbol{0}} & \underline{\boldsymbol{K}}_{uu} & \underline{\boldsymbol{K}}_{u\varphi} \\ \underline{\boldsymbol{0}} & & \underline{\boldsymbol{K}}_{\varphi u} & \underline{\boldsymbol{K}}_{\varphi\varphi} \end{bmatrix} \begin{pmatrix} \underline{\boldsymbol{a}} \\ \underline{\boldsymbol{\phi}}_{red} \\ \underline{\boldsymbol{u}} \\ \underline{\boldsymbol{\varphi}} \end{pmatrix} = \begin{pmatrix} \underline{\boldsymbol{Sh}}_{mag}^{\Omega_m} \\ \underline{\boldsymbol{Sh}}_{mag}^{\partial\Omega_m} \\ \underline{\boldsymbol{Sh}}_{mecha} \\ \underline{0} \end{pmatrix} \tag{3.103}$$

along with the appropriate boundary conditions. The definition of assembled matrices can be found in Sections 3.2.3 and 3.4.2. In (3.103), again, the colored matrices refer to single-physics problems, they are therefore in the diagonal of the assembled matrix system diagonal. Light colors relate to sparse FEM matrices, while dark colors relate to full BEM matrices.

3.5.2 Nonlinear magneto-mechanical piezoelectric formulation

For the case of nonlinear magneto-mechanical coupling, we consider the constitutive laws (3.68) and (3.69). The nonlinear ME effects are then

obtained by the coupled resolution of (3.75), (3.76) together with (3.87) and (3.88). The electrical weak form reads, find φ such that,

$$\int_{\Omega_m} \nabla\delta\varphi \cdot \boldsymbol{\varepsilon} \cdot \nabla\varphi \; d\Omega_m + \int_{\Omega_{em}} \nabla\delta\varphi \cdot \boldsymbol{e} \cdot \boldsymbol{S} \; d\Omega_m = 0 \quad \forall\delta\varphi, \tag{3.104}$$

with $\varphi = \varphi_0$ at $\partial\Omega_m^{\varphi}$. The mechanical weak form reads, find $\boldsymbol{u}$ such that,

$$\int_{\Omega_m} \nabla^S \boldsymbol{\delta u} : \boldsymbol{T}(\boldsymbol{S}, \boldsymbol{E}, \boldsymbol{B}) \; d\Omega_m = \int_{\partial\Omega_m} \delta\boldsymbol{u} \cdot (\boldsymbol{T} \cdot \boldsymbol{n}) \; d\partial\Omega_m \quad \forall\boldsymbol{\delta u}, \tag{3.105}$$

with $\boldsymbol{u} = \boldsymbol{u}^s$ at $\partial\Omega_m^u$. More explicitly, in the magnetostrictive region, the mechanical weak form reads: find $\boldsymbol{u}$ such that,

$$\int_{\Omega_{mm}} \nabla^S \boldsymbol{\delta u} : \boldsymbol{T}(\boldsymbol{S}, \boldsymbol{E}, \boldsymbol{B}) \; d\Omega_{mm} = \int_{\partial\Omega_{mm}} \delta\boldsymbol{u} \cdot (\boldsymbol{T} \cdot \boldsymbol{n}) \; d\partial\Omega_{mm} \quad \forall\boldsymbol{\delta u}, \tag{3.106}$$

whereas in the piezoelectric region, it reads find $\boldsymbol{u}$ such that,

$$\begin{aligned} \int_{\Omega_{em}} \nabla^S \boldsymbol{\delta u} : \boldsymbol{c}^{\boldsymbol{E},\boldsymbol{B}} : \boldsymbol{S} \; d\Omega_{em} - \int_{\Omega_{em}} \nabla^S \boldsymbol{\delta u} : {}^{\mathrm{t}}\boldsymbol{e} \cdot \boldsymbol{E} \; d\Omega_{em} \\ = \int_{\partial\Omega_{em}} \delta\boldsymbol{u} \cdot (\boldsymbol{T} \cdot \boldsymbol{n}) d\partial\Omega_{em} \quad \forall\boldsymbol{\delta u}. \end{aligned} \tag{3.107}$$

The magnetic weak form inside the active material reads, find $(\boldsymbol{a}, \phi_{red})$,

$$\begin{aligned} \int_{\Omega_m} \nabla \times \delta\boldsymbol{a} \cdot \boldsymbol{H}(\boldsymbol{B}, \boldsymbol{S}) \; d\Omega_m + \int_{\partial\Omega_m} \nabla \times \delta\boldsymbol{a} \cdot \boldsymbol{n} \; \phi_{red} \; d\partial\Omega_m \\ = \int_{\partial\Omega_m} (\delta\boldsymbol{a} \times \boldsymbol{n}) \cdot \boldsymbol{H_0} \; d\partial\Omega_m \quad \forall\delta\boldsymbol{a}. \end{aligned} \tag{3.108}$$

After considering the discretizations (2.66), (2.70), (2.77) (2.85) and (2.86), we obtain the global matrix (3.109). As the magneto-mechanical coupling is introduced via the nonlinear constitutive laws, in the expression of $\boldsymbol{H}$ and $\boldsymbol{T}$, there are no magneto-mechanical coupling matrices.

$$\begin{bmatrix} \underline{\boldsymbol{K}}_{aa} & \underline{\boldsymbol{0}} & \underline{0} & \\ & \underline{\boldsymbol{K}}_{a\phi} & & \\ \underline{\boldsymbol{0}} & \underline{\boldsymbol{TC}} & \underline{\boldsymbol{H}} & \\ \underline{0} & & \underline{\boldsymbol{K}}_{uu} & \underline{\boldsymbol{K}}_{u\varphi} \\ & & \underline{\boldsymbol{K}}_{\varphi u} & \underline{\boldsymbol{K}}_{\varphi\varphi} \end{bmatrix} \begin{pmatrix} \underline{\boldsymbol{a}} \\ \underline{\boldsymbol{\phi}}_{red} \\ \underline{\boldsymbol{u}} \\ \underline{\boldsymbol{\varphi}} \end{pmatrix} = \begin{pmatrix} \underline{\boldsymbol{Sh}}_{mag}^{\Omega_m} \\ \underline{\boldsymbol{Sh}}_{mag}^{\partial\Omega_m} \\ \underline{\boldsymbol{Sh}}_{mecha} \\ \underline{0} \end{pmatrix} \tag{3.109}$$

In terms of implementation, in the iterative multi-physics resolution, when the magnetic problem is to be solved, the mechanical strains are interpolated at the Gauss points of the mesh and $\boldsymbol{H}$ reconstructed from its analytical expression (3.69) at the Gauss-Points of the mesh. The result is then projected onto the curl of the edge shape functions as expressed by (3.108). When the mechanical problem is to be solved, from the current magnetic solution, the magnetic flux density is interpolated at the Gauss-Points of the mesh. This field is used to construct $\boldsymbol{T}$ from (3.68). The electro-mechanical coupling of the piezoelectric phase is introduced by a second hand term equal to,

$$\underline{\boldsymbol{K}}_{u\varphi}^{IJ} \cdot \underline{\boldsymbol{\varphi}} = \left(\int_{\Omega_{em}} \mathbb{B}_u^I \cdot {}^{\mathrm{t}}\boldsymbol{e} \cdot \mathbb{B}_\varphi^J \, d\Omega_{em} \right) \cdot \underline{\boldsymbol{\varphi}}, \tag{3.110}$$

which is then subtracted to the residue of the mechanical Newton-Raphson.

3.6 Resolution of multi-physics problems with more than two physics

When solving problems involving two physics with the block Gauss-Seidel algorithm, the two problems have to be solved alternatively and the resolution order is a non-issue, besides the choice of which problem to solve at the first iteration. For problems with more than two physics, many possibilities regarding the solving order arise. In problems driven by a particular physics, and in order to have non-zero solutions for the first iterations, a natural resolution order can sometimes be found. If a particular physics drives the problem, it is natural to solve it first.

In [171], multiple resolution patterns are proposed for fluid-structure interaction with more than one fluid region. The different physics are solved in a previously defined and fixed order within a black-box multi-physics solver. When solving the three cellular problems of the strain induced magnetoelectric effects, iteratively solving them in a predefined order comes down to Algorithm 1. In Algorithms 1, 2 and 3, nb_{prob} refers to the number of problems to be solved. These problems and their partial solutions are ordered, and each problem and its solution are indexed by an integer. The same notations as in Section 3.2.4 are used.

Algorithm 1 Ordered Gauss-Seidel multi-physics solver for linear problems

for i $< n_{prob}$ **do**
  $\underline{\mathbf{x}}_i \leftarrow \underline{0}$
end for
do
  $\underline{\mathbf{x_0}}_i \leftarrow \underline{\mathbf{x}}_i$
  $\underline{Sh}_i \leftarrow \underline{Sh}_i - \sum_{j=0}^{i-1} [\underline{\mathbf{K}}_{ij}] \cdot \underline{\mathbf{x}}_j - \sum_{j=i+1}^{nb_{prob}} [\underline{\mathbf{K}}_{ij}] \cdot \underline{\mathbf{x_0}}_j$
  $\underline{x_i} \leftarrow \text{solve}(\underline{\mathbf{K}}_{ii}, \underline{\mathbf{Sh}}_i)$ ▷ problem "i" is solved
  $i \leftarrow i + 1 \mod nb_{prob}$ ▷ the next problem is to be solved
while $\neg(\forall\, i < nb_{prob},\ \frac{\|\underline{\mathbf{x}}_i - \underline{x_{0i}}\|}{\|\underline{\mathbf{x}}_i\|} < \epsilon)$

The resolution of a single-physics problem "i" can be written as a function $\mathcal{F}_i$ of the solutions to all the physics, which returns the solution to the current problem $\underline{\mathbf{x}}_i$,

$$\mathcal{F}_i : (\underline{\mathbf{x}}_1, ..., \underline{\mathbf{x}}_{nb_{prob}}) \rightarrow \underline{\mathbf{x}}_i. \tag{3.111}$$

With these notations, the block Gauss-Seidel algorithm can be written as presented in Algorithm 2, and can then be generalized for nonlinear problems, for the case where $\mathcal{F}_i$ has a nonlinear dependence on the set of solutions.

Another approach to solving the multi-physics problem is to have no imposed resolution order besides for the first three resolutions. After each resolution, the convergence of all single-physics solutions are computed by (3.54). Then, among the problems which have not been immediately solved before, the problem with the worst convergence, i.e., the index "i" of the highest ϵ_i, "i_{max}" is solved. This choice of problem to be solved is represented by the function "$\max_{\text{Index}}$" in Algorithm 3.

Algorithm 2 Gauss-Seidel multi-physics solver for the nonlinear case

for i $< nb_{prob}$ **do**
  $\underline{\mathbf{x}}_i \leftarrow \underline{0}$
end for
do
  $\underline{\mathbf{x_0}}_i \leftarrow \underline{\mathbf{x}}_i$
  $\underline{x_i} \leftarrow \mathcal{F}_i(\underline{\mathbf{x}}_1, ..., \underline{\mathbf{x}}_{nb_{prob}})$ ▷ problem "i" is solved
  $i \leftarrow i + 1 \mod nb_{prob}$ ▷ the next problem is to be solved
while $\neg(\forall\ i < nb_{prob},\ \frac{\|\underline{\mathbf{x}}_i - \underline{\mathbf{x_0}}_i\|}{\|\underline{\mathbf{x}}_i\|} < \epsilon)$

Algorithm 3 Adaptive Gauss-Seidel multi-physics solver

for i $< nb_{prob}$ **do**
  $\underline{\mathbf{x}}_i \leftarrow \underline{0}$
end for
for $i < nb_{prob}$ **do**
  $\underline{\mathbf{x_0}}_i \leftarrow \underline{\mathbf{x}}_i$
  $\underline{x_i} \leftarrow \mathcal{F}_i(\underline{\mathbf{x}}_1, ..., \underline{\mathbf{x}}_{nb_{prob}})$ ▷ problem "i is solved
  $\epsilon_i = \frac{\|\underline{\mathbf{x}}_i - \underline{\mathbf{x}}_{0_i}\|}{\|\underline{\mathbf{x}}_i\|}$ ▷ the convergence state of solution "i" is computed
  lastSolved $= nb_{prob}$
end for
while $\neg(\forall\ i < nb_{prob},\ \frac{\|\underline{\mathbf{x}}_i - \underline{\mathbf{x_0}}_i\|}{\|\underline{\mathbf{x}}_i\|} < \epsilon)$ **do**
  $i_{max} \leftarrow \max_{\text{Index}}(\epsilon_1, ..., \epsilon_{nb_{prob}}, \text{lastSolved})$ ▷ determination of i_{max}
  $\underline{\mathbf{x_0}}_{i_{max}} \leftarrow \underline{\mathbf{x}}_{i_{max}}$
  $\underline{\mathbf{x}}_{i_{max}} \leftarrow \mathcal{F}_{i_{max}}(\underline{\mathbf{x}}_1, ..., \underline{\mathbf{x}}_{nb_{prob}})$ ▷ problem "i_{max}" is solved
  $\epsilon_{i_{max}} = \frac{\|\underline{\mathbf{x}}_{i_{max}} - \underline{\mathbf{x_0}}_{i_{max}}\|}{\|\underline{\mathbf{x}}_{i_{max}}\|}$ ▷ convergence state of solution "i_{max}"
  lastSolved $= i_{max}$
end while

For our particular application, as the magnetic and electric problem are uncoupled, the mechanical problem must be solved at least every two resolutions. This resolution algorithm was implemented and actively used for solving linear and nonlinear problems in order to speed up the resolution times. We will explore the behavior of both versions of the iterative multi-physics resolution after having introduced the test cases of the full coupled problem.

3.7 Conclusion

In this chapter, we present the chosen constitutive laws of magneto-mechanical and electro-mechanical coupling and their corresponding weak and discrete forms. In particular, two linear FEM-BEM forms of the magneto-mechanical problem are developed and a nonlinear one, which takes into account nonlinear constitutive laws derived from invariant theory. They are all compared to an analytical solution and all converge towards the analytical solution as the mesh is refined. We also develop and validate the FEM approach to modeling piezoelectricity which also shows good agreement with the analytical solution. We also present the developed weak and discrete forms of the FEM-BEM electro-magneto-mechanical problem, which will be applied to a set of test cases in the following chapter. The resolution of the discrete form of the developed formulations is challenging, the use of a block Gauss-Seidel type solver proved to be efficient at solving the multi-physics problems by the use of adapted solvers for each physics. Two versions of the block Gauss-Seidel are presented, a version with a fixed resolution order and an adaptive solver which solves in priority the least converging problem.

Chapter 4

Two applications of the proposed modeling approach

4.1 Introduction

In this chapter, we apply the formulations and resolution algorithms developed in the previous chapter to two ME devices. The first is a layered composite ME harvester made of a piezoelectric phase in between two layers of a magnetostrictive material. For this topology, the results of the three developed FEM-BEM approaches are compared, the h-convergence of the two linear formulations is studied, and our results compared to those of to a pure FEM approach. The second application can be used as an alternative voltage generator or as an actuator. It is made of a disk of a giant magnetostrictive material perfectly bonded onto a piezoelectric layer with a specific electrode configuration, subject to the effect of a permanent magnet. For the second topology, we study the output voltage in generator mode and the mechanical torque between interacting elements when in actuator mode.

4.2 Three-layer ME composite

4.2.1 Device description

The three-layer ME composite is made of two layers of magnetostrictive material and a layer of piezoelectric material in between, the geometry of the ME composite is presented in Figure 4.1. On both the top and bottom

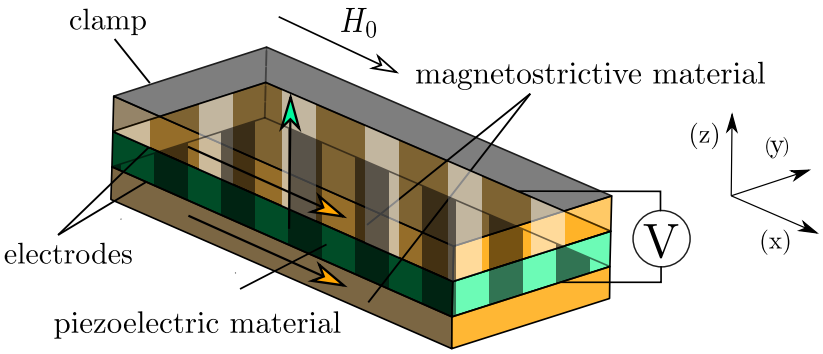

Figure 4.1: Schematics of the three-layer ME composite, the arrows represent the poling direction of materials. For the nonlinear model, the magnetostrictive material is considered isotropic. The device measures 3×6×14 mm. The striped surfaces represent the electrodes

of the piezoelectric material are two electrodes, one serves as reference, the other one is at a floating potential. The piezoelectric material is poled perpendicularly to the electrodes in order to produce an electric voltage between the electrodes under longitudinal strains.

The operating principle of the three-layer ME composite is as follows: under the effect of a source field, the magnetostrictive phases will change in shape in the direction of the applied field. Because the magnetostrictive phases are bonded to the piezoelectric phase, a mechanical strain will appear in the piezoelectric phase. An electric voltage will appear between the electrodes of the piezoelectric phase.

4.2.2 Linear FEM-BEM modeling of the 3-layer ME composite

The application of the modeling approaches of Sections 3.5.1.1 and 3.5.1.2 applied to the modeling of the three-layer ME composite gives similar results between both developed formulations. To evaluate the convergence of the three-physics problem we considered four discretizations of the geometry presented in Figure 4.1, each corresponding to 2, 3, 4 and 5 hexagonal elements per mm. The number of DoFs of each considered discretization are given in Tables 4.1 and 4.2. For readability reasons, the ϕ_{red}-ϕ_{red}-u-φ formulation will be referred to as ϕ_{red}-ϕ_{red} and the a-ϕ_{red}-u-φ as a-ϕ_{red}. The physical properties of the piezoelectric and piezomagnetic phases are those of [127] and correspond to Terfenol-D for the magnetostrictive phase and PZT-5A for the piezoelectric phase. For the three simulations, the field

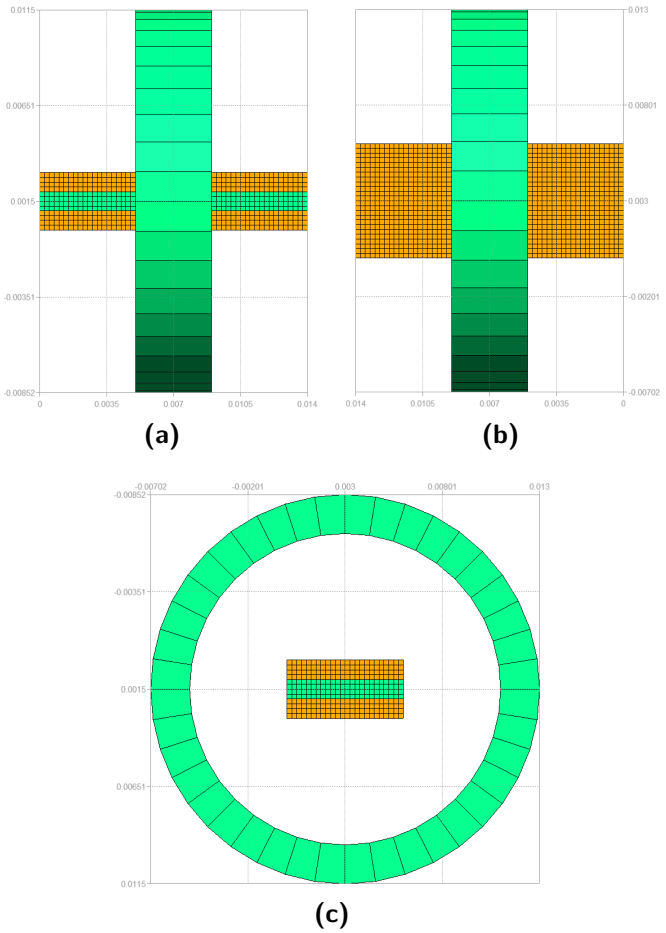

Figure 4.2: Mesh of the three-layer ME composite and the coil for the case of 4 discretizations per mm, seen from the three axes

source was a coil positioned as presented in Figures 4.2a-4.2c with a current density of 12.5 $\mathrm{A\,mm^{-2}}$ amounting to a total current I of 100 At.

The simulation results of the a-ϕ_{red} formulation are presented in Figure 4.3. In these, we observe in Figure 4.3a that, as expected, the application of a magnetic field resulted in the elongation along the poling direction of the piezomagnetic phase, we also observe the deformation of the piezoelectric phase. In Figures 4.3b and 4.3c the presence of an electric voltage and an electric field in the direction of the poling between the electrodes. Also, we observe in Figure 4.3d due to the higher permeability of the piezomagnetic phase with respect to the piezoelectric phase, the magnetic flux density $\boldsymbol{B}$ was found to be higher in the piezomagnetic phase.

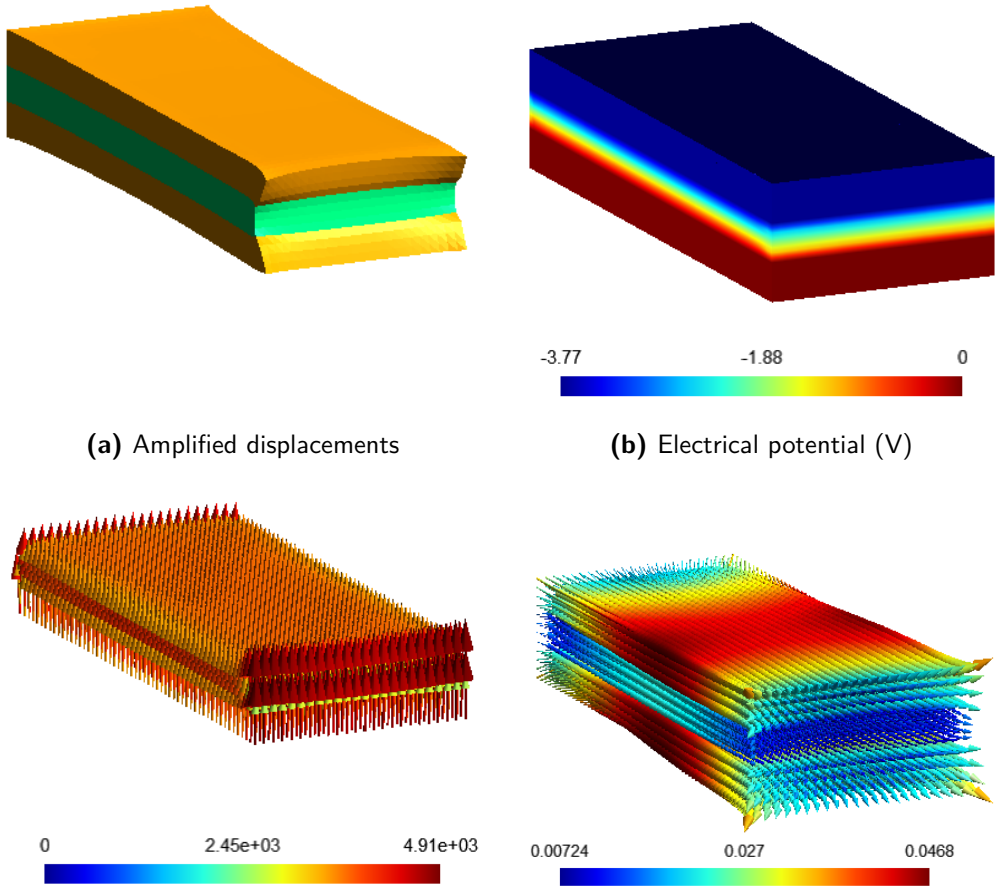

(a) Amplified displacements **(b)** Electrical potential (V)

(c) Electric field ($\mathrm{V\,m^{-1}}$) **(d)** Magnetic flux density (T)

Figure 4.3: Plots of the multiphysics solution of the a-ϕ_{red}

Figure 4.4 shows the output voltage of the three-layer structure vs the number of total degrees of freedom for the two formulations ϕ_{red}-ϕ_{red} and a-ϕ_{red}. Figure 4.5 presents the relative difference between the output voltages vs the number of discretizations per mm. We observe that they give very close results: the difference between output voltages decreases with the number of discretizations up to the case of 4 discretizations per mm. Afterward, the relative error increases. This may be caused by the finer discretization of the perfect edges which induce the divergence of fields around the perfect edges of the geometry and the two formulations not having the same response regarding these edge effects.

Figure 4.7 shows the mechanical displacement in the ME structure for the case of 4 discretizations per mm, resulting from the two formulations of the

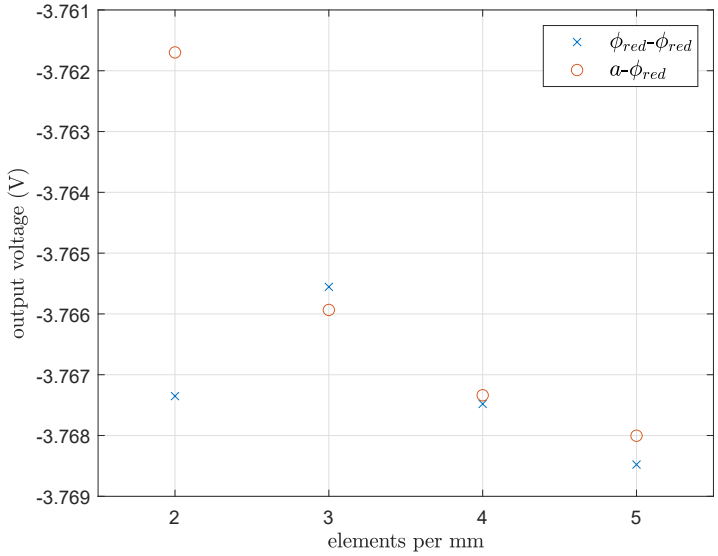

Figure 4.4: Output voltage of the ME device for the two linear formulations vs the number of discretizations per mm

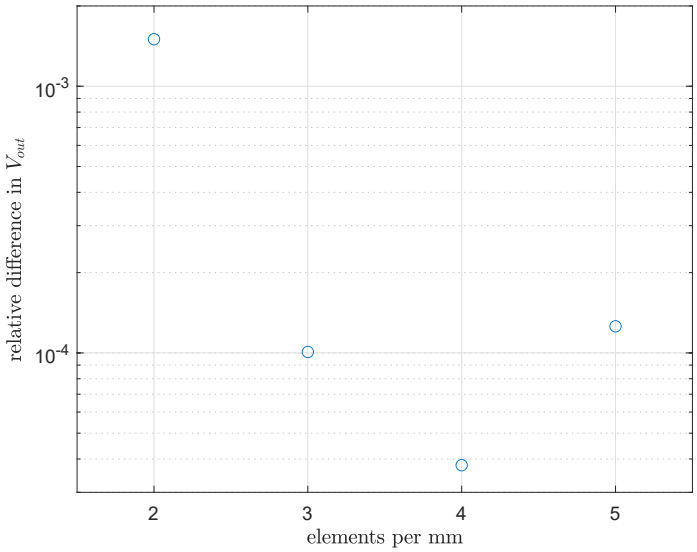

Figure 4.5: Relative difference in the output voltage of the ME device between the two linear formulations vs the number of discretizations per mm

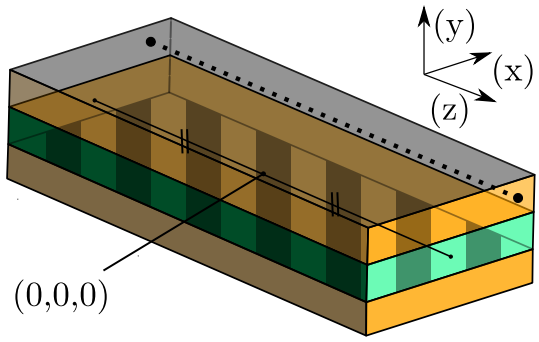

Figure 4.6: Schematics of the three-layer ME composite. The displacements shown in Figure 4.7 are plotted following the dotted line. It goes from (2.5,1,-7) mm to (2.5,1,7) mm

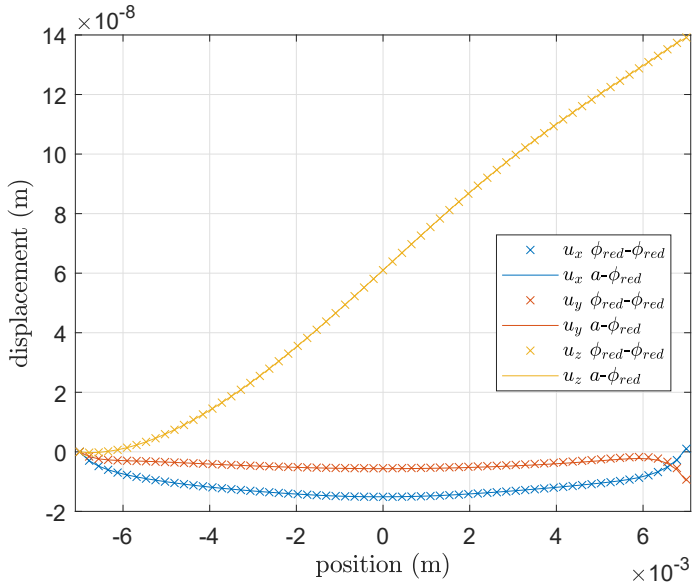

Figure 4.7: Plot of the mechanical displacement of the two formulations folowing the path presented in Figure 4.6 for the case of 4 discretizations per mm

Table 4.1: # of DoFs of the three discretizations for the ϕ_{red}-ϕ_{red}

disc. per mm	2	3	4	5
# DoFs mag.	3,791	10,762	23,133	42,416
# DoFs mecha.	7,644	23,940	54,600	104,160
# DoFs elec.	1,886	6,537	15,676	30,815

Table 4.2: # of DoFs of the three discretizations for the a-ϕ_{red}

disc. per mm	2	3	4	5
# DoFs mag.	8,398	25,665	57,692	109,015
# DoFs mecha.	7,644	23,940	54,600	104,160
# DoFs elec.	1,886	6,537	15,676	30,815

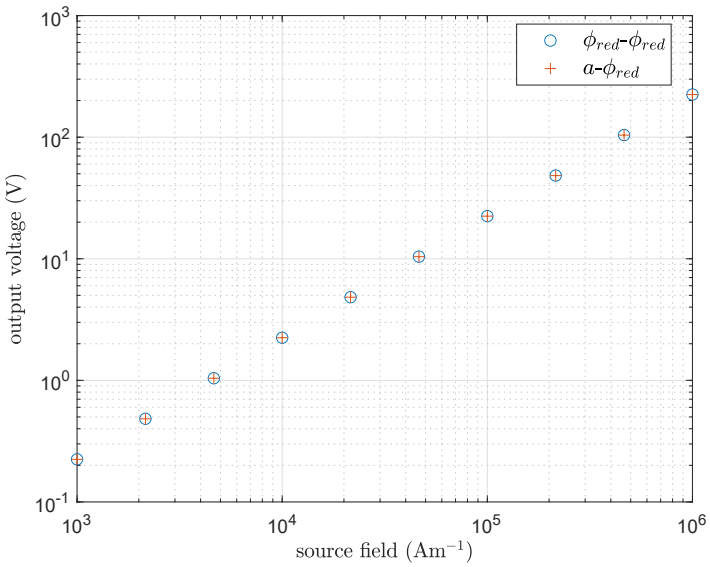

Figure 4.8: Output voltage of the three-layer ME composite vs the amplitude of the source field

full ME problem along the path presented in Figure 4.6. We observe that the mechanical solutions are almost identical.

Figure 4.8 presents the obtained output voltages of the three-layer structure now under the effect of a uniform source field in the (z) direction. As expected, given the considered linear properties of piezoelectric and piezomagnetic

phases, we observe that the linear modeling of the three-layer ME composite leads to a linear relation between the amplitude of the source field and the resulting output voltage, i.e., a DC magnetoelectric coefficient α equal to the slope of the plots of Figure 4.8,

$$\alpha = 0.811 \quad \mathrm{mV\,m\,A^{-1}}, \tag{4.1}$$

for both linear formulations.

4.2.3 Behavior of the multi-physics solver

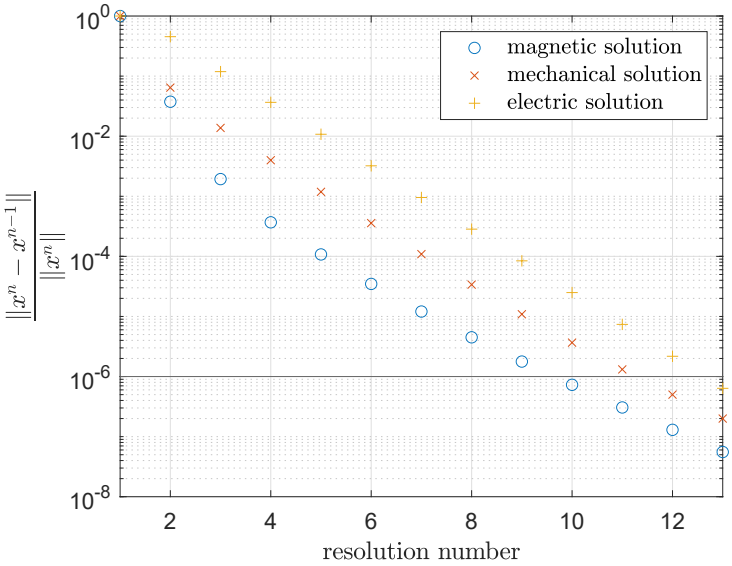

Figure 4.9: Convergence of the single-physics solutions vs iteration number of the ordered block Gauss-Seidel algorithm for the ϕ_{red}-ϕ_{red} formulation

Concerning the behavior of the multi-physics solver, in Figure 4.9 we see the convergence of the three multi-physics solutions for the magnetic ϕ_{red}-ϕ_{red} vs the Gauss-Seidel iteration number for the case presented in Section 4.2.2 and the mesh with 4 discretizations per mm. The convergence of the multi-physics problem tolerance was set to 10^{-6}, while the tolerance of the magnetic solver was set to 10^{-7}. In figure 4.12 we present the same results for the magnetic a-ϕ_{red}, we see that for this geometry and discretization, both formulations were solved in the same number of Gauss-Seidel iterations, 13.

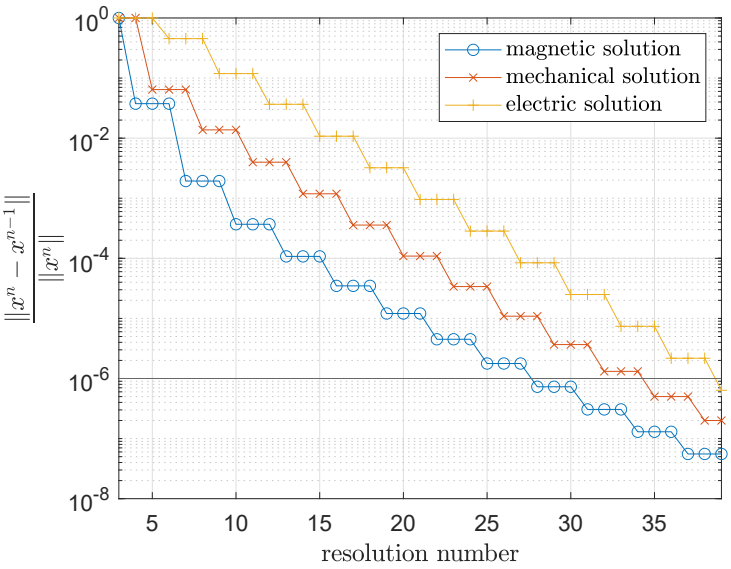

Figure 4.10: Convergence of the single-physics solutions vs number of resolutions within the block Gauss-Seidel algorithm for the ϕ_{red}-ϕ_{red} formulation. In its ordered form, each physicsis solved every three resolutions

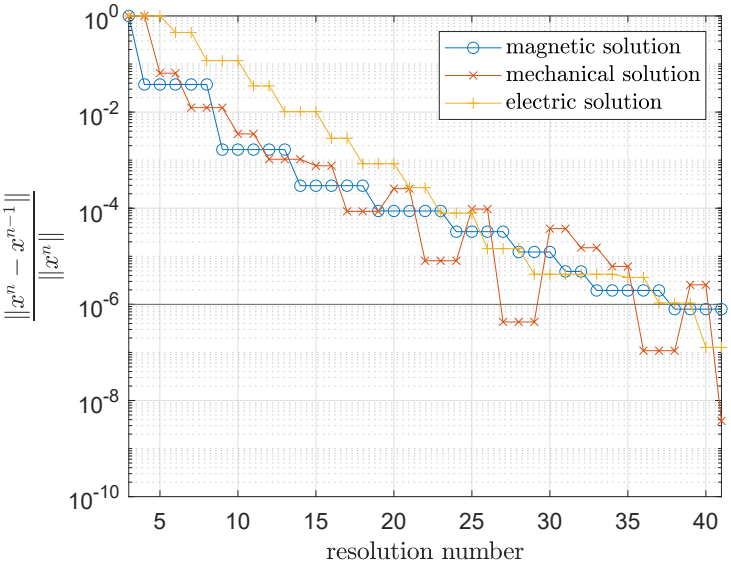

Figure 4.11: Convergence of the single-physics solutions vs number of resolutions using Algorithm 3 for the ϕ_{red}-ϕ_{red} formulation

In Figures 4.9 and 4.12, each iteration corresponds to three single-physics resolutions. As the magnetic problem drives the problem and in order to have non-zero second hand terms for the other single-physics problems, the mechanical problem was solved second and the electrical problem third.

If now these curves are plotted not in terms of the convergence vs the number of iterations of the block Gauss-Seidel but vs the number of resolutions performed, Figure 4.9 becomes Figure 4.10 and 4.12 becomes Figure 4.13. In these Figures, x^n refers to the nth solution to the given problem, and the change in the state of convergence corresponds to a resolution of the given problem. In order to better visualize the behavior of the solutions, full lines instead of markers are used in Figures 4.10, 4.11, 4.13 and 4.14.

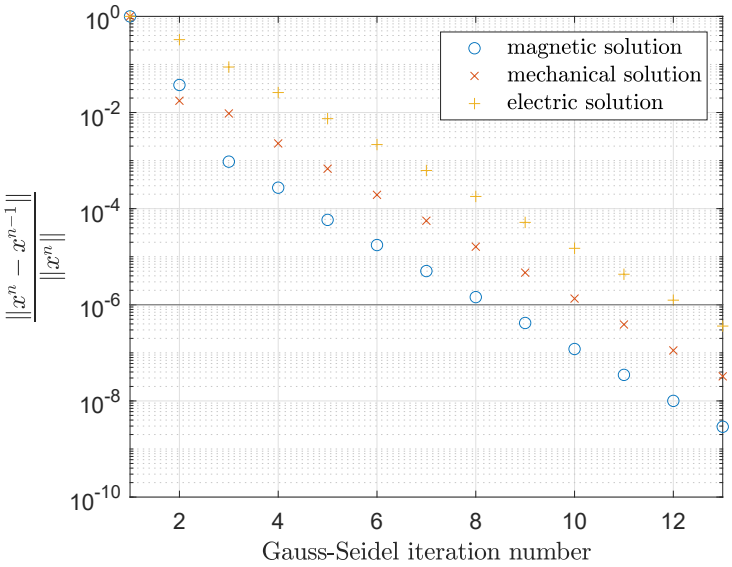

Figure 4.12: Convergence of the single-physics solutions vs iteration number of the ordered block Gauss-Seidel algorithm for the a-ϕ_{red} formulation

These figures can be compared to Figures 4.11 and 4.14, which present the results of the use of Algorithm 3 in which problems are not solved in a predefined order but depending on their rate of convergence. In this particular situation, we observe that the adaptive resolution is advantageous for both formulations of the three-physics problem for the given tolerance. The behavior of the multi-physics solutions seems to be more unstable for the ϕ_{red}-ϕ_{red}, but the relative difference between both resolution algorithms remained under the tolerance of the multi-physics solver for both situations.

The details of the comparison between solvers for this particular situation

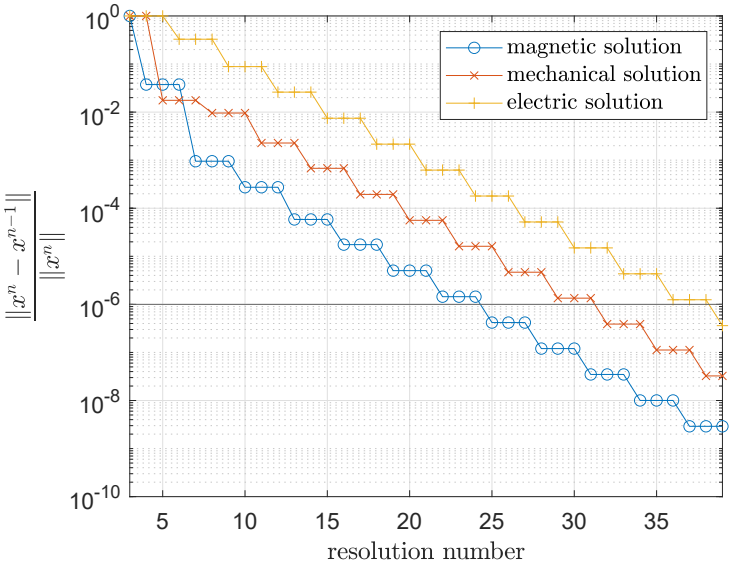

Figure 4.13: Convergence of the single-physics solutions within the ordered block Gauss-Seidel algorithm for the a-ϕ_{red} formulation

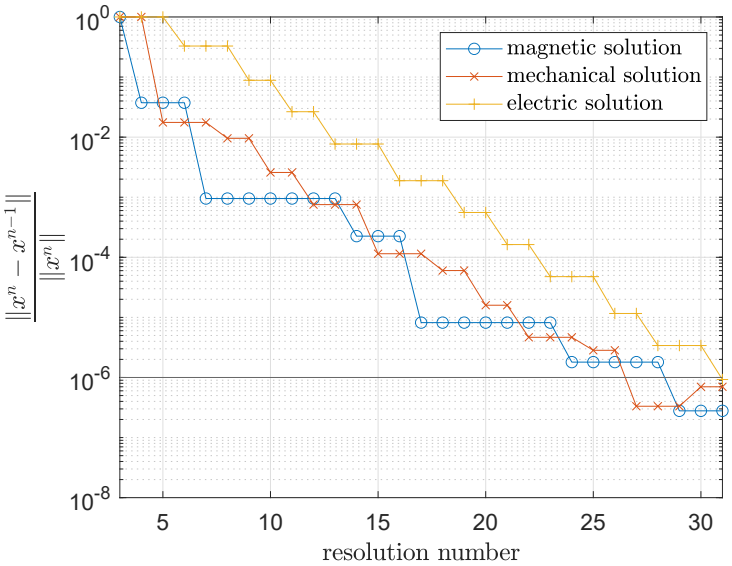

Figure 4.14: Convergence of the single-physics solutions within the multi-physics solver of Algorithm 3 and the a-ϕ_{red} formulation

Table 4.3: Solver comparison for the magnetic ϕ_{red}-ϕ_{red}

Problem	ord. G-S	adap. G-S
# of magnetic resolutions	13	10
# of electric resolutions	13	17
# of mechanical resolutions	13	14
total resolution time (s)	698	661

Table 4.4: Solver comparison for the magnetic a-ϕ_{red}

Problem	ord. G-S	adap. G-S
# of magnetic resolutions	13	7
# of electric resolutions	13	12
# of mechanical resolutions	13	12
total resolution time (s)	773	462

are presented in Tables 4.3 and 4.4 for a computer with the following configuration: Intel ©Core ™i7-10610U CPU @ 1.80GHz 2.30 GHz and 16 GB of RAM. In Tables 4.3 and 4.4, we see that the proposed resolution scheme gives for the particular studied situation leads to a smaller resolution time than the ordered Gauss-Seidel, this, even if the total number of resolutions is higher (36 vs 35 for the ϕ_{red}-ϕ_{red}). This can be explained by the smaller number of resolutions of the magnetic problem, which converges fast and is costly to solve.

4.2.4 Comparison with the FEM

In order to position and compare the proposed approach to the FEM, a pure FEM approach based on a reduced scalar potential formulation was implemented in the software GetDP 3.5.0 [172] and compared to the FEM-BEM ϕ_{red}-ϕ_{red} formulation. The study domains are those of Figure 4.15, therefore, an air region and an infinite box [173], both contained in the domain Ω_0, are added to the geometry, and the leaks of the magnetic field taken equal to zero at the boundary of the infinite box $\partial\Omega_0$. The arrangement and mesh of both the coil and ME composite is shown in Figures 4.16a-4.16c. It consists of a ME laminate structure identical to the one presented in Figure 4.1 and an uncentered coil. The uncentered coil makes the source field inhomogeneous and non-symmetric, thus giving the advantage to numerical tools with respect to analytical approaches for the accurate modeling of the system.

Two geometries of the FEM problem are considered, both having the same

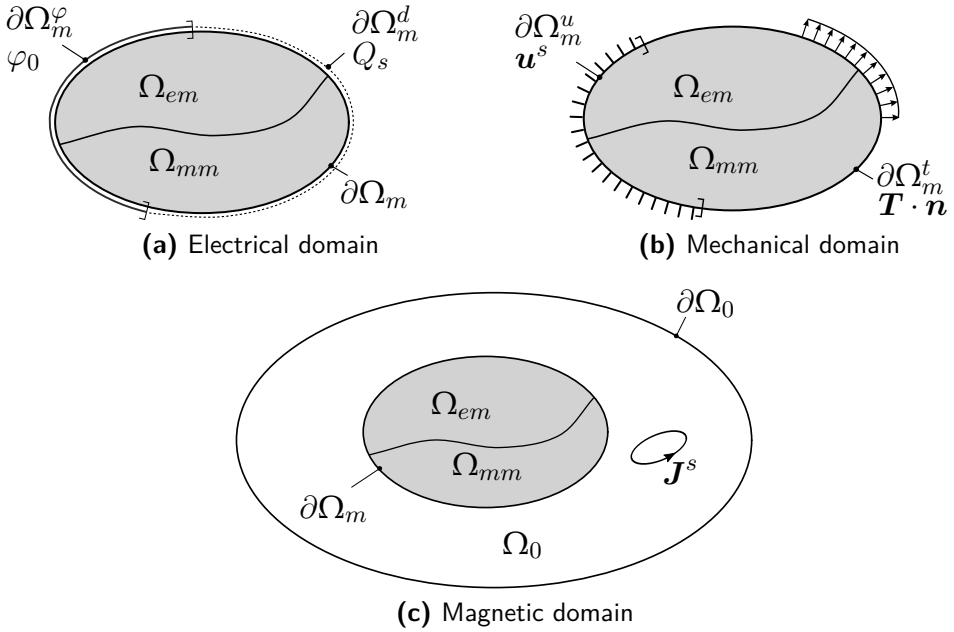

Figure 4.15: Representation of the study domains of the electro-magneto-mechanical problem by the FEM. Now $\Omega = \Omega_m \cup \Omega_0$ is a closed domain, and B_n taken equal to zero at $\partial\Omega_0$

discretizations of the ME composite and coil but with different sizes of the air region box and the infinite box. They will be referred to as FEM 1 and FEM 2 respectively. The meshes of FEM1 and FEM2 were produced with the software Gmsh [161]. The ME composite is centered at (0,0,0), whereas the coil is centered around the point (30, 10, 0) mm and is of length of 3 mm with an inner radius of 15 mm and an outer radius of 18 mm.

For FEM1, the air region has a radius of 316 mm and the infinite box, a radius of 474 mm. For FEM2, the air region has a radius 443 mm whereas the infinite box has a radius 664 mm. The increased size of the air and infinite box of FEM2 with respect to FEM1 should result in better accuracy of the solution. A cut of the full mesh of FEM2 is presented in Figure 4.17.

The discretized system associated to the weak forms of the ME problem is presented in (4.2), it was discretized using 1-st order nodal elements. The same notations that in (3.99) are used for the FEM matrices, except for the matrix $\underline{\boldsymbol{K}'}_{\phi\phi}$ and the second hand term $\underline{\boldsymbol{Sh}'}_{mag}$, which are now integrated over the entire domain Ω. All material parameters were taken from [127]. The linear system of equations (4.2) was preconditioned using an LU decomposition and solved using MUMPS direct solver. The source field is computed by the FEM as presented in Section 2.5.1.

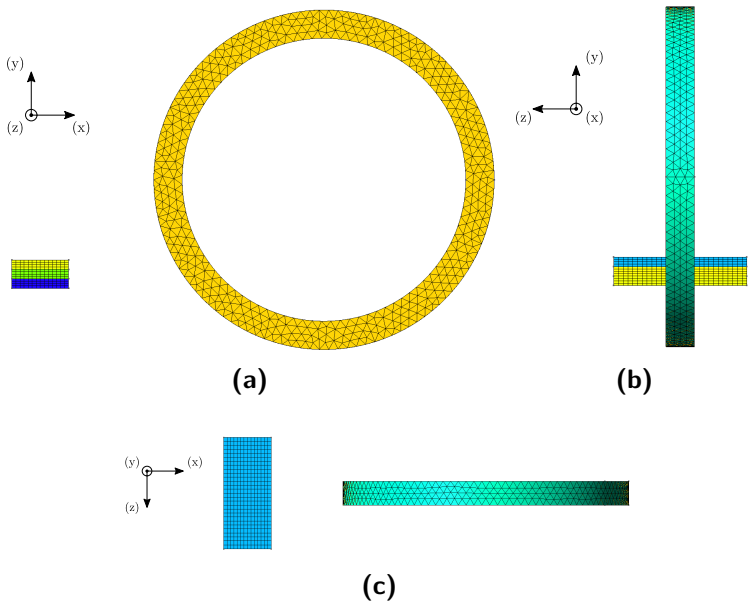

Figure 4.16: Mesh of the ME composite and the coil, seen from the three axes

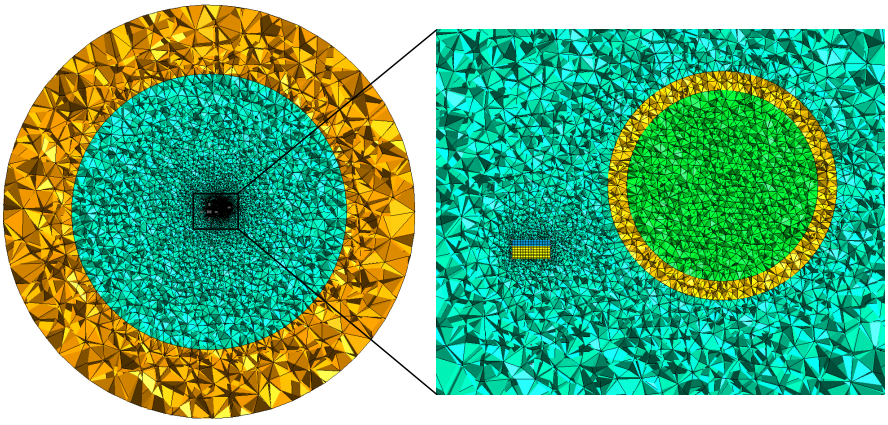

Figure 4.17: Mesh of the ME composite and the coil for the FEM 1 case.

$$\begin{bmatrix} \underline{\boldsymbol{K}'_{\phi\phi}} & \underline{\boldsymbol{K}}_{\phi u} & \underline{\mathbf{0}} \\ \underline{\boldsymbol{K}}_{u\phi} & \underline{\boldsymbol{K}}_{uu} & \underline{\boldsymbol{K}}_{u\varphi} \\ \underline{\mathbf{0}} & \underline{\boldsymbol{K}}_{\varphi u} & \underline{\boldsymbol{K}}_{\varphi\varphi} \end{bmatrix} \begin{pmatrix} \underline{\boldsymbol{\phi}}_{red} \\ \underline{\boldsymbol{u}} \\ \underline{\boldsymbol{\varphi}} \end{pmatrix} = \begin{pmatrix} \underline{\boldsymbol{Sh}'}_{mag} \\ \underline{\boldsymbol{Sh}}_{meca} \\ \underline{\boldsymbol{Sh}}_{elec} \end{pmatrix} \tag{4.2}$$

For the first case (FEM 1), the ME problem consists of a mesh containing 83,921 nodes and 514,887 elements. For the computation of the source field, the matrix system to be solved involved 664,821 DoFs while the ME problem involved 103,190 DoFs. This difference in the number of DoFs between the ME problem and the computation of the source field comes mainly from the formulation for computing the source field which relying on edge elements, and the much higher number of edges than nodes in a given mesh [174].

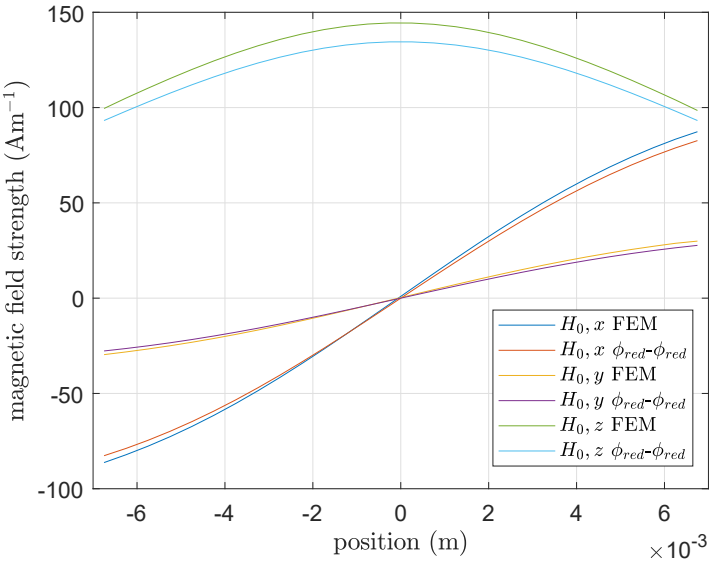

Figure 4.18: Comparison between the source fields $\boldsymbol{H_0}$ between the FEM 1 and FEM-BEM ϕ_{red}-ϕ_{red} approaches along the (z) component of the position inside the ME composite at its center.

The comparison between the resolution times of the FEM-BEM ϕ_{red}-ϕ_{red} formulation and the two considered FEM formulations, including the assembly, is presented in Table 4.5. We see that there is a major difference in the number of DoFs and in the total computing time of the multi-physics solution between the FEM-BEM ϕ_{red}-ϕ_{red} approach and between both FEM simulations. The difference in the computation method of the source field contributes to the large difference in the total computing time due to the large number of DoFs of the magnetostatic resolution leading to the source

field.

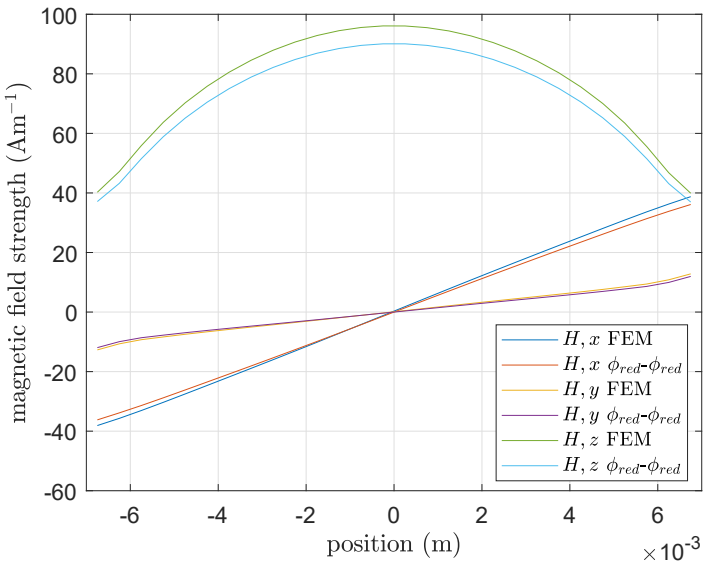

Figure 4.19: Comparison between the resulting magnetic field $\boldsymbol{H}$ between the FEM 1 and FEM-BEM ϕ_{red}-ϕ_{red} approaches along the (z) component of the position inside the ME composite at its center.

In the FEM approach, the source field is computed and stored in the edges of the entire meshed domain Ω, contrary to the FEM-BEM approach, in which it is only computed at the edges of the meshed domain Ω_m [150]. Therefore, the storage space of the source field is considerably lower for the FEM-BEM ϕ_{red}-ϕ_{red} than for the FEM approach: The FEM-BEM ϕ_{red}-ϕ_{red} approach allocated a maximum of 3.1 GB of RAM vs 35.8 GB for FEM 1. Also, HCA compression applied to the BEM matrices allowed for a compression ratio of 30 % on each BEM matrix.

In Figures 4.18-4.20, the results of FEM1 are compared to the results of the FEM-BEM ϕ_{red}-ϕ_{red} formulation. In Figure 4.18 are presented the plots of the source field along the length of the laminate structure at its center, in Figure 4.19 the plots of the magnetic field and in Figure 4.20 the plots of the displacements. While being very similar, we observe minor differences in the computed source field, for example, a maximum difference of its (z) component of 7.3 % at the center of the ME composite. Similar maximum relative differences are found in the other presented quantities. The output voltage of the device is of 43.78 mV for the FEM-BEM ϕ_{red}-ϕ_{red} approach, vs 46.26 mV for the FEM approach, amounting to a difference of 5.8 %

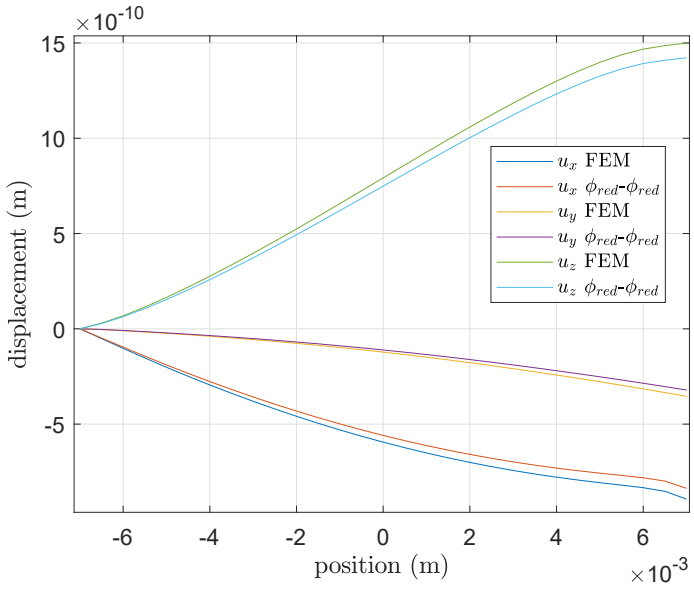

Figure 4.20: Comparison between the resulting displacements between the FEM 1 and FEM-BEM ϕ_{red}-ϕ_{red} approaches along the (z) component of the position inside the ME composite at its center.

between the two approaches. Some of these results are summarized in Table 4.6.

We see that the FEM approach tends to overestimate the computed source field with respect to the FEM-BEM ϕ_{red}-ϕ_{red} approach, and therefore, we observe this trend over all the computed fields. For the FEM-BEM ϕ_{red}-ϕ_{red} approach, the block Gauss-Seidel resolution algorithm converged in 14 iteration to a tolerance of 10^{-10} amounting to a total resolution time of 5.7 s. Concerning FEM2, in Table 4.6 we observe that its solution better agrees with the FEM-BEM solution. Nevertheless, the computational cost of the complete problem, including the computation of the source field, is considerably higher: 24.7 % more DoFs of the ME problem and 30 % more DoFs for the computation of the source field, resulting in 2.5 times the computing time of FEM 1.

In this section, we see the clear advantages of the proposed approach vs a pure FEM implementation in terms of computational cost. The smaller difference on the solutions between FEM2 and the FEM-BEM ϕ_{red}-ϕ_{red} than between FEM1 and the FEM-BEM ϕ_{red}-ϕ_{red} approach, suggest that further refining the mesh and increasing the size of the air region we would obtain even closer solutions. Furthermore, if the field source is positioned at a greater distance than in the current simulation, an even larger air region

Table 4.5: Comparison between DoFs used for the computation of the source field, DoFs of the ME problem (having computed the source field) and total resolution time, including the computation of the source field, between the two FEM simulations and the proposed FEM-BEM ϕ_{red}-ϕ_{red} approach using the ordered G-S solver.

Approach	FEM-BEM ϕ_{red}-ϕ_{red}	FEM 1	FEM 2
# nodes	5278	83,921	108,927
# DoFs for computing $\boldsymbol{H_0}$	-	664,821	869,672
# DoFs of ME problem	28,613	103,190	128,683
total computing time	3 min 32 s	21 h 17 min 47 s	52 h 30 min 45 s
maximum allocated memory	3.1 GB	35.8 GB	43.8 GB

Table 4.6: Comparison between the maximum relative difference of the source field along the (z) direction $\delta_r(\boldsymbol{H_0}, z)$, magnetic field along the (z) direction $\delta_r(\boldsymbol{H}, z)$ and the relative difference between the output voltage of the ME composite between the FEM approach and the proposed FEM-BEM ϕ_{red}-ϕ_{red} approach $\delta_r(v)$.

Approach	$\delta_r(\boldsymbol{H_0}, z)$	$\delta_r(\boldsymbol{H}, z)$	$\delta_r(v)$
FEM 1	7.3 %	6.7 %	5.8 %
FEM 2	6.9 %	6.2 %	5.2 %

would have to be considered and meshed, adding more DoFs to the already large FEM systems. This is not the case for both FEM-BEM approaches, in which the computational cost of evaluating the source field is independent of the distance between the field source and the device.

A notable difference between the ϕ_{red}-ϕ_{red} formulation and the scalar FEM formulation is also present in the amplitude of the edge effects, which are a lot more important in the FEM simulations than in the FEM-BEM ϕ_{red}-ϕ_{red} approach: the FEM 1 solution gave a field with a norm of 317.9 $\mathrm{A\,m^{-1}}$ at the center of the element containing the edge closer to the coil vs 135.1 at the same point for the FEM-BEM ϕ_{red}-ϕ_{red} approach, while being very similar elsewhere.

4.2.5 Formulation with invariant approach to magneto-mechanical behavior

The same three-layer ME composite can be modeled with magnetic and mechanical constitutive laws (3.68) and (3.69) deriving from the invariant approach to magneto-mechanical coupling, with Galfenol as the magne-

tostrictive material and PZT-5A with coefficients from [127]. A series of simulations of the three-layer ME composite under the effect of magnetic source fields in the (z) direction were conducted. As shown in Figure 4.21, the output voltage saturates as the source field increases. The ME coefficient of the ME composite, given by the output voltage divided by the amplitude of the source field, is presented in Figure 4.22, we observe that it has a maxima at $H_0 = 70.77\ \mathrm{A\,m^{-1}}$.

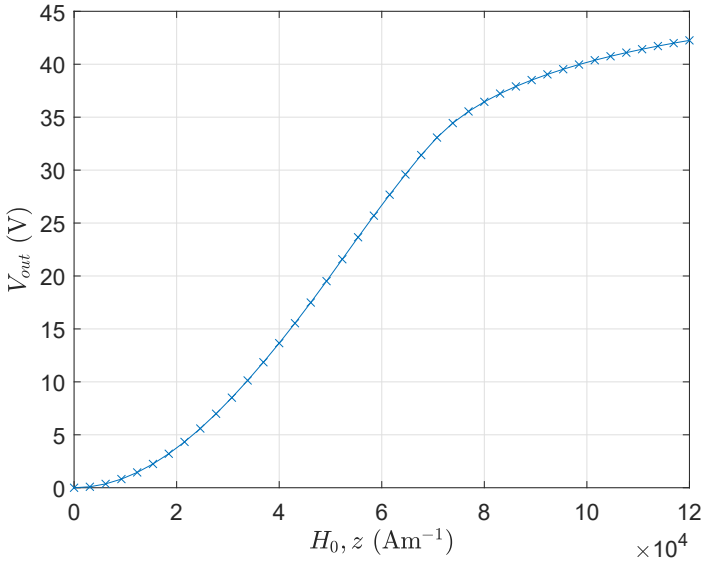

Figure 4.21: Output voltage of the three-layer ME composite with the invariants approach to magneto-mechanical coupled behavior

To solve for the multi-physics problem, the three physics were solved iteratively in a predefined order until all solution converged to the desired tolerance, here set at 10^{-5}. First the magnetic problem was solved, then the mechanical problem, and the electric problem at last. The convergence of the single-physics solutions, for a source field of $104.62\ \mathrm{kA\,m^{-1}}$ is presented in Figure 4.23. The multiphysics problem was solved in 10 iterations of the ordered Gauss-Seidel algorithm, this was the case for all resolutions, beside the resolution for $H_0 = 0$, which for obvious reasons converged in one iteration. This supports the hypothesis that the multiphysics convergence depends only on the properties of the global and coupling matrices.

Depending on the strength of the source field, which drives the problem, the single-physics resolutions of the nonlinear magnetic and mechanical problems by the Newton-Raphson method takes more or less iterations to

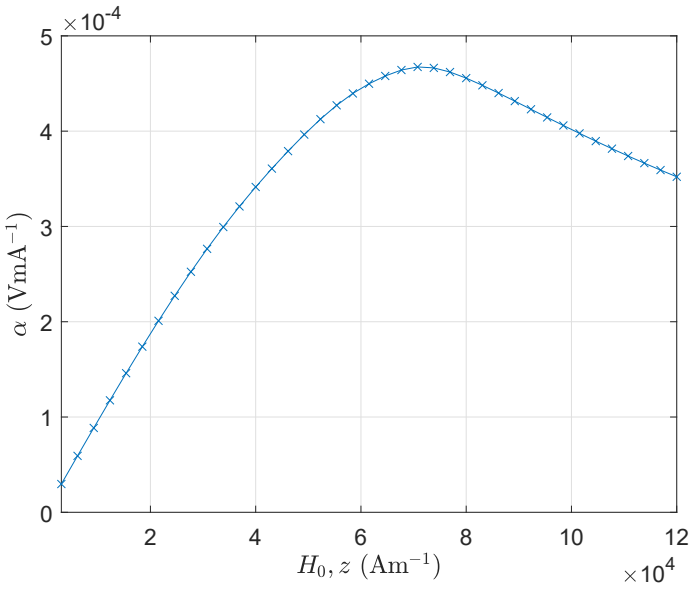

Figure 4.22: Output voltage of the three-layer ME composite with the invariants approach to magneto-mechanical coupled behavior

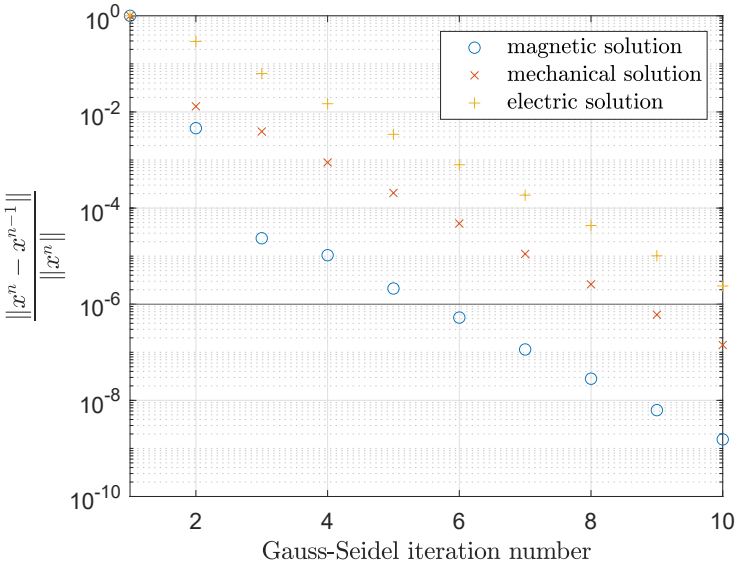

Figure 4.23: Convergence of the single-physics solutions within the multi-physics solver for the three-layer ME composite with the nonlinear magnetostriction model at $\boldsymbol{H_0}, z = 104.62$ kA m^{-1}

reach the wanted tolerance of 10^{-6}. For very low excitations, the Newton-Raphson solvers converge in one iteration. For higher fields, higher number of

iterations are required to reach the tolerance. For example, for a source field of 104.62 kA m^{-1}, the magnetic problem was solved in 7 Newton-Raphson iterations, while the mechanical problem in 4 iterations.

4.3 Rotating coilless ME device

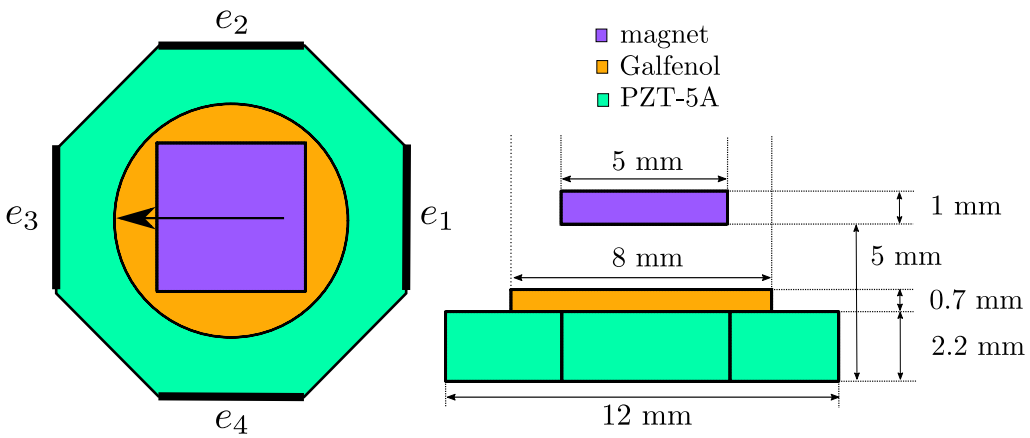

Figure 4.24: Geometry of the rotation coilless ME composite. The arrow in the magnet region denotes the magnetization direction in the magnet. The black bold lines represent the electrodes used to excite the piezoelectric material, e_1, e_2, e_3 and e_4.

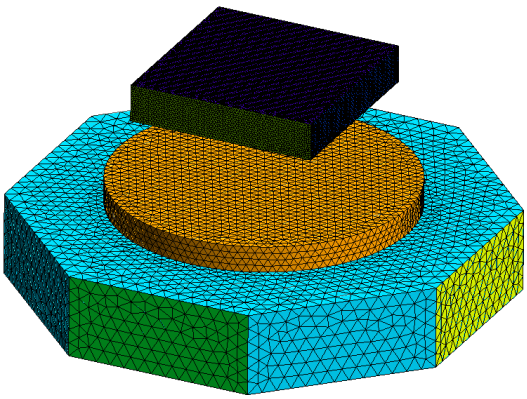

Figure 4.25: Discretization of the device of Figure 4.24. This mesh contains 28,479 nodes and 91,630 elements

The magnetization behavior described in Section 3.3.2 can be exploited in an ME composite in order to recover an electric voltage generated by a rotating magnetic source field or to generate a mechanical torque. In order to achieve

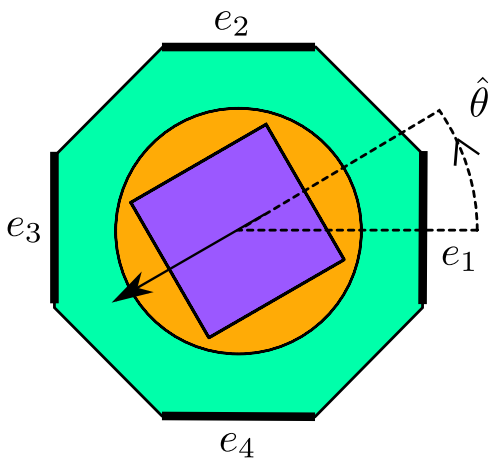

Figure 4.26: Geometry of the rotating coilless ME composite. The arrow in the magnet region denotes the magnetization direction in the magnet, and $\hat{\theta}$, the angle between the magnet and the device

this response, we exploit the appearance of an easy axis in an isotropic soft magnetic material subjected to a uni-axial mechanical stress. Depending on how this easy magnetization direction is generated in the ferromagnetic layer, two modes of operation of the ME structure are possible: in generator mode, the directional magnetic anisotropy is induced by a rotating magnetic source field, in actuator mode, the mechanical stress controls the directional magnetic anisotropy.

To illustrate this phenomenon, we consider the structure presented in Figure 4.24 which constitutes a rotating coilless ME device. The device consists of one layer of piezoelectric material excited by four electrodes and a disk-shaped magnetostrictive phase under the effect of a permanent magnet.

In the following simulations, the magnetostrictive layer is considered to be made of Galfenol, and the piezoelectric layer made of PZT-5A. The two layer are assumed to be perfectly bonded to each other. The magnet is supposed to be a NdFeB magnet with a remanent field of 1.13 T. This topology is close to the energy harvester used in [175] used to produce an alternating electric voltage and the rotating coilless actuator of [176].

In the following simulations, due to the lack of data on the magnetic characteristics of the considered piezoelectric material, PZT-5A, it will be considered as having the permeability of vacuum, its mechanical, dielectric and piezoelectric coefficient are taken from [177].

4.3.1 Generator mode

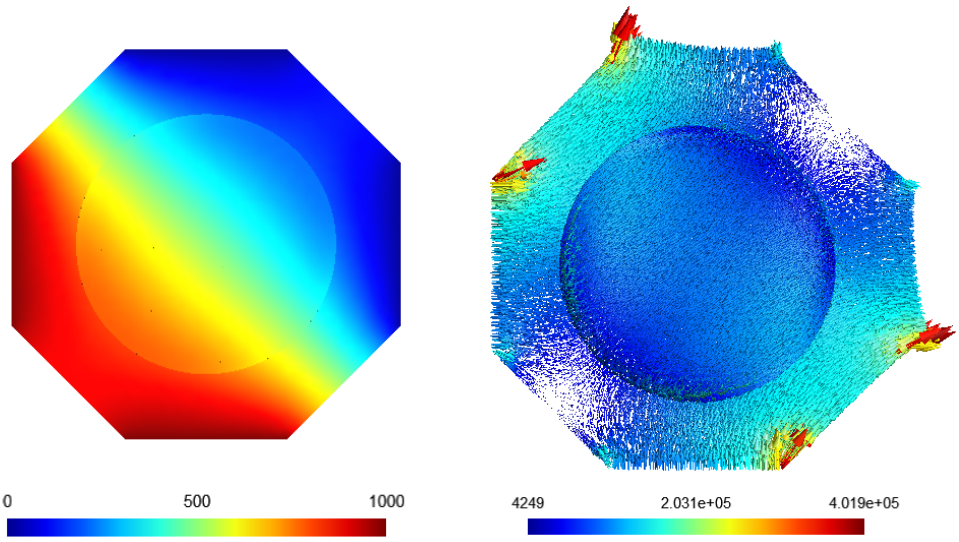

(a) Electric potential used for the poling of the piezoelectric phase (V)

(b) Electric field resulting from the electrostatic resolution ($\mathrm{V\,m^{-1}}$)

Figure 4.27: Poling pattern employed, coupling tensors $\boldsymbol{c}^{\boldsymbol{E}}$, $\boldsymbol{\varepsilon}^{\boldsymbol{S}}$ and $\boldsymbol{e}$ were rotated in the direction of the resulting electric field in order to take into account of the non-trivial poling pattern

In generator mode, it is the rotation of the magnet that controls the direction of magnetization in the magnetostrictive material and thus, the deformations of the magnetostrictive and piezoelectric layers. The rotation of the magnet leads to the appearance of a potential difference between the electrodes, which is dependent on the angle of rotation $\hat{\theta}$ defined in Figure 4.26.

The poling pattern of the piezoelectric phase is considered fixed, and the piezoelectric material considered poled by the application of electric potentials to a specific configuration of the electrodes: 1 kV on e_3 and e_4 and 0 V on e_2 and e_1. This results in a poling of the piezoelectric phase mainly along the $\hat{\theta} = \pi/4$ direction. Once poled, the potentials of e_1 and e_2 are set to 0 V while e_3 and e_4 have a floating potential condition.

The discretization of the device is shown in Figure 4.25 and consists of a mesh containing 28,479 nodes and 91,630 elements. In generator mode, this translates into 79,573 magnetic DoFs, 34,443 mechanical DoFs and 11,011 electrical DoFs. Matrix compression techniques are used, FMM compression allowed to reduce the size of each BEM matrix of 80 %.

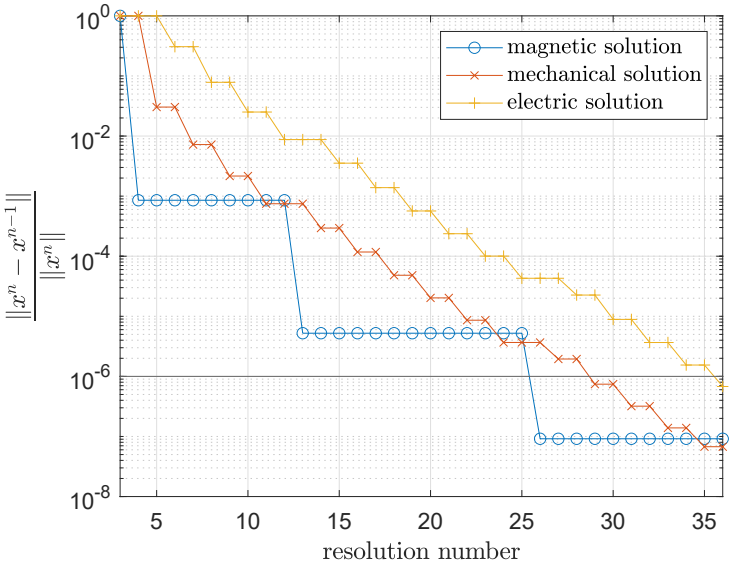

Figure 4.28: Convergence of the single-physics solutions within the multi-physics solver for the ME generator at $\hat{\theta} = 0$ rad

From a numerical point of view, the poling pattern is obtained by an electrostatic FEM resolution in the active domain Ω_m, considering the permittivity of the unpoled material, with the electrodes as Dirichlet boundary conditions and null Neumann boundary conditions elsewhere. The angle and orientation of the resulting electric field is used to locally rotate the constitutive laws of the piezoelectric material. More details on the rotation of tensors are given in Appendix C. This device is modeled with the three-physics formulation described in Section 3.5.2 with the invariant description of magneto-mechanical coupling, and the piezoelectric material poled in the direction of the electric field of Figure 4.27b.

For mechanics, in order to study the unconstrained response of the device, no Dirichlet boundary conditions are imposed, and the system solved iteratively with a BICGStab solver. To solve the multi-physics problem, the adaptive iterative solver of Algorithm 3 is used. The permanent magnet was modeled in an Amperian description: instead of considering a volume domain with a remanent magnetization $\boldsymbol{M_r}$, a surface domain undergoing surface currents produce a field equivalent to the one created by a magnetized volume domain, this surface current is given by [24],

$$\boldsymbol{J^S} = \boldsymbol{M_r} \times \boldsymbol{n} = \frac{1}{\mu_0}(\boldsymbol{B_r} \times \boldsymbol{n}), \tag{4.3}$$

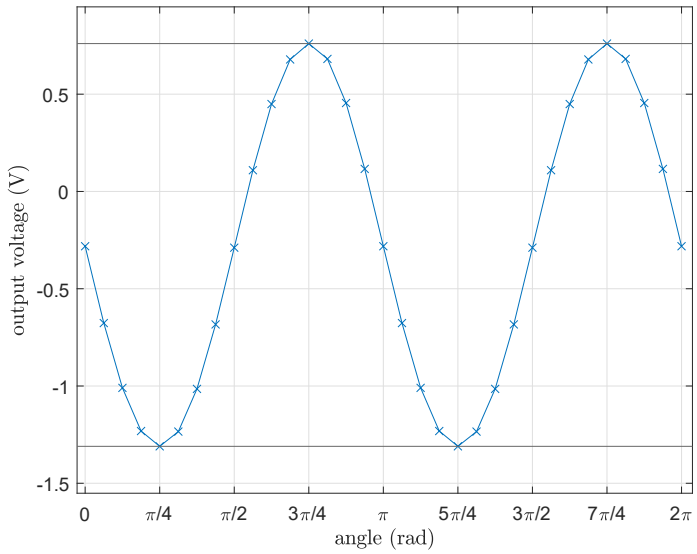

Figure 4.29: Potential difference between the reference electrodes, e_1 and e_2, and the floating potential electrodes, e_3 and e_4, vs the angle $\hat{\theta}$ between the magnet and the structure

where $\boldsymbol{B_r}$ refers to the remanent magnetic flux density in the permanent magnet, considered uniform and $\boldsymbol{n}$ the vector normal to the surface of the magnet. The source field in the ME composite is then computed by the Biot-Savart law.

We observed a very nonlinear mechanical response. For every resolution of the mechanical problem, it takes 21 iterations of the mechanical Newton-Raphson for the residue to converge under the set tolerance of relative 10^{-7}. The magnetic Newton-Raphson converges in 2 iterations to the same tolerance. To illustrate the behavior of the solver for the simulations in generator mode, for $\hat{\theta} = 0$ rad, but with very small variations between the magnet positions, the magnetic problem is solved 4 times while the mechanical and electric problems are solved 16 times to obtain a tolerance of the multi-physics solutions lower to 10^{-6}. The total integration time of BEM and linear matrices was of 36 s and the resolution time of each simulation of ME device took around 2 h on a computer equipped with Intel© Xeon© Gold 6240R CPU @ 2.4 GHz, 256 Gb of RAM.

The rotation of the magnet on a complete turn was discretized into 32 angles. From the multi-physics resolution of the full coupled problem considering the poling pattern of Figure 4.27b, the output voltage plotted as a function of the angle between the magnet and the ME composite. In Figure 4.29 is presented the output voltage of the ME composite vs the angle $\hat{\theta}$ between

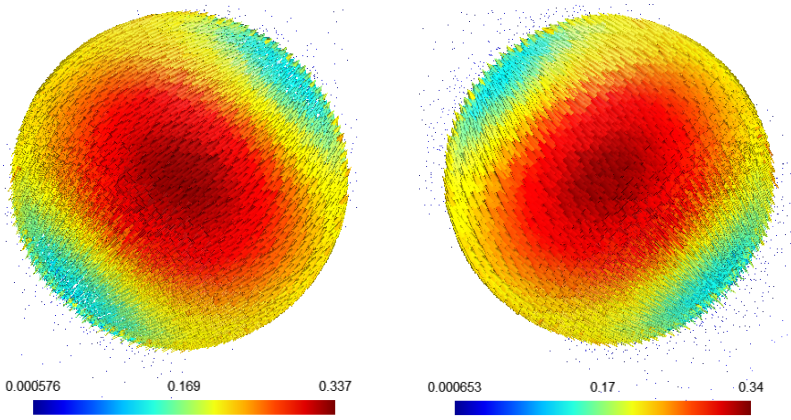

(a) $\hat{\theta} = \pi/4$ rad **(b)** $\hat{\theta} = 3\pi/4$ rad

(c) $\hat{\theta} = 5\pi/4$ rad **(d)** $\hat{\theta} = 7\pi/4$ rad

Figure 4.30: Magnetic flux density (T) in the ME composite for angles $\hat{\theta} = \pi/4, 3\pi/4, 5\pi/4$ & $7\pi/4$ rad, top view

the magnet and the structure. We observe a sinusoidal output voltage with two periods per rotation of the magnet. This is because the magnetostrictive strains depend only on the direction of the applied field and not on its sense.

In Figures 4.30b-4.30d are presented the magnetic flux density in the Galfenol layer for $\hat{\theta} \in \{\pi/4, 3\pi/4, 5\pi/4 \ \& \ 7\pi/4\}$. We observe that the magnetic flux density follows the direction of the rotation of the magnet, with small differences in the amplitude of the fields. These differences are the result of the magneto-mechanical coupled response of Galfenol and anisotropic mechanical properties of poled PZT-5A [177].

In Figures 4.31a-4.31d are shown the amplified displacements ($\times 10^5$) of the

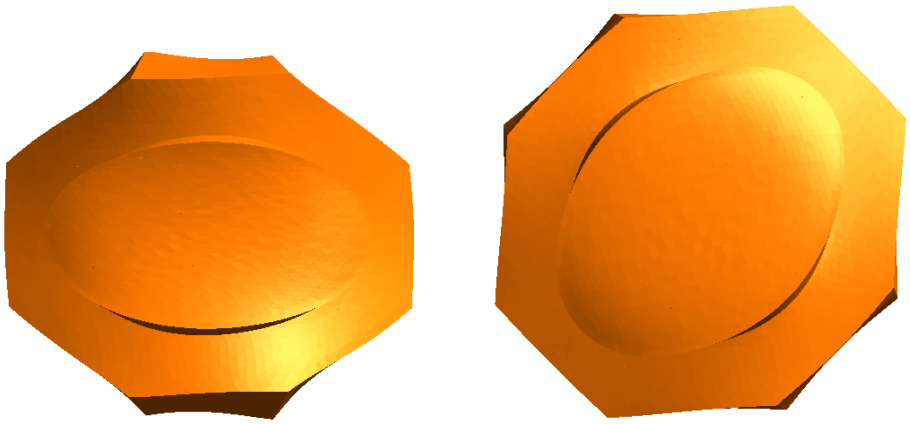

(a) $\hat{\theta} = 0$ rad

(b) $\hat{\theta} = \pi/4$ rad

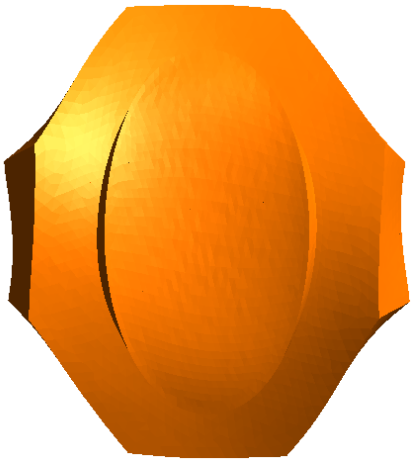

(c) $\hat{\theta} = \pi/2$ rad

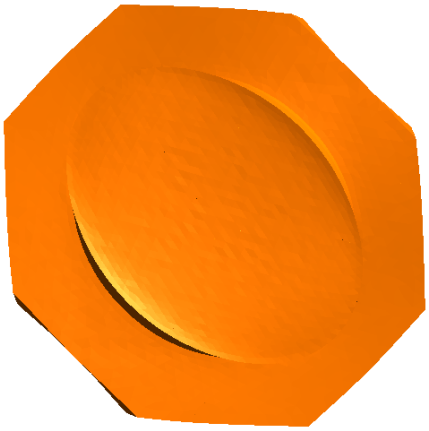

(d) $\hat{\theta} = 3\pi/4$ rad

Figure 4.31: Amplified displacements ($\times 10^5$) of the ME composite for angles $\hat{\theta} = 0, \pi/4, \pi/2$ & $3\pi/4$ rad, top view

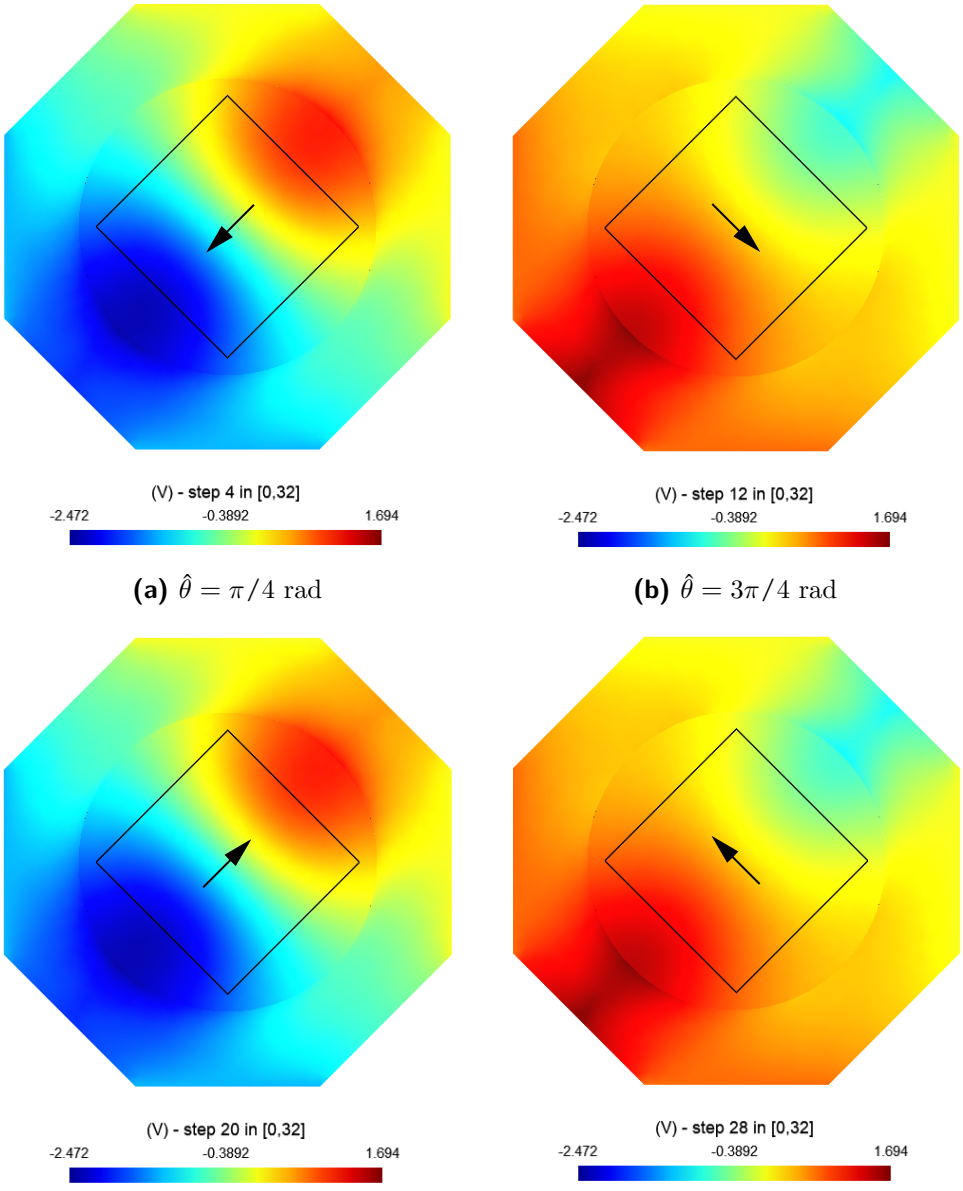

(a) $\hat{\theta} = \pi/4$ rad **(b)** $\hat{\theta} = 3\pi/4$ rad

(c) $\hat{\theta} = 5\pi/4$ rad **(d)** $\hat{\theta} = 7\pi/4$ rad

Figure 4.32: Electric potential (V) in the ME composite for angles $\hat{\theta} = \pi/4, 3\pi/4, 5\pi/4$ & $7\pi/4$ rad, top view

device, they illustrate its mechanical response to the magnetic excitation. In them, we see the that the deformation of the device occurs mainly along the angle $\hat{\theta}$ even if some slight anisotropies in the mechanical response are visible for $\hat{\theta} = 0$ & $\pi/2$ rad. These anisotropies in the mechanical response can be explained by the anisotropic mechanical properties of poled PZT-5A.

Figures 4.32a-4.32d show the output voltages obtained for $\hat{\theta} \in \{\pi/4, 3\pi/4, 5\pi/4$ & $7\pi/4\}$ rad. We observe that the same voltage distributions are obtained for opposite directions of the magnet, this is a consequence of the magnetostrictive strains developed in the Galfenol phase depending only on the direction of the applied field. We also see that the peak voltage, -1.31 volts occurs when the elongation of the piezoelectric phase is in the direction of the poling pattern, $\hat{\theta} \in \{\pi/4, 5\pi/4\}$ rad, whereas the peak positive voltage occurs when the excitation is perpendicular to the main direction of the poling pattern, $\hat{\theta} \in \{3\pi/4, 7\pi/4\}$ rad.

4.3.2 Actuator mode

In actuator mode, it is the stress field developed in the magnetostrictive layer which controls the directional magnetic anisotropy. For the rotating coilless ME device, the piezoelectric layer generates this stress. By applying a positive electric voltage V_{in} between the reference electrodes e_1-e_2 and electrodes e_3-e_4, the piezoelectric layer mainly produces tension in the Galfenol layer, thus changing its magnetic properties. This induces a change in the direction of magnetization. The effect of the magnetic interaction between the Galfenol layer and the magnet will be opposing mechanical forces and torques which depend on the angle between the magnet and the ME composite, as defined in Figure 4.26, and the exciting voltage V_{in}.

The same geometry and mesh as in generator mode were considered, only the number of electric DoFs decreased by 1 DoFs as a region with a fixed voltage was added. The same matrix compression techniques are used, as well as the same poling pattern of the piezoelectric region was considered. This poling pattern contributes to an anisotropic mechanical load of the piezoelectric material onto the magnetostrictive phase in the direction of poling of the piezoelectric layer. Because the piezoelectric phase is treated as poled by the same exciting electrodes, this mechanical load is mainly tension in the bottom part of the Galfenol phase.

For $\hat{\theta} = 0$ and a voltage of 1 kV applied to the piezoelectric layer, the convergence of the multi-physics solutions to a tolerance of 10^{-6} took 32

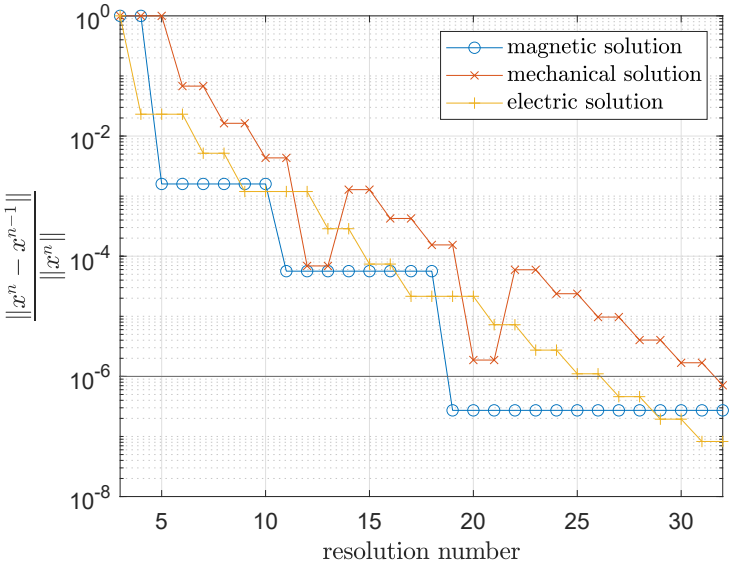

Figure 4.33: Convergence of the single-physics solutions within the multi-physics solver for the rotating coilless ME actuator at $\hat{\theta} = 0$ rad and 1 kV applied to the piezoelectric phase

resolutions, the magnetic problem was solved 4 times, the electrical problem 13 times and the mechanical problem 15 times. The convergence within the single-physics solutions took 22 iterations of the Newton-Raphson solver to a tolerance of 10^{-7} for the mechanical problem, whereas the Newton-Raphson of the magnetic problem took 2 iterations. The convergence of the single physics solutions for $\hat{\theta} = 0$ rad is presented in Figure 4.33. The total integration and resolution time for each simulation of the ME problem was similar to the simulations in generator mode, The total integration time of BEM and linear matrices was of 36 s, whereas the total resolution time was of around 2 h in a computer equipped with Intel©Xeon©Gold 6240R CPU @ 2.4 GHz, 256 Gb of RAM.

Some mechanical results for $\hat{\theta} = 0$ are presented in Figures 4.34a to 4.35d They are the result of the computation of the spectral components of the Cauchy stress tensor computed by element. The principal stress defined as the eigenvalue with the highest absolute value, and its direction given by its corresponding eigenvector, and so on for the second principal stress [178]. In figure 4.34a we observe that the principal stress is mainly in the direction of the poling of the piezoelectric phase. The reaction of the Galfenol disk to the traction in the bottom part of the disk is also observed, it produces stress on the top of the disk in the direction perpendicular to the traction.

In Figure 4.35a we observe that indeed, in the bottom part of the Galfenol

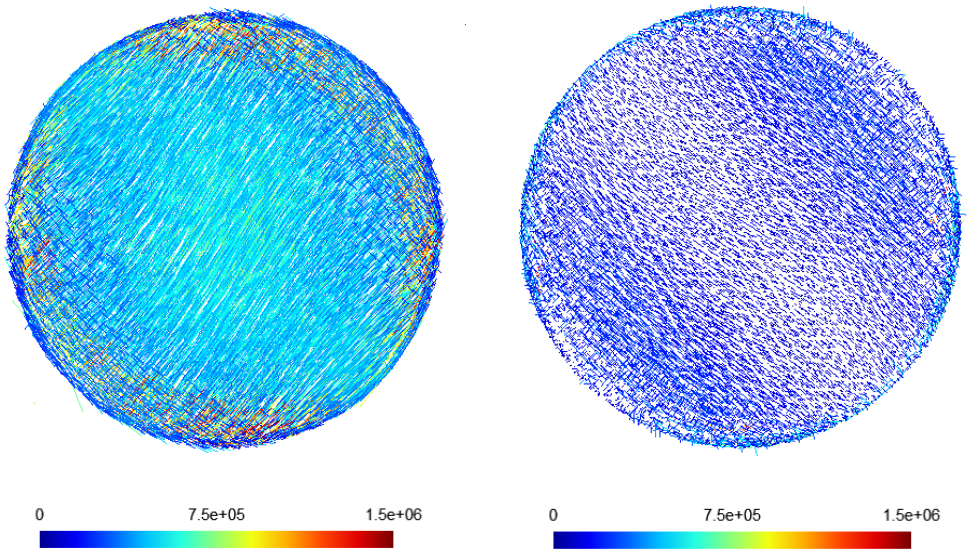

(a) direction of the principal stress in the Galfneol phase scaled by its absolute value (Pa), top view

(b) direction of the second principal stress in the Galfneol phase scaled by its absolute value (Pa), top view

Figure 4.34: Directions of first and second principal stress in the Galfenol layer for $V_{in} = 1$ kV and the considered poling pattern

disk, the principal stress is tensile stress. Figure 4.35c shows that the Galfenol disk undergoes tension at its center, even though compressive stress is observed at the edges of the top of the Galfenol disk. They correspond to the reaction of the disk to the tensile stress on the bottom. In Figures 4.35a to 4.35d it appears also that the principal stress is more important than the second principal stress, this anisotropy in the loading of the Galfenol is expected and will result in an anisotropy of the magnetic response of the device.

In Figures 4.36a and 4.36b we see the resulting magnetization in the Galfenol disk for $V_{in} = 0$ V and $V_{in} = 1.5$ kV respectively. In them, the effect of the magneto-mechanical coupling on the magnetization is not apparent at first sight. To better visualize the effect of the magneto-mechanical coupling, we can compute the difference between both magnetization states, i.e., the vector field $\boldsymbol{M}(1500 \text{ kV})$ - $\boldsymbol{M}(0 \text{ V})$. Figures 4.37a and 4.37b show the difference between both magnetization states in the bottom and top parts of the Galfenol disk. They show a complex rearranging of the magnetization, mostly a reorientation of the magnetization in the direction of the tensile stress. In Figure 4.37a, showing the bottom part of the Galfenol disk seen

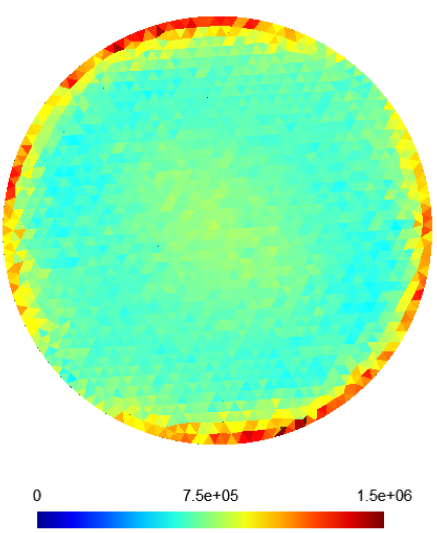

(a) principal stress in the Galfenol layer (Pa), bottom view

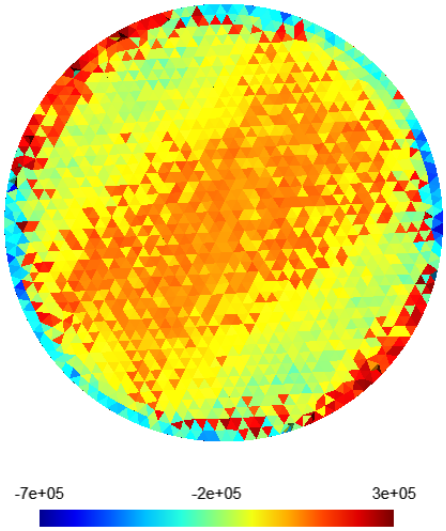

(b) second principal stress in the Galfenol layer (Pa), bottom view

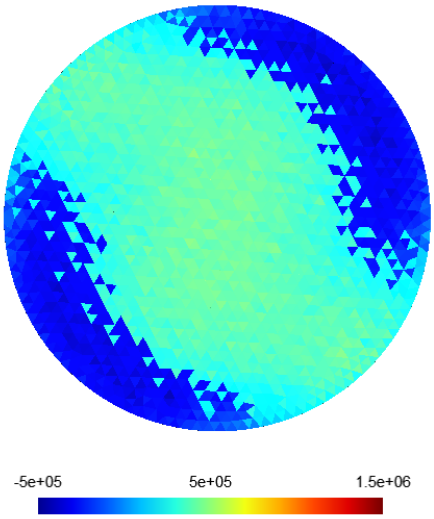

(c) principal stress in the Galfenol layer (Pa), top view

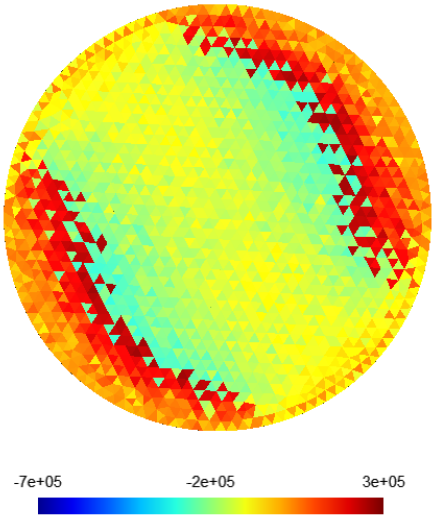

(d) second principal stress in the Galfenol layer (Pa), top view

Figure 4.35: Principal stress and second principal stress in the Galfenol layer for $\hat{\theta} = 0$ and $V_{in} = 1$ kV

from top, we mainly observe an increase in magnetization and a reorientation of the magnetization in the direction of the poling of the piezoelectric layer.

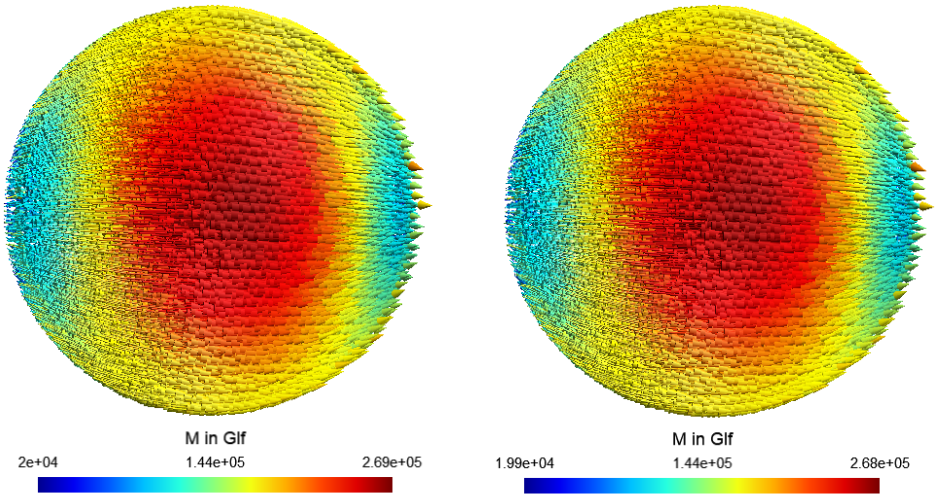

(a) magnetization ($\mathrm{A\,m^{-1}}$) for $V_{in} = 0$ V, top view

(b) magnetization ($\mathrm{A\,m^{-1}}$) for $V_{in} = 1.5$ kV, top view

Figure 4.36: Magnetization of the Galfenol for two states of electric excitation

In the top layer, shown in Figure 4.37b we observe the reorientation of the magnetization in the direction of the poling of the piezoelectric layer in the middle of the disk. However, in the edges of the top layer, the magnetization shifts away from the direction of polarization of the piezoelectric layer.

4.3.3 Easy magnetization direction

To study the anisotropy of magnetization in the Galfenol layer, a spectral study on the magnetic susceptibility χ_m, defined as,

$$\boldsymbol{M} = \boldsymbol{\chi_m} \cdot \boldsymbol{H} \tag{4.4}$$

can be conducted. The direction of the eigenvector corresponding to the highest eigenvalue of $\boldsymbol{\chi_m}$ corresponds to the favored direction of magnetization. The difference between the eigenvalues quantifies the magnetic anisotropy of the material. [179] [180] [181]. After having solved the multi-physics problem, the magnetic susceptibility can be reconstructed as:

$$\boldsymbol{\chi_m} = \nu_0 \, \boldsymbol{\nu}^{-1} - \boldsymbol{I_3} \tag{4.5}$$

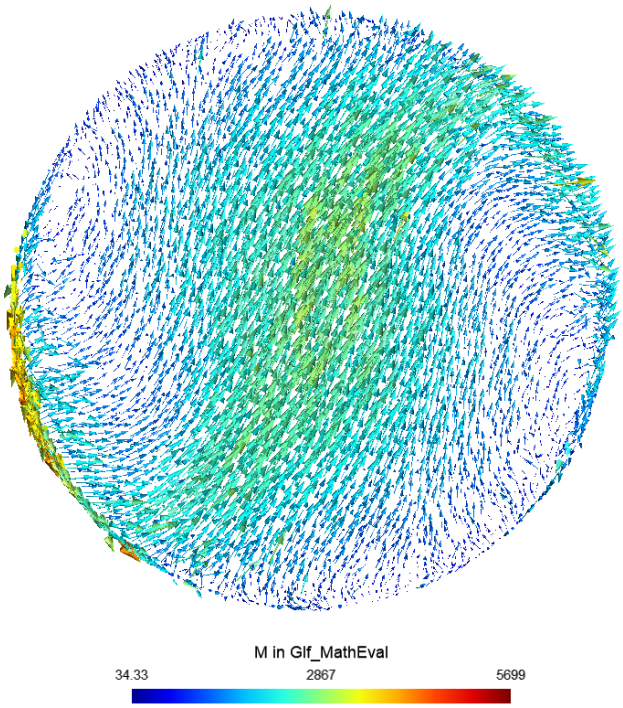

(a) M(1.5 kV) - M(0 V) $(\mathrm{A/m})$ on the bottom part of the Galfenol disk, top view

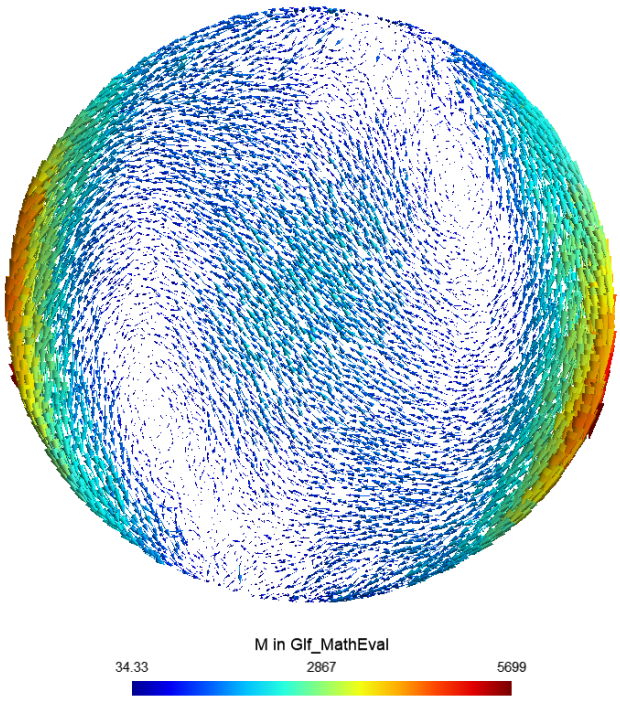

(b) on the top part of the Galfenol disk, top view

Figure 4.37: $\boldsymbol{M}$(1500 kV) - $\boldsymbol{M}$(0 V), top view

$\boldsymbol{\chi_m}$ Can be reconstructed in every cell of the volume mesh by averaging $\boldsymbol{B}$ per element and reconstructing $\boldsymbol{\nu}(\boldsymbol{B})$ from its analytical expression. The inverse of $\boldsymbol{\nu}$ is trivial, as it is a 3×3 matrix, and so is the spectral decomposition of $\boldsymbol{\chi_m}$. We conducted this study for $\hat{\theta} = 0$ and observed, as shown in Figures 4.38a-4.38d an anisotropy in $\boldsymbol{\chi_m}$.

In Figures 4.38a to 4.38d we observe that there is a difference in the eigenvalues of $\boldsymbol{\chi_m}$ translating in a magnetic anisotropy of the Galfenol layer due to its coupled magneto-mechanical properties. We also observe that the main easy magnetization direction for $\hat{\theta} = 0$ is mostly in the direction of the mechanical tension, while the second magnetization direction is mainly perpendicular to the first magnetization direction. This magnetic anisotropy is analog to the anisotropy in the mechanical response of the Galfenol layer and coherent with the results from Section 3.3.2, in which tensile stress leads to greater magnetization for a given field $\boldsymbol{H}$. We will show that a mechanical force and torque between the two interacting magnetic elements, the magnet and the Galfenol disk, appears for certain angles $\hat{\theta}$.

4.3.4 Computation of the mechanical force and torque

The torque is computed by two methods: the magnetic charge method, which will be applied to compute the effect of the field generated by the permanent magnet onto the Galfenol layer, and the Laplace force, in which the effect of the field generated by the Galfenol layer onto the permanent magnet will be computed. They both require the computation of the magnetization as a post-processing of the magnetic solution.

4.3.4.1 Computation of mechanical torque by the magnetic charge method

The magnetic charge method [23] allows for the computation the magnetic force by calculating the divergence of $\boldsymbol{M}$ and calculating

$$\boldsymbol{df} = (\nabla \cdot \boldsymbol{M})\ \boldsymbol{H}_0, \tag{4.6}$$

then the global torque in respect to the center of the disk $\boldsymbol{O}$ can be computed as,

$$\Gamma = \int_{\Omega_{mm}} \boldsymbol{r} \times \boldsymbol{df}\ d\Omega_{mm}. \tag{4.7}$$

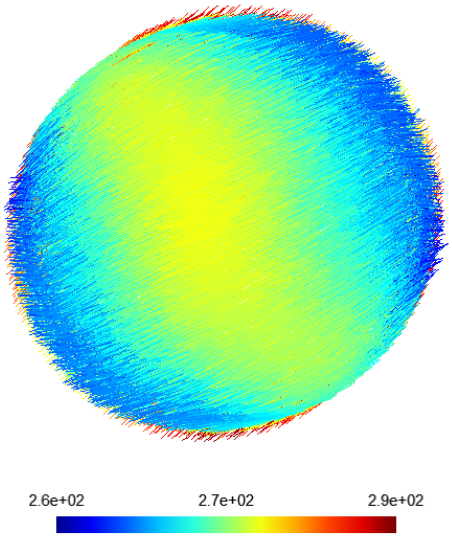

(a) direction of the prefered magnetization scaled by its absolute value, top view

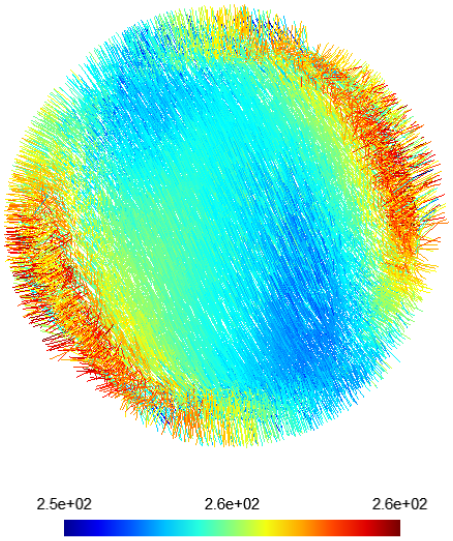

(b) second direction of the prefered magnetization scaled by its absolute value, top view

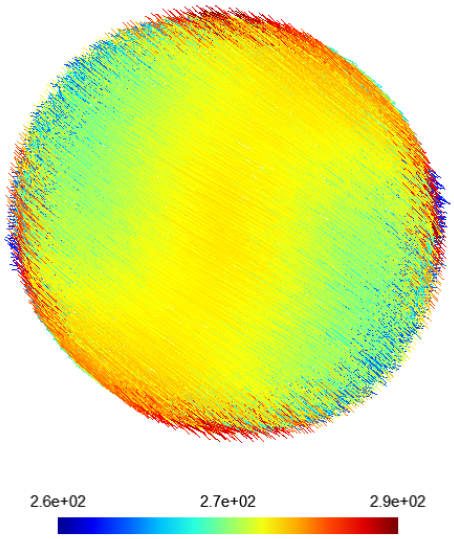

(c) direction of the prefered magnetization scaled by its absolute value, bottom view

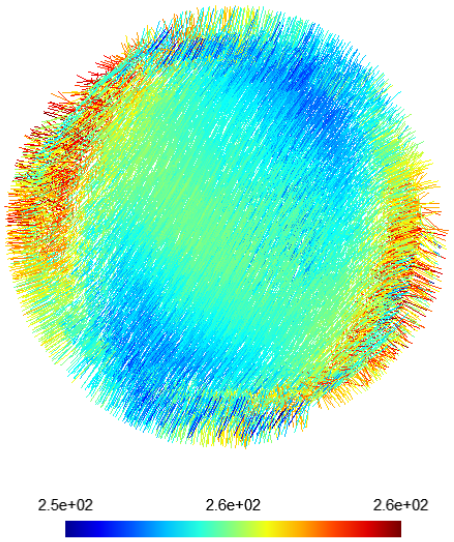

(d) second direction of the prefered magnetization scaled by its absolute value, bottom view

Figure 4.38: Results of the spectral study conducted on χ_m, reconstructed per element, in terms of its ranged eigenvalues and its corresponding eigenvectors. They are interpreted as the favored magnetization directions of the material

The divergence of $\boldsymbol{M}$ in (4.6) can be interpreted as a charge density and computed from the jump of magnetization between neighboring elements. In terms of implementation, in order to compute the local force, a loop between the facet elements of the Galfenol region of the mesh is performed, and the difference between the magnetization of the two elements sharing each facet, with the notations of figure 4.39, σ_m at a given facet element is calculated as follows,

$$\sigma_m = \boldsymbol{M_1} \cdot \boldsymbol{n_1} - \boldsymbol{M_2} \cdot \boldsymbol{n_2}, \tag{4.8}$$

where $\boldsymbol{M_1}$, $\boldsymbol{M_2}$ are the magnetization in the two neighboring elements, and $\boldsymbol{n_1}$ and $\boldsymbol{n_2}$ the outwards normal vectors to the elements at the facet. The source field, calculated at the Gauss point of each facet element, is then scaled by the equivalent charge, σ_m, in order to obtain the local force $\boldsymbol{df}$ in (4.6). The global torque can be then computed according to (4.7).

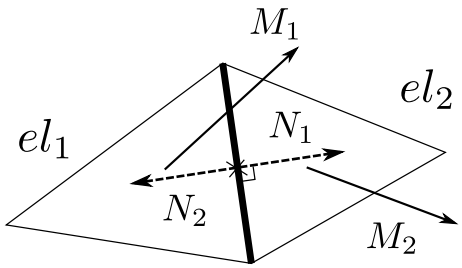

Figure 4.39: Schematics of the computation of magnetic charge density in the facet highlighted in bold, facet shared by two elements, el_1 and el_2

4.3.4.2 Computation of Laplace force and torque

The Laplace force also allows for calculating the magnetic force and torque. With this method, we will compute the effect of the field created by the magnetization in the Galfenol layer onto the magnet, which in its Amperian description, is equivalent to a coil undergoing surface currents. The mechanical torque can then be computed as the torque on the magnet produced by the field created by the magnetization of the Galfenol layer onto the surface currents, i.e., the torque of a Laplace force, generated by the local force,

$$\boldsymbol{df} = \boldsymbol{J^S} \times \mu_0 \boldsymbol{H_0}, \tag{4.9}$$

where $\boldsymbol{H_0}$ is the field generated by the magnetization of the Galfenol layer onto the surface of the magnet, given by,

$$\boldsymbol{H}_0 = \int_{\Omega_{mm}} \frac{1}{r^5} \left((\boldsymbol{M} \cdot \boldsymbol{r})\ \boldsymbol{r} - r^2 \boldsymbol{M} \right) d\Omega_{mm}, \tag{4.10}$$

and $\boldsymbol{J^S}$ given by (4.3). This method for calculating the torque in the magnet is very time-consuming compared to the magnetic charge method [1]. Indeed, it requires the integration over the volume of Galfenol of a complex expression of rational functions for every Gauss-Point of the surface elements of the permanent magnet region, it is however very accurate in the computation of magnetic interactions. Therefore, it was mainly used as a verification step of the magnetic charge method.

In Figure 4.40 we see that as predicted by Newton third law, the forces between the magnet and the Galfenol disk are opposite and equal in magnitude. Indeed, as the PZT region is treated as having the permeability of vacuum, it has null magnetization and no effect on the magnet. Both methods predict a force, mainly along the vertical direction: the (z) direction (there is a difference of 4 orders of magnitude between the force in the (z) direction and the other components). Both methods for calculating the magnetic force give very similar results: a relative difference in the (z) component of the force of $1.397 \cdot 10^{-4}$. Obtaining a force mainly in the (z) direction is an expected result, as the magnet and the Galfenol disk are magnetized in opposite directions. We also see very little variation in the global force as we increase the voltage applied to the piezoelectric layer: an increase of 0.36 % in the (z) component of the force in the Galfenol layer, and an increase of 0.25 % in the (z) component of the Laplace force.

In figure 4.41 is presented the mechanical torque as a function of the voltage applied to the piezoelectric layer for $\hat{\theta} = 0$. It shows that the computed torque in the magnet is mainly in the (z) direction. Figure 4.41 also shows that both methods of computation of the torque give very similar results. It also shows that, as expected, the higher the voltage, the higher the mechanical torque between the two interacting magnetic elements. The relation between the torque and the input voltage shows a very linear relation for the conditions of our simulations.

[1] the computation of the global torque takes an amount of time equivalent to the integration and resolution time of the ME problem

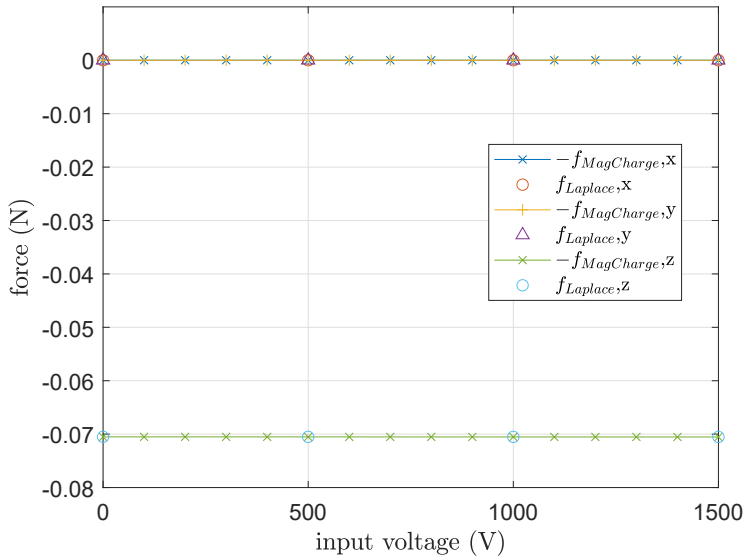

Figure 4.40: Components of the global force between the Galfenol disk and the magnet vs the voltage applied to the piezoelectric layer. The plot shows the components of the Laplace force and the opposite of the force computed by the magnetic charge method. They are very similar, which agrees with Newton's third law

4.3.5 Torque as a function of the angle between the device and the magnet

The magnetic force is also dependent on the angle between the magnet and the ME composite. To study this dependence, the rotation of the magnet on a complete turn was discretized into 32 angles, and the magnetic force computed with the two previous method for every position of the magnet and an input voltage $V_{in} = 1$ kV.

Using the same geometry and discretization as in the previous simulations and with little variations between the angles, the convergence of the multi-physics solutions to a tolerance of 10^{-6} took 32 iterations, the magnetic problem was solved 4 times, the electrical problem 13 times and the mechanical problem 15 times. The convergence within the single-physics solutions took 22 iterations of the Newton-Raphson solver to a tolerance of 10^{-7} for the mechanical problem, whereas the Newton-Raphson of the magnetic problem took 2 iterations. The convergence of the single physics solutions for $\hat{\theta} = 0$ rad is presented in Figure 4.42.

In figure 4.43 we see the mechanical torque as a function of the angle $\hat{\theta}$ as defined in Figure 4.26. In Figure 4.43, we see that for angles $\pi/4$, $3\pi/4$,

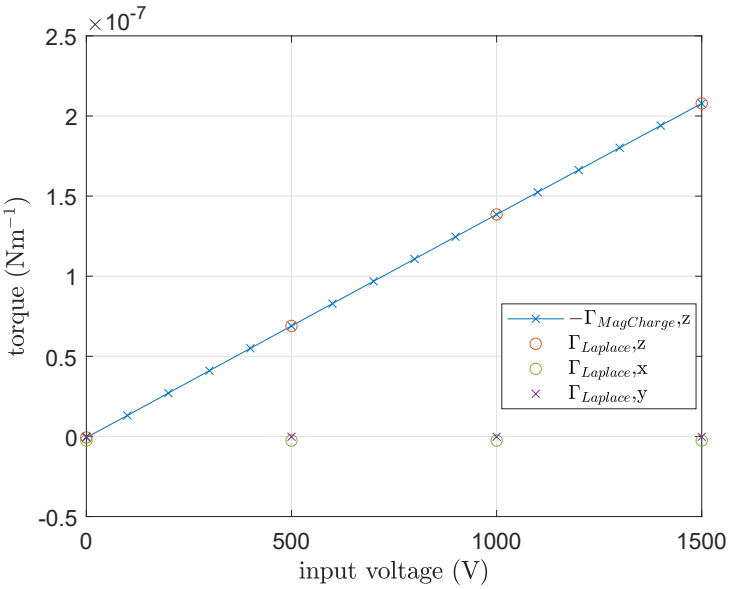

Figure 4.41: Global torque between the Galfenol disk and the magnet vs the voltage applied to the piezoelectric layer. It is computed as a Laplace force in the magnet, and, its (z) component is compared to the torque computed by the magnetic charge method in the Galfenol layer

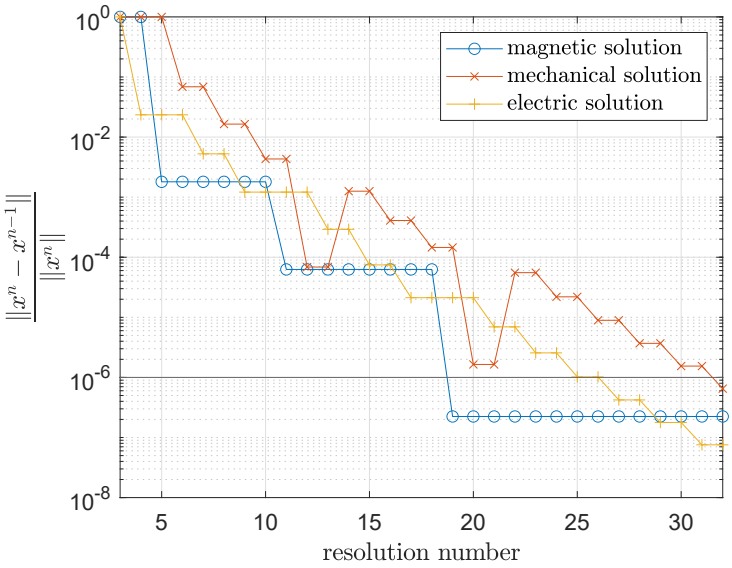

Figure 4.42: Convergence of the single-physics solutions within the multi-physics solver for the ME actuator at $\hat{\theta} = \pi/2$ rad

$5\pi/4$ and $7\pi/4$ rad, the torque is almost equal to zero, this comes from

the fact that at these directions, the mechanical anisotropy induced by the mechanical loading of the Galfenol phase are in the same direction as the magnetization, there is therefore no global shifting in the direction of magnetization in the Galfenol phase and therefore, the torque in the (z) direction is almost equal to zero. Conversely, angles, 0, $\pi/2$, π and $3\pi/2$ rad correspond to maxima of the torque. Given the poling pattern of the electrodes, which results in a poling and mechanical traction along the $\pi/4$ rad direction, the anisotropy of the magnetization in the Galfenol layer will be maximal for $\hat{\theta}$ equal to directions multiple of $\pi/2$ rad, i.e, $\pi/4$ rad relative to the $\pi/4$ rad main poling direction.

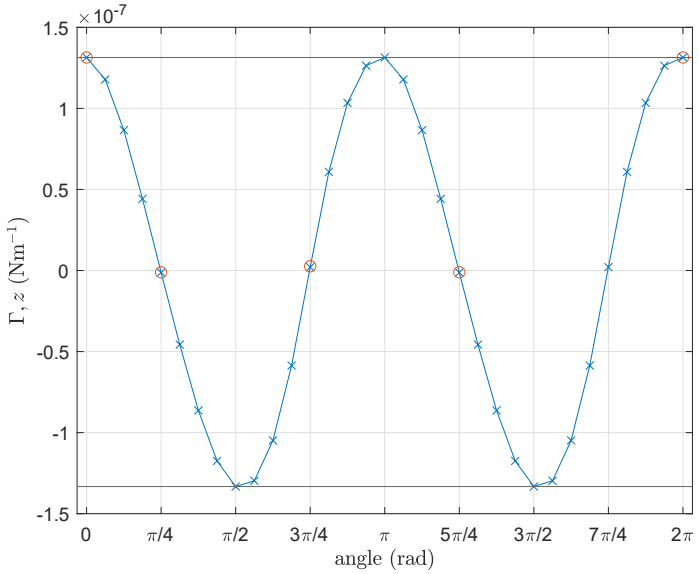

Figure 4.43: The blue markers show the (z) component of the torque in the magnet, $-\Gamma, z$, computed by the magnetic charge method in the Galfenol layer, and the red circles, the torque Γ_L in the magnet computed by the Laplace force, for 33 angles $\hat{\theta}$ describing the full rotation of the magnet.

In order for this device to function as a motor, the idea is to change the voltage applied to the electrodes in order both to pole the piezoelectric material and also excite it in its new poled state at the speed of the rotating magnet. If such a procedure can be achieved, a constant (or at least of same sign) mechanical torque can be obtained by creating rotating electric fields and therefore rotating stress & strains in the piezoelectric layer. This functioning is somewhat analog to the one of a variable reluctance motor in which the preferred path for the magnetic field is determined by the path of the magnetic circuit, for the bilayer structure, the preferred direction

for the fields is set by the stress state and the magnetic anisotropy of the magnetostrictive layer. From the previous study, we can also deduce that a phase shift of $\pi/4$ rad between the rotating electric field and the position of the magnet corresponds to the state of maximum torque.

4.4 Conclusion

In this chapter, we applied the formulations developed in Chapter 3 to two devices, a three-layer energy harvester and a more challenging rotating coilless ME composite, which can function both as a generator or an actuator. The two developed linear formulations were applied to the three-layer ME composite, and its response studied in terms of output voltage as a function of the source field surrounding the device. The ϕ_{red}-ϕ_{red} formulation was compared with a pure FEM approach and proved to give what seems to be a more accurate result while being considerably less computationally expensive in terms of DoFs, computing time and allocated memory. The nonlinear formulations with an invariant approach to magnetostriction were applied to both the three-layer ME composite, this time showing a saturation in the output voltage, and to the rotating coilless ME composite. This bi-layer structure was studied as an alternating voltage generator in which a rotating magnet is used to generate a voltage through the strain induced ME effect. In actuator mode, we observed how the application of an electric voltage onto the piezoelectric layer creates a magnetic anisotropy in the Galfenol layer. Under the effect of a magnet and depending on its angle in comparison with the structure, will result in a mechanical torque between the ME device and the magnet. The influence of the electric voltage imposed onto the torque developed was also studied, resulting in an almost linear relation between both quantities for the conditions of our simulations.

Chapter 5

Conclusions and perspectives

5.1 General Conclusions

In the present manuscript, we introduced the ME effect, in particular, the strain-induced ME effect and its constituent phenomena, local electro-mechanical and magneto-mechanical coupling. In the first place we developed the single-physics formulations involved in the strain-induced ME effect. The mechanical and the electrical problems were treated using the FEM while two formulations of the magnetic problem, involving a coupling of the FEM and the BEM, were considered. The first formulation was based on a magnetic reduced scalar potential formulation inside the active material and on its boundary and referred to as ϕ_{red}-ϕ_{red} formulation. The second was based on a magnetic vector potential formulation inside the active material and a magnetic reduced scalar potential formulation on the boundary of the active material and referred to as a-ϕ_{red} formulation. The two FEM-BEM formulations were tested and compared to an analytical solution, showing their h-convergence towards the analytical solution. The ϕ_{red}-ϕ_{red} formulation proved to be closer to the analytical solution for the linear case. Their behavior for nonlinear constitutive laws was also studied, showing the better convergence of the Newton-Raphson solver of the a-ϕ_{red} formulation.

In a second place, the multi-physics couplings were introduced into the previously established single-physics weak forms, resulting in:

- two FEM-BEM formulations of the linear magneto-mechanical problems, each one deriving from the two magnetostatic formulations.
- a FEM-BEM formulation of nonlinear magneto-mechanical coupling, which based on the a-ϕ_{red} formulation but considering constitutive

laws deriving from a description of the Helmholtz free energy in terms of its scalar invariants.

- a FEM formulation of the electro-mechanical problem, for which a linear approach to ferroelectricity was considered taking into account a nontrivial poling pattern of the piezoelectric materials.
- two linear formulations of the full electro-magneto-mechanical problem, each deriving from the two magnetostatic FEM-BEM formulations.
- a nonlinear electro-magneto-mechanical formulation based on the nonlinear magneto-mechanical formulation and linear electro-mechanical modeling.

All two-physics formulations were validated and showed good agreement with analytical solutions. The introduction of multi-physics couplings in the FEM-BEM formulations resulted in the presence of both full and sparse matrices in the global block matrix system resulting from the discrete forms. The use of a block Gauss-Seidel iterative method allowed overcoming the resolution difficulties by using an adapted solver for each single-physics problem. An adaptive solver based on the block Gauss-Seidel method was also implemented in order to reduce the resolution time of the electro-magneto-mechanical problems. It adapts the choice of the current problem to be solved by testing the convergence of the single-physics solutions and resolution for the worst converging problem.

The results of the linear fully coupled problem was compared to a FEM approach for the case of the three-layer ME composite. The FEM approach was based on a magnetic reduced scalar potential formulation. The FEM approaches required a considerable number of additional DoFs, higher computation times and higher allocated memory to obtain similar accuracy than the FEM-BEM ϕ_{red}-ϕ_{red} approach. The nonlinear formulation of the fully coupled problem was applied to the modeling of a three layer ME composite made of two layers of Terfenol-D and a layer of PZT-5A, and a maximum DC ME coefficient determined for the considered geometry and materials.

We applied the nonlinear FEM-BEM approach to the modeling of a rotating coilless ME composite, made of a Galfenol material and a PZT-5A material, under the effect of a permanent magnet. In generator mode, a rotating magnet generated an alternating voltage between the electrodes of the piezoelectric layer. In actuator mode, the application of an electric voltage onto the piezoelectric phase introduced an anisotropic loading onto the magnetostrictive phase. It was shown by applying different voltages that the result of this loading is a shift of the magnetization in the Galfenol phase.

This was also shown by a spectral study on the magnetic susceptibility. It showed that the effect of the anisotropic loading introduced an anisotropy in the magnetic susceptibility of the magnetostrictive phase: a preferred magnetization direction appeared according to the principal stress direction. This principal magnetization direction was given by the direction of the eigenvector corresponding to the highest eigenvalue of the susceptibility tensor reconstructed at every element of the discretized domain.

The change in polarization suggested the presence of a mechanical torque between the Galfenol phase and the magnet. Numerical simulations confirmed the presence of this mechanical torque in both the Galfenol phase and the magnet. This torque was computed by two methods, in the Galfenol phase by computing the effect of magnetic charges, and in the magnet by an evaluation of the Laplace force. According to Newton's third law, the magnetic forces, as well as the torque along the vertical direction, computed in the Galfenol layer and in the magnet, were equal in amplitude and in opposite directions

5.2 Perspectives

The presented work opens up various perspectives for both the modeling and applications of ME devices.

5.2.1 Modeling approach

All conducted simulations were conducted in static regime, whereas all application devices are designed to function in time varying conditions. Therefore, it seems important to study the time-dependent response of ME devices at the simulation stage. It has for example been shown that the frequency of excitation of ME composites can have an important impact on their response. For example, accentuating their properties when the excitation frequencies are close to the mechanical, or electromagnetic resonant frequencies of the device.

The presence of eddy currents, as a consequence of time-varying fields, should be evaluated and the losses computed. Moreover, from an energetic point of view, for the modeled energy harvesters an output voltage is obtained from the application of a magnetic field, whereas for actuators, a force (and torque) is produced by the application of an electric voltage. However, the

value of these voltages gives no information about the energy produced by the harvester or the energy needed to produce the given force or torque. This information would be a very useful when considering the use of such devices.

Concerning the modeling of the electrodes, the use of surface electrodes accompanied by the treatment by the FEM of electric phenomena can lead to singularities in the electric solution, introducing large errors in the simulated response. A FEM-BEM formulation of electrical phenomena would allow the accurate computing of the leaks of the displacement field, thus correctly modeling the effect of these surface electrodes.

Material models more representative of the considered materials should be considered, for example the nonlinear or even hysteretic modeling of active materials. The multiscale modeling magneto-mechanical and electro-mechanical seems to be a promising approach and has proved to predict an accurate response of ferromagnetic materials. One disadvantage of the invariants approach to magneto-mechanical coupling seems to be the domain of validity of the coefficients of the invariants, which depend on the conditions of the fitted data. The multiscale approach does not suffer from these limitations.

5.2.2 Material characterization

For the accurate simulation of ME devices, an accurate description of their response is necessary, for this, not only proper constitutive laws are needed, but also, proper material coefficients. As in this manuscript, we studied the response of magnetostrictive materials under mechanical tension, a magneto-mechanical characterization of magnetostrictive materials in this state seems necessary, as well as an electro-mechanical characterization of piezoelectric materials. In the case of piezoelectricity, this study would allow determining the domain of validity of the used linear constitutive laws, and determining whether a nonlinear model is more adapted to the description of electro-mechanical phenomena. Also, a magnetic characterization of piezoelectric materials is needed, in particular, the lead content PZT suggest a slight ferromagnetic response. For these purposes, adequate characterization benches have to be conceived and employed.

5.2.3 Optimization of the coilless rotating ME composite

Having established a relevant model for ME effects in composite structures, it is relevant to consider its use in an optimization scheme. Concerning the rotating coilless ME composite, the magnetic interaction between the magnet and the magnetostrictive phase depends on the magnetization of the magnetostrictive disk. Therefore, the choice of appropriate magnetostrictive materials should be studied. In particular, different materials could be used in generator mode and in actuator mode.

Besides the choice of the material, the volume ratios and shape of the layers of the rotating coilless ME device has to be optimized in order to maximize the torque or the output voltage. It is also expected that the optimized geometries in generator and actuator mode would be different. The shape of the magnet could also be optimized, its square shape was indeed chosen to simplify its modeling, nevertheless, a magnet of circular cross-section would be more aerodynamic.

Concerning the positioning of the electrodes, the use of interdigitated electrodes could allow increasing the generated strains in the piezoelectric layer. In actuator mode, if the aim is to produce rotating strains, the optimized positioning of the interdigitated electrodes is not a trivial problem. Other electrode patterns than the pattern considered in this manuscript should be studied.

5.2.4 Comparison to experimental data on ME devices

In this work, we focused on the modeling of ME devices. An important step in the evaluation of the proposed approach is the comparison of the results of our simulations with experimental data. In order to conduct this comparison, the construction and testing of prototypes of the simulated devices is needed. For the rotating coilless ME composite in generator mode, a study could be conducted on the output voltage of the ME composite. In actuator mode, its modeling involved calculating torques and forces, these forces and torques could be measured in a real device and compared to the simulation results. These studies would quantify the pertinence of the presented modeling approaches and suggest if further aspects of the modeling of ME devices should be taken into account.

Bibliography

[1] E. Ascher, H. Rieder, H. Schmid, and H. Stössel, "Some properties of ferromagnetoelectric nickel-iodine boracite, Ni3B7O13I," *Journal of Applied Physics*, vol. 37, no. 3, pp. 1404–1405, 1966.

[2] K. K. Leang, Q. Zou, and G. Pannozzo, "Teaching modules on modeling and control of piezoactuators for system dynamics, controls, and mechatronics courses," *IEEE Transactions on Education*, vol. 53, no. 3, pp. 372–383, 2009.

[3] R. DeVries and J. Burke, "Microstructure of barium titanate ceramics," *Journal of the American Ceramic Society*, vol. 40, no. 6, pp. 200–206, 1957.

[4] R. Paradies and M. Melnykowycz, "Numerical stress investigation for piezoelectric elements with a circular cross section and interdigitated electrodes," *Journal of Intelligent Material Systems and Structures*, vol. 18, no. 9, pp. 963–972, 2007.

[5] F. Narita and M. Fox, "A review on piezoelectric, magnetostrictive, and magnetoelectric materials and device technologies for energy harvesting applications," *Advanced Engineering Materials*, vol. 20, no. 5, p. 1700743, 2018.

[6] B. D. Cullity and C. D. Graham, *Introduction to magnetic materials*. John Wiley & Sons, 2011.

[7] E. W. Lee, "Magnetostriction and magnetomechanical effects," *Reports on progress in physics*, vol. 18, no. 1, p. 184, 1955.

[8] M. Domenjoud, E. Berthelot, N. Galopin, R. Corcolle, Y. Bernard, and L. Daniel, "Characterization of giant magnetostrictive materials under static stress: influence of loading boundary conditions," *Smart Materials and Structures*, vol. 28, 2019.

[9] T. Ueno and T. Higuchi, "Novel composite of magnetostrictive material and piezoelectric actuator for coil-free magnetic force control," *Sensors and Actuators A: Physical*, vol. 129, no. 1-2, pp. 251–255, 2006.

[10] J. Lou, D. Reed, M. Liu, and N. Sun, "Electrostatically tunable magnetoelectric inductors with large inductance tunability," *Applied Physics Letters*, vol. 94, no. 11, p. 112508, 2009.

[11] G. Meunier, *The finite element method for electromagnetic modeling*. John Wiley & Sons, 2010.

[12] A. Bossavit, *Computational electromagnetism: variational formulations, complementarity, edge elements*. Academic Press, 1998.

[13] C. Hafner, J. Smajic, and M. Agio, "Numerical methods for the electrodynamic analysis of nanostructures," *Nanoclusters and nanostructured surfaces*, pp. 207–274, 2010.

[14] U. Ahmed, U. Aydin, M. Zucca, S. Palumbo, R. Kouhia, and P. Rasilo, "Modeling a Fe-Ga energy harvester fitted with magnetic closure using 3d magneto-mechanical finite element model," *Journal of Magnetism and Magnetic Materials*, vol. 500, p. 166390, 2020.

[15] X. D. Zhang and C. T. Sun, "Formulation of an adaptive sandwich beam," *Smart Materials and Structures*, vol. 5, pp. 814–823, 1996.

[16] K. Fujiwara, Y. Okamoto, A. Kameari, and A. Ahagon, "The newton-raphson method accelerated by using a line search - comparison between energy functional and residual minimization," *IEEE Transactions on Magnetics*, vol. 41, pp. 1724–1727, 2004.

[17] W. Voigt, *Lehrbuch der kristallphysik:(mit ausschluss der kristalloptik)*, vol. 34. BG Teubner, 1910.

[18] A. Bossavit, "A rationale for 'edge-elements' in 3-d fields computations," *IEEE Transactions on Magnetics*, vol. 24, pp. 74–79, 1988.

[19] P. Dular and F. Pirou, *The finite element method for electromagnetic modeling*, ch. Static Formulations: Electrostatic, Electrokinetic, Magnetostatics. John Wiley & Sons, 2010.

[20] A. Vigneron, *Formulations par équations intégrales de surface pour la simulation numérique du contrôle non destructif par courants de Foucault. (Formulations by surface integral equations for numerical simulation of non-destructive testing by eddy currents).* Phd thesis, Ecole Polytechnique, 2015.

[21] R. Hiptmair, "Boundary element methods for eddy current computation," *Boundary element analysis: mathematical aspects and applications*, pp. 213–248, 2007.

[22] A. P. Wills, *Vector analysis, with an introduction to tensor analysis.* Dover Publications, 1958.

[23] J. L. Coulomb, "A methodology for the determination of global electromechanical quantities from a finite element analysis and its application to the evaluation of magnetic forces, torques and stiffness," *IEEE Transactions on Magnetics*, vol. 19, no. 6, pp. 2514–2519, 1983.

[24] E. Durand, *Magnétostatique.* Masson et Cie, 1968.

[25] W. Eerenstein, N. D. Mathur, and J. F. Scott, "Multiferroic and magnetoelectric materials," *Nature*, vol. 442, pp. 759–765, Aug. 2006.

[26] J.-P. Rivera, "A short review of the magnetoelectric effect and related experimental techniques on single phase (multi-) ferroics," *The European Physical Journal B*, vol. 71, pp. 299–313, Oct. 2009.

[27] W. F. Brown, R. M. Hornreich, and S. Shtrikman, "Upper Bound on the Magnetoelectric Susceptibility," *Physical Review*, vol. 168, pp. 574–577, Apr. 1968.

[28] G. Catalan and J. F. Scott, "Physics and Applications of Bismuth Ferrite," *Advanced Materials*, vol. 21, pp. 2463–2485, June 2009.

[29] J. Wu, Z. Fan, D. Xiao, J. Zhu, and J. Wang, "Multiferroic bismuth ferrite-based materials for multifunctional applications: Ceramic bulks, thin films and nanostructures," *Progress in Materials Science*, vol. 84, pp. 335–402, Dec. 2016.

[30] J. Curie and P. Curie, "Développement par compression de l'électricité polaire dans les cristaux hémièdres à faces inclinées," *Bulletin de minéralogie*, vol. 3, no. 4, pp. 90–93, 1880.

[31] J. Curie and P. Curie, "Contractions et dilatations produites par des tensions électriques dans les cristaux hémièdres à faces inclinées," *Compt. Rend*, vol. 93, pp. 1137–1140, 1881.

[32] C. Rosen, B. V. Hiremath, and R. Newnham, *Piezoelectricity*. Springer Science & Business Media, 1992.

[33] P. Hareesh, I. Misri, S. Yang, and D. L. DeVoe, "Transverse interdigitated electrode actuation of homogeneous bulk PZT," *Journal of microelectromechanical systems*, vol. 21, no. 6, pp. 1513–1518, 2012.

[34] R. G. Bryant, R. T. Effinger Iv, I. Aranda Jr, B. M. Copeland Jr, E. W. Covington Iii, and J. M. Hogge, "Radial field piezoelectric diaphragms," *Journal of intelligent material systems and structures*, vol. 15, no. 7, pp. 527–538, 2004.

[35] C. Chang, P. Chang, R.-S. S. Huang, C. P. Chang, and M. Cheng, "Microelectrode array: a new method for the design of electrostatic microactuators and capacitive microsensors," in *Smart Electronics and MEMS*, vol. 3242, pp. 145–156, SPIE, 1997.

[36] J. P. Joule, "On the effects of magnetism upon the dimensions of iron and steel bars," *The London, Edinburgh, and Dublin Philosophical Magazine and Journal of Science*, vol. 30, no. 199, pp. 76–87, 1847.

[37] É. Du Trémolet de Lacheisserie, "Magnétisme (tome II)," 1999.

[38] G. Engdahl, "Physics of Giant Magnetostriction," in *Handbook of Giant Magnetostrictive Materials*, pp. 1–125, Elsevier, 2000.

[39] A. Belahcen, "Vibrations of rotating electrical machines due to magnetomechanical coupling and magnetostriction," *IEEE Transactions on Magnetics*, vol. 42, no. 4, pp. 971–974, 2006.

[40] P. I. Anderson, A. J. Moses, and H. J. Stanbury, "Assessment of the stress sensitivity of magnetostriction in grain-oriented silicon steel," *IEEE transactions on magnetics*, vol. 43, no. 8, pp. 3467–3476, 2007.

[41] B. Weiser, H. Pfutzner, and J. Anger, "Relevance of magnetostriction and forces for the generation of audible noise of transformer cores," *IEEE Transactions on magnetics*, vol. 36, no. 5, pp. 3759–3777, 2000.

[42] T. Tanzer, H. Pregartner, M. Riedenbauer, R. Labinsky, M. Witlatschil, A. Muetze, and K. Krischan, "Magnetostriction of electrical steel and its relation to the no-load noise of power transformers," *IEEE Transactions on Industry Applications*, vol. 54, no. 5, pp. 4306–4314, 2018.

[43] N. Nersessian, S.-W. Or, and G. P. Carman, "Magneto-thermo-mechanical characterization of 1–3 type polymer-bonded terfenol-d composites," *Journal of Magnetism and Magnetic Materials*, vol. 263, no. 1-2, pp. 101–112, 2003.

[44] X. Dai, "An vibration energy harvester with broadband and frequency-doubling characteristics based on rotary pendulums," *Sensors and Actuators A: Physical*, vol. 241, pp. 161–168, 2016.

[45] H. Palneedi, V. Annapureddy, S. Priya, and J. Ryu, "Status and Perspectives of Multiferroic Magnetoelectric Composite Materials and Applications," *Actuators*, vol. 5, p. 9, Mar. 2016.

[46] Y. Yan, L. D. Geng, L. Zhang, C. Tu, R. Sriramdas, H. Liu, X. Li, M. Sanghadasa, K. D. Ngo, Y. U. Wang, *et al.*, "High-power magneto-electric voltage tunable inductors," *IEEE Transactions on Industrial Electronics*, vol. 68, no. 6, pp. 5355–5365, 2020.

[47] C. M. Leung, J. Li, D. Viehland, and X. Zhuang, "A review on applications of magnetoelectric composites: From heterostructural uncooled magnetic sensors, energy harvesters to highly efficient power converters," *Journal of Physics D: Applied Physics*, vol. 51, no. 26, p. 263002, 2018.

[48] S. Dong, J. Li, and D. Viehland, "Voltage gain effect in a ring-type magnetoelectric laminate," *Applied physics letters*, vol. 84, no. 21, pp. 4188–4190, 2004.

[49] C. S. Lynch, "The effect of uniaxial stress on the electro-mechanical response of 8/65/35 PLZT," *Acta Materialia*, vol. 44, pp. 4137–4148, 1996.

[50] A. Schnell, "Nonlinear charge release of piezoelectric ceramics under uniaxial pressure," *Ferroelectrics*, vol. 28, pp. 351–353, 1980.

[51] T. Fett, S. Muller, D. Munz, and G. Thun, "Nonsymmetry in the deformation behaviour of PZT," *Journal of Materials Science Letters*, vol. 17, pp. 261–265, 1998.

[52] C. PeterJ. and M. StephenT., "A macroscopic theory for the existence of the hysteresis and butterfly loops in ferroelectricity," *Ferroelectrics*, vol. 23, pp. 199–207, 1980.

[53] P. J. Chen, "Three dimensional dynamic electromechanical constitutive relations for ferroelectric materials," *International Journal of Solids and Structures*, vol. 16, pp. 1059–1067, 1980.

[54] R. M. McMeeking and C. M. Landis, "A phenomenological multi-axial constitutive law for switching in polycrystalline ferroelectric ceramics," *International Journal of Engineering Science*, vol. 40, pp. 1553–1577, 2002.

[55] C. M. Landis, "Fully coupled, multi-axial, symmetric constitutive laws for polycrystalline ferroelectric ceramics," *Journal of The Mechanics and Physics of Solids*, vol. 50, pp. 127–152, 2002.

[56] A. Avakian, R. Gellmann, and A. Ricoeur, "Nonlinear modeling and finite element simulation of magnetoelectric coupling and residual stress in multiferroic composites," *Acta Mechanica*, vol. 226, pp. 2789–2806, Aug. 2015.

[57] A. Avakian and A. Ricoeur, "Finite element simulation of nonlinear magnetoelectric coupling and damage behaviour in multiferroic composites," *PAMM*, vol. 17, no. 1, pp. 497–498, 2017.

[58] J. Schröder and D. Gross, "Invariant formulation of the electromechanical enthalpy function of transversely isotropic piezoelectric materials," *Archive of Applied Mechanics*, vol. 73, no. 8, pp. 533–552, 2004.

[59] M. Kamlah and C. Tsakmakis, "Phenomenological modeling of the non-linear electro-mechanical coupling in ferroelectrics," *International Journal of Solids and Structures*, vol. 36, pp. 669–695, 1999.

[60] W. Zouari, T. B. Zineb, and A. Benjeddou, "A FSDT—MITC piezoelectric shell finite element with ferroelectric non-linearity," *Journal of*

Intelligent Material Systems and Structures, vol. 20, no. 17, pp. 2055–2075, 2009.

[61] "IEEE Standard on Piezoelectricity," *ANSI/IEEE Std 176-1987*, pp. 0–1, 1988.

[62] X. Zhang and C. Sun, "Formulation of an adaptive sandwich beam," *Smart Materials and Structures*, vol. 5, no. 6, p. 814, 1996.

[63] T. Guo, Z. Xu, L. Jin, and M. Hu, "Optimized structure design of a bridge-like piezoelectric energy harvester based on finite element analysis," in *2017 20th International Conference on Electrical Machines and Systems (ICEMS)*, pp. 1–5, IEEE, 2017.

[64] V. Piefort and A. Preumont, "Modeling of smart piezoelectric shell structures with finite elements," in *Proceedings of the International Seminar on Modal Analysis*, vol. 2, pp. 869–876, KU Leuven; 1998, 2001.

[65] S. M. Hasheminejad and A. Kasaeisani, "Smart hybrid active/semi-active distributed structural acoustic control of thin- and thick-walled piezo-sandwich bimorph spherical shell cloaks," *Journal of Sound and Vibration*, vol. 552, p. 117591, 2023.

[66] W. W. Clark, "Vibration control with state-switched piezoelectric materials," *Journal of intelligent material systems and structures*, vol. 11, no. 4, pp. 263–271, 2000.

[67] "IEEE Standard on Magnetostrictive Materials: Piezomagnetic Nomenclature," tech. rep., IEEE.

[68] D. L. Hall and A. B. Flatau, "On analog feedback control for magnetostrictive transducer linearization," *Journal of Sound and Vibration*, vol. 211, pp. 481–494, 1998.

[69] J. Yoo and N. J. Jones, "A performance prediction for fe–ga magnetostrictive strain sensor using simplified model," *IEEE Transactions on Magnetics*, vol. 53, pp. 1–4, 2017.

[70] V. Berbyuk and J. Sodhani, "Towards modelling and design of magnetostrictive electric generators," *Computers & Structures*, vol. 86, pp. 307–313, 2008.

[71] D. Jiles and J. Thoelke, "Theoretical modelling of the effects of anisotropy and stress on the magnetization and magnetostriction of Tb0.3Dy0.7Fe2," *Journal of Magnetism and Magnetic Materials*, vol. 134, no. 1, pp. 143–160, 1994.

[72] W. D. Armstrong, "Magnetization and magnetostriction processes in Tb (0.27- 0.30) Dy (0.73- 0.70) Fe (1.9- 2.0)," *Journal of Applied Physics*, vol. 81, no. 5, pp. 2321–2326, 1997.

[73] W. D. Armstrong, "Nonlinear behavior of magnetostrictive particle actuated composite materials," *Journal of applied physics*, vol. 87, no. 6, pp. 3027–3031, 2000.

[74] J. B. Restorff, M. Wun-Fogle, A. E. Clark, and K. B. Hathaway, "Induced magnetic anisotropy in stress-annealed galfenol alloys," *IEEE Transactions on Magnetics*, vol. 42, pp. 3087–3089, 2006.

[75] J. Atulasimha and A. B. Flatau, "Energy-based model for the magnetostrictive behavior of polycrystalline iron-gallium alloys," in *Smart Structures and Materials 2006: Active Materials: Behavior and Mechanics*, vol. 6170, pp. 145–153, SPIE, 2006.

[76] G. P. Carman and M. Mitrovic, "Nonlinear constitutive relations for magnetostrictive materials with applications to 1-d problems," *Journal of Intelligent Material Systems and Structures*, vol. 6, no. 5, pp. 673–683, 1995.

[77] Y. Wan, D. Fang, and K.-C. Hwang, "Non-linear constitutive relations for magnetostrictive materials," *International Journal of Non-Linear Mechanics*, vol. 38, no. 7, pp. 1053–1065, 2003.

[78] X. Liu and X. Zheng, "A nonlinear constitutive model for magnetostrictive materials," *Acta Mechanica Sinica*, vol. 21, no. 3, pp. 278–285, 2005.

[79] D.-G. Zhang, M.-H. Li, and H.-M. Zhou, "A general one-dimension nonlinear magneto-elastic coupled constitutive model for magnetostrictive materials," *AIP advances*, vol. 5, no. 10, p. 107201, 2015.

[80] P. Shi, K. Jin, and X. Zheng, "A general nonlinear magnetomechanical model for ferromagnetic materials under a constant weak magnetic field," *Journal of Applied Physics*, vol. 119, no. 14, p. 145103, 2016.

[81] P. Shi, "A nonlinear theoretical model of magnetization and magnetostriction for ferromagnetic materials under applied stress and magnetic fields," *Chinese Physics Letters*, vol. 37, no. 8, p. 087502, 2020.

[82] Buiron, N., Hirsinger, L., and Billardon, R., "A multiscale model for magneto-elastic couplings," *J. Phys. IV France*, 1999.

[83] L. Daniel, O. Hubert, F. Ossart, and R. Billardon, "Experimental analysis and multiscale modelling of the anisotropic mechanical and magnetostrictive behaviours of electrical steels," *J. Phys. IV France*, vol. 105, pp. 247–254, 2003.

[84] L. Daniel and N. Galopin, "A constitutive law for magnetostrictive materials and its application to terfenol-d single and polycrystals," *The European Physical Journal - Applied Physics*, vol. 42, no. 2, p. 153–159, 2008.

[85] U. Aydin, P. Rasilo, F. Martin, D. Singh, L. Daniel, A. Belahcen, M. Rekik, O. Hubert, R. Kouhia, and A. Arkkio, "Magneto-mechanical modeling of electrical steel sheets," *Journal of Magnetism and Magnetic Materials*, vol. 439, pp. 82–90, 2017.

[86] L. Daniel, O. Hubert, and M. Rekik, "A simplified 3-d constitutive law for magnetomechanical behavior," *IEEE Transactions on Magnetics*, vol. 51, no. 3, pp. 1–4, 2015.

[87] S. K. Wahi, M. Kumar, S. Santapuri, and M. J. Dapino, "Computationally efficient locally linearized constitutive model for magnetostrictive materials," *Journal of Applied Physics*, vol. 125, no. 21, p. 215108, 2019.

[88] L. Bernard, X. Mininger, L. Daniel, G. Krebs, F. Bouillault, and M. Gabsi, "Effect of stress on switched reluctance motors: a magneto-elastic finite-element approach based on multiscale constitutive laws," *IEEE Transactions on Magnetics*, vol. 47, no. 9, pp. 2171–2178, 2011.

[89] N. Galopin, X. Mininger, F. Bouillault, and L. Daniel, "Finite element modeling of magnetoelectric sensors," *IEEE Transactions on Magnetics*, vol. 44, no. 6, pp. 834–837, 2008.

[90] T. T. Nguyen, F. Bouillault, L. Daniel, and X. Mininger, "Finite element modeling of magnetic field sensors based on nonlinear magnetoelectric effect," *Journal of Applied Physics*, vol. 109, no. 8, p. 084904, 2011.

[91] K. Fonteyn, A. Belahcen, R. Kouhia, P. Rasilo, and A. Arkkio, "FEM for directly coupled magneto-mechanical phenomena in electrical machines," *IEEE Transactions on Magnetics*, vol. 46, no. 8, pp. 2923–2926, 2010.

[92] U. Aydin, P. Rasilo, D. Singh, A. Lehikoinen, A. Belahcen, and A. Arkkio, "Coupled magneto-mechanical analysis of iron sheets under biaxial stress," *IEEE Transactions on magnetics*, vol. 52, no. 3, pp. 1–4, 2015.

[93] U. Ahmed, J. Jeronen, M. Zucca, S. Palumbo, and P. Rasilo, "Finite element analysis of magnetostrictive energy harvesting concept device utilizing thermodynamic magneto-mechanical model," *Journal of Magnetism and Magnetic Materials*, vol. 486, p. 165275, 2019.

[94] U. Ahmed, U. Aydin, L. Daniel, and P. Rasilo, "3-d magneto-mechanical finite element analysis of galfenol-based energy harvester using an equivalent stress model," *IEEE Transactions on Magnetics*, vol. 57, no. 2, pp. 1–5, 2020.

[95] V. Loyau, V. Morin, G. Chaplier, M. LoBue, and F. Mazaleyrat, "Magnetoelectric effect in layered ferrite/PZT composites. Study of the demagnetizing effect on the magnetoelectric behavior," *Journal of Applied Physics*, vol. 117, p. 184102, May 2015.

[96] S. Dong, J.-F. Li, and D. Viehland, "Longitudinal and transverse magnetoelectric voltage coefficients of magnetostrictive/piezoelectric laminate composite: theory," *IEEE Transactions on Ultrasonics, Ferroelectrics, and Frequency Control*, vol. 50, no. 10, pp. 1253–1261, 2003.

[97] S. Dong and J. Zhai, "Equivalent circuit method for static and dynamic analysis of magnetoelectric laminated composites," *Science Bulletin*, vol. 53, pp. 2113–2123, July 2008.

[98] C.-W. Nan, "Magnetoelectric effect in composites of piezoelectric and piezomagnetic phases," *Physical Review B*, vol. 50, no. 9, p. 6082, 1994.

[99] E. Pan, "Three-dimensional green's functions in anisotropic magneto-electro-elastic bimaterials," *Zeitschrift für angewandte Mathematik und Physik ZAMP*, vol. 53, no. 5, pp. 815–838, 2002.

[100] M. I. Bichurin, V. M. Petrov, and G. Srinivasan, "Theory of low-frequency magnetoelectric coupling in magnetostrictive-piezoelectric bilayers," *Phys. Rev. B*, vol. 68, p. 054402, Aug 2003.

[101] G. Harshe, J. Dougherty, and R. Newnham, "Theoretical modelling of multilayer magnetoelectric composites," *Int. J. Appl. Electromagn. Mater.*, vol. 4, pp. 145–159, 1993.

[102] M. Avellaneda and G. Harshé, "Magnetoelectric effect in piezoelectric/-magnetostrictive multilayer (2-2) composites," *Journal of Intelligent Material Systems and Structures*, vol. 5, no. 4, pp. 501–513, 1994.

[103] G. Wu, T. Nan, R. Zhang, N. Zhang, S. Li, and N. X. Sun, "Inequivalence of direct and converse magnetoelectric coupling at electromechanical resonance," *Applied Physics Letters*, vol. 103, no. 18, p. 182905, 2013.

[104] T. I. Muchenik and E. J. Barbero, "Charge, voltage, and work-conversion formulas for magnetoelectric laminated composites," *Smart Materials and Structures*, vol. 24, p. 025039, jan 2015.

[105] R. Newnham, D. Skinner, and L. Cross, "Connectivity and piezoelectric-pyroelectric composites," *Materials Research Bulletin*, vol. 13, no. 5, pp. 525–536, 1978.

[106] T.-Z. Wang and Y.-H. Zhou, "A theoretical study of nonlinear magnetoelectric effect in magnetostrictive–piezoelectric trilayer," *Composite Structures*, vol. 93, no. 5, pp. 1485–1492, 2011.

[107] Y. Shi, N. Li, Y. Wang, and J. Ye, "An analytical model for nonlinear magnetoelectric effect in laminated composites," *Composite Structures*, vol. 263, p. 113652, 2021.

[108] M. I. Bichurin, V. M. Petrov, and G. Srinivasan, "Theory of low-frequency magnetoelectric coupling in magnetostrictive-piezoelectric bilayers," *Phys. Rev. B*, vol. 68, p. 054402, Aug 2003.

[109] Y. Benveniste, "Magnetoelectric effect in fibrous composites with piezoelectric and piezomagnetic phases," *Phys. Rev. B*, vol. 51, pp. 16424–16427, Jun 1995.

[110] J.-Y. Kim, "Micromechanical analysis of effective properties of magneto-electro-thermo-elastic multilayer composites," *International Journal of Engineering Science*, vol. 49, no. 9, pp. 1001–1018, 2011.

[111] K. Jin and J. Aboudi, "Macroscopic behavior prediction of multiferroic composites," *International Journal of Engineering Science*, vol. 94, pp. 226–241, 2015.

[112] H. Xu, Y. Pei, F. Li, and D. Fang, "A multi-scale and multi-field coupling nonlinear constitutive theory for the layered magnetoelectric composites," *Journal of the Mechanics and Physics of Solids*, vol. 114, pp. 143–157, 2018.

[113] J. Zhang, C. Fang, and G. J. Weng, "Direct and converse nonlinear magnetoelectric coupling in multiferroic composites with ferromagnetic and ferroelectric phases," *Proceedings of the Royal Society A: Mathematical, Physical and Engineering Sciences*, vol. 475, no. 2225, p. 20190002, 2019.

[114] J. Y. Li and M. L. Dunn, "Micromechanics of magnetoelectroelastic composite materials: Average fields and effective behavior," *Journal of Intelligent Material Systems and Structures*, vol. 9, no. 6, pp. 404–416, 1998.

[115] S. Srinivas and J. Y. Li, "The effective magnetoelectric coefficients of polycrystalline multiferroic composites," *Acta Materialia*, vol. 53, no. 15, pp. 4135–4142, 2005.

[116] T. Tang and W. Yu, "Variational asymptotic homogenization of heterogeneous electromagnetoelastic materials," *International Journal of Engineering Science*, vol. 46, no. 8, pp. 741–757, 2008.

[117] T. Tang and W. Yu, "Micromechanical modeling of the multiphysical behavior of smart materials using the variational asymptotic method," *Smart Materials and Structures*, vol. 18, p. 125026, nov 2009.

[118] J. H. Huang, "Analytical predictions for the magnetoelectric coupling in piezomagnetic materials reinforced by piezoelectric ellipsoidal inclusions," *Phys. Rev. B*, vol. 58, pp. 12–15, Jul 1998.

[119] J. Y. Li and M. L. Dunn, "Anisotropic coupled-field inclusion and inhomogeneity problems," *Philosophical Magazine A*, vol. 77, no. 5, pp. 1341–1350, 1998.

[120] I. Babuska, "Error-bounds for finite element method.," *Numerische Mathematik*, vol. 16, pp. 322–333, 1970/71.

[121] I. Babuska and B. Szabo, "On the rates of convergence of the finite element method," *International Journal for Numerical Methods in Engineering*, vol. 18, no. 3, pp. 323–341, 1982.

[122] I. Babuška and B. Guo, "The h, p and h-p version of the finite element method; basis theory and applications," *Advances in Engineering Software*, vol. 15, no. 3, pp. 159–174, 1992.

[123] T. T. Nguyen, X. Mininger, F. Bouillault, and L. Daniel, "Finite element harmonic modeling of magnetoelectric effect," *IEEE Transactions on Magnetics*, vol. 47, no. 5, pp. 1142–1145, 2011.

[124] H. Talleb, A. Gensbittel, and Z. Ren, "Multiphysics modeling of a magnetoelectric composite rosen-type device," *Composite Structures*, vol. 137, pp. 1–8, 2016.

[125] G. R. Buchanan, "Layered versus multiphase magneto-electro-elastic composites," *Composites Part B: Engineering*, vol. 35, no. 5, pp. 413–420, 2004.

[126] J. Zhang, X. Wang, X. Chen, H. Du, and G. J. Weng, "Finite element analysis of the magnetoelectric effect on hybrid magnetoelectric composites," *Composite Structures*, vol. 296, p. 115876, 2022.

[127] T. A. Do, H. Talleb, A. Gensbittel, and Z. Ren, "Homogenization of Magnetoelectric 0–3 Type Composites by 3-D Multiphysics Finite-Element Modeling," *IEEE Transactions on Magnetics*, vol. 55, pp. 1–4, June 2019.

[128] A. Urdaneta-Calzadilla, N. Galopin, I. Niyonzima, I. Niyonzima, O. Chadebec, B. Bannwarth, and G. Meunier, "A FEM-BEM coupling strategy for the modeling of magnetoelectric effects in composite structures," *Engineering analysis with boundary elements*, 2023.

[129] W. Scott Dunbar, "The volume integral method of eddy current modeling," *Journal of Nondestructive Evaluation*, vol. 5, pp. 9–14, 1985.

[130] O. Chadebec, J.-L. Coulomb, and F. Janet, "A review of magnetostatic moment method," *IEEE Transactions on Magnetics*, vol. 42, no. 4, pp. 515–520, 2006.

[131] A. Carpentier, O. Chadebec, N. Galopin, G. Meunier, and B. Bannwarth, "Resolution of nonlinear magnetostatic problems with a volume integral method using the magnetic scalar potential," *IEEE transactions on magnetics*, vol. 49, no. 5, pp. 1685–1688, 2013.

[132] V. Le-Van, G. Meunier, O. Chadebec, and J.-M. Guichon, "A volume integral formulation based on facet elements for nonlinear magnetostatic problems," *IEEE Transactions on Magnetics*, vol. 51, no. 7, pp. 1–6, 2015.

[133] W. M. Rucker, R. Hoschek, and K. R. Richter, "Various BEM formulations for calculating eddy currents in terms of field variables," *IEEE transactions on magnetics*, vol. 31, no. 3, pp. 1336–1341, 1995.

[134] A. Vigneron, É. Demaldent, and M. Bonnet, "Surface integral equations for electromagnetic testing: the low-frequency and high-contrast case," *IEEE transactions on magnetics*, vol. 50, no. 2, pp. 117–120, 2014.

[135] Q.-A. Phan, O. Chadebec, G. Meunier, J.-M. Guichon, and B. Bannwarth, "3-d BEM formulations for eddy-current problems with multiply-connected domains and circuit coupling," *IEEE Transactions on Magnetics*, vol. 58, no. 4, pp. 1–4, 2020.

[136] G. Meunier, J.-L. Coulomb, S. Salon, and L. Krähenbühl, "Hybrid finite element boundary element solutions for three dimensional scalar potential problems," *IEEE Transactions on Magnetics*, vol. 22, no. 5, pp. 1040–1042, 1986.

[137] D. Pusch and J. Ostrowski, "Robust FEM/BEM coupling for magnetostatics on multiconnected domains," *IEEE transactions on magnetics*, vol. 46, no. 8, pp. 3177–3180, 2010.

[138] R. Albanese and G. Rubinacci, "Magnetostatic field computations in terms of two-component vector potentials," *International journal for numerical methods in engineering*, vol. 29, no. 3, pp. 515–532, 1990.

[139] J. P. A. Bastos and N. Sadowski, *Electromagnetic modeling by finite element methods*. CRC press, 2003.

[140] C. Brebbia and J. Dominguez, "Boundary element methods for potential problems," *Applied Mathematical Modelling*, vol. 1, no. 7, pp. 372–378, 1977.

[141] P. D. Lax and A. N. Milgram, *IX. Parabolic Equations*, pp. 167–190. Princeton: Princeton University Press, 1955.

[142] F. Brezzi, "On the existence, uniqueness and approximation of saddle-point problems arising from lagrangian multipliers," *Publications mathématiques et informatique de Rennes*, no. S4, pp. 1–26, 1974.

[143] F. Brezzi, D. Boffi, L. Demkowicz, R. Durán, R. Falk, and M. Fortin, "Mixed finite elements, compatibility conditions, and applications," *Springer*, vol. 2, pp. 4–2, 2008.

[144] M. Harutyunyan and B. Simeon, "On a saddle point problem arising from magneto-elastic coupling," *Applied Mathematics Letters*, vol. 83, pp. 156–163, 2018.

[145] M. Harutyunyan, *Mathematical Modeling and Numerical Simulation of Magnetoelastic Coupling*. Phd thesis, Technische Universität Kaiserslautern, 2019.

[146] Z. Ren and A. Razek, "Computation of 3-d electromagnetic field using differential forms based elements and dual formulations," *International Journal of Numerical Modelling: Electronic Networks, Devices and Fields*, vol. 9, no. 1-2, pp. 81–98, 1996.

[147] J.-C. Nédélec, "Mixed finite elements in $\mathbb{R}^3$," *Numerische Mathematik*, vol. 35, no. 3, pp. 315–341, 1980.

[148] A. Bossavit, "Whitney forms: A class of finite elements for three-dimensional computations in electromagnetism," *IEE Proceedings A (Physical Science, Measurement and Instrumentation, Management and Education, Reviews)*, vol. 135, no. 8, pp. 493–500, 1988.

[149] A. A. Shabana, *Computational continuum mechanics*. John Wiley & Sons, 2018.

[150] O. Biro, K. Preis, G. Vrisk, K. Richter, and I. Ticar, "Computation of 3-d magnetostatic fields using a reduced scalar potential," *IEEE Transactions on Magnetics*, vol. 29, no. 2, pp. 1329–1332, 1993.

[151] J. Simkin and C. W. Trowbridge, "On the use of the total scalar potential on the numerical solution of fields problems in electromagnetics," *International Journal for Numerical Methods in Engineering*, vol. 14, pp. 423–440, 1979.

[152] J. B. Manges and Z. J. Cendes, "A generalized tree-cotree gauge for magnetic field computation," *IEEE Transactions on Magnetics*, vol. 31, no. 3, pp. 1342–1347, 1995.

[153] P. D. Ledger and S. Zaglmayr, "hp-finite element simulation of three-dimensional eddy current problems on multiply connected domains," *Computer Methods in Applied Mechanics and Engineering*, vol. 199, pp. 3386–3401, 2010.

[154] R. Zhuoxiang, "Solving 3d static field problems by dual formulations using potential variables," *Electric and Magnetic Fields: From Numerical Models to Industrial Applications*, pp. 213–216, 1995.

[155] P. Amestoy, I. Duff, and J.-Y. L'Excellent, "Multifrontal parallel distributed symmetric and unsymmetric solvers," *Computer Methods in Applied Mechanics and Engineering*, vol. 184, no. 2, pp. 501–520, 2000.

[156] L. Greengard and V. Rokhlin, "A fast algorithm for particle simulations," *Journal of Computational Physics*, vol. 73, pp. 325–348, 1987.

[157] S. Börm and L. Grasedyck, "Hybrid cross approximation of integral operators," *Numerische Mathematik*, vol. 101, pp. 221–249, 2005.

[158] Y. Saad, *Iterative Methods for Sparse Linear Systems*. Society for Industrial and Applied Mathematics, second ed., 2003.

[159] R. Albanese and G. Rubinacci, "Integral formulation for 3d eddy-current computation using edge elements," *IEE Proceedings A (Physical Science, Measurement and Instrumentation, Management and Education, Reviews)*, vol. 135, no. 7, pp. 457–462, 1988.

[160] C. Rubeck, J.-P. Yonnet, H. Allag, B. Delinchant, and O. Chadebec, "Analytical calculation of magnet systems: Magnetic field created by charged triangles and polyhedra," *IEEE Transactions on Magnetics*, vol. 49, no. 1, pp. 144–147, 2013.

[161] C. Geuzaine and J.-F. Remacle, "Gmsh: A 3-d finite element mesh generator with built-in pre-and post-processing facilities," *International journal for numerical methods in engineering*, vol. 79, no. 11, pp. 1309–1331, 2009.

[162] G. Mur, "Edge elements, their advantages and their disadvantages," *IEEE Transactions on Magnetics*, vol. 30, pp. 3552–3557, 1994.

[163] C. Neagoe and F. Ossart, "Analysis of convergence in nonlinear magnetostatic finite elements problems," *IEEE Transactions on Magnetics*, vol. 30, pp. 2865–2868, 1994.

[164] H. G. Matthies and J. Steindorf, "Partitioned strong coupling algorithms for fluid–structure interaction," *Computers & Structures*, vol. 81, no. 8, pp. 805–812, 2003. K.J Bathe 60th Anniversary Issue.

[165] J. Poblet-Puig and A. Rodríguez-Ferran, "The block Gauss–Seidel method in sound transmission problems," *Journal of Computational Acoustics*, vol. 18, pp. 13–30, 2010.

[166] M. Mehl, B. Uekermann, H. Bijl, D. Blom, B. Gatzhammer, and A. van Zuijlen, "Parallel coupling numerics for partitioned fluid–structure interaction simulations," *Computers & Mathematics with Applications*, vol. 71, no. 4, pp. 869–891, 2016.

[167] G. H. Hardy, J. E. Littlewood, and G. Pólya, *Inequalities (Cambridge mathematical library)*. cambridge university press, 1934.

[168] D. G. Feingold and R. S. Varga, "Block diagonally dominant matrices and generalizations of the Gerschgorin circle theorem," *Pacific Journal of Mathematics*, 1962.

[169] A. Spencer, "Theory of Invariants," in *Mathematics*, pp. 239–353, Elsevier, 1971.

[170] W. Beckert and W. S. Kreher, "Modelling piezoelectric modules with interdigitated electrode structures," *Computational Materials Science*, vol. 26, pp. 36–45, 2003.

[171] B. Uekermann, B. Gatzhammer, and M. Mehl, "Coupling algorithms for partitioned multi-physics simulations," *Lecture Notes in Informatics (LNI), Proceedings - Series of the Gesellschaft fur Informatik (GI)*, 01 2014.

[172] P. Dular, C. Geuzaine, F. Henrotte, and W. Legros, "A general environment for the treatment of discrete problems and its application to the finite element method," *IEEE Transactions on Magnetics*, vol. 34, no. 5, pp. 3395–3398, 1998.

[173] X. Brunotte, *Modélisation de l'Infini et Prise en Compte de Régions Magnétiques Minces Application à la Modélisation des Aimantations de Navires*. PhD thesis, Institut National Polytechnique Grenoble (INPG), 1991.

[174] P. Kotiuga, "Essential arithmetic for evaluating three dimensional vector finite element interpolation schemes," *IEEE transactions on magnetics*, vol. 27, no. 6, pp. 5208–5210, 1991.

[175] T. Lafont, L. Gimeno, J. Delamare, G. A. Lebedev, D. Zakharov, B. Viala, O. Cugat, N. Galopin, L. Garbuio, and O. Geoffroy, "Magnetostrictive–piezoelectric composite structures for energy harvesting," *Journal of Micromechanics and Microengineering*, vol. 22, 2011.

[176] O. Geoffroy, D. O'Brien, O. Cugat, and J. Delamare, "Practical and theoretical investigations of a rotating coilless actuator using the inverse magnetostrictive effect," *IEEE Transactions on Magnetics*, vol. 46, no. 2, pp. 606–609, 2010.

[177] A. Jemai, F. Najar, M. Chafra, and Z. Ounaies, "Advanced parametric analysis of piezoelectric actuators with interdigitated electrodes having various cross-sections," *Lecture Notes in Control and Information Sciences*, vol. 789, pp. 489–499, 01 2015.

[178] M. E. Gurtin, E. Fried, and L. Anand, *The mechanics and thermodynamics of continua*. Cambridge University Press, 2010.

[179] R. W. Girdler, "The measurement and computation of anisotropy of magnetic susceptibility of rocks," *Geophysical Journal International*, vol. 5, pp. 34–44, 1961.

[180] B. R. Lienert, "Monte carlo simulation of errors in the anisotropy of magnetic susceptibility: A second-rank symmetric tensor," *Journal of Geophysical Research: Solid Earth*, vol. 96, no. B12, pp. 19539–19544, 1991.

[181] P. Rochette, M. Jackson, and C. Aubourg, "Rock magnetism and the interpretation of anisotropy of magnetic susceptibility," *Reviews of Geophysics*, vol. 30, no. 3, pp. 209–226, 1992.

Appendix A

Analytical expressions of the magneto-mechanical consitutive laws based on the invariants approach

A.1 Expression of the Helmholtz free energy

As expressed in Section 3.3, under the hypothesis of the isotropy of the Helmholtz free energy, it can be expressed as a polynomial expression of 6 invariants :

$$I_1 = tr(\boldsymbol{S}), \tag{A.1}$$
$$I_2 = tr(\boldsymbol{S}^2), \tag{A.2}$$
$$I_3 = tr(\boldsymbol{S}^3), \tag{A.3}$$
$$I_4 = \boldsymbol{B} \cdot \boldsymbol{B}, \tag{A.4}$$
$$I_5 = \boldsymbol{B} \cdot \tilde{\boldsymbol{S}} \cdot \boldsymbol{B}, \tag{A.5}$$
$$I_6 = \boldsymbol{B} \cdot \tilde{\boldsymbol{S}}^2 \cdot \boldsymbol{B}, \tag{A.6}$$

with $\tilde{\boldsymbol{S}}$ the deviatoric part of the strain tensor. Under the hypothesis of linear elasticity for the uncoupled mechanical behavior, the Helmholtz free energy can be expressed by a polynomial expression of 5 invariants,

$$\psi = \frac{1}{2}\lambda I_1 + \mu I_2 + \sum_{i=1}^{n_\alpha} \alpha_i I_4^i + \sum_{i=1}^{n_\beta} \beta_i I_5^i + \sum_{i=1}^{n_\gamma} \gamma_i I_6^i, \tag{A.7}$$

where n_α is the number of considered α coefficients, and so on for n_β aand n_γ. The Cauchy stress tensor and magnetic field can then be obtained by the analytical differentiation of ψ,

$$\boldsymbol{T}(\boldsymbol{B}, \boldsymbol{S}) = \frac{\partial \psi}{\partial \boldsymbol{S}}, \tag{A.8}$$

$$\boldsymbol{H}(\boldsymbol{B}, \boldsymbol{S}) = \frac{\partial \psi}{\partial \boldsymbol{B}}. \tag{A.9}$$

A.2 Expression of the magnetic constitutive law and reluctivity

The derivative of the invariants involving the magnetic flux density with respect to the magnetic flux density are the following:

$$\frac{\partial I_4^i}{\partial \boldsymbol{B}} = 2i\ I_4^{i-1} \boldsymbol{B}, \tag{A.10}$$

$$\frac{\partial I_5}{\partial \boldsymbol{B}} = 2\tilde{\boldsymbol{S}} \cdot \boldsymbol{B}, \tag{A.11}$$

$$\frac{\partial I_5^i}{\partial \boldsymbol{B}} = i\ I_5^{i-1} \frac{\partial I_5}{\partial \boldsymbol{B}}, \tag{A.12}$$

$$\frac{\partial I_6}{\partial \boldsymbol{B}} = 2\tilde{\boldsymbol{S}}^2 \cdot \boldsymbol{B}, \tag{A.13}$$

$$\frac{\partial I_6^i}{\partial \boldsymbol{B}} = i\ I_6^{i-1} \frac{\partial I_6}{\partial \boldsymbol{B}}. \tag{A.14}$$

Considering (A.9), (A.7) and (A.10)-(A.14), the magnetic constitutive law is,

$$\boldsymbol{H} = \sum_{i=1}^{n_\alpha} 2i\alpha_i (\boldsymbol{B} \cdot \boldsymbol{B})^{i-1} \cdot \boldsymbol{B} + \sum_{i=1}^{n_\beta} 2i\beta_i I_5^{i-1} \tilde{\boldsymbol{S}} \cdot \boldsymbol{B} + \sum_{i=1}^{n_\gamma} 2i\gamma_i I_6^{i-1} \tilde{\boldsymbol{S}}^2 \cdot \boldsymbol{B}. \tag{A.15}$$

By identification, the analytical expression of the magnetic reluctivity is the following,

$$\boldsymbol{\nu} = \sum_{1}^{n_\alpha} 2i\alpha_i (\boldsymbol{B}\cdot\boldsymbol{B})^{i-1}\boldsymbol{I_3} + \sum_{1}^{n_\beta} 2i\beta_i I_5^{i-1}\tilde{\boldsymbol{S}} + \sum_{1}^{n_\gamma} 2i\gamma_i I_6^{i-1}\tilde{\boldsymbol{S}}^2, \tag{A.16}$$

with $\boldsymbol{I_3}$ the second order identity tensor.

A.3 Expression of mechanical behavioral law

The symmetry of the strain tensor makes the analytical differentiation of the energy not as trivial as for the magnetic field. Indeed,

$$\frac{\partial \boldsymbol{S}}{\partial \boldsymbol{S}} \tag{A.17}$$

is not equal to the fourth order identity tensor, this makes its writing in tensor form more complicated than for the magnetic field. Concerning the two first invariants I_1 and I_2,

$$\frac{\partial}{\partial \boldsymbol{S}}\left(\frac{1}{2}\lambda I_1 + \mu I_2\right) = \boldsymbol{c} : \boldsymbol{S} \tag{A.18}$$

where $\boldsymbol{c}$ is the elasticity tensor of an isotropic material with λ and μ as Lamé coefficients. In a Cartesian coordinate system, the analytical differentiation of I_5 by $\boldsymbol{S}$ gives:

$$\frac{\partial I_5}{\partial \boldsymbol{S}} = \begin{bmatrix} \frac{2}{3}B_1^2 - \frac{1}{3}B_2^2 - \frac{1}{3}B_3^2 & 2B_1B_2 & 2B_1B_3 \\ 2B_1B_2 & -\frac{1}{3}B_1^2 + \frac{2}{3}B_2^2 - B_3^2/3 & 2B_2B_3 \\ 2B_1B_3 & 2B_2B_3 & -\frac{1}{3}B_1^2 - \frac{1}{3}B_2^2 + \frac{2}{3}B_3^2 \end{bmatrix}. \tag{A.19}$$

The analytical differentiation of I_6 by $\boldsymbol{S}$ gives the following symmetric second order tensor,

$$\left(\frac{\partial I_6}{\partial \boldsymbol{S}}\right)_{11} = \frac{8}{9}B_1^2S_{11} + \frac{2}{9}B_2^2S_{11} + \frac{2}{9}B_3^2S_{11} - \frac{4}{9}4B_1^2S_{22} - \frac{4}{9}B_2^2S_{22} + \frac{2}{9}B_3^2S_{22} - \frac{4}{9}B_1^2S_{33} + \frac{2}{9}B_2^2S_{33} - \frac{4}{9}B_3^2S_{33} + \frac{2}{3}B_1B_2S_{12} + \frac{2}{3}B_1B_3S_{13} - \frac{4}{3}B_2B_3S_{23}, \tag{A.20}$$

$$\left(\frac{\partial I_6}{\partial \boldsymbol{S}}\right)_{12} = 2B_1^2S_{12} + 2B_2^2S_{12} + \frac{2}{3}B_1B_2S_{11} + 2B_2B_3S_{13} + \frac{2}{3}B_1B_2S_{22} + 2B_1B_3S_{23} - \frac{4}{3}B_1B_2S_{33}, \tag{A.21}$$

$$\left(\frac{\partial I_6}{\partial \boldsymbol{S}}\right)_{13} = 2B_1^2S_{13} + 2B_3^2S_{13} + \frac{2}{3}B_1B_3S_{11} + 2B_2B_3S_{12} + 2B_1B_2S_{23} - \frac{4}{9}B_1B_3S_{22} + \frac{2}{3}B_1B_3S_{33}, \tag{A.22}$$

$$\left(\frac{\partial I_6}{\partial \boldsymbol{S}}\right)_{22} = \frac{2}{9}B_3^2S_{11} - \frac{4}{9}B_2^2S_{11} - \frac{4}{9}B_1^2S_{11} + \frac{2}{9}B_1^2S_{22} + \frac{8}{9}B_2^2S_{22} + \frac{2}{9}B_3^2S_{22} + \frac{2}{9}B_1^2S_{33} - \frac{4}{9}B_2^2S_{33} - \frac{4}{9}B_3^2S_{33} + \frac{2}{3}B_1B_2S_{12} - \frac{4}{3}B_1B_3S_{13} + \frac{2}{3}B_2B_3S_{23}, \tag{A.23}$$

$$\left(\frac{\partial I_6}{\partial \boldsymbol{S}}\right)_{23} = 2B_2^2S_{23} + 2B_3^2S_{23} + 2B_1B_2S_{13} + 2B_1B_3S_{12} - \frac{4}{3}B_2B_3S_{11} + \frac{2}{3}B_2B_3S_{22} + \frac{2}{3}B_2B_3S_{33}, \tag{A.24}$$

$$\left(\frac{\partial I_6}{\partial \boldsymbol{S}}\right)_{33} = \frac{2}{9}B_2^2S_{11} - \frac{4}{9}B_1^2S_{11} - \frac{4}{9}B_3^2S_{11} + \frac{2}{9}B_1^2S_{22} - \frac{4}{9}B_2^2S_{22} - \frac{4}{9}B_3^2S_{22} + \frac{2}{9}B_1^2S_{33} + \frac{2}{9}B_2^2S_{33} + \frac{8}{9}B_3^2S_{33} - \frac{4}{3}B_1B_2S_{12} + \frac{2}{3}B_1B_3S_{13} + \frac{2}{3}B_2B_3S_{23}, \tag{A.25}$$

The contribution of powers of invariants can then be written as,

$$\frac{\partial I_5^i}{\partial \boldsymbol{S}} = i I_5^{i-1} \frac{\partial I_5}{\partial \boldsymbol{S}}, \tag{A.26}$$

$$\frac{\partial I_6^i}{\partial \boldsymbol{S}} = i I_6^{i-1} \frac{\partial I_6}{\partial \boldsymbol{S}}. \tag{A.27}$$

The mechanical constitutive law can then be written as,

$$\boldsymbol{T} = \boldsymbol{c} : \boldsymbol{S} + \sum_1^{n_\beta} i I_5^{i-1} \frac{\partial I_5}{\partial \boldsymbol{S}} + \sum_1^{n_\gamma} i I_6^{i-1} \frac{\partial I_6}{\partial \boldsymbol{S}} \tag{A.28}$$

Appendix B

Identification of materials coefficients from the experimental B(H) curves

The expression of the magneto-mechanical constitutive laws from the Helmholtz free energy is made in terms of a number of material coefficients λ, μ, α_i, β_i and γ_i. They have to be identified from experimental data. the fitting of the experimental $B(H)$ curves of Galfenol from [14] was performed as follows: supposing an isotropic material, the fitting of a single $B(H)$ curve is needed. As the use of 11 α, 1 β and 2 γ coefficients proved to fit accurately the experimental $B(H)$ curves at -40 MPa in the literature [14], we decided to use this number of coefficients. Also, the Lamé coefficients, representing the mechanical response at low magnetic fields, were taken identical to their values in [14].

In order to fit the experimental $B(H)$ curves, it is needed to express $\boldsymbol{H}$ only as a function of $\boldsymbol{B}$ and the stress conditions of the experimental curves, in our case, a uni-axial stress T_0. The expressions (A.9) and (A.8) can be simplified by assuming uni-axial stress, magnetic field and magnetic flux density along the (z) direction. In particular, considering uni-axial stress, S_{11}, taken equal to S_{22}, can be expressed analytically as a function of T_0 and S_{33}, we can therefore remove the dependence of H_3 on S_{11} and S_{22}. If now we consider $n_\beta = 1$ and $n_\gamma = 2$ The equation,

$$T_{33} = T_0, \tag{B.1}$$

with T_0 a given stress, can be solved analytically, giving three complex solutions for S_{33}. For B between the range of the curves to be fitted,

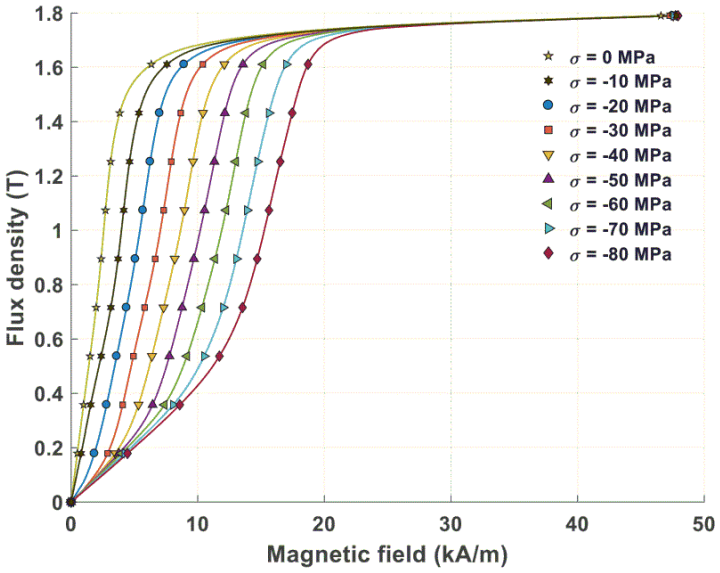

Figure B.1: Experimental B(H) curves for Galfenol at different stress levels, from [14]

this complex part was observed to be around 7 orders of magnitude lower than their real part for all three solutions, and was therefore neglected. Concerning the real part, two of the solutions give strains of the order of 300 whereas the last, values lower to 10^{-3}. Given that only one solution gives acceptable values for strains, we identify this solution as the value for S_{33}. This solution is given by an analytical expression of S_{33} as a function of B_3, β, μ, λ, γ_1 and γ_2. S_{33} Can then be replaced by this analytical expression in (A.9). Having removed the dependence of H_3 on S_{33}, we can construct the scalar function,

$$\epsilon_{H(B)}(\alpha_1, ...\alpha_{11}, \beta, \gamma_1, \gamma_2) = \int (H(\alpha_1, ...\alpha, \beta, \gamma_1, \gamma_2, B_3) - H_{\text{exp}}(B))^2 dB, \tag{B.2}$$

which computes, for a given set of coefficients, the error between the $H(B)$ curve described by the set of coefficients in question and the experimental $H(B)$ curve, H_{exp}. A method of gradient descent was used in order to minimize this function, with the 0 MPa experimental curves from [14]. As a starting point of the gradient descent, the set of coefficients presented in [14] were chosen, which represent the $H(B)$ curves at -40 MPa. The fitted

curve is presented in Figure B.1.

The function $\epsilon_{H(B)}$ was found to have numerous local minima, resulting in coefficients translating into non-physical behavior, such as negative reluctivity and or a non-physical dependence on T_0: tension leading to higher H_3 for a given B_3 and conversely, compression leading to lower H_3 for a given B_3.

After some manipulation, particularly of coupled coefficients β_1, γ_1 and γ_2, the following set of coefficients was found to fit very well the experimental $B(H)$ curves and gave a physical response to compressive and tensile stress:

$$\alpha_1 = 1514.24332 \tag{B.3}$$
$$\alpha_2 = 0 \tag{B.4}$$
$$\alpha_3 = 91.27778 \tag{B.5}$$
$$\alpha_4 = 0 \tag{B.6}$$
$$\alpha_5 = 64.87962 \tag{B.7}$$
$$\alpha_6 = -113.95817 \tag{B.8}$$
$$\alpha_7 = 44.23025 \tag{B.9}$$
$$\alpha_8 = 0 \tag{B.10}$$
$$\alpha_9 = 0 \tag{B.11}$$
$$\alpha_{10} = -1.36993 \tag{B.12}$$
$$\alpha_{11} = 0.28591 \tag{B.13}$$
$$\beta_1 = -6.97049 \cdot 10^6 \tag{B.14}$$
$$\gamma_1 = 1.12800 \cdot 10^{10} \tag{B.15}$$
$$\gamma_2 = -6.97696 \cdot 10^5 \tag{B.16}$$

The $B(H)$ curves for stress of 0 MPa, -10 MPa and 10 MPa generated from the set of coefficients above are presented in Figure B.2 along with the experimental curves for 0 MPa and -10 MPa [14]. We observe that both set of curves are in good agreement. The experimental curves in question were determined under compressive stress only, we will nevertheless use the proposed model for compressive and tensile stress and therefore extrapolate the behavior of Galfenol for tensile stress. Under relatively low stress, this seems to be a reasonable approximation.

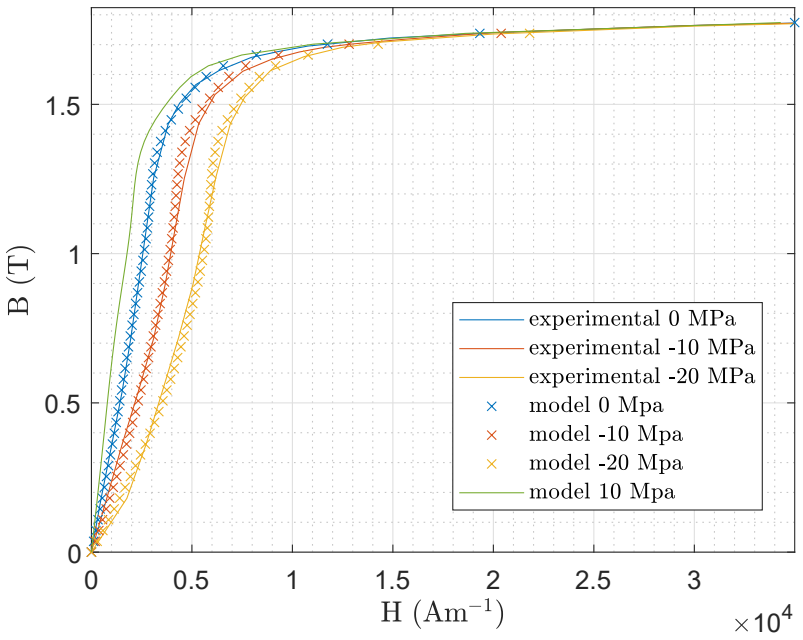

Figure B.2: B(H) curves of model vs experimental curves [14]

Appendix C

Rotation of coupling tensors

Coupling tensors, piezoelectric and piezomagnetic are usually available for materials poled in the (z) direction. In order to model materials in other directions, these tensors have to be rotated, this corresponds to a reference change for matrices form reference frame $\mathcal{R}$ related to axes (xyz) to reference frame $\mathcal{R}'$ related to axes (x'y'z'). If materials are considered poled in a given direction, in all generality, three rotations have to be considered.

For the particular case of piezoelectric and poled magnetostrictive materials, these tensors are isotropic in the (xOy) plane, therefore, only two rotations are needed, one of angle θ, in the (xOz) plane, and the other of angle ϕ in the (xOy) plane. Each of these rotations is associated to a rotation matrix,

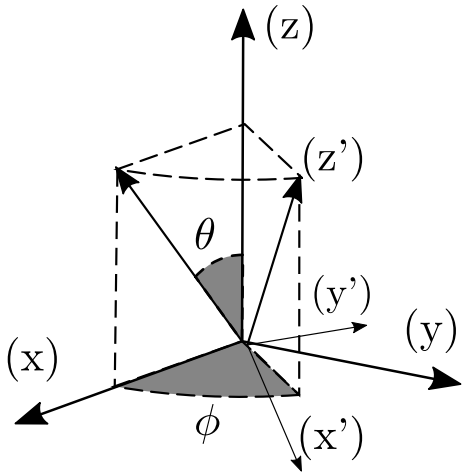

Figure C.1: Rotations necessary for the change of reference from (xyz) to (x'y'z')

$$\boldsymbol{A_\theta} = \begin{bmatrix} \cos\theta & 0 & -\sin\theta \\ 0 & 1 & 0 \\ \sin\theta & 0 & \cos\theta \end{bmatrix}, \tag{C.1}$$

$$\boldsymbol{A_\phi} = \begin{bmatrix} \cos\phi & \sin\phi & 0 \\ -\sin\phi & \cos\phi & 0 \\ 0 & 0 & 1 \end{bmatrix}. \tag{C.2}$$

The application of these two rotations corresponds to a rotation matrix $\boldsymbol{A}$,

$$\boldsymbol{A} = \boldsymbol{A_\theta A_\phi} \tag{C.3}$$

Therefore, for a vector, $\boldsymbol{D}$ and a tensor $\boldsymbol{T}$ in $\mathcal{R}$, the expression of $\boldsymbol{D}$ and $\boldsymbol{T}$ in $\mathcal{R}'$, $\boldsymbol{D'}$ and $\boldsymbol{T'}$ is given by:

$$\boldsymbol{D'} = \boldsymbol{AD}, \tag{C.4}$$

$$\boldsymbol{M'} = \boldsymbol{A}\ \boldsymbol{M}\ {}^{\mathrm{t}}\boldsymbol{A}, \tag{C.5}$$

and conversely,

$$\boldsymbol{D} = {}^{\mathrm{t}}\boldsymbol{AD'}, \tag{C.6}$$

$$\boldsymbol{M} = {}^{\mathrm{t}}\boldsymbol{A}\ \boldsymbol{M}\ \boldsymbol{A'}. \tag{C.7}$$

For a tensor $\boldsymbol{T_V}$ in Voigt notation, second order tensors $\boldsymbol{\Lambda}$ and $\boldsymbol{\Lambda'}$ can be obtained such as:

$$\boldsymbol{T'_V} = \boldsymbol{\Lambda T_V}, \tag{C.8}$$

$$\boldsymbol{T_V} = \boldsymbol{\Lambda' T'_V}, \tag{C.9}$$

by developing relation (C.5) and identifying term by term. The following matrix is obtained,

$$\boldsymbol{\Lambda} = \begin{bmatrix} A_{11}^2 & A_{12}^2 & A_{13}^2 & 2A_{12}A_{13} & 2A_{13}A_{11} & 2A_{11}A_{12} \\ A_{21}^2 & A_{22}^2 & A_{23}^2 & 2A_{22}A_{23} & 2A_{23}A_{21} & 2A_{21}A_{22} \\ A_{31}^2 & A_{32}^2 & A_{33}^2 & 2A_{32}A_{33} & 2A_{33}A_{31} & 2A_{31}A_{32} \\ A_{21}A_{31} & A_{22}A_{32} & A_{23}A_{33} & A_{22}A_{33}+A_{23}A_{32} & A_{21}A_{33}+A_{23}A_{31} & A_{22}A_{31}+A_{21}A_{32} \\ A_{31}A_{11} & A_{32}A_{12} & A_{33}A_{13} & A_{12}A_{33}+A_{13}A_{32} & A_{13}A_{31}+A_{11}A_{33} & A_{11}A_{32}+A_{12}A_{31} \\ A_{11}A_{21} & A_{12}A_{22} & A_{13}A_{23} & A_{12}A_{23}+A_{13}A_{22} & A_{13}A_{21}+A_{11}A_{23} & A_{11}A_{22}+A_{12}A_{21} \end{bmatrix} \tag{C.10}$$

and,

$$\boldsymbol{\Lambda'} = \begin{bmatrix} A_{11}^2 & A_{21}^2 & A_{31}^2 & 2A_{21}A_{31} & 2A_{31}A_{11} & 2A_{11}A_{21} \\ A_{12}^2 & A_{22}^2 & A_{32}^2 & 2A_{22}A_{32} & 2A_{32}A_{12} & 2A_{12}A_{22} \\ A_{13}^2 & A_{23}^2 & A_{33}^2 & 2A_{23}A_{33} & 2A_{33}A_{13} & 2A_{13}A_{23} \\ A_{12}A_{13} & A_{22}A_{23} & A_{32}A_{33} & A_{22}A_{33}+A_{32}A_{23} & A_{12}A_{33}+A_{32}A_{13} & A_{22}A_{13}+A_{12}A_{23} \\ A_{13}A_{11} & A_{23}A_{21} & A_{33}A_{31} & A_{21}A_{33}+A_{31}A_{23} & A_{31}A_{13}+A_{11}A_{33} & A_{11}A_{23}+A_{21}A_{13} \\ A_{11}A_{12} & A_{21}A_{22} & A_{31}A_{32} & A_{21}A_{32}+A_{31}A_{22} & A_{31}A_{12}+A_{11}A_{32} & A_{11}A_{22}+A_{21}A_{12} \end{bmatrix} \tag{C.11}$$

The piezoelectric constitutive laws in $\mathcal{R}'$, the reference frame of study have to be obtained by rotating the piezoelectric constitutive laws (3.84) and (3.83) in the $\mathcal{R}$ reference frame with tensors poled in the (z) direction, $\boldsymbol{e}$, $\boldsymbol{\epsilon}$ and $\boldsymbol{c}$. These rotated tensors are obtained by applying (C.6) and (C.7) to coupling terms. Indeed, the coupling term $\boldsymbol{e} : \boldsymbol{S'}$ being a vector, therefore, its expression in $\mathcal{R}'$ is given by :

$$\boldsymbol{e} : \boldsymbol{S'} = \boldsymbol{A}\boldsymbol{e}\boldsymbol{\Lambda'}\boldsymbol{S_{Voigt}}, \tag{C.12}$$

leading to,

$$\boldsymbol{e'} = \boldsymbol{A}\boldsymbol{e}\boldsymbol{\Lambda'}. \tag{C.13}$$

In the same way, the following transformations have therefore to be taken into account for the change in the poling direction of coupling tensors:

$$\boldsymbol{\varepsilon'} = \boldsymbol{A}\ \boldsymbol{\varepsilon}\ {}^{\mathrm{t}}\boldsymbol{A} \tag{C.14}$$
$$\boldsymbol{\mu'} = \boldsymbol{A}\ \boldsymbol{\mu}\ {}^{\mathrm{t}}\boldsymbol{A} \tag{C.15}$$
$$\boldsymbol{\nu'} = \boldsymbol{A}\ \boldsymbol{\nu}\ {}^{\mathrm{t}}\boldsymbol{A} \tag{C.16}$$
$$\boldsymbol{h'} = \boldsymbol{A}\ \boldsymbol{h}\ \boldsymbol{\Lambda'} \tag{C.17}$$
$$\boldsymbol{q'} = \boldsymbol{A}\ \boldsymbol{h}\ \boldsymbol{\Lambda'} \tag{C.18}$$
$$\boldsymbol{c'} = \boldsymbol{\Lambda}\ \boldsymbol{c}\ \boldsymbol{\Lambda'}. \tag{C.19}$$

Résumé étendu

La découverte de matériaux actifs, qui présentent un couplage intrinsèque entre leurs propriétés électriques et magnétiques, a suscité beaucoup d'intérêt, pour les nouvelles applications qu'ils permettent et pour les applications où le couplage électromagnétique souhaité est autrement négligeable. En effet, la conversion d'énergie dans les transducteurs ou actionneurs électriques est basée sur des interactions électromagnétiques, qui lient la force électromotrice aux variations temporelles de la densité dd l'induction magnétique. Ces phénomènes sont parfois difficiles à exploiter, notamment pour les petits dispositifs soumis à des champs de très basse fréquence.

L'effet magnétoélectrique (ME) se présente sous la forme d'une polarisation électrique induite par une aimantation ou, inversement, d'une aimantation induite par une polarisation électrique. Les matériaux susmentionnés, qui sont ferroélectriques et ferromagnétiques, présentent des effets ME. Si les matériaux ME monophasés présentent des propriétés prometteuses, pour l'instant, cet effet apparaît principalement à des températures cryogéniques. L'utilisation de structures composites actives constituées de l'association mécanique de matériaux ferroélectriques et ferromagnétiques permet d'obtenir un effet ME à température ambiante, supérieur de plusieurs ordres de grandeur à l'effet ME des matériaux monophasés. Ces structures composites sont constituées de matériaux piézoélectriques, qui présentent un fort couplage électromécanique, et de matériaux magnétostrictifs, qui présentent de fortes propriétés magnéto-mécaniques. Les structures hétérogènes qui en résultent présentent des effets ME. Elles permettent de nouvelles applications et rivalisent avec leurs homologues conventionnels. Le présent travail porte sur la modélisation de ces structures.

La modélisation des dispositifs ME peut être effectuée par des approches analytiques pour obtenir une estimation de leur réponse. Elles sont cependant limitées à des géométries triviales. Les méthodes numériques, telles que la méthode des éléments finis, ne souffrent pas de telles limitations. Cependant, la modélisation des phénomènes magnétiques nécessite la modélisation des phénomènes magnétiques non seulement dans le dispositif ME mais aussi dans l'air entourant le dispositif, car les phénomènes magnétiques se produisent dans tout l'espace libre entourant le dispositif et entourant la source du champ magnétique. Une grande région d'air représentant la troncature de l'espace libre infini entourant le dispositif et la source du champ doit alors être prise en compte, et la précision de la solution dépendra de la taille du domaine d'air tronqué considéré : plus la région d'air est

grande, plus la solution est précise. Néanmoins, la prise en compte de cette grande région d'air se traduit par le fait que de nombreuses, voire la plupart des inconnues du problème (également appelées degrés de liberté, ou DoF, du problème) sont situées à l'extérieur de l'appareil à modéliser. Pour notre application, dans un contexte purement FEM, conserver un nombre raisonnable d'inconnues au problème est incompatible avec une précision acceptable de la solution.

Dans ce manuscrit, une nouvelle approche de la modélisation des effets ME consistant à coupler la FEM avec la méthode des éléments de frontière (BEM) est proposée. Cette approche réduit le problème à l'extérieur du domaine à un problème sur la frontière du dispositif, ce qui diminue considérablement le nombre de DoF. En outre, en évitant la troncature de l'espace libre entourant le dispositif, elle prédit mieux le comportement du champ magnétique à l'intérieur du domaine actif. Malgré sa mise en œuvre plus complexe et les défis numériques qu'elle implique, en particulier en ce qui concerne la résolution du problème discret, le couplage entre la FEM et de la BEM apparaît comme une approche très puissante pour la modélisation des effets de l'EM dans les structures composites.

Ce manuscrit est organisé en quatre chapitres. Dans le premier chapitre, l'effet ME est présenté plus en détail, dans les matériaux monophasés ainsi que dans les structures composites. Nous présentons les phénomènes constitutifs à l'origine de l'effet ME, les couplages électromécaniques et magnéto-mécaniques locaux et leur modélisation. Ensuite, nous introduisons les approches de modélisation des effets ME : d'abord par des approches analytiques et ensuite par des méthodes numériques. La dernière section concerne l'introduction de la stratégie proposée pour la modélisation numérique des effets électromécaniques dans les structures composites.

Le deuxième chapitre est consacré à la formulation des outils numériques pour les problèmes monophysiques, sans couplage multiphysique. Nous présentons les équations à résoudre : Les équations de Maxwell et les équations des milieux continus, dans leurs formes fortes et faibles. Ces équations sont discrétisées, ce qui donne un système matriciel à résoudre. La précision des deux formulations FEM-BEM magnétiques, moins classiques que leurs homologues électriques et mécaniques, est étudiée pour des lois constitutives linéaires et non linéaires.

Le troisième chapitre concerne la modélisation multi-physique des matériaux actifs, la modélisation FEM des effets électromécaniques et l'approche FEM-BEM de la modélisation des phénomènes magnétiques. Les lois constitutives choisies sont présentées et les problèmes multi-physiques impliqués sont

formulés en termes de leurs formes faibles et discrètes. Les défis liés à la résolution des systèmes discrets sont traités et des algorithmes de résolution adaptés sont proposés et étudiés : des algorithmes de type Gauss-Seidel par bloc.

Dans le quatrième chapitre, nous appliquons les approches de modélisation proposées pour les effets ME à la modélisation de deux structures composites ME. La première est un composite ME à trois couches qui fonctionne comme un récuperateur d'énergie. Toutes les formulations développées sont appliquées à la modélisation de ce dispositif, en particulier, les deux formulations linéaires sont comparées et validées par rapport à une approche FEM. L'autre application choisie est un composite ME rotatif sans bobine composé d'une structure composite ME sous l'effet d'un aimant permanent. Par son interaction magnétique avec l'aimant, ce dispositif peut fonctionner comme un générateur ou comme un actionneur. Il est étudié dans les deux situations. En particulier, le calcul des forces et des couples mécaniques est étudié et deux méthodes de calcul sont présentées.